Process Chain Development of a ReSOC System

with ammonia as fuel and steam electrolysis

Amogh G. Amladi



Process Chain Development of a ReSOC System

with ammonia as fuel and steam electrolysis

by

Amogh G. Amladi

to obtain the degree of Master of Science at the Delft University of Technology, to be defended publicly on Tuesday February 25, 2020 at 9:30 AM.

Student number: 4728335

Project duration: April 15, 2019 – February 25, 2020

Thesis committee: Prof. Dr. P. V. Aravind, TU Delft, Thesis supervisor

Prof. Dr. A. J. M. van Wijk, TU Delft Prof. Dr. B. J. Boersma, TU Delft Dr. J. A. Posada Duque, TU Delft Ir. T. Woudstra, TU Delft

This thesis is confidential and cannot be made public until February 25, 2020.

An electronic version of this thesis is available at http://repository.tudelft.nl/.





Acknowledgements

Firstly, I would like to thank Prof. Aravind for believing in me and giving me an opportunity to work in his group. This thesis has been the most interesting part of my Master programme, and has inspired me to continue my career in this field. His meticulous scrutiny, advice and scientific approach have helped me to a very great extent, granting new perspectives to my thesis.

I gratefully acknowledge Prof. A.J.M. van Wijk, Prof. B.J. Boersma, Dr. J.A. Posada Duque and Ir. T. Woudstra for their participation in my thesis committee.

I would like to thank Dr. Vikrant Venkataraman for introducing this topic to me and his steadfast support at every stage of my research. His continued support through video calls, even after moving away, helped me shape my thesis to a significant extent. I would again like to thank Theo Woudstra for the long and deep discussions on system analysis over many afternoons. I would like to thank Tom, Biju, Luc, and other members of the fuel cells group for their recommendations, feedback and input throughout my research. Discussions with them were very fruitful and their knowledge and recommendations helped me immensely in the project.

I would also like to thank all my fellow students Srijan, Siddharth, Shashish, Maneesh, Karthick, Arjun, Rohan, and many others for creating a cheerful environment and healthy discussions related to our theses and our lives. My special thanks to Paridnya, and to Chaitanya, for their constant encouragement and support throughout the journey of this thesis.

Lastly, my deepest gratitude goes to my parents and my grandfather, whose value to me only grows with age, and without whom none of this would have been possible.

Abstract

Energy storage systems are an emerging field of interest for the future of electrical grids. With the rapid growth of renewable but intermittent sources of electricity, energy storage systems can help smooth the variations, making the grid more stable and reducing the need for maintaining an overcapacity of power production infrastructure. Among energy storage solutions, power-to-chemical storage is of particular interest due to the high energy density of chemicals and seasonal storage capabilities. Developments made in power-to-chemical technologies can also go a long way towards making the transportation and chemical and industries sustainable. The chemical considered in this work is ammonia (NH₃), which has advantages of being an easily liquefiable fuel, and has also been in industrial use for over a century.

This thesis project aims towards the development of an efficient power-to-ammonia energy storage system using reversible solid oxide cells. The system designed in this thesis is based on direct ammonia utilisation in fuel cell mode, and steam electrolysis coupled with Haber-Bosch ammonia synthesis in the electrolysis mode. A steady state process model is designed in Aspen Plus. This is followed by extensive thermodynamic exergy analysis, used as the basis for the further design and optimisation of the system, with a goal to maximise the round trip efficiency. Exergy analysis is used to identify the sources with most scope for improvement.

The final system can attain a maximum round trip efficiency of 61.20 %, improved from a basic system efficiency of 19.79 %. The maximum round trip efficiency is comparable to values reported in recent times for thermodynamically studied models from literature using other fuels, such as 56.72 % for methanol. The optimised system attains high efficiencies without the need for thermal energy storage or an afterburner. Further, it is demonstrated that the designed system is efficient enough that heat integration across modes with high temperature energy storage does not provide any significant benefit.

List of Abbreviations

Abbreviations

AICR Adiabatic indirect cooling reactor AQCR Adiabatic quench cooling reactor

ASC Anode-supported cell ASR Area specific resistance BoP Balance of plant

CaSZ Calcia-stabilised zirconia
CoP Coefficient of performance
CT Cold turbine (configuration)

EC Electrolysis cell

ESC Electrolyte-supported cell

FC Fuel cell

GDC Gadolinia-doped ceria
HT Hot turbine (configuration)
IDCR Internal direct cooling reactor
LCOE Levelised cost of electricity
LCOS Levelised cost of storage
LHV Lower heating value

LSGF Lanthanum strontium cobalt ferrite
LSGM Lanthanum strontium gallate magnesite
LSM Lanthanum strontium manganite

OCV Open circuit voltage PCM Phase change material

PEM Proton exchange membrane / polymer electrolyte membrane

PSA Pressure swing adsorption
ReSOC Reversible solid oxide cell
RTE Round trip efficiency
SDC Samaria-doped ceria
SMR Steam methane reforming
SOEC Solid oxide electrolysis cell

SOFC-H Proton-conducting solid oxide fuel cell SOFC-O Oxygen ion-conducting solid oxide fuel cell

TES Thermal energy storage
TIT Turbine inlet temperature
TPB Triple phase boundary
YSZ Yttria-stabilised zirconia

 \boldsymbol{x}

y

Symbols and Variables

```
Area [m<sup>2</sup>]
        Symmetry factor for electron transfer [-]
\alpha
β
        Approach to equilibrium [-]
        Specific heat capacity at constant pressure [JK<sup>-1</sup> mol<sup>-1</sup>]
c_{\rm p}
        Diffusion coefficient [m^2 s^{-1}]
\hat{D}
        Thickness (of cell layers) [m]
δ
d_{p}
        Pore diameter [m]
        Activation energy [J mol<sup>-1</sup>]
E_{act}
        Enthalpy [J mol<sup>-1</sup>]
        Entropy [J \, mol^{-1} \, K^{-1}]
s
        Porosity [-]
\epsilon
        Overpotential [V]
η
        Efficiency [-]
\eta
Ex
        Exergy [J]
        Faraday constant [Cmol<sup>-1</sup>]
        Gibbs free energy [J \, mol^{-1}]
g
        Pre-exponential factor for exchange current density [Am<sup>-2</sup>]
γ
        Current [A]
        Current density [Am<sup>-2</sup>]
        Exchange current density [Am<sup>-2</sup>]
j_0
        Molecular\ mass\ [gmol^{-1}]
        Number of cells in the stack [-]
        Number of electrons transferred in a reaction [-]
n
        Pressure [bar]
P
        Power [W]
0
        Heat [J]
        Reaction quotient [-]
Q_{\rm r}
        Specific resistivity [\Omega m^2]
        Universal gas constant [J mol<sup>-1</sup> K<sup>-1</sup>]
R
        Electrical resistance [\Omega]
R_{\rm e}
        Conductivity [\Omega^{-1} \, m^{-1}]
        Pre-exponential factor for conductivity [\Omega^{-1} m^{-1}]
\sigma_0
        Temperature [°C]
T
        Tortuosity [-]
U
        Voltage [V]
        Volume [m<sup>3</sup>]
V
W
        Work [J]
        Mole fraction [-]
```

Mole fraction (typically only in gas phase) [-]

Subscripts

act Activation

AE Air-side electrode

bulk Bulk flow
cell Cell
ch Chemical
conc Concentration
const Constant
d Diffusion

D Destruction (of exergy)EC Electrolysis mode

eff Effective elec Electrolyte eq Equilibrium ex Exergy

FC Fuel cell mode FE Fuel-side electrode

g Gaseous
irr Irreversible
Kn Knudsen
l Liquid
ohm Ohmic
rev Reversible
stack Stack

tm Thermo-mechanical tn Thermoneutral

TPB Triple-phase boundary

Contents

Lis	t of T	ables :	χv			
Lis	t of I	igures x	vii			
1	Intr	oduction	1			
2	2 Theoretical Background					
	2.1	Fundamentals of Reversible Solid Oxide Cells	3			
		2.1.1 Design and Materials for Solid Oxide Cells	3			
		2.1.2 Thermodynamics of Reversible Fuel Cells	4			
		2.1.3 Losses in Electrochemical Cells	5			
		2.1.4 Polarisation Curve and Thermal Behaviour	7			
	2.2	Fundamentals of Ammonia Synthesis	8			
	2.3	Exergy	9			
		2.3.1 Thermo-mechanical Exergy	9			
		2.3.2 Chemical Exergy	10			
		2.3.3 Exergy Loss	11			
3	Lite	rature Survey	13			
			13			
	3.2		16			
			19			
	3.4		21			
			22			
			~~			
4			23			
	4.1		23			
			23			
		8	24			
	4.0	0 0	24			
	4.2		26			
			26			
			26			
	4.3		27			
			27			
			28			
		I and the second se	29			
		4.3.4 Concentration Overpotentials				
	1 1	4.3.5 Cell Voltage and Stack Power				
	4.4		31			
			31			
			32			
		V 1	32			
	4 5		33			
	4.5	ı v	34			
	4.6	I and the second se	35			
		· · · · · · · · · · · · · · · · · · ·	35			
			35			
		8	36 36			
		// b // Hay Hychanger	< h			

xii Contents

	4.7		mance Analysis
		4.7.1	Definitions of Efficiency
5	Prel	liminaı	ry Analysis 39
	5.1	Stack	Performance Analysis
		5.1.1	Stack Level Parametric Analysis
			Thermoneutral Electrolysis Regions
			Conclusion of Stack Performance Analysis
	5.2		n Analysis - Basic Configuration
		5.2.1	Temperature Variation
		5.2.2	Current Density Variation
		5.2.3	Pressure Variation
		5.2.4	Conclusion of Basic Configuration Study
6			Configurations and Analysis 49
	6.1	Fuel C	ell Mode - Hot Turbine Configuration
		6.1.1	Methodology
		6.1.2	Effect of Air Recirculation Variation
		6.1.3	Effect of Stack Temperature Variation
		6.1.4	Effect of Current Density Variation
		6.1.5	Effect of Stack Pressure Variation
		6.1.6	Conclusion of Hot Turbine Configuration Analysis
	6.2		tell Mode - Cold Turbine Configuration
		6.2.1	Methodology
		6.2.2	Effect of Air Recirculation Variation
		6.2.3	Effect of Stack Temperature Variation
		6.2.4 6.2.5	Effect of Current Density Variation.65Effect of Stack Pressure Variation.66
		6.2.6	Conclusions of the Cold Turbine Configuration Analysis
	6.3		cell Mode - Comparison of Hot and Cold Turbine Configurations
	6.4		olysis Mode - Hot Turbine Configuration
	0.1	6.4.1	Design of Heat Integration Scheme
		6.4.2	Methodology
		6.4.3	Effect of Air Recirculation Variation
		6.4.4	Effect of Current Density Variation
		6.4.5	Effect of Stack Temperature Variation
		6.4.6	Effect of Stack Pressure Variation
		6.4.7	Conclusions of Hot Turbine Electrolysis Configuration Analysis
	6.5	Electr	olysis Mode - Cold Turbine Configuration
		6.5.1	Methodology
		6.5.2	Effect of Air Recirculation Variation
		6.5.3	Discussion
	6.6	Round	l Trip System Analysis
		6.6.1	Variation in Optimum Stack Pressure
		6.6.2	Variation of Optimum Current Density and Stack Temperature
		6.6.3	Optimised Parameters for the Reversible System
			Final Round Trip Results
	6.7	Key Ta	ke-aways
7	Eval	luatior	of the Use of Afterburner and Thermal Energy Storage
	7.1	Comp	arison with Afterburner systems
		7.1.1	Fuel Cell System with Afterburner
		7.1.2	Fuel Cell System with Auxiliary Power Cycle
		7.1.3	Electrolysis Mode for System with Afterburner
		7.1.4	Round Trip Operation for System with Afterburner
		7.1.5	Conclusion of Afterburner Study

Contents xiii

	7.2 Thermal Energy Storage	98
	7.2.1 Modelling	98
	7.2.2 Simulation Methodology	
	7.2.3 Variation in Heat Demand and Generation	
	7.2.4 System Performance with TES	
	7.3 Key Take-aways	105
8	Conclusions and Future Work 8.1 Conclusions and Discussion 8.2 Future Work	
Α	Ammonia Synthesis Loop	111
В	Stack Performance Tests	113
С	Fuel Cell Air Flow Variations	115
D	Exergy Flow Diagrams	119
Bik	bliography	125

List of Tables

2.1	Standard chemical exergy of species relevant to this system [1]	10
4.1	ReSOC stack parameters for base case.	26
4.2	Cell geometry for electrochemical calculations [2]	28
4.3	Material parameters for electrochemical calculations [2]	29
4.4	Operating parameters for ammonia synthesis loop	34
4.5	Operating parameters for gas purification subsystem	34
4.6	Miscellaneous balance of plant (BoP) operating parameters	36
4.7	Lower heating values of the fuels relevant to this system	38
5.1	Stack performance results - Base case ($T = 800$ °C, $p = 1.5$ bar, $j = 5000$ Am ⁻² , $U_f = 0.8$)	40
5.2	System simulation results - Basic configuration	43
5.3	Optimal operating points for basic configuration	48
6.1	Comparison of HT and CT configurations through energy and exergy analysis.	68
6.2	Optimum operating points for each mode - Hot turbine FC configuration	81
6.3	Optimum operating points in each mode - Cold turbine FC configuration	81
6.4	Energy and exergy analysis results of the improved configurations at the optimised operating points.	82
6.5	Comparison of exergy losses and round trip efficiency in the optimised basic and improved con-	-
	figurations	83
7.1	Energy and exergy analysis comparison of systems in fuel cell mode: system with no afterburner	
	(AB) vs. system with afterburner. Operating Point 1 is an example of an ordinary operating point. Operating Point 2 is an example of a point where the system without afterburner is at the oxygen	
	starvation limit.	88
7.2	Efficiency comparison of systems in fuel cell mode: system with no afterburner (AB) vs. system with afterburner vs. system with afterburner and auxiliary cycle. Stack operating parameters:	
	800 °C, 2500 Am ⁻²	89
7.3	Energy and exergy analysis comparison of systems in fuel cell mode: system with no afterburner	00
	(AB) vs. system with afterburner vs. system with afterburner and auxiliary cycle	91
7.4	Efficiency comparison of systems in electrolysis mode: system without afterburner vs. sys-	
	tem with afterburner (in FC mode). Stack operating parameters that are held constant: 800 °C,	
	2500 Am ⁻²	95
7.5	Energy and exergy analysis comparison of systems in electrolysis mode: system with no after-	
	burner (AB) vs. system with afterburner.	96
7.6	Comparison of exergy stored in chemical tanks: system without afterburner (AB) vs. system with	
	afterburner. Stack operating parameters: 800° C, $2500\mathrm{Am^{-2}}$, $5\mathrm{bar}$	96
7.7	Round trip efficiency comparison of systems: system without afterburner vs. system with afterburner and auxiliary cycle (in FC mode). Stack operating parameters that are held constant:	
	800 °C, 2500 Am ⁻²	97
7.8	Overall exergy analysis of reversible systems: system with no afterburner (AB) vs. system with	
	afterburner and auxiliary power cycle	97
8.1	Comparison of all the major configurations analysed in this thesis. All the configurations are	
	compared at their own optimum operating points for round trip efficiency.	108

List of Figures

2.1	Schematics of a solid oxide cell and planar cell stack					
2.2	Variation in thermodynamic quantities in a hydrogen-steam system with temperature. Figure by Butler [3], modified by Diaz-Rodriguez [4].					
2.3	Sample polarisation curve for a fuel cell [5]. The three regions of operation are shown					
2.4	4 Sample polarisation curve for a reversible cell. The reversible voltage, thermoneutral voltage and the thermal regions are also shown. Figure taken from Wendel [6].					
3.1	A comparison between the IDCR, 3-bed AQCR and 3-bed AICR under optimal conditions in terms of (a) N_2 conversion, and (b) temperature profiles. Figures taken from the work of Khademi and Sabbaghi [7]	2				
4.1	Process flowsheet for fuel cell mode - Basic configuration	2				
4.2	Process flowsheet for electrolysis mode - Basic configuration	2				
4.3	Schematic of Aspen Plus model of ReSOC stack in fuel cell mode	2				
4.4	Schematic of Aspen Plus model of ReSOC stack in electrolysis mode	2				
4.5	Process flowsheet for ammonia synthesis model	3				
4.6	Process flowsheets for water separation / gas purification in each mode	3				
5.1	Locus of thermoneutral points in electrolysis mode.	4				
5.2	Distribution of system exergy losses with the basic configuration - Base case and optimised case.	4				
5.3	Variation of fuel cell system performance with stack temperature - Basic configuration	4				
5.4	Variation of electrolysis system performance with stack temperature - Basic configuration	4				
5.5	Variation of the system performance with current density - Basic configuration. The exergy losses and airflow values are differential, with the first point of each line as the datum	4				
5.6	Variation of fuel cell system performance with stack pressure - Basic configuration	4				
5.7	Variation of electrolysis system performance with stack pressure - Basic configuration	4				
6.1	Process flowsheet for fuel cell mode - Improved hot turbine configuration	5				
6.2	Heat integration scheme for fuel cell mode - Improved hot turbine configuration	5				
6.3	Effect of air recirculation on fuel cell system performance. Power / Exergy loss values show the variation compared with first point of each line as datum. The operating parameters used in this example: 800° C, 10bar and 7500Am^{-2}	5				
6.4	Exceptional cases - Air recirculation limit reached before elimination of electric heating. Stack	J				
	parameters used in this example: 800 °C, 10 bar, 2500 Am ⁻²	5				
6.5	Variation of fuel cell system performance with stack temperature, in hot turbine configuration. The exergy losses are differential, with the first point of each line as the datum.	5				
6.6	Variation of fuel cell system performance with current density, in hot turbine configuration. The	J				
5.0	exergy loss values are differential, with the first point of each line as the datum.	5				
6.7	Variation of fuel cell system performance with stack pressure, in hot turbine configuration. The	Ü				
	exergy loss values are differential, with the first point of each line as the datum	5				
6.8	Process flowsheet for fuel cell mode - Improved cold turbine configuration	5				
	Heat integration schemes for fuel cell mode - Improved cold turbine configuration	6				
	Effect of air recirculation on system performance - Energy analysis	6				
6.11	Effect of air recirculation on system performance - Exergy analysis	6				
6.12	Variation of fuel cell system performance with stack temperature, in cold turbine configuration.					
	Exergy loss values in the plots are differential, with first point of each graph as datum	6				
6.13	Variation of fuel cell system performance with current density, in cold turbine configuration.					
	Exergy loss values in the plots are differential, with first point of each graph as datum.	6				

xviii List of Figures

6.14	Variation of fuel cell system performance with pressure, in cold turbine configuration. Exergy	
	loss values in the plots are differential, with first point of each graph as datum.	66
6.15	Efficiency comparison of hot and cold turbine configurations in fuel cell mode	69
6.16	Process flowsheet for electrolysis mode - Improved hot turbine configuration	71
6.17	Heat integration scheme for electrolysis mode - Improved hot turbine configuration	72
6.18	Effect of air recirculation on electrolysis system performance in endothermic region. Power /	
	Exergy loss values are differential, with first point of each line as datum.	73
6.19	Variation of electrolysis system performance with current density, in hot turbine configuration.	
	The power and exergy loss values are differential, with the first point of each line as the datum.	74
6.20	Variation of electrolysis system performance with temperature, in hot turbine configuration.	• -
0.20	The exergy loss values are differential, with the first point of each line as the datum.	75
6 21	Variation of electrolysis system performance with stack pressure, in hot turbine configuration.	13
0.21	The exergy loss values are differential, with the first point of each line as the datum.	76
6 22		70
6.22	Effect of air recirculation on system performance of cold turbine electrolysis configuration. Stack	
	parameters used in this example: 650 °C, 2.5 bar, 5000 Am ⁻² . The power/exergy loss values are	
	differential, with the first point of each line as the datum.	78
6.23	Effect of reversible operation on optimum stack pressure	80
- 1		0.0
7.1	Process flowsheet for fuel mode - Afterburner configuration.	86
7.2	Heat integration scheme for fuel mode - Afterburner configuration	87
7.3	Process flowsheet for fuel cell mode - Auxiliary power cycle configuration	90
7.4	Process flowsheet for electrolysis mode - Afterburner configuration	93
7.5	Heat integration scheme for electrolysis mode - Afterburner configuration.	94
7.6	Schematic of ReSOC stack models including thermal energy storage	99
7.7	Variation of system exergy efficiency, exergy loss, and system power output with respect to amount	
	of heat exergy stored in the TES	102
A.1	Various recycling configurations for ammonia synthesis. The components are labelled as fol-	
	lows: a = Synthesis Reactor, b = Refrigerated Condensation, c = Ambient Condensation, d =	
	Feed/Make-up gas compressor, e = Recycle gas compressor. Figure taken from the work of Appl	
	[8]	111
D 1	Westerface of a Harakan and the standard and a second and	114
B.I	Variation of cell voltage with stack operating parameters.	114
C.1	Simple schematic for air flows in a fuel cell stack with recirculation	115
C.1	Variation of fresh and exhaust airflows with air recirculation.	
	Variation of oxygen content with air recirculation.	
	Variation of oxygen content with fresh airflow.	117
C.5	Variation of the ratio of recirculated airflow to fresh airflow, based on variation in air recircula-	
	tion ratio	118
D 1	Evenery Flow Diagram for basic configuration in fuel cell made, entimized for DTE Steels oney	
D.1	Exergy Flow Diagram for basic configuration in fuel cell mode - optimised for RTE. Stack oper-	100
D A	ating parameters: 700 °C, 8.5 bar, 2500 Am ⁻² .	120
D.2	Exergy Flow Diagram for improved configuration in fuel cell mode - optimised for RTE. Stack	
	operating parameters: 800 °C, 7.5 bar, 2500 Am ⁻²	121
D.3	Exergy Flow Diagram for basic configuration in electrolysis mode - optimised for RTE. Stack	
	operating parameters: 700° C, 8.5 bar, $2500\mathrm{Am}^{-2}$	122
D.4	Exergy Flow Diagram for improved configuration in electrolysis mode - optimised for RTE. Stack	
	operating parameters: 800 °C, 7.5 bar, 2500 Am ⁻² .	123

Introduction

The generation of power from renewable sources is growing at a fast pace. From 2019 to 2024, the installed capacity of renewable power is expected to increase by 1200 GW [9]. However, the capacity factors for renewable power, especially from wind and solar PV, remain very low (25-50 %) [10] due to the intermittent nature of renewable sources. In order to make maximum use of the large capacity that is expected to come up, there is a pressing need for development of cheap and efficient large scale energy storage solutions. Large scale energy storage can can be beneficial even in grids that are not heavily based on renewables. The presence of efficient, large scale decentralised energy storage can also enhance the resilience of a grid during times of disasters or power plant failures.

Energy storage requirements differ according to their application. Short-term grid balancing requires quick response times, while seasonal energy storage requires high energy density. Various energy storage solutions differ widely in their characteristics. Batteries, flywheels, supercapacitors, etc. offer very quick response times and high energy density. However, these systems have low energy capacities and can also self-discharge over time [11], which limits them to only short or medium term storage. Pumped hydro storage, or compressed air storage can have large energy and power capacities, and quick response times. But they have low energy density [12], and therefore it can be difficult to find geographically suitable locations for storing large amounts of energy, especially for hydro power.

Chemical energy storage meets both the main criteria for long term energy storage, viz. high energy capacity and high energy density [12]. Using chemical energy storage, it is also possible to decouple energy and power capacities. Development of power-to-chemical conversion technologies can also help de-carbonise the chemical industry by providing sustainable non-fossil feedstock. However, the major drawback of chemical energy storage technologies is their high cost, and relatively low round-trip efficiency [12]. To improve these parameters, there has been significant research in the field of electrochemical systems for chemical energy storage solutions.

Reversible solid oxide cells (ReSOCs) are high temperature electrochemical cells, which offer the potential for reversible operation i.e. as electrolysers (power-to-chemical), or as fuel cells (chemical-to-power). Reversible operation can increase the utilisation factor of the equipment, lowering the effective cost of the system. Operation at high temperature has many advantages. It reduces losses, which enables more efficient operation. It also eliminates the need for precious metal catalysts, and increases the variety of fuels that can be used [13]. Lower losses in the electrolysis mode enable endothermic operation, which provides opportunities for integrating waste heat from industry, or from the fuel cell mode itself. For all these reasons, ReSOCs are a promising option for chemical energy storage. The working principles of solid oxide cells are described at an introductory level in Chapter 2, while an overview of the research in this field is given in Chapter 3.

Hydrogen is one of the simplest substances to produce in an electrochemical cell, through electrolysis of water or steam. It is also the chemical fuel with the highest specific energy [14]. However, it has very low density, and is difficult to liquefy due to its low critical temperature. This makes it a difficult substance to store in the large quantities that are required for seasonal storage . Therefore, it can be desirable to store hydrogen in the form of its chemical derivatives, particularly one that is easily liquefied. Hydrogen derivatives are also often desirable feedstock for chemical industries. Light hydrocarbons like syngas, methane and methanol have been widely studied for this purpose, as is elaborated in Chapter 3. Another simple and common derivative of hydrogen is ammonia. It is a light gas that can be easily liquefied under relatively mild conditions $(-33\,^{\circ}\text{C})$ at

2 1. Introduction

1 atm [15]). Being one of the most synthesised chemicals in the world, ammonia is also a valuable industrial feedstock. Therefore, ammonia is a chemical that is worth studying in the context of energy storage.

Therefore, the goal of this thesis is to develop and optimise a process design for a high efficiency energy storage system using ReSOC, that stores energy in the form of ammonia. The feasibility of ammonia as a fuel for ReSOC will thus be investigated through thermodynamic analysis of the developed design. However, this thesis will not include a techno-economic study of the process.

This thesis was started as a part of the BALANCE project¹, which was a joint project of several European organisations including TU Delft, receiving funding the European Union's Horizon 2020 research and innovation programme (under grant agreement No 731224). The goal of the project was the development of ReSOC technology to balance the mismatch between wind and solar electricity production and consumption patterns, to help the integration of these power sources into the electrical grid. One of the activities towards this goal was the study of the suitability of ReSOCs in industrial environments, with various fuels. This thesis was started as a part of this activity within the BALANCE project, with the goal to design an energy storage system with ammonia as the fuel, and optimise it to achieve high efficiency.

Outline of the Report

The basic theoretical concepts needed to understand the work in this thesis are introduced in Chapter 2. A study of the existing literature on ReSOC systems is undertaken in Chapter 3. The chapter contains further discussion on other works in literature that motivate some design choices. The modelling of the system with its various subsections is elaborated in Chapter 4. In Chapter 5, the results of preliminary analysis carried out on the stack and on a very basic system design are described. This design is improved to achieve high efficiencies in Chapter 6, accompanied by an exergy analysis of the improved system. The improved design is compared to a reference design in Chapter 7, and one more pathway to higher efficiencies is investigated. Finally, the learning from this work is summarised in Chapter 8, and a path for future research is laid out.

¹https://www.balance-project.org/

Theoretical Background

The background information about reversible solid oxide cells that is necessary to follow the modelling and analysis presented in this thesis is laid out in this chapter.

2.1. Fundamentals of Reversible Solid Oxide Cells

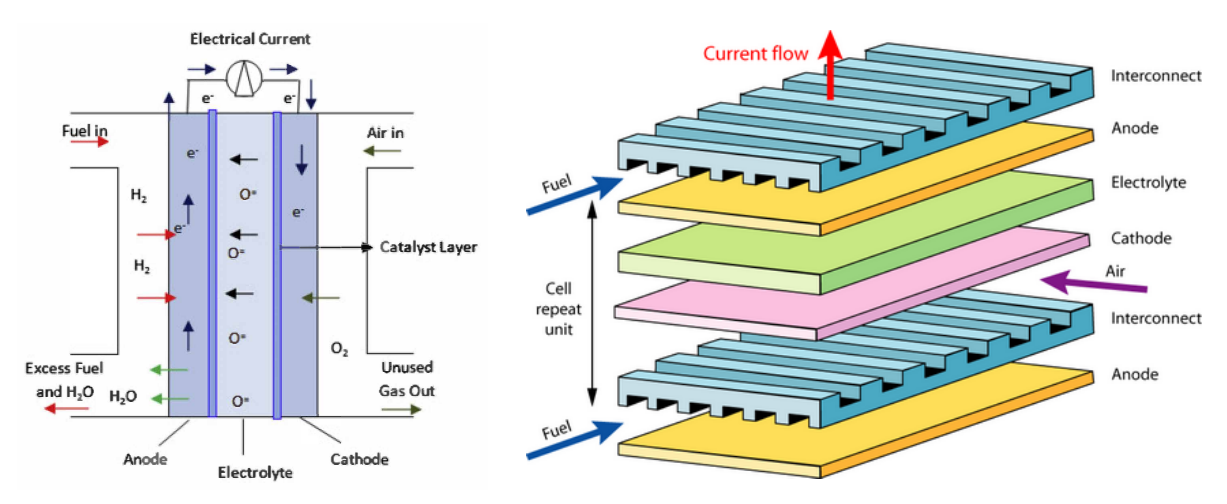
Fuel cells are electrochemical devices that can convert chemical energy directly into electrical energy, as opposed to conventional engines which accomplish this conversion indirectly via thermal and mechanical energy. In contrast, electrolysis cells convert electrical energy into chemical energy. The use of electricity enables certain reactions to take place which are not feasible to drive only with thermal energy. Splitting of water into hydrogen and oxygen is the most relevant example of such a reaction.

Fuel cells and electrolysis cells are simply counterparts of each other, and thus it is possible to design a single reversible device to operate in both modes. The solid oxide cell (SOC) is an example of such a device. It is a solid state high-temperature electrochemical cell.

Much of the information in this section is taken from literature sources [16].

2.1.1. Design and Materials for Solid Oxide Cells

A solid oxide cell can have many form factors, for example planar, tubular, etc. However, planar cells are the most common. Many such cells are often combined to form a stack. A schematic of a single solid oxide cell, and a unit block of a stack of planar cells are shown in Figure 2.1.



(a) Schematic of an SOC in fuel cell mode [17]. (b) Construction schematic of a planar SOC stack in fuel cell mode [18].

Figure 2.1: Schematics of a solid oxide cell and planar cell stack.

Like any electrochemical cell, a solid oxide cell fundamentally consists of two electrodes with an electrolyte between them. Since this thesis is about reversible cells, this report will refer to the electrodes as "fuel

electrode" and "air electrode" instead of "anode" and "cathode". The electrochemical reactions occur at the triple phase boundary (TPB), i.e at the intersection of the electrolyte, the electrode catalyst and the pores containing the reactants.

The electrolyte is made out of solid mineral oxides. The typical SOC electrolyte materials include oxide ion conducting materials yttria-stabilised zirconia (YSZ), lanthanum strontium gallate magnesite (LSGM), gadolinia-doped ceria (GDC), samaria-doped ceria (SDC), etc. Proton conducting perovskite electrolytes also exist. YSZ is the most common among these [16].

The most common fuel electrode material used with YSZ electrolytes is a Ni-YSZ cermet, where the nickel provides catalytic activity and the YSZ provides support and thermal matching with the electrolyte. Other fuel electrode materials include doped ceria, and LSCV-YSZ composites. The most common air electrode catalyst used with YSZ electrolytes is lanthanum strontium manganite (LSM). The air electrodes are made of LSM-YSZ composites. lanthanum strontium cobalt ferrite (LSCF) is another possible air electrode catalyst [16].

Meanwhile, when forming a stack, electrodes from neighbouring cells are joined using interconnects which carry the current between the two cells. The interconnects contain channels for the flow of reactants and products. The interconnects can be made out ceramics (lanthanum chromites) or metals (chromium alloys)[16].

2.1.2. Thermodynamics of Reversible Fuel Cells

For a chemical reaction at constant pressure, the change in the total energy of the components is called the enthalpy change of the reaction Δh [J mol⁻¹]. This definition gives rise to the the sign convention, that the reaction absorbs energy when Δh is positive, while the reaction releases energy when Δh is negative. Every reaction is associated with a change in entropy Δs [J mol⁻¹ K⁻¹], which results from (among other factors) a change in the number of moles of gas caused the reaction. The Gibbs energy change Δg [J mol⁻¹], is the minimum (non-expansion) work that must be performed for the reaction to take place. The sign convention used is the same as for enthalpy. When the Gibbs energy change for a reaction is negative, the reaction can be said to be spontaneous. The change in Gibbs energy is related to the enthalpy and entropy changes by Equation (2.1) [16].

$$\Delta g = \Delta h - T \Delta s \tag{2.1}$$

We apply these thermodynamic concepts particularly to electrochemical cells. For a fuel cell, $-\Delta h$ [J mol⁻¹] represents the total energy released by the reaction, while $-\Delta g$ [J mol⁻¹] represents the maximum electrical work that can be extracted from the cell. For an electrolysis cell, Δh [J mol⁻¹] represents the total energy that must be provided to the cell, while Δg [J mol⁻¹] represents the minimum electrical work that must be provided to the cell.

SOCs often operate under non-standard conditions. The resulting variation in Gibbs energy change for the reaction can be calculated with Equation (2.2) [16], which assumes the standard entropy change Δs^0 [Jmol⁻¹K⁻¹] is independent of temperature. R, which has a value of 8.314 JK⁻¹ mol⁻¹, is the universal gas constant.

$$\Delta g = \Delta g^{0} - \Delta s^{0} (T - T_{0}) + RT \ln(Q_{r})$$
(2.2)

 $Q_{\rm r}$ [-] is the reaction quotient of the reaction, calculated by Equation (2.3) [16], where a [-] is the activity of the species, and v [-] is the stoichiometric coefficient of the species in the reaction.

$$Q_{\rm r} = \frac{\prod a_{i,\rm products}^{v_i}}{\prod a_{i,\rm reactants}^{v_i}} \tag{2.3}$$

Reaction (2.4) represents the oxidation of hydrogen. The thermodynamic quantities for the reaction are also stated [19].

$$H_2(g) + \frac{1}{2} O_2(g) \iff H_2O(g)$$

$$\Delta h^0 = -241.83 \text{ kJ mol}^{-1}$$

$$\Delta s^0 = -44.42 \text{ J mol}^{-1} \text{ K}^{-1}$$

$$\Delta g^0 = -228.59 \text{ kJ mol}^{-1}$$

For this system, Equation (2.2) turns to Equation (2.5). Since SOCs are high temperature cells, the reactants and products are all gases. If we assume them to be ideal gases, activities can be replaced by the ratio of partial pressure to standard pressure [16]. The expression can then be further expanded as Equation (2.6), which separates the effect of temperature, pressure and gas composition.

$$\Delta g = \Delta g^0 - \Delta s^0 (T - T_0) + RT \ln \left(\frac{a_{\text{H}_2\text{O}}}{a_{\text{H}_2} a_{\text{O}_2}^{0.5}} \right)$$
 (2.5)

$$\Delta g = \Delta g^{0} - \Delta s^{0} (T - T_{0}) - \frac{RT}{2} \ln \left(\frac{p}{p_{0}} \right) + RT \ln \left(\frac{y_{H_{2}O}}{y_{H_{2}} y_{O_{2}}^{0.5}} \right)$$
 (2.6)

For a fuel cell, $-\Delta g$ [J mol⁻¹] is the theoretically maximum electrical work that can be obtained. For an electrolysis cell, $-\Delta g$ [J mol⁻¹] represents the minimum electrical work that needs to be provided to drive the reaction. Since we deal with electrical systems, it is more convenient to express the change in Gibbs free energy in terms of the corresponding voltage change.

Accordingly, the reversible voltage U_{rev} [V] for an electrochemical system is given by Equation (2.7), where n [-] is the moles of electrons transferred per mole of a reactant (=2 for hydrogen combustion) and F is the Faraday constant, which has a value of 96485 Cmol⁻¹. It represents the charge carried by one mole of electrons. Note that the sign convention is that voltage is positive when the cell produces power, i.e. for a fuel cell.

Equation (2.8) is a modified version of the Nernst Equation, which is a very important equation in electrochemistry. The actual Nernst equation has the standard cell potential U^0 [V] as the first term, and it does not account for the effect of temperature. In Equation (2.8), U_T [V] represents the cell potential at standard pressure, but at the actual reaction temperature [16]. The reversible voltage is also called as the Nernst voltage.

$$U_{\text{rev}} = -\frac{\Delta g}{n F}$$

$$= -\frac{\Delta g^0}{2F} + \frac{\Delta s^0}{2F} (T - T_0) + \frac{RT}{4F} \ln\left(\frac{p}{p_0}\right) - \frac{RT}{2F} \ln\left(\frac{y_{\text{H}_2\text{O}}}{y_{\text{H}_2} y_{\text{O}_2}^{0.5}}\right)$$
(2.7)

$$= U_T + \frac{RT}{4F} \ln\left(\frac{p}{p_0}\right) + \frac{RT}{2F} \ln\left(\frac{y_{\text{H}_2} y_{\text{O}_2}^{0.5}}{y_{\text{H}_2\text{O}}}\right)$$
(2.8)

For the hydrogen-steam reaction system from Reaction (2.4), we can evaluate the trends of the reversible voltage. From Equation (2.8), we can see that the reversible voltage increases with an increase in pressure. Since the entropy change of Reaction (2.4) is negative, we can also see that the reversible voltage decreases with an increase in temperature. This trend is shown in Figure 2.2.

2.1.3. Losses in Electrochemical Cells

The reversible voltage is the maximum possible voltage that can be achieved by a fuel cell (or minimum for an electrolysis cell). However, in reality, such a reversible reaction can only occur in an open circuit condition. For practical usage, a non-zero current flow is required, and there are several irreversible losses that are associated with a non-zero current flow. These losses lead to a deviation in cell voltage from the reversible value. This voltage difference is called overpotential. There are many types of overpotential based on the type of irreversible loss. This section explains these losses briefly, in a qualitative sense. A quantitative treatment of these losses has been undertaken in Section 4.3. For more in-depth knowledge, please refer to other sources [13, 16, 20].

Activation Losses

Activation losses are losses that are incurred in order to overcome the limitations of reaction kinetics. The overall reaction in an electrochemical cell is a combination of a set of half-cell reactions at each electrode. Like all chemical reactions, the rate of the half-cell reaction(s) depends on, among other factors, the activation energy of the reaction(s). The activation energy for a reaction in each direction depends upon the shape of the free energy curve of the reaction under consideration.

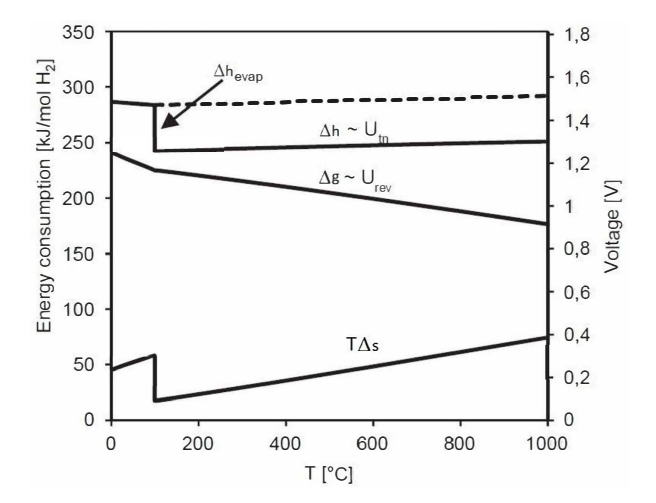


Figure 2.2: Variation in thermodynamic quantities in a hydrogen-steam system with temperature. Figure by Butler [3], modified by Diaz-Rodriguez [4].

The free energy curve of a reaction is usually not symmetric. Since electrochemical reactions deal with charged species, the free energy curve can be modified by an electrical potential difference across the electrode interface. At equilibrium, a reversible (or equilibrium) potential develops across the cell, which modifies the free energy curve in such a manner that the forward and reverse reaction rates are equal, resulting in zero net current.

In order to get a finite non-zero current, the activation energy curve has to be modified away from this equilibrium state. This is done by changing the voltage across the electrode interface to a value different from the reversible/equilibrium value. This potential difference represents energy that is lost in order to overcome the activation barrier and achieve a non-zero net reaction rate, and is called the activation overpotential. Such an overpotential is required at each electrode for the cell to function.

Ohmic Losses

Ohmic losses correspond to the charge transport within an electrochemical cell. Like any electrical system, the current through the various components of an electrochemical cell encounters resistance to the flow of charge (both electrons and ions). This can include the ionic resistance in the electrolyte, and the electronic resistance in the electrodes, the interconnects, the wiring and the inter-facial resistance between these components. Typically, the contribution of ionic resistance tends to dominate over electronic resistance [16].

The voltage drop caused by this resistance is called the Ohmic overpotential, since it follows Equation (2.9), which is called Ohm's Law. It states that the voltage difference ΔU [V] across a material is proportional to the current I [A] through a material. The proportionality constant is the electrical resistance $R_{\rm e}$ [Ω] of the material.

$$\Delta U = I \cdot R_{\rm e} \tag{2.9}$$

Diffusion Losses

Diffusion losses correspond to the mass transport within an electrochemical cell. The gas diffusion layer of an electrode has a porous structure, where the pores are narrow and tortuous. Therefore the transport of the reacting species through the electrodes to the triple phase boundaries (TPBs) is dominated by diffusion. Since diffusion is a slow process, the production or consumption of species at the TPB leads to a concentration gradient across the electrode, which is what drives the diffusion.

At high current densities, the diffusion-driven mass transfer cannot match the rate of consumption or production of the chemical species. Thus, a large concentration gradient can develop, because of which the reaction sites encounter a species concentration significantly different from that in the bulk flow. Accordingly, the actual cell voltage is also different from that predicted by the Nernst equation using bulk concentrations. This difference shows up in the Nernst voltage. The activation losses can also be affected by local concentrations at the TPB. This overall difference in voltage due to mass transport limitations is called the concentration overpotential.

Other Losses

Some other losses can also occur in electrochemical cells. These include internal leakage currents across, and fuel crossover. Ideally, the electrolyte is supposed to conduct only ions, while preventing the flow of electrons and fuels/reactants. However, in practice, fuels and electrons can sometimes leak through the electrolyte. These lead to voltage reduction even in open circuit condition.

2.1.4. Polarisation Curve and Thermal Behaviour

Polarisation Curve

The losses that are described in the previous section affect the cell voltage such that the actual cell voltage is different from the reversible voltage. For a fuel cell, the overpotentials are deducted from the reversible voltage, while they get added to the reversible voltage in an electrolysis cell.

The plot of cell voltage against current density is called the I-V curve, or the polarisation curve of a cell. Figure 2.3 shows an example of a polarisation curve for a fuel cell. The polarisation curve shows three distinct regions. At low current density is the activation region, where the other losses are very small and the activation losses dominate. Because of this, this curve is highly non-linear in this region. At higher current densities, the activation losses stabilise and the curve moves into the Ohmic region. Here, the curve is dominated by the Ohmic losses, which have a linear dependence on current. Finally, at very high current densities, the curve moves to the mass-transport region, where the diffusion losses become very large. After this, the voltage drops very quickly, eventually reaching zero at the limiting current density.

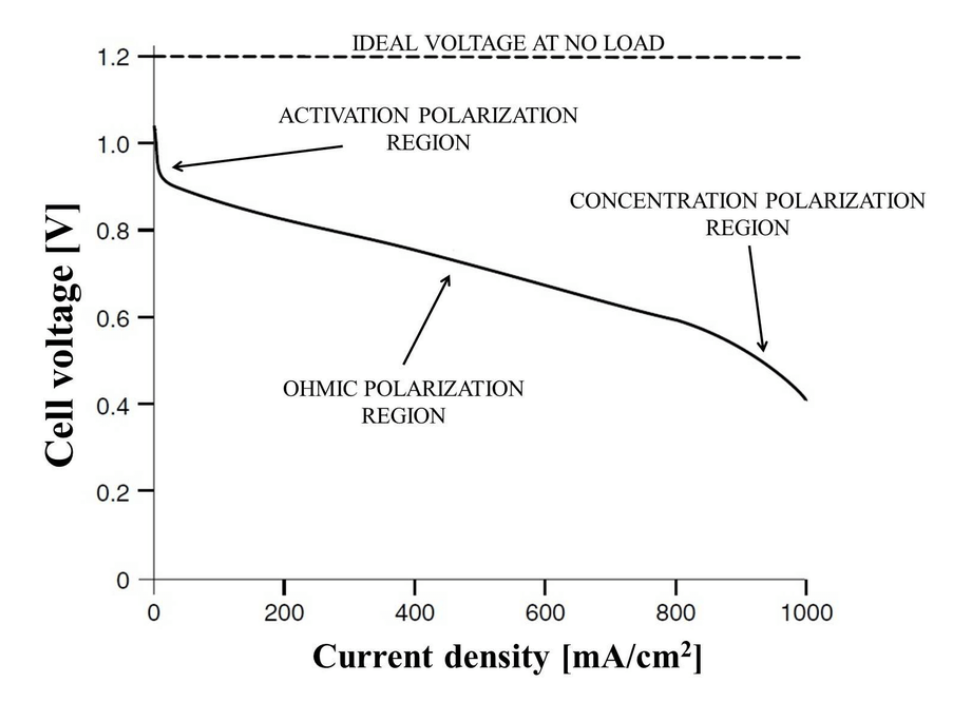


Figure 2.3: Sample polarisation curve for a fuel cell [5]. The three regions of operation are shown.

Thermoneutral Voltage

The previous sections have explained the behaviour of the cell voltage. However, recall that the cell voltage only represents the electrical work being done on/by the system. The actual energy change of the reaction is given by the enthalpy change Δh [J mol⁻¹]. The value of voltage corresponding to the enthalpy change of the reaction is called the thermoneutral voltage $U_{\rm tn}$ [V]. It is expressed by Equation (2.10).

$$U_{\rm tn} = \frac{\Delta h}{nF} \tag{2.10}$$

The difference between the cell voltage and the thermoneutral voltage corresponds to the heat released or absorbed by the cell. This concept is very important to a solid oxide cell in electrolysis mode. If the voltage of an electrolysis cell is less than the thermoneutral voltage (thanks to low overpotentials), it implies that the energy provided with electricity is not sufficient to fulfil the energy needs of the reaction. This shortfall

of energy is met by absorbing heat, and therefore the cell operates in an endothermic manner. On the other hand, if the electrolysis cell voltage is higher than the thermoneutral voltage (due to high overpotentials), then it implies that the energy provided by electricity is more than required by the reaction. This excess energy appears as heat output, and the stack operates in exothermic mode.

The relationship between Nernst voltage, overpotentials, cell voltage and the thermoneutral voltage of the cell is nicely summarised in Figure 2.4. It also shows the various regions of thermal behaviour based on the thermoneutral voltage.

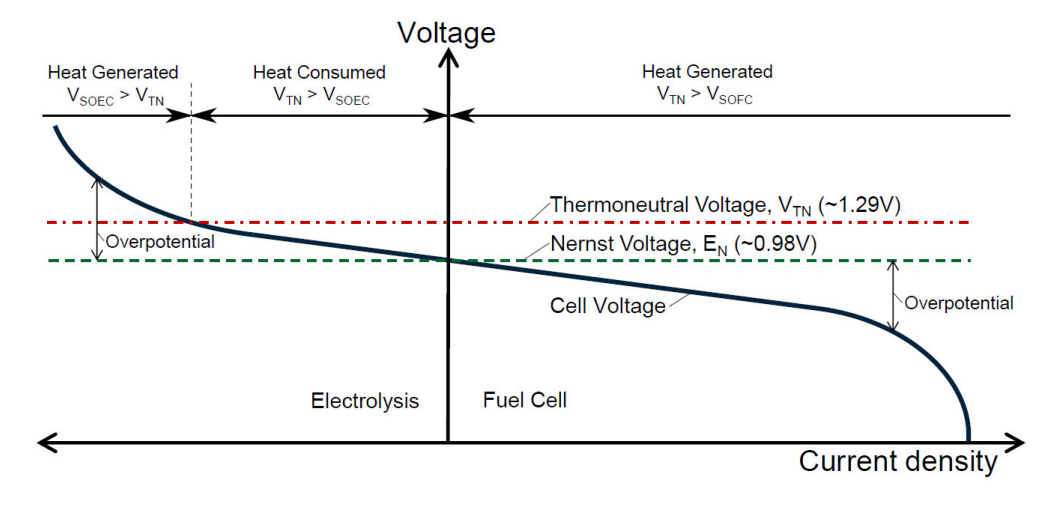


Figure 2.4: Sample polarisation curve for a reversible cell. The reversible voltage, thermoneutral voltage and the thermal regions are also shown. Figure taken from Wendel [6].

As shown in Figure 2.4, for a fuel cell, the cell voltage is always lower than the thermoneutral voltage. This implies that the energy released by the reaction is more than the energy extracted through electrical work. The remaining energy is released as heat, and thus a fuel cell is always exothermic. Due to this, the thermoneutral voltage is not a relevant concept for fuel cells.

Operation in endothermic region is one of the main benefits of solid oxide cells for electrolysis. In low-temperature electrolysis cells, the overpotentials are too high, which causes the cell to always operate in exothermic mode. Whereas operation at high-temperatures enables the overpotentials to be low enough for endothermic operation. Endothermic operation can be advantageous to offset electricity costs by using excess heat sources where available.

2.2. Fundamentals of Ammonia Synthesis

The most common method of ammonia synthesis is the Haber-Bosch process [8] which synthesises ammonia directly from hydrogen and nitrogen via an exothermic reaction, represented by Reaction (2.11) [19].

$$\frac{3}{2} H_2(g) + \frac{1}{2} N_2(g) \longrightarrow NH_3(g) \qquad \Delta h^0 = -46.22 \text{ kJ mol}^{-1}$$

$$\Delta s^0 = -99.06 \text{ J mol}^{-1} \text{ K}^{-1}$$

$$\Delta g^0 = -16.41 \text{ kJ mol}^{-1}$$

The activation energy for this synthesis reaction is so high that achieving measurable reaction rates without a catalyst would require temperature above 800-1200 K [8]. Therefore, catalyst materials are required to reduce the reaction temperatures. The most common catalysts are based on iron, which can reduce the reaction temperature in the range of $380-500\,^{\circ}\text{C}$ [21].

Since the entropy change of the synthesis reaction is negative, applying Equation (2.2), we can see that the Gibbs energy change of the reaction increases with rising temperature. This means the reaction becomes thermodynamically unfavourable at higher temperatures. Since high temperatures are required for favourable reaction kinetics, even with catalysts, the Gibbs energy change has to be reduced by other means. That is why, ammonia synthesis reactions are carried out at high pressures. Typical pressures range from 130-400 bar depending on catalysts and other process design [8]. High pressure also improves the kinetics further.

2.3. Exergy 9

Nevertheless, the ammonia synthesis reaction provides very little conversion (<25 %) in a single pass [21]. This requires a recycling of the feed gas (containing valuable hydrogen). A high recycle ratio entails higher losses from separation, compression, and other processing of the recycled gas. On the other hand, increasing the pressure to improve conversion leads to significant losses in the compression of feed gas.

Therefore, efforts to find catalysts that are active at low temperatures have been ongoing, with the ammonia synthesis catalyst problem being the most extensively studied problem in industrial catalysis [8]. Some catalysts based on ruthenium are also in use, which are active at lower temperatures. However, iron remains the most commonly industrially used catalyst due to its significantly lower price [22].

2.3. Exergy

Exergy is a concept that represents the "quality" of energy. It depends on the environment (also called "dead state"). Exergy is the amount of work that can be obtained from a certain amount of energy, in the natural environment [23]. Alternatively, it can also be defined in the reverse manner, as formulated by Riekert [24]:

Exergy expresses the amount of mechanical work necessary to produce a material in its specified state from components common in the natural environment, in a reversible way, heat being exchanged only with the environment.

Mechanical or electrical work is considered to be highest quality of energy, which means the value of exergy equals the energy flow. On the other hand, for most practical temperatures, heat is a low quality form of energy. The maximum work δW [J] obtained from a small heat flow δQ [J] at temperature T [K] can be obtained by a Carnot cycle operating between the temperatures T [K] and the dead state temperature T_0 [K]. Thus, the exergy of a small heat flow is given by the Carnot efficiency:

$$\delta W = \delta Q \left(1 - \frac{T_0}{T} \right) \tag{2.12}$$

Exergy can be considered to be made up of several components [23]: kinetic exergy, potential exergy, nuclear exergy, thermo-mechanical exergy, and chemical exergy. Analogous to their energy counterparts, kinetic, potential and nuclear forms of exergy undergo very small changes in chemical process plants. Therefore, these forms of exergy are typically neglected for analysis of chemical systems. The following section elaborates further on the two relevant forms of exergy contained in a material: physical and chemical exergy.

2.3.1. Thermo-mechanical Exergy

Thermo-mechanical exergy ex_{tm} [Jmol⁻¹] is the maximum work that is obtained by bringing the mixture to thermal and mechanical equilibrium with the environment, without a change in its chemical composition. This entails taking the mixture to the dead state temperature and pressure in a reversible way.

The thermal exergy is the maximum work that can be obtained by bringing the material into thermal equilibrium with the environment at constant pressure. To calculate this, we can consider the heat obtained from cooling the material from its given temperature T [K] to T_0 [K], and apply the Carnot efficiency to get the maximum work obtained. It must be noted, that as the temperature goes down, the exergy of the heat flow also reduces. Considering this, the thermal exergy ex_t [J mol $^{-1}$] of the material can then be described by the integral shown in Equation (2.13a), where c_p [J K $^{-1}$ mol $^{-1}$] is the specific heat capacity at constant pressure. If the specific heat capacity is independent of temperature, we arrive at Equation (2.13b).

$$ex_{t} = \int_{T_{0}}^{T} c_{p} \left(1 - \frac{T_{0}}{T} \right) dT$$
 (2.13a)

$$ex_{t} = c_{p} \left(T - T_{0} - T_{0} \ln \frac{T}{T_{0}} \right)$$
 (2.13b)

Once the material is at environmental temperature, then the mechanical exergy $ex_{\rm m}$ [J mol⁻¹] is the work obtained from reversible isothermal expansion/compression of the material from its specified pressure p [bar] to environmental pressure p_0 [bar]. For an ideal gas, this is given by Equation (2.14).

$$ex_{\rm m} = RT_0 \ln \frac{p}{p_0} \tag{2.14}$$

Aspen Plus can directly provide the thermo-mechanical exergy flow $\dot{E}x_{\rm tm}$ [W] of any material stream.

2.3.2. Chemical Exergy

Chemical exergy arises from the difference between a given material and the environment in terms of chemical composition. Thus, chemical exergy is the maximum work obtained when a given material at environmental pressure and temperature, is converted to environmental components at their respective partial pressures in the environment. The procedure for calculating the exergy follows the following steps:

- 1. The various chemical components of the given mixture are reversibly separated and each component is isothermally compressed from its partial pressure in the given mixture, to the environmental pressure.
- 2. Any chemical species necessary for the next step are taken from the environment and isothermally compressed from their partial pressure to the environmental pressure.
- 3. These environmental components are reacted with the components from the given material isothermally and isobarically, to produce other environmental species.
- 4. These environmental species are then isothermally expanded to their respective partial pressures in the environment, and reversibly mixed with the environment.

The chemical exergy of the material $ex_{\rm ch}$ [J mol⁻¹] is the sum of the work obtained in all the above steps. To make the calculations easier, the exergy obtained from Steps 2-4 can be combined, which is called the "standard chemical exergy" $ex_{\rm ch}^0$ [J mol⁻¹] of that component. For many common chemical species, the precalculated standard chemical exergy values are available from reference literature, like Morris and Szargut [1]. These reference values for the chemical species relevant to the current work are listed in Table 2.1. The work of compression for Step 1 has to be calculated for every mixture, which can be done similarly as in Equation (2.14), where p/p_0 term inside the log function reduces to the mole fraction y [-] of each species in the mixture.

Chemical Species	Chemical Formula	Standard Chemical Exergy
Ammonia	NH ₃	$337.90{\rm kJmol^{-1}}$
Nitrogen	N ₂	$0.72\mathrm{kJ}\mathrm{mol}^{-1}$
Hydrogen	H ₂	$236.09{\rm kJmol^{-1}}$
Water - liquid	H ₂ O (l)	$0.90\mathrm{kJ}\mathrm{mol}^{-1}$
Water - vapour	H ₂ O (g)	$9.50\mathrm{kJ}\mathrm{mol}^{-1}$
Oxygen	O_2	$3.97\mathrm{kJ}\mathrm{mol}^{-1}$

Table 2.1: Standard chemical exergy of species relevant to this system [1].

The chemical exergy of a material flow $\dot{E}x_{\mathrm{ch},k}$ [W] can then be calculated as shown by Equation (2.15), where i is an index for chemical species and k is an index for flow streams.

$$\vec{E}x_{\text{ch},k} = \sum_{i} \left(\dot{n}_{k,i} \cdot \left(ex_{\text{ch},k,i}^{0} + RT_0 \ln \left(x_{k,i} \right) \right) \right)$$
 (2.15)

However, the last term in Equation (2.15) only applies to components that are present as gases in the environment. Some substances can be present both liquids and gases in the environment. For the purpose of this thesis, water is the only species with this property. The procedure for calculating the exergy of stream containing such substances is slightly different [25].

At the dead state, the maximum mole fraction of water in the gas phase $y_{\rm H_2O,sat}$ is derived from its saturation pressure. For the dead state considered in this thesis (25 °C and 1 atm), this value is 0.03128. If the mole fraction of water in the stream, $x_{\rm H_2O}$ is less than $y_{\rm H_2O,sat}$, then all the water is in gas phase at dead state, and Equation (2.15) applies directly. However, if $x_{\rm H_2O}$ is greater than $y_{\rm H_2O,sat}$, then the gaseous mole fraction of water $y_{\rm H_2O}$ is limited to $y_{\rm H_2O,sat}$. The remaining water is present as a liquid. Being incompressible, liquids have no compression term for chemical exergy, and are only described by their standard chemical exergy. Now, the mole flow of water in each phase, and the (gaseous) mole fractions of all the species in the gas phase have to be recalculated taking into account the condensed water. If this new mole fraction is denoted by y_i' , then the total exergy flow of the stream k is given by Equation (2.16).

2.3. Exergy 11

$$\dot{E}x_{\text{ch},k} = \sum_{i \neq \text{H}_2\text{O}} \left(\dot{n}_{k,i} \cdot \left(ex_{\text{ch},k,i}^0 + RT_0 \ln \left(y_{k,i}' \right) \right) \right)
+ \dot{n}_{k,\text{H}_2\text{O(g)}} \cdot \left(ex_{\text{ch},k,\text{H}_2\text{O(g)}}^0 + RT_0 \ln \left(y_{\text{H}_2\text{O,sat}} \right) \right) + \dot{n}_{k,\text{H}_2\text{O(l)}} \cdot ex_{\text{ch},k,\text{H}_2\text{O(l)}}^0$$
(2.16)

2.3.3. Exergy Loss

Unlike energy, exergy is not conserved in any irreversible (or "real") process. An proper analysis of exergy losses in the system can be a good way to determine which process or equipment requires the most improvement. Exergy loss can be classified into two parts: internal and external exergy loss.

Internal exergy loss is related to the actual process occurring within a system boundary. This is a consequence of the second law of thermodynamics. This kind of exergy loss can also be termed as "exergy destruction". The exergy destroyed in an irreversible process Ex_D [J] can be found by Equation (2.17), where ΔS_{irr} [JK⁻¹] is the net entropy generation in the process.

$$Ex_{\rm D} = T_0 \Delta S_{\rm irr} \tag{2.17}$$

Meanwhile, external exergy loss is related to the release of waste products into the environment, in which case the exergy contained in the waste products is lost. In this report, the term "exergy destruction" shall be used exclusively for internal exergy losses, while the term "exergy loss" may be used in a generic sense for internal loss, external loss, or a combination of both. The external exergy loss has also been called "environment loss" in this report.

Literature Survey

In this chapter, a number of studies from literature that are relevant to this work are presented, which can provide valuable information on the design and modelling of an energy storage system using ReSOCs. The progress made in the research and development of energy storage systems using ReSOCs is studied in Section 3.1. From this section, various strategies can be found to improve the efficiency of ReSOC systems. It also shows which fuels have already been studied for use in ReSOCs, and the range of efficiencies obtained. Studies on the feasibility of using ammonia directly in SOFCs (i.e. without external cracking reactors) are explored in Section 3.2. Various studies pertaining to the production of ammonia using electricity are presented in Section 3.3. The possible utility of high temperature heat pipes for thermal management in SOFCs is reviewed very briefly in Section 3.4. The insight gained from these studies is then used to frame the approach that will be taken to achieve the goal defined in Chapter 1, i.e. development of a high efficiency ReSOC system using ammonia. This approach is defined in Section 3.5.

3.1. Reversible Solid Oxide Cells for Energy Storage

In the past decade, there has been considerable spurt of interest in the use of fuel cells and electrolysers for smoothing out fluctuations in power production from renewable sources. In this section, the use of ReSOCs is studied in the context of isolated energy storage systems with hydrogen or its various derivatives.

Bierschenk et al. [26] introduced a way to reduce the problem of providing heat to the endothermic electrolysis reactions to increase the stack round trip efficiency (RTE) of ReSOC systems. They proposed using exothermic reactions like Sabatier methanation within the stack to provide the required heat. It was proved through experiments that Ni-YSZ electrodes acted as good catalysts to promote the Sabatier methanation reaction inside the stack. However, either low temperature ($\sim 600\,^{\circ}$ C) or high pressure ($\sim 10\,\text{bar}$) is necessary for sufficient methanation. Performance with YSZ at 600 $^{\circ}$ C was found to be not sufficient to operate between the two targeted mixture compositions; and either pressurisation, or the use of intermediate temperature electrolytes like LSGM were recommended.

Cuellar [27] evaluated the feasibility of a hydrogen ReSOC system for energy storage. TES based on phase change materials (PCMs) was implemented. Various configurations were tested, with a peak RTE of $74\,\%$ being achieved.

Al-musleh et al. [28] proposed an Aspen Plus model of an energy storage system for a solar thermal power plant, to maintain a constant power output of $140\,\mathrm{MW}$. They compared the use of methanol with liquid and gaseous methane, which were used as fuel for an ReSOC. The CO_2 produced during FC mode was also stored as a liquid in all cases. An auxiliary steam Rankine cycle was also used to utilise waste heat where possible. The liquid methane system was found to have a RTE of $54.9\,\%$ against an efficiency of $53.3\,\%$ for the methanol system. One of the reasons stated for this was the larger heat of reaction of methanation. The presence of this exothermic reaction reduced external heat requirement for electrolysis. Another reason was the synergistic refrigeration-evaporation of CO_2 and CH_4 , which reduces refrigeration costs. This synergy was not available for the methanol case, since methanol is already a liquid at ambient temperature. Methanol also produces greater amounts of CO_2 for the same power, exacerbating this issue. The gaseous methane system also faces the same lack of synergistic refrigeration, leading to a slightly lower RTE of $54.4\,\%$.

3. Literature Survey

Sebastiani [29] conducted a thermodynamic analysis of a hydrogen-steam ReSOC energy storage system. A 0-D model was created in Aspen Plus, and losses were expressed using an area specific resistance (ASR). He showed the benefits of pressurisation of the FC mode, combined with a gas turbine. Pressurisation of electrolysis cell (EC) mode was shown to be contentious, to be decided based on whether ASR benefits overcome the losses to Nernst potential. Air and fuel-side recirculation was also implemented in FC mode, eventually achieving a system RTE of 53 %.

Sensoli [30] conducted 4 case studies at different scales and locations for an ReSOC energy storage system with hydrogen. Using Aspen Plus models of a ReSOC system with thermal energy storage, functions were generated to correlate power flow, hydrogen flow and stored heat flow in each mode. These functions were used to scale the system for each case using weekly electricity trends in the chosen locations. A techno-economic analysis concluded that an electricity cost of $0.30 \in /kWh$ could be achieved for the best case.

Mor [31] analysed a bi-directional SOC system using with pure hydrogen as well as syngas (CO/H_2) . The benefits of cathode air recirculation, and the effect of pressurisation were studied with two different gas turbine configurations in fuel cell mode. In order to match realistic power demands, there was no balancing restriction on the system, i.e. the amount of fuel used in FC mode did not necessarily equal the fuel produced in EC mode. Therefore, instead of using RTE, a metric was introduced to calculate exergy efficiency over a given year, named "Year-round Cumulative Exergy". The FC mode had a much higher efficiency than the EC mode, and thus the yearly exergy efficiency varied significantly based on the operating hours of each mode, which were taken from capacity excess/shortfall estimates for the Dutch market.

Jensen et al. [32] proposed a large-scale ReSOC energy storage system, involving the storage of $\mathrm{CH_4}$ and $\mathrm{CO_2}$ in large pressurised underground caverns. They adopted the recommendations of Bierschenk et al. [26], using a pressurised intermediate temperature stack to promote internal methanation. Pressurisation of the stack reduced the minimum current density required for thermoneutral operation. However, it also increased BoP power demands for air compression. Thus, an optimum system RTE of 72 % was achieved at an intermediate pressure of 20 bar and a current density of $7000\,\mathrm{Am^{-2}}$. An estimated storage cost of \sim 3 ¢/kWh was calculated.

Wendel et al. [6, 33] put forward the importance of the thermoneutral voltage as a useful parameter for analysing ReSOC systems. They then analysed the effects of operating conditions on the thermoneutral voltage of systems using a carbonaceous hydrogen mixture. They developed 0-D cell and 1-D stack models of a ReSOC using a carbonaceous hydrogen mixture [6, 34] and used it to design an energy storage system [6, 35]. Using the findings of previous research [26], an intermediate-temperature cell was used for promoting exothermic methanation reaction within the stack to manage the heat demand of the endothermic EC mode. They made comparisons between vapour storage and condensed water storage, and between distributed-scale and bulk-scale systems [6, 36]. A system RTE (round trip efficiency) of 74 % was achieved at both scales. A techno-economic analysis was also carried out.

Reznicek [37, 38] continued with the work of Wendel [6], assessing the effects of tank dynamics and off-design BoP component behaviour on the system. A novel floating-piston tank concept was modelled, in order to reduce the variability of tank conditions. For a distributed storage system with a stack pressurised at ~ 10 bar, a system RTE of 68.8 % was achieved at a levelised cost of storage (LCOS) of 16.4 ¢/kWh. Reznicek and Braun [38] also analysed a power-to-gas to integrate storage with CO $_2$ and natural gas pipelines, achieving a system LHV RTE of 65.7 % and a levelised cost of electricity (LCOE) of 2.7-4.3 ¢/kWh.

Di Giorgio and Desideri [39] designed and compared two configurations with a hydrogen ReSOC: storing the steam directly, or condensing the water out. They made use of two ways to integrate heat between the operating modes. One was a thermal energy storage in a PCM integrated within the stack. In the condensed water configuration, they also used the heat from the condensing steam to evaporate water in a steam tank for use in EC mode. (Thus, both configurations actually required storing steam between modes). The condensing configuration achieved 72 % RTE with fuel utilisation of only 60%. However, the system could only operate in EC mode for a short while due to lack of steam. Additionally, stack pressurisation was not possible, since the heat availability for steam generation would reduce. The stored vapour configuration was more flexible, but required high fuel utilisation of 90 % to achieve only 64 % RTE. However, pressurisation was possible for this configuration, raising the RTE to 74 %.

Mottaghizadeh et al. [40] designed a methane-based system to store energy, using a commercially available ReSOC. The system was modelled in Aspen Plus. Internal methanation was used to partially offset the demand of endothermic electrolysis. TES was also implemented using PCMs at two different temperatures. At reference conditions, the system RTE was 54.3 %. It was observed that the the stored thermal energy was used not only to meet the endothermic demand (41 %), but also for preheating the streams (59 %). Both the

stack and system saw reduced RTE with increasing current density. An increase in pressure saw a rise in stack RTE, but a drop in system RTE due to compressor demands. Implementing compressed air storage was seen to eliminate this drawback, and the system RTE was increased to 60.4% at 25 bar.

Santhanam [41] modelled a closed-boundary ReSOC electricity storage system using pure hydrogen as well as a hydrocarbon mixture. He also modelled an open-boundary system using methane which was stored in existing natural gas grids, thus fulfilling energy storage as well as sector coupling needs. Air recirculation, PCM-based thermal energy storage as well as pressurised air storage were implemented in all systems, reducing the parasitic BOP consumption. Round-trip efficiencies of 55 % for the pressurised hydrogen system, 60 % for the pressurised hydrocarbon system, and 53 % for the open-boundary pressurised methane system were achieved. He stressed the importance of thermal energy storage, even in exothermic EC mode for the hydrocarbon system.

Diaz Rodriguez [4] modelled a high-temperature ReSOC system to store energy in syngas, while ensuring minimal methane content. A 0-D system model was constructed in Aspen Plus. After studying the effects of stack operating conditions, he demonstrated the beneficial effect of air recirculation on both operating modes. Due to a system RTE of only 44%, syngas by itself was concluded to be of questionable value for grid-balancing, and was recommended to be supplemented by methanation or Fischer-Tropsch reactions.

Giannoulidis [42] investigated an energy storage system using a high-temperature ReSOC with methanol. His 0-D Aspen Plus model simulated a ReSOC with external methanol synthesis and reforming. Various operating parameters were optimised, leading to a RTE of 46.7 %. Thermal energy storage with a PCM was conceptualised, where the storage is integrated directly into the stack. This thermal energy storage raised the RTE of the system by ~ 10 %, finally achieving 56.72 %, which was higher than seen in previous literature [28].

Meanwhile, attempts at the integration of ammonia with reversible solid oxide cells are fairly recent. Before beginning this work, there had only been one detailed modelling study on energy storage systems using ammonia in a ReSOC.

Wang et al. [43] designed a steady-state ammonia-based energy storage system using ReSOC. They optimised their system independently for maximum RTE and minimum LCOE. They operated the stack in exothermic region for both modes, and used dedicated external reactors for ammonia synthesis and cracking. Pure oxygen was used as sweep-gas/oxidant in both modes, and oxygen and nitrogen were both stored as liquids. A coupled refrigeration system was used where the liquid oxygen was used to cool the produced nitrogen in FC mode, and vice versa in EC mode. However, no thermal energy storage was used for inter-mode integration, since both modes had an exothermic stack. A triple-bed reactor at ~200 bar with direct intercooling (i.e. quenching) was used for ammonia synthesis, and a two-stage ambient temperature flash was used for ammonia separation. They attained an optimum RTE of 72% operating the stack at 50 bar, and a stack inlet temperature of 750 °C (fuel-side, EC mode) and 700 °C (air-side, FC mode). They also attained a minimum LCOE of while operating the stack at 26 bar, with stack inlet temperatures of 750 °C in each mode. The difference in operating points for different optimisations led to the conclusion that there is a trade-off between performance and cost.

Two more papers have been published regarding energy storage in ammonia. However, these studies were not focused on the use of ReSOCs, and were published after the beginning of this thesis in 2019.

Siddiqui et al. [44] developed an energy storage system with ammonia, integrating various processes like SOFC, proton exchange membrane / polymer electrolyte membrane (PEM) electrolysis, ammonia synthesis and even water desalination. Rouwenhorst et al. [45] designed an energy storage system with ammonia, using a "battolyser", proton-conducting solid oxide fuel cell (SOFC-H) and ruthenium-based ammonia synthesis.

In summary,

- Most studies on ReSOC energy storage consider hydrogen [27, 29–31, 41], or various hydrogen-carbon mixtures (including syngas) [4, 6, 31, 37, 41] as the fuel. Some studies have used methane [28, 32, 40, 41] or methanol [28, 42]. Only one study [43] has used ammonia instead of hydrocarbons as the hydrogen carrier.
- One of the major benefits of an high temperature electrolysis is the possibility of endothermic operation. This implies that some of the energy demand of electrolysis can be met from heat sources (if available), thus reducing the electrical demand. In a reversible system, the heat from the exothermic FC mode itself can be used in the endothermic EC mode. Thermal energy storage, especially through PCMs, is a very common strategy used to implement this heat integration between modes [27, 30, 39–42].

3. Literature Survey

• Exothermic reactions (like methanation) can be promoted inside the stack simultaneously with electrolysis, to meet the heat demand from endothermic electrolysis [6, 26, 32, 37, 40]. The reverse can also be applicable for the exothermic fuel cell mode and endothermic cracking/reforming reactions.

- Pressurisation has a very positive effect on the stack performance in FC mode, but significantly increases air compression power. This means that a gas turbine is required at the air exhaust to make pressurisation beneficial. Pressurisation can also have positive effects on EC mode, but this is less straightforward [29]. However, the combined effect of pressurisation for a well designed ReSOC system is mainly positive [6].
- Air recirculation has been shown to provide benefits, by reducing power consumption of the BoP (specifically, air preheaters and compressors) [4, 29, 31, 39, 41].
- Synergistic refrigeration (i.e. sub-ambient evaporation of one species integrated with the sub-ambient condensation of another species) can be used to significantly reduce refrigeration costs when two or more gases have to be liquefied in different modes [28, 43].
- Most work has been done on steady state systems. While most sources calculate efficiency with fixed power output [4, 6, 27, 28, 32–36, 40–43], some researchers have varied their power output using actual supply-demand data to analyse efficiency. [30, 31]. One author studied the effects of tank dynamics on his system [37, 38].
- Energy storage in ammonia has been proposed at a current maximum RTE of 72 %, achieved with stack operation at 50 bar, synergistic refrigeration, a gas turbine and an auxiliary steam turbine [43]. The effect of air recirculation (in FC mode) and thermal energy storage in ammonia systems are still to be explored. While sensitivity analysis for cost has been done, sensitivity analysis for efficiency has not been published. Exergy analysis is also yet to be done.

3.2. Use of Ammonia in solid oxide fuel cells

The use of ammonia in SOFCs was first explored as a method to produce NO (for producing nitric acid), while enabling extraction of energy in the form of electricity instead of heat [46]. Metkemeijer and Achard [47] carried out an analysis of ammonia as a fuel for alkaline fuel cells, with a dedicated cracking unit. Ammonia was also used as a mixed fuel for SOFCs along with alcohols [48, 49 cited in 50]. The direct use of pure ammonia in SOFC specifically for energy production began to be explored in the early 2000s.

Wojcik et al. [50] carried out the first investigations on the use of pure ammonia in SOFCs with low NOx production. They used a tubular SOFC with YSZ electrolyte and silver anodes. The ammonia was decomposed in-situ, using a novel method involving steel wool with iron powder packed into a section of the tubular cell near the inlet. Another SOFC with platinum anode and no iron catalyst was also tested. These cells were tested at different temperatures with a pure ammonia feed and a pure hydrogen feed. They found that the ammonia gave performances very similar to pure hydrogen when used in the cell with silver anode and iron catalyst. The platinum anode cell gave much higher current densities due to the higher active area of Pt, but was deemed unsuitable due to NOx production. Nickel cermets were indicated as a good candidate for future studies due to larger active areas than Ag and existing use in SOFCs.

Staniforth and Ormerod [51] investigated the behaviour of ammonia in SOFCs due to the presence of ammonia in biogas to be used in SOFC. Through experiments on a tubular YSZ-based cell, they found that the ammonia is fully decomposed above 590 °C. They found no direct electrochemical oxidation of ammonia since the behaviour of open circuit voltage (OCV) vs. temperature above 600 °C followed what is expected from thermodynamics of hydrogen oxidation, and not that of ammonia. Additionally, they found no formation of NOx even at their highest current draw.

Dekker and Rietveld [52] tested direct ammonia SOFCs with an electrolyte-supported cell (ESC) and an anode-supported cell (ASC). Several mixtures of ammonia and cracked ammonia ($3\,H_2/N_2$) in various proportions were tested. The cell voltage was observed to be independent of the gas composition above 750 °C, thus confirming that ammonia is decomposed completely near the inlet. But even at 700 °C, the ammonia concentration at the outlet was only ~250 ppm and the maximum voltage penalty from insufficient cracking was only ~25 mV. No cracks were detected in either cell after 3000 h, and voltage degradation was less than 1 % per 1000 h. Exhaust NOx concentrations were <0.5 ppm up to 950 °C, but 4 ppm at 1000 °C.

Fournier et al. [53] tested YSZ and calcia-stabilised zirconia (CaSZ) electrolytes in intermediate temperature cell with various anode materials like nickel, silver and platinum. A tubular cell and a YSZ pellet cell were tested. YSZ showed higher power densities than CaSZ due to faster oxygen transport. Among anode materials, nickel cermet demonstrated the highest ammonia conversion (92 % at $800\,^{\circ}$ C) as well as the highest power densities. In the pellet cell at $800\,^{\circ}$ C, ammonia showed higher power densities than pure hydrogen, which was explained by the authors using Nernst potential calculations. Thus, the use of YSZ-Ni cermet at a temperature of at least $700\,^{\circ}$ C was concluded to have excellent potential for direct use in fuel cells.

Ma et al. [54] compared ammonia and hydrogen in a SOFC-H with pure oxygen and CO2-free air as oxidants. The ammonia and hydrogen I-V curves had very similar slopes, indicating that ammonia decomposition was fast and nearly complete. The OCV and power densities were only slightly lower for ammonia, with any difference being explained by dilution of hydrogen by nitrogen. The OCV was also shown to deviate from theoretical values as temperature increased, which was attributed to increased electron leakage through the electrolyte. The use of the proton-conducting electrolyte ensured that no oxygen was available at the anode for NOx formation.

Later, Ma et al. [55] also tested an intermediate temperature oxygen ion-conducting solid oxide fuel cell (SOFC-O) from 500-700 °C for NO formation and long-term endurance. The ammonia was cracked almost completely at 600 °C and above, with an OCV drop <5 mV (<1 % drop) vis-à-vis pure hydrogen and <1 % residual ammonia at the anode outlet. At 500 °C, there was >30 mV drop in OCV, with 5-21% residual ammonia at the anode outlet. The difference in power densities also reduced with temperature, being <20 mW cm⁻² (<7 % drop) at 700 °C. Additionally, at all temperatures and flow rates, no NO was detected at the anode outlet. No detectable performance drop was observed after 50 hours.

Ma et al. [56] also tested a high-temperature SOFC-O from 650-850 °C. It was found that below 750 °C, the NiO anode needs to be pre-reduced to Ni using hydrogen before use, while above this temperature, ammonia itself can serve as the reducing agent. The decreasing nature of the OCV with temperature confirmed that ammonia was being thermally cracked before oxidation, and not oxidised electrochemically. The OCVs for the ammonia and hydrogen tests were similar, despite nitrogen dilution for ammonia. A maximum power density of $526\,\mathrm{mW\,cm^{-2}}$ was achieved at $850\,\mathrm{^{\circ}C}$, compared to $530\,\mathrm{mW\,cm^{-2}}$ for hydrogen.

Meng et al. [57] compared hydrogen and ammonia in an intermediate temperature SOFC-O with an SDC electrolyte. They found significantly lower performance for ammonia at 550-650 °C. They attributed this to incomplete decomposition due to their high liquid ammonia flow rate. They recommend raising the cell temperature, lowering the flow rate, or pre-heating the ammonia before entering the cell.

Using a tubular anode-supported YSZ-based SOFC with ammonia and hydrogen, Zhang et al. [58] found no trace of NOx in the anode effluent. While the used cell had not been optimised for power density, the power density of ammonia was comparable to hydrogen, with a peak power density of 200 mW cm $^{-2}$ at 800 °C, compared to 202 mW cm $^{-2}$ for hydrogen. No degradation was seen after 100 h. They also found that ammonia was completely decomposed before reaching the TPB.

Ni et al. [59] developed an electrochemical model for an SOFC-H, comparing ASCs and ESCs. They found that the performance of hydrogen and ammonia in ESCs is very similar, while ammonia has a lower voltage and power density than hydrogen in ASCs at larger current densities, especially with thin-film electrolytes. This was found to be due to significantly larger anodic concentration overpotential in anode-supported ammonia cells, caused by dilution of hydrogen with nitrogen. The ASC was found to have better ammonia cracking than the ESC, due to the higher concentration of Ni in the ASC anode.

Ni et al. [60] improved their previous model [59] by including the kinetics of thermocatalytic cracking of ammonia. In a 0.5 mm thick Ni anode, they found that ammonia was completely decomposed within 30 μ m at 800 °C, and within 300 μ m at 600 °C. Ammonia decomposition was only 40 % at 500 °C, and only 10 % at 400 °C. Rate of decomposition increased slightly at higher current densities due to faster consumption of hydrogen deeper in the anode.

Ni et al. [61] also compared SOFCs by electrolyte type. They showed that while SOFC-Hs have potential thermodynamic benefits due to avoiding dilution of fuel by steam, their actual performance under typical working conditions is lower than SOFC-Os due to higher ohmic overpotential. At $800\,^{\circ}$ C and atmospheric pressure, oxygen-conducting cells outperformed proton-conducting cells above $5000\,\mathrm{Am^{-2}}$, while the performance was very similar at lower current densities. Considerable improvements in concentration overpotentials were also seen by increasing electrode porosity.

Fuerte et al. [62] carried out tests with ammonia-hydrogen mixtures on a micro-tubular Ni-YSZ-LSM SOFC. Gradual decreases in cell voltage were observed with increments in proportion of ammonia in the feed. The drop was largest between 80% and 100%, and was attributed to the dilution of hydrogen by nitrogen.

18 3. Literature Survey

Maximum power density was also found to be $15\,\%$ lower for ammonia compared to hydrogen for the same reason. The authors also reiterated the conclusions of previous authors [51, 56] on the two-step oxidation of ammonia inferred from the OCV vs. temperature trends. They noted that ammonia decomposition is slow at low temperatures around 700 °C, leading to slight differences in polarisation resistances.

Ni [63] carried forward his work from [59–61] by developing a 2-D cross-section model of a planar SOFC integrating thermochemistry, electrochemistry and CFD sub-models in a 20 cm long anode-supported cell. They found that the ammonia was almost fully cracked in the cell at $700\,^{\circ}$ C, but barely cracked at $500\,^{\circ}$ C. However the fast endothermic decomposition at $700\,^{\circ}$ C led to large thermal gradients ($\sim 130\,^{\circ}$ C). Increasing the power density (and thus heat production) led to a lower temperature gradient. However, it must be noted that the cell power densities were quite low. Since parts of the cell were highly cooled down due to the decomposition, the rate of hydrogen oxidation was also lowered, and fuel utilisation achieved was very low (maximum 15.2%). Thus, energy needed for decomposition of ammonia was never fully compensated by the oxidation reaction at any of the tested operating points.

Yang et al. [64], tested the effects of ammonia on a NiO/YSZ SOFC over 24 h. It was found that exposure to ammonia caused nitriding and sintering of the nickel particles, leading to increased ohmic and polarisation resistances. This effect was strongest near the inlet where pure ammonia was encountered, while hydrogen produced by cracking had a protective effect. Lastly, temperature-cycling caused severe degradation due to de-lamination and leakage caused by repeated nitriding and de-nitriding.

Molouk et al. [65] studied the performance of ammonia, hydrogen and methane on a Ni/YSZ cell in terms of power density, impedance, etc. They found that ammonia was better than methane but worse than hydrogen, but the difference disappeared at higher temperatures (800 °C). This means that ammonia was decomposed at lower temperatures compared to methane. Additionally, they found that presence of nitrogen or steam does not affect ammonia decomposition (for the residence time under consideration), while hydrogen in the feed suppresses ammonia decomposition.

Cinti et al. [66] tested a cell with hydrogen, ammonia and pre-cracked ammonia at temperatures of $700\,^{\circ}$ C to $800\,^{\circ}$ C. They found no significant differences (<2%) in the OCVs or the polarisation curves for the three fuels. A system model was made using fitted values from the experiments, which then demonstrated the beneficial effect of cooling provided by internal ammonia cracking (upto 22% increase in system energy efficiency compared to external cracking).

Afif et al. summarised these findings in a comprehensive review [67]. Higher temperatures bring the performance of ammonia closer to hydrogen due to better decomposition, while hydrogen fuel cells themselves have an optimum temperature based on the balance between OCV and overpotentials. 100 % decomposition is possible at temperatures above 600 °C. SOFC-Hs have higher theoretical power densities than SOFC-Os, while actual power densities are better for SOFC-Os, especially at higher temperatures.

Stoeckl et al. [68] found an average 14 % reduction of performance using ammonia. This was found to be due to a temperature decreases caused by endothermic ammonia cracking, which appeared to be the most influential parameter on cell performance. They confirmed the two-step cracking mechanism, and also found evidence of nitriding at the anode inlet.

In summary,

- Behaviour of OCV with temperature indicates that oxidation of ammonia in an SOFC with nickel anodes is a two-step process: thermocatalytic cracking of ammonia into hydrogen and nitrogen, followed by electrochemical oxidation of hydrogen [51, 56, 62, 65, 68]. There is no evidence for direct electrochemical oxidation of ammonia, and no ammonia reaches the TPB [58].
- The performance of ammonia fuel cells and hydrogen fuel cells is very similar, as long as decomposition is sufficient. While one source notes a larger power density for ammonia cells [53], most sources report small (0-15 %) decreases in OCV and power density [54–56, 58, 62], which are explained by Nernst potential reduction and greater anode concentration overpotential caused by dilution with nitrogen. Thus, for modelling purposes, the two-step mechanism implies that an ammonia SOFC can be modelled just like a hydrogen SOFC, as long as the effect of nitrogen is taken into consideration.
- Nickel in the anode is capable of completely cracking the ammonia, however the extent of this is affected by temperature and residence time. While flow rates differ widely in tests, the effect of temperature is more significant. While it is agreed that higher temperature allows better decomposition, various sources differ quantitatively in their results: from full decomposition at 600 °C [51], to 92 % decomposition.

tion at 800 °C [53]. However, with proper preheating of ammonia up to stack temperature, most sources agree with full decomposition at stack temperatures over 700 °C [51, 52, 55, 59, 62, 63, 65].

- Anode-supported cells show better cracking of ammonia than electrolyte-supported cells. But the increase in concentration potential due to nitrogen dilution is much more severe in anode-supported cells. [59]
- With nickel anodes at typical operating conditions of SOFC (500-1000 °C), NOx formation is of no concern. Most sources found no detectable NOx emissions [51, 55, 58], while one study found only 4 ppm of NOx at 1000 °C, and less than 0.5 ppm below 950 °C [52].
- Direct ammonia fuel cells have a marked benefit in system efficiency due to cooling effect provided by the decomposition [66]. However, this can lead to very high local temperature drops [63], which can limit further decomposition as well as reduce stack performance [68]. Therefore, the heat transport inside the stack has to be very good in order to prevent large gradients and performance reduction.
- Nitriding and sintering of nickel catalyst occurs on exposure to high concentrations of ammonia near the anode inlet [64, 68]. This reduces performance slightly, but the extent of nitriding reaches steady state quickly. Nitriding is reversed by exposure to hydrogen produced from the decomposition, which depends on temperature. Thus, temperature cycling causes repeated nitriding and de-nitriding in the deeper parts of the anode near the inlet, leading to rapid voltage degradation, delamination and leakage [64]. It can be inferred that cycling between ammonia fuel cell and steam electrolysis modes is likely to have the same effect. This will have to be considered in the design of a ReSOC system with ammonia.

3.3. Ammonia Production with Electricity

Conventional ammonia synthesis through the Haber-Bosch process is a widely studied and mature process, with 90 % of the world consumption being produced in this way [8]. However, due to the use of natural gas as feedstock, this process is quite carbon-intensive. Integration with renewable energy requires electrification of this process. In this section, recent studies on the topic of electrical ammonia production are discussed. This electric production can either be through use of electrolytic hydrogen in a conventional Haber-Bosch process, or through direct electrochemical synthesis of ammonia. Studies evaluating various Haber-Bosch configurations are also presented in this section.

Frattini et al. [69] first modelled a renewable path for ammonia synthesis in Aspen Plus. The Haber-Bosch loop consisted of an RGIBBS reactor, followed by heat recovery and a two-stage flash, one of which was cooled with product gas. After designing the Haber-Bosch loop, they compared three sources of hydrogen and nitrogen: "real" syngas from biomass gasification (i.e. syngas with water vapour, CO_2 and N_2), biogas, and electrolysis + pressure swing adsorption (PSA). These were compared to the conventional steam methane reforming (SMR) process. They found that all the processes had very similar primary energy consumption. In fact, the electrolysis path had the highest energy efficiency, followed by syngas, despite the large amount of inerts in the syngas. This proved that a wide range of renewable sources can be integrated into ammonia synthesis without any thermodynamic drawbacks.

Cinti et al. [70] coupled an solid oxide electrolysis cell (SOEC) with PSA separation of nitrogen and a Haber-Bosch process for green ammonia synthesis. They compared this combination with the conventional ammonia synthesis from natural gas and with green ammonia synthesis from low temperature electrolysers. In order to enable heat recovery from synthesis reactor to the SOEC, both these processes were operated at $650\,^{\circ}$ C. Hence the Haber-Bosch reactor had to operate at a very high pressure of 550 bar compared to the other configurations (250 bar, 550 $^{\circ}$ C). Both the electrolysis processes were found to have significantly higher ammonia synthesis conversion and efficiency compared to the conventional process, due to very low concentration of inert gases. However, on a system level, the heat integration and lower power consumption of the SOEC system was found to enable significantly higher energy efficiencies than the conventional and low-temperature systems (62.41 % compared to 35.50 % and 36.35 % respectively).

As described in Section 3.1, Wang et al. [43] designed an energy storage system using ammonia in a ReSOC. They used a 200 bar triple-bed synthesis reactor with direct (quench) cooling for ammonia synthesis, and ambient temperature two-stage flash for separation. Heat from the synthesis reaction was used to preheat the feed, as well as to generate steam for the SOEC.

Penkuhn and Tsatsaronis [71] used advanced exergy analysis to compare two configurations of the Haber-Bosch ammonia synthesis loop. One configuration had a triple fixed-bed reactor at \sim 200 bar with direct

20 3. Literature Survey

quenched cooling, while the other configuration had a tube-reactor which was directly cooled with thermal fluid. They found multiple advantages to the latter configuration. The cooled reactor had a larger conversion rate and three times smaller exergy destruction due to the recovery of high-temperature heat rather than quenching with cold feed. The heat exchangers also showed higher exergy efficiency in the second configuration. Significantly larger exergy was transferred in the steam generator in the cooled reactor design. The mixing of make-up reactant after ammonia separation was found to be more exergetically efficient. In general, the reactor type, heat integration and position of introducing make-up gas were found to be major factors influencing efficiency. Advanced exergy analysis showed that the heat integration and make-up compressor were the only components with a significant scope for improvement, without carrying out structural changes to the process.

Khademi and Sabbaghi [7] developed mathematical models to compare three ammonia synthesis reactor cooling configurations: internal direct cooling reactor (IDCR), adiabatic quench cooling reactor (AQCR) and adiabatic indirect cooling reactor (AICR). Their results are presented in Fig. 3.1. After optimising the models, they found that the AQCR had the lowest conversion rates, while the other two had almost the same conversion. The second and third beds of the AQCR were much larger than the first, but only offered marginal conversion improvements. The IDCR had a lower outlet temperature and also did not require an additional cooling medium. The authors found this to be an advantage for IDCR since it improves the catalyst life. However, it must be noted that the higher temperature and intercooling of the AICR can be useful depending on how and where the additional heat is used.

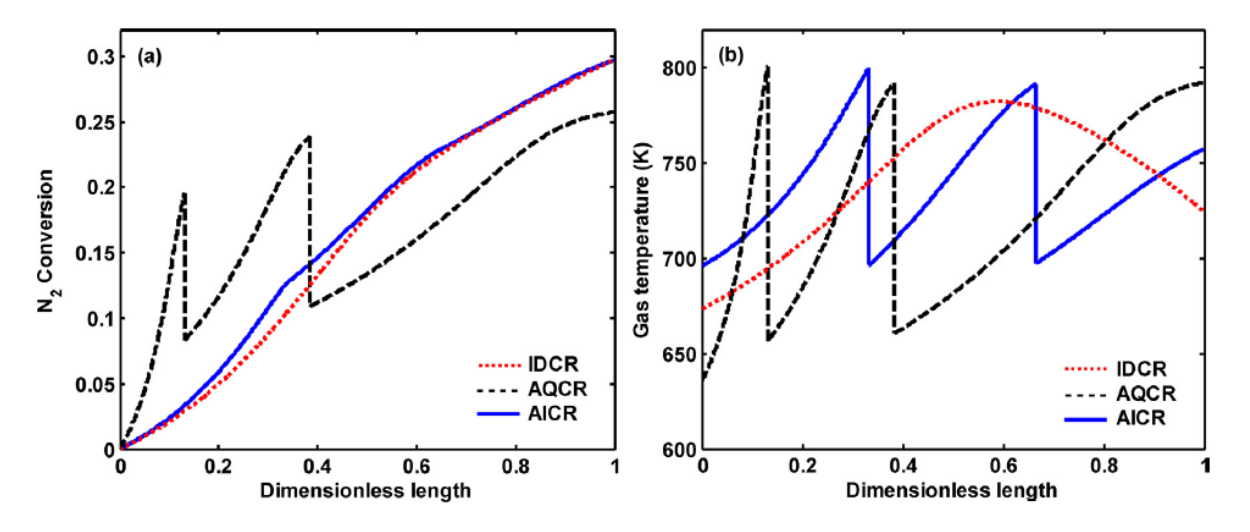


Figure 3.1: A comparison between the IDCR, 3-bed AQCR and 3-bed AICR under optimal conditions in terms of (a) N_2 conversion, and (b) temperature profiles. Figures taken from the work of Khademi and Sabbaghi [7].

Sánchez and Martín [72] optimised ammonia production from water and air using wind and solar energy. Hydrogen was produced using alkaline electrolysis, and nitrogen was captured from air using Linde's double column. They analysed an ammonia synthesis loop with a triple-bed reactor running between 400-500 °C and 168 bar, in both direct and indirect cooling configurations. Simulations were performed with non-linear programming and multi-start optimisation procedures. Over 90 % of the produced ammonia was recovered before recycling the gases. Both configurations performed similarly, with an ammonia production cost of 1.35 €/kg, and indirect cooling being only 3 % more expensive.

Cheema and Krewer [73] analysed the operating envelope of an autothermic Haber-Bosch process in order to test the flexibility of the process, enabling the integration of the Haber-Bosch process with hydrogen produced from intermittent renewable electricity. The various components were modelled and simulated in MATLAB. The main reactor bed was modelled as a radial flow bed, with fine particles of magnetite (Fe_3O_4) catalyst. For the particular combination of reactor and heat exchanger designs chosen, they varied six parameters one-by-one, including reactor pressure, inlet temperature, inlet ammonia concentration, etc. The operating region was bounded by the requirement for an autothermic process at the one end, and the upper limit of catalyst temperature at the other end. They found that the system was most flexible towards variation in the H_2/N_2 /inerts composition of the feed (up to 67 % decrease in H_2 from stoichiometric ratio could be tolerated), which makes the Haber-Bosch process resilient for operation with intermittent hydrogen production

from renewables.

Giddey et al. [74] conducted a review of electrochemical ammonia production. They found that electrochemical techniques were able to achieve high Faradaic efficiency only at the expense of low ammonia production rates (maximum 10^{-8} molcm⁻² s⁻¹). Stability of membranes was also an issue. In general, as of 2013, the technology still required significant advances in catalysts and other materials.

Guo et al. [75] reviewed several electrolyte and catalyst combinations for electrochemical ammonia synthesis. They also found the electrochemical techniques to be still in the experimental phase. The major impediments for each type of cell were an ammonia production rate in the order of 10^{-8} mol cm⁻² s⁻¹ for Nafion membrane cells, the lack of solid oxide electrolytes in the range of 200-500 °C, reverse decomposition of ammonia in molten salt electrolytic cells, and limited liquid electrolytes with solubility for N₂.

Jiao and Xu [76] reviewed three electrochemical techniques to synthesise ammonia. As of 2018, none of the methods were found to present a viable challenge to the Haber-Bosch process, with energy consumption ranging from 1.08-5.3 MJ/mol $_{\rm NH_3}$, compared to 0.48 MJ/mol $_{\rm NH_3}$ for the Haber-Bosch process. They also reviewed low temperature ammonia fuel cells, finding them to be severely limited due to the lack of a efficient catalysts for direct ammonia oxidation, as well as due to problems with ammonia crossover through the electrolyte.

Chen et al. [77] considered low Faradaic efficiency due to competition with hydrogen evolution, and lack of a bifunctional catalyst for both hydrogen evolution and nitrogen activation as major challenges to the electrochemical synthesis of ammonia.

In summary,

- As of 2018-19, direct electrochemical synthesis techniques are still not mature enough to compete with the Haber-Bosch process [74–77].
- Ammonia production with Haber-Bosch process using sustainable feed-stock is thermodynamically
 competitive with the conventional Haber-Bosch process which uses natural gas [69]. The Haber-Bosch
 process is also flexible enough to deal with intermittent reduction in hydrogen supply due to fluctuations in power production from renewable sources [73].
- The use of high temperature electrolysis is more suitable for ammonia production than low temperature electrolysis, due to heat integration possibilities between the endothermic high temperature electrolysis (or steam production for electrolysis feed) and the exothermic ammonia synthesis [70].
- Synthesis reactors with indirect or internal cooling show better performance than reactors with quench cooling [7, 71], with only a small cost penalty [72].

3.4. Heat Pipe Integration with SOCs

It was found in Section 3.2 that internal cracking of ammonia in SOFC is possible and can be beneficial to system performance. However, some studies [63, 68] in that section found a drop in stack performance due to temperature gradients caused by the endothermic ammonia cracking. Therefore, employing methods to reduce the thermal gradients can retain the system performance benefits of internal cracking while avoiding the disadvantages of uneven cooling. Dillig et al. introduced a new method to reduce temperature gradients in SOFCs, using liquid alkali metal heat pipes within the interconnects (bipolar plates) of the SOFC. This novel method could, in theory, be used to reduce thermal gradients in the stack. Additionally, this concept can also enable the integration of a thermal energy storage system without excessive air flows for heat transfer, and also operation of the heat storage at temperatures very close to the stack temperature.

Dillig et al. [78] tested planar sodium heat pipes with various capillary structures for use in high temperature SOCs. They demonstrated the almost isothermal heat transfer up to $100\,\mathrm{W\,cm^{-2}}$ provided by heat pipes with screen-meshed capillary structures, making them ideal for maintaining uniform temperature and avoiding cold spots in SOFCs, or for more effective cooling of the stacks. They demonstrated the permeation of hydrogen into the heat pipe to be a major concern during use in SOCs, and provided several counter-measures to mitigate this problem.

They then investigated planar sodium heat pipes further, through experiments with heat pipe interconnects used in a short SOC stack [79]. The heat pipes were shown to consistently make the temperature across the stack more uniform, as evaluated by various metrics. An SOFC with internal methane reforming was compared to a hydrogen cell at open circuit conditions. The endothermic reforming reactions usually lead to high

22 3. Literature Survey

temperature differences. The use of the integrated heat pipe enabled the reduction of the maximum temperature difference from 45 K to 15 K. However, the use of the heat pipe lowered the power density of the cell slightly, mainly due to contacting and sealing issues from heat pipe fabrication.

3.5. Activities Undertaken in this Thesis

As mentioned in Chapter 1, the goal of this thesis is to develop a process design to achieve high round trip efficiency in an ammonia-based ReSOC system, and to gain a thermodynamic understanding of the effect of the process decisions.

The study of literature in Section 3.1 revealed that while there are a larger number of studies on hydrogen and hydrocarbon-based ReSOC systems in recent years, there is very little work done in the topic of integrating ammonia with ReSOC systems. In 2017, Wang et al. [43] developed a detailed mathematical model for such a system and carried out operating point optimisations, reporting an optimum round trip efficiency of 72%. However, there was little thermodynamic discussion on the losses incurred in the system. The sensitivity analysis was focused on techno-economics. Therefore, there is a need to carry out an exergy analysis on such a system, to identify the losses, explain the efficiency achieved, and discover any scope for improvement.

Accordingly, the primary task of this thesis will be to design an efficient ReSOC system using ammonia, along with a detailed thermodynamic exergy analysis of the same. Additionally, some opportunities to improve the efficiency were observed during the literature study. These opportunities are described in the following points, and will be analysed in this thesis.

- 1. Pressurisation of ReSOC systems has been stated in literature to be beneficial for system efficiency. Pressurised systems consume significant power for air compression, and the importance of a gas turbine at the cathode exhaust has been noted in literature. However, heat from the stack exhaust is also required for preheating the incoming flows. This signifies competition for the energy from the exhaust, which is decided by the relative placement of the turbine and recuperation heat exchangers. Most models in literature place the air turbine downstream after a heat exchanger to preheat inlet flows. But this tends to reduce the power output of the turbine. Mor [31] made a brief comparison of this in FC mode, but a detailed comparison of performance based on turbine placement can be a useful design guideline. Therefore in the current work, a detailed comparison will be made between the two configurations in both operating modes, based on exergy analysis, to recommend a more beneficial position for the gas turbine.
- 2. It appears to be common practice to use an afterburner to take care of unutilised fuel in FC mode [27, 29, 31, 43]. The heat from an afterburner makes preheating of inlet flows easier, and it can increase the inlet temperature of the exhaust air turbine in pressurised systems. However, combustion is known to cause significant exergy losses. Therefore, eliminating an afterburner can be one possible pathway to improve the efficiency of a reversible system. A reversible system is specially suitable for burner-less operation, since the exhaust gases are stored and not emitted to the environment. However, without an afterburner, it can be challenging to meet the preheating needs of the inlet streams, especially in pressurised systems with a turbine. Therefore, in this work an attempt will be made to develop a ReSOC system without an afterburner, in order to establish if it is thermodynamically feasible for an ammonia ReSOC system. Through exergy analysis, a thermodynamic comparison will also be made with a similar system containing an afterburner.
- 3. Thermal energy storage has been discussed in literature [27, 30, 39–42] as a feasible strategy to improve integration in ReSOC systems. The use of thermal energy is also one of the major advantages of endothermic high temperature electrolysis. In this thesis, an investigation is carried out to understand whether thermal energy storage is a suitable candidate to further enhance the efficiency of an ammonia ReSOC system without and afterburner.

All these design choices will be studied through analysis of exergy flows and round-trip efficiency. Finally, one set of design choices and operating points will be recommended for optimal operation of an energy storage system based on ammonia and ReSOCs, and the thermodynamic reasons behind these choices will be discussed.

4

Modelling and Simulations

The model of the ReSOC system was made in Aspen Plus V8.8. Two separate models were created for fuel cell and electrolysis respectively. There is no module for fuel cell electrochemistry in Aspen Plus, therefore thermochemical reactions were modelled in Aspen, and electrochemical results were calculated from the thermochemical results by executing the appropriate electrochemical equations using Fortran/Excel calculator blocks. The in-built Aspen Excel Plugin was used, which translates the spreadsheet calculations into Fortran. The Aspen model has been inspired by the work of Sebastian Diaz Rodriguez [4], and adapted to the purpose of this thesis.

In this chapter, the overview of the entire system design is provided first. This is followed by a more detailed description of each subsystem model, along with the reasons for the particular design choices made for those subsystems. Finally, the metrics used to analyse the performance of the system are described.

4.1. System Model - Basic Configuration

The basic skeleton of the energy storage system is described in this section. The basic configuration does not include any heat integration. The purpose of this basic design is to find the thermodynamic feasibility of a very simple system, and to serve as a reference for any improvements carried out later. The system design, even in the basic configuration, already includes the provision for pressurised operation, as one of the recommended process improvements from literature, seen in Section 3.1. A gas turbine is provided at the air electrode exhaust to recover the energy of pressurisation.

4.1.1. Basic Configuration - Fuel Cell Mode

The basic configuration of the system in fuel cell mode can be seen in Figure 4.1. Liquid ammonia from the tank is pumped to stack pressure, and then brought to ambient temperature. It is further superheated to the desired stack inlet temperature and passed into the stack for internal cracking and electrochemical oxidation. Since one of the activities of this thesis is to investigate a system without an afterburner, no afterburner is used in the basic configuration, and the fuel electrode exhaust of the SOFC is directly sent to the gas purification system. The purified gas (which is a mixture of nitrogen and hydrogen) is compressed in the multi-stage compressor and stored in its tank. The intercoolers in this case are placed after each compression stage, because the inlet of the first stage is already cold, having passed through the steam condenser. The condensed water is expanded to ambient pressure and stored. Air for oxidation and cooling is taken from the atmosphere and compressed to the pressure of the stack. It is preheated to the appropriate inlet temperature and sent to the stack. The exhaust from the air electrode is expanded in a turbine and then released into the atmosphere.

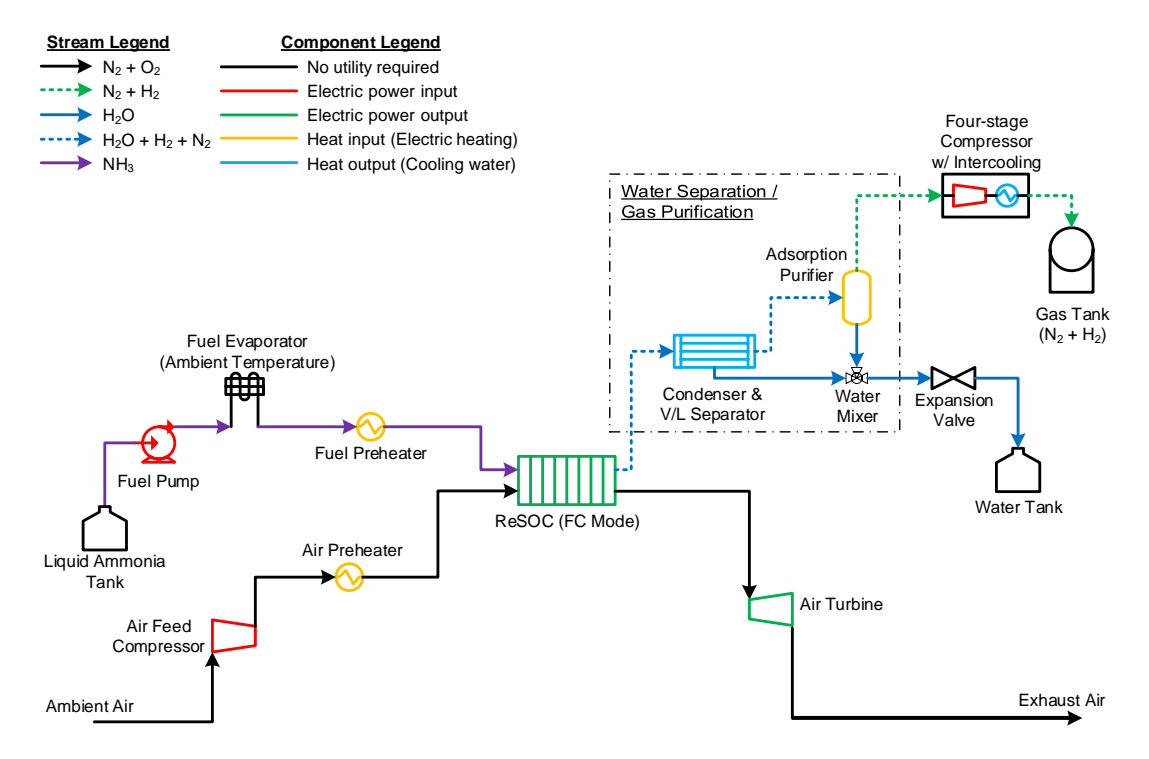


Figure 4.1: Process flowsheet for fuel cell mode - Basic configuration.

4.1.2. Basic Configuration - Electrolysis Mode

The basic configuration of the system in electrolysis mode can be seen in Figure 4.2. Liquid water from the tank is pumped to stack pressure, evaporated, and superheated. It is then mixed with the hydrogen-steam mixture recirculated from the exhaust. This is in order to ensure a hydrogen content of at least 10 % in the SOEC inlet to maintain reducing conditions for the nickel catalyst [80]. The steam is superheated to the appropriate temperature such that after mixing with the recirculated hydrogen/steam, the mixture attains the required stack inlet temperature. After bleeding some portion of the mixture for recirculation, the fuel side exhaust of the SOEC is then directed to the separation and purification system. The recirculation of hydrogen is carried out before the condensation and purification, because this reduces purification energy cost, recycles some unreacted steam along with the hydrogen, and also reduces the required steam superheating temperature. The purified hydrogen is compressed in the multi-stage compressor and directed to the ammonia synthesis system. In this case, the intercoolers are placed before each compression stage. There is no cooler after the last compression stage, to keep the synthesis feed gas as hot as possible. The condensed water is expanded to ambient pressure and returned to its tank. The nitrogen-hydrogen gas mixture stored in the fuel cell exhaust is drawn from its tank, expanded to synthesis loop pressure and mixed with the freshly created hydrogen. This stoichiometric reactant mixture now goes to the ammonia synthesis loop. The produced ammonia is expanded to ambient pressure, cooled further if required, and stored in its tank. The sweep air is taken from the atmosphere and compressed to stack pressure. It is heated to the appropriate temperature and sent to the stack. The exhaust air is expanded in a turbine and then released into the atmosphere.

4.1.3. Stack Operating Parameters

The variation ranges considered for the stack operating parameters in this thesis is listed in Table 4.1. These ranges were based on project requirements for the BALANCE project. The values chosen for the base case are also specified.

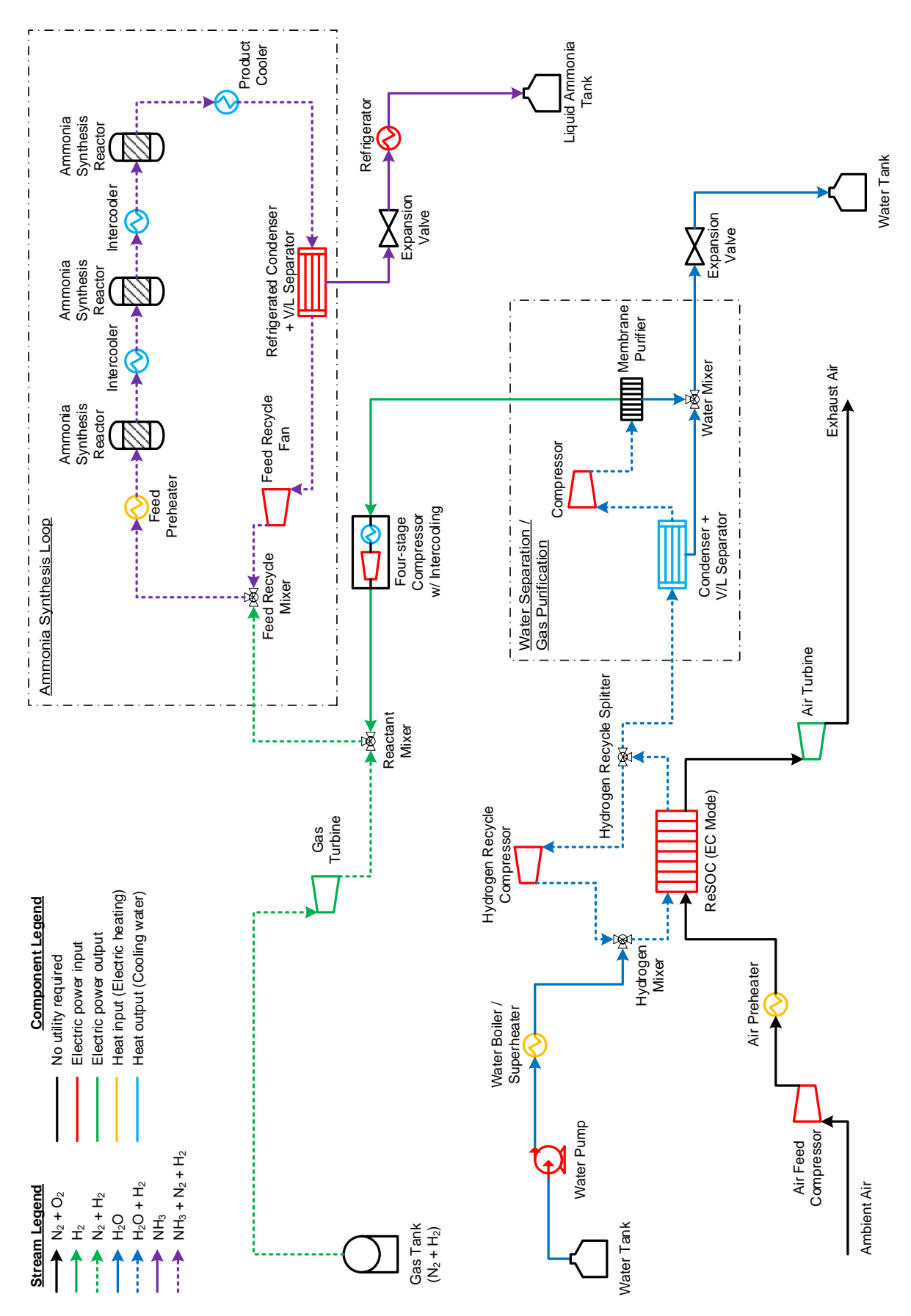


Figure 4.2: Process flowsheet for electrolysis mode - Basic configuration.

Parameter	Variation Range	Base Case Value	Unit
Stack Temperature	650-800	800	°C
Stack Pressure	1.5-10	1.5	bar
Current Density	2500-10000	5000	Am ⁻²
Fuel/Steam Utilisation	-	0.8	-

Table 4.1: ReSOC stack parameters for base case.

4.2. Reversible SOC Stack Model

The stack model is based on certain assumptions to simplify the calculations to make a 0-D model. The stack body is assumed to have a uniform temperature, with all the reactions occurring at this temperature. The outlet gases are also assumed to be in thermal equilibrium with the stack. In order to reduce mechanical stresses and catalyst sintering caused by excessive thermal gradients, inlet air streams need to be preheated close to stack temperature, with a typical temperature difference of $100\text{-}200^{\circ}\text{C}$ [6]. A temperature difference of 100°C is assumed in this model. The inlet streams on the fuel-side are always 100°C lower than the stack temperature. The air-side streams are used for thermal management of the stack. If the stack is endothermic, the inlet air temperature is 100°C lower than the stack. The pressure drop in the stack is assumed to be 15 mbar, as per Tjaden et al. [81].

4.2.1. SOFC Model

Insights from the literature study described in Section 3.2 were used to develop this model of an ammonia-fed SOFC. Ammonia is directly introduced in the fuel cell, and undergoes complete cracking. As shown in the literature study, this is a reasonable assumption, especially above 700 °C. The hydrogen produced from this cracking undergoes electrochemical oxidation.

Figure 4.3 shows the Aspen flowsheet of the stack model in FC mode. The ammonia fuel stream "FF1" and the air inlet stream "FA1" enter the stack and get heated up to stack temperature by the stack body, represented by the two heater blocks. The heated ammonia in stream "FF2" is cracked at the nickel catalyst, forming a stoichiometric mixture of nitrogen and hydrogen, named stream "FF3". The cracking is modelled as a RSTOIC1 reactor block, which enforces the complete cracking of ammonia. The energy required for ammonia cracking is drawn from the stack body in the form of heat. The separator block separates the desired amount of oxygen from the air stream "FA2". The transport of oxygen ions through the electrolyte is represented by the stream "FO1". In the model, this stream contains oxygen gas, and not ions, because the Aspen model is not an electrochemical model. The amount of oxygen separated is calculated according to the desired current density using an Aspen calculator block. The electrochemical oxidation of the hydrogen in "FF3" is represented in another RSTOIC reactor block, where all the oxygen introduced by "FO1" is consumed. The electrical power output of the fuel cell stack is calculated as described in Section 4.3. The difference between the enthalpy change of the oxidation reaction and the electric power output is the heat generated by the reaction. This heat is also transferred to the stack body. The flow rate of the inlet air "FA1" is manipulated using a Design-Spec block until the stack body achieves energy balance. In FC mode, the stack is typically expected to operate in exothermic region, unless the fuel utilisation is very low. This means the inlet air flow is always colder than the stack.

4.2.2. SOEC Model

The stack in EC mode is operated as normal steam electrolysis. Figure 4.4 shows the Aspen flowsheet of the stack model in EC mode. The general structure of the model is the same as in FC mode. The steam inlet stream (with some hydrogen) "EF1" and the sweep air inlet stream "EA1" enter the stack and get heated up (or cooled down) to stack temperature by the stack body, represented by the two heater blocks. The heated steam "EF2" is then electrolysed in the RSTOIC¹ block. The amount of water electrolysed is based on the assigned "reactant" utilisation factor. The generated oxygen is then separated into the stream "EO1", which represents the ionic flow in the electrolyte. This is added to the heated sweep air stream "EA2" in the mixer block. The stack electric power input is calculated as described in Section 4.3. The difference between the

 $^{^{1}}$ RSTOIC is an inbuilt chemical reactor model in Aspen Plus. It forces a given reaction to a desired level of completion, disregarding equilibrium.

4.3. Electrochemical Model 27

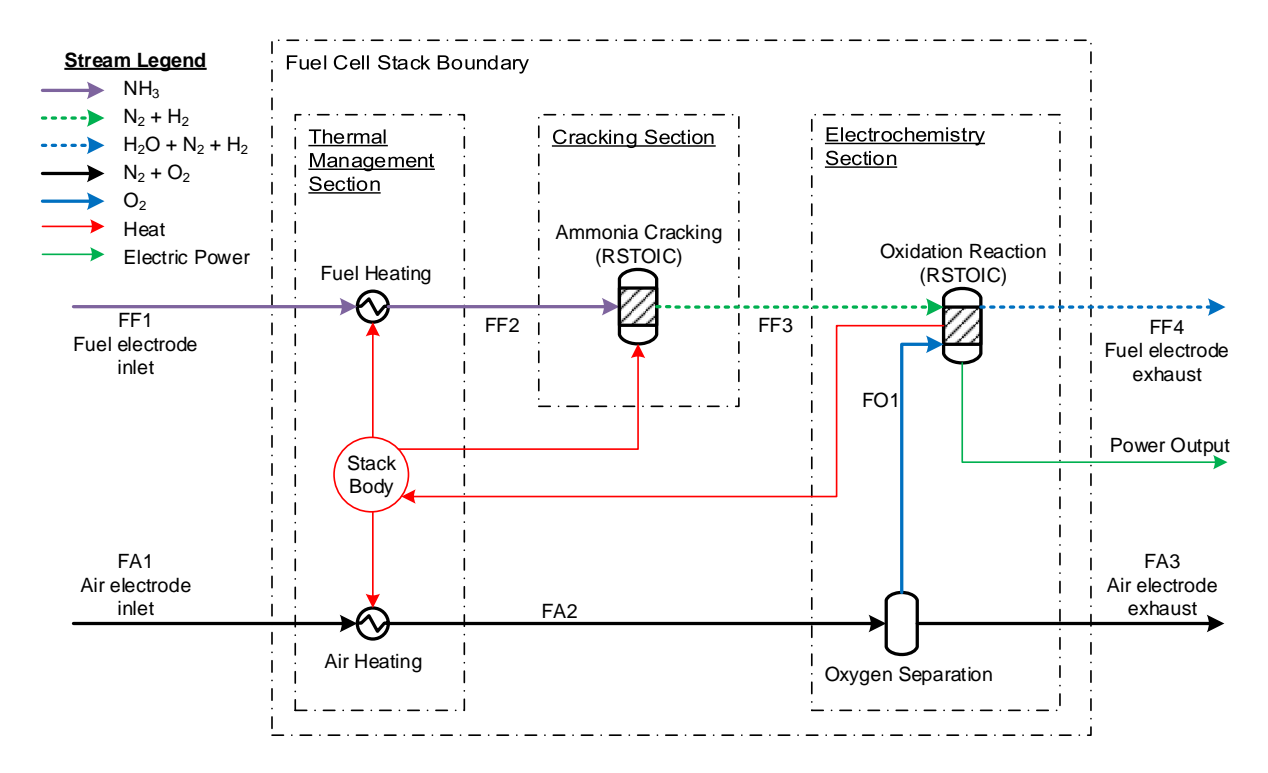


Figure 4.3: Schematic of Aspen Plus model of ReSOC stack in fuel cell mode.

enthalpy change of the reduction reaction and the electrical power input is the heat demand of the stack. If the calculated power input is more than the enthalpy change, then the reaction is exothermic, while if the calculated power input is less than the enthalpy change, the reaction is endothermic. Depending on this, the heat is either transferred to or from the stack body. Just like the SOFC model, the energy balance of the stack is maintained by manipulating the flow rate of the sweep gas "EA1". Unlike the FC mode, the stack can be either endothermic or exothermic in EC mode. Therefore, the sweep air inlet temperature is selected accordingly to be 100 °C above or below stack temperature.

4.3. Electrochemical Model

The fundamentals of an electrochemical cell were explained in Section 2.1. This section explains how those concepts were implemented quantitatively to make an electrochemical model for simulations. The electrochemical model that was implemented in this thesis was originally developed by Hauck et al. [2]. Instead of using a simplified ASR, each polarisation loss is calculated separately. Since this is only a 0-D model, the reversible voltage is averaged across the cell, and polarisation losses are calculated at the average current density. They have validated the model with experiments from literature, and also conducted various parametric studies which agree with previous results from literature. The electrochemical equations used by Hauck et al. are described in the following subsections. Further, Table 4.2 and 4.3 show the cell geometry and material parameters, respectively, chosen for the electrochemical calculations. These parameters (except the number of cells an cell area) were also taken from the work of Hauck et al. These parameters will be described in the following sections.

4.3.1. Reversible Voltage

The reversible voltage U_{rev} [V] at any point in a cell can be given by Equation (2.8), which is called the Nernst equation. However, the Nernst equation cannot be applied directly in a 0-D model, since reactant concentrations differ from point to point in an actual cell. In order to obtain the average reversible voltage across a cell in the stack, voltage was calculated from the Gibbs energy change ΔG [J]. Gibbs Free Energy values for the streams were obtained from the Aspen simulation, and the overall change was calculated only for the electrochemical section of the stack, i.e. all blocks except the heaters and cracker. This is shown in Equations (4.1) and (4.2), where the subscripts on the right-hand side refer to streams from Figures 4.3 and 4.4 respectively.

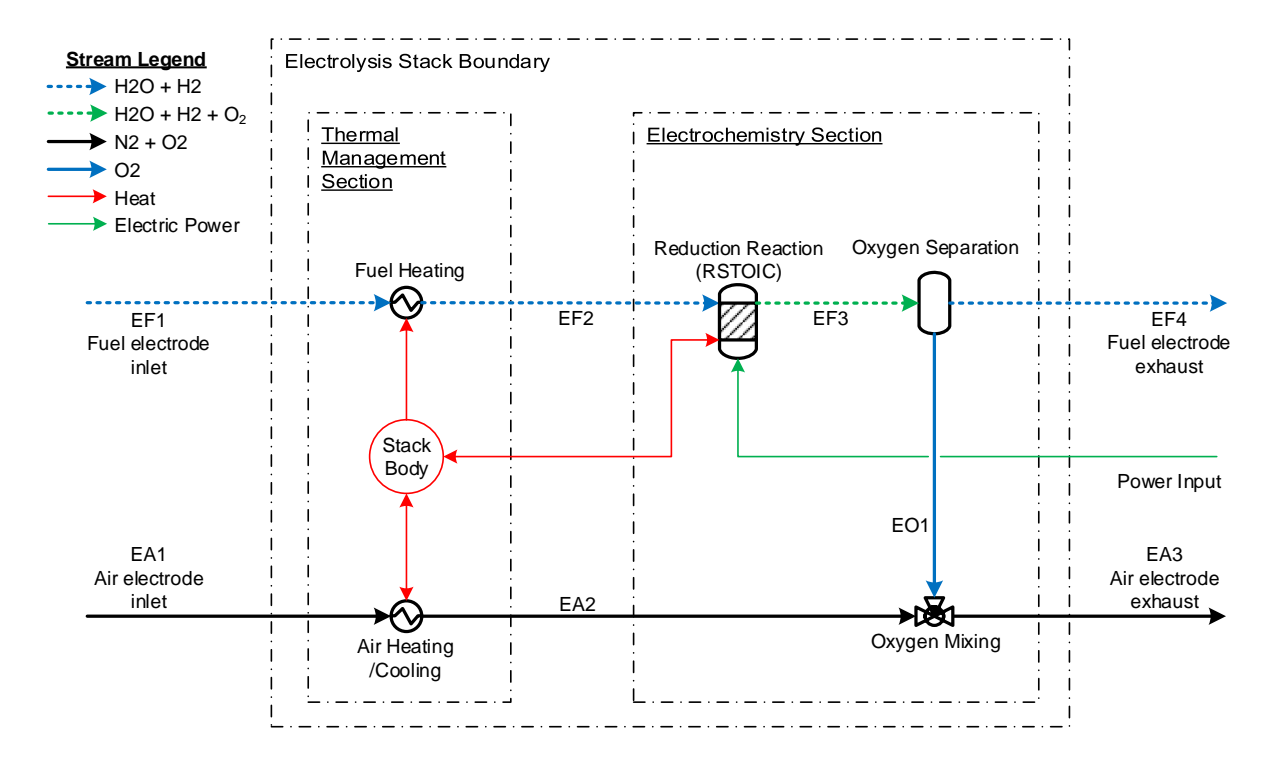


Figure 4.4: Schematic of Aspen Plus model of ReSOC stack in electrolysis mode.

$$\Delta G_{FC} = G_{FF4} + G_{FA3} - G_{FF3} - G_{FA2} \tag{4.1}$$

$$\Delta G_{\rm EC} = G_{\rm EF4} + G_{\rm EA3} - G_{\rm EF2} - G_{\rm EA2} \tag{4.2}$$

The Gibbs energy change denotes the reversible electric power of the stack, which can also be denoted with the reversible voltage and current. This gives us the reversible voltage from the Gibbs energy change as shown in Equation (4.3).

$$V_{\text{rev}} = \frac{P_{\text{rev}}}{I} = \frac{|\Delta G|}{I} \tag{4.3}$$

4.3.2. Activation Overpotentials

Activation overpotential represents the energy required to overcome activation energy barriers for electrochemical reactions. The relationship between current density j [Am⁻²] and the activation overpotential $\eta_{\rm act}$

Parameter	Symbol	Value	Unit
Fuel Electrode Thickness (fitted)	$\delta_{ ext{FE}}$	32.0	μm
Air Electrode Thickness	$\delta_{ ext{AE}}$	17.5	μm
Electrolyte Thickness	$\delta_{ m el}$	12.5	μm
Porosity of Electrodes	ϵ	0.3	-
Tortuosity of Electrodes	τ	5.0	-
Mean Diameter of Electrode pores	$d_{ m p}$	2.0	μm
Cell Area	A_{cell}	0.01	m ²
Number of cells in the stack	N	3000	-

Table 4.2: Cell geometry for electrochemical calculations [2].

4.3. Electrochemical Model 29

Parameter	Symbol	Value	Unit
Pre-Exponential Factor - Fuel Electrode		1.34×10^{10}	Am^{-2}
Activation Energy - Fuel Electrode	$E_{ m act,FE}$	1.00×10^{5}	Jmol ^{−1}
Pre-Exponential Factor - Air Electrode	$\gamma_{ m AE}$	2.05×10^{9}	$\mathrm{Am^{-2}}$
Activation Energy - Air Electrode	$E_{ m act,AE}$	1.20×10^{5}	Jmol ⁻¹
Pre-Exponential Factor - Electrolyte Ionic Conductivity	$\sigma_{0, m elec}$	33330	$\Omega^{-1}\mathrm{m}^{-1}$
Activation Energy - Electrolyte Ionic Conductivity		85 634	Jmol ⁻¹
Specific Resistivity of Electronic Conductors	$r_{ m const}$	5.70×10^{-6}	Ωm^2
Diffusion Volume - Hydrogen	$V_{ m d,H_2}$	6.12	-
Diffusion Volume - Water	$V_{ m d,H_2O}$	13.1	-
Diffusion Volume - Oxygen	$V_{ m d,O_2}$	16.3	-
Diffusion Volume - Nitrogen	$V_{ m d,N_2}$	18.5	-
Molecular Mass - Hydrogen	$M_{ m d,H_2}$	2.01588	$gmol^{-1}$
Molecular Mass - Water	$M_{ m d,H_2O}$	18.01528	$gmol^{-1}$
Molecular Mass - Oxygen	$M_{ m d,O_2}$	32.00000	$gmol^{-1}$
Molecular Mass - Nitrogen	$M_{ m d,N_2}$	28.01340	gmol ⁻¹

Table 4.3: Material parameters for electrochemical calculations [2].

[V] is represented by the Butler-Volmer Equation (4.4), which applies individually to each electrode, denoted by the index i [16].

$$j = j_{0,i} \left[\exp\left(\frac{n_i F \alpha_i}{RT} \eta_{\text{act},i}\right) - \exp\left(\frac{n_i F (1 - \alpha_i)}{RT} \eta_{\text{act},i}\right) \right]$$
(4.4)

The Butler-Volmer equation cannot be solved explicitly for the activation overpotential. Therefore, we can use explicit simplifications. This model uses the hyperbolic sine approach, defined in Equation (4.5), which has been found to perform well across all operating regions [82].

$$\eta_{\text{act},i} = \frac{RT}{n_i F \alpha_i} \sinh^{-1} \left(\frac{j}{2j_{0,i}} \right)$$
(4.5)

 n_i [-] denotes the number of electrons transferred in a reaction, which equals 2 for the fuel electrode and 4 for the air electrode, since the reacting species are H_2 - H_2 O, and O_2 respectively. α [-] is a factor which represents the extent of symmetry in how electric potential affects the activation energy curve. It lies between 0.2 and 0.5 for most electrochemical reactions [16]. For simplicity, α is assumed to be 0.5, which represents a "symmetric" reaction. $j_{0,i}$ [Am⁻²] is the exchange current density, which represents the current density of the reaction and reverse reaction at equilibrium, which are equal to each other. Equation (4.6) defines the exchange current density with an Arrhenius-type relation taken from Buttler et al. [3], using empirically determined quantities such as activation energy $E_{act,i}$ [J mol⁻¹] and a pre-exponential factor γ_i [Am⁻²].

$$j_{0,i} = \gamma_i \exp\left(\frac{-E_{\text{act},i}}{RT}\right) \tag{4.6}$$

4.3.3. Ohmic Overpotential

Ohmic overpotential is generated in order to overcome the ohmic resistance of the various materials. As the name suggests, this overpotential follows Ohm's Law, and is directly proportional to the current density and resistance. The ionic resistance of the electrolyte is usually higher than the electronic resistance of the other components of the cell. The change in ionic resistance with temperature is also much larger than electronic resistance. Therefore, the change in electronic resistance is neglected. Accordingly, Hauck et al. [2] have used Equation (4.7) to calculate the Ohmic overpotential, where $\delta_{\rm elec}$ [m] is the thickness of the electrolyte layer,

 $\sigma_{\rm elec}$ [$\Omega^{-1}\,{\rm m}^{-1}$] is the ionic conductivity of the electrolyte, and $r_{\rm const}$ [$\Omega\,{\rm m}^2$] is the specific resistance of the electron conducting layers.

$$\eta_{\text{ohm}} = j \left(\frac{\delta_{\text{elec}}}{\sigma_{\text{elec}}} + r_{\text{const}} \right)$$
(4.7)

The conductivity of the electrolyte σ_{el} is also determined empirically and fitted into the Arrhenius-type Equation (4.8), similar to Equation (4.6).

$$\sigma_{\rm el} = \sigma_{0,\rm elec} \exp\left(\frac{-E_{\rm act,elec}}{RT}\right)$$
 (4.8)

4.3.4. Concentration Overpotentials

The concentration overpotentials are a result of diffusion limitations in the porous electrodes. At high current densities, the diffusion-driven mass transfer through the electrode pores cannot match the rate of consumption or production of the chemical species at the TPB. Thus, the reaction sites see a different concentration at each species than the bulk. This leads to a difference between the actual voltage and the reversible voltage, which is calculated from bulk concentrations. This difference is called the concentration overpotential. Equations to derive concentration overpotentials resemble the second term of the Nernst Equation since they serve to replace the bulk concentration in the Nernst equation with the actual concentration at the reaction sites. Equations (4.9a) and (4.9b) represent the concentration overpotentials at the fuel and air electrode respectively, for the FC mode. Equations (4.9c) and (4.9d) represent the same for the EC mode.

$$\eta_{\text{conc,FE,FC}} = \frac{RT}{2F} \ln \left(\frac{p_{\text{H}_2,\text{bulk}} \cdot p_{\text{H}_2\text{O,TPB}}}{p_{\text{H}_2,\text{TPB}} \cdot p_{\text{H}_2\text{O,bulk}}} \right)$$
(4.9a)
$$\eta_{\text{conc,AE,FC}} = \frac{RT}{2F} \ln \left(\frac{p_{\text{O}_2,\text{bulk}}^{0.5}}{p_{\text{O}_2,\text{TPB}}^{0.5}} \right)$$
(4.9b)

$$\eta_{\text{conc,FE,EC}} = \frac{RT}{2F} \ln \left(\frac{p_{\text{H}_2,\text{TPB}} \cdot p_{\text{H}_2\text{O,bulk}}}{p_{\text{H}_2,\text{bulk}} \cdot p_{\text{H}_2\text{O,TPB}}} \right)$$
(4.9c)
$$\eta_{\text{conc,AE,EC}} = \frac{RT}{2F} \ln \left(\frac{p_{\text{O}_2,\text{TPB}}^{0.5}}{p_{\text{O}_2,\text{bulk}}^{0.5}} \right)$$
(4.9d)

Among other things, the partial pressures of the species at the reaction sites depend on the effective diffusion coefficient of a species through the porous electrode. This coefficient depends on the geometry of the electrode and the gas composition. Diffusion in an SOC can be considered to consist of both Knudsen and molecular diffusion [83], and the effective diffusion coefficient $D_{\text{eff},i}$ [$\text{m}^2 \, \text{s}^{-1}$] of the species i is calculated with Equation (4.10). D_{i-j} [$\text{m}^2 \, \text{s}^{-1}$] represents the binary molecular diffusion of the two species i and j into each other. $D_{\text{Kn},i}$ [$\text{m}^2 \, \text{s}^{-1}$] represents Knudsen diffusion, which relates to a gas diffusing through long, thin pores. ϵ [-] and τ [-] are the porosity and tortuosity of the electrode respectively.

$$D_{\text{eff},i} = \frac{\epsilon}{\tau} \frac{D_{\text{Kn},i} D_{i-j}}{D_{\text{Kn},i} + D_{i-j}}$$

$$\tag{4.10}$$

The binary diffusion coefficient is expressed using the Fuller equation [84 cited in 2], shown in Equation (4.11). p [Pa] is the pressure, M_i [gmol⁻¹] and M_j [gmol⁻¹] are the molecular weights of the two diffusing species and $V_{\mathrm{d},i}$ [-] and $V_{\mathrm{d},j}$ [-] are their diffusion volumes. Equation (4.11) is valid only for gases with two components. Hauck et al. [2] assumed both gases to consist of only two species each. Nitrogen and oxygen are the only two dominant components of air. While the fuel gas can have more than two components, the situation is simplified by considering only hydrogen and water. Hauck et al. justified this assumption arguing that water and hydrogen are the only electrochemically active components. The same assumption can be made in the present case, since ammonia is assumed to be completely cracked, while nitrogen is electrochemically inert.

$$D_{i-j} = \frac{1.43 \times 10^{-7} \cdot T^{1.75}}{p\sqrt{\frac{2M_i M_j}{M_i + M_j} \left(V_{d,i}^{1/3} + V_{d,j}^{1/3}\right)^2}}$$
(4.11)

The Knudsen diffusion coefficient is expressed using Equation (4.12), where $d_{\rm p}$ [m] is the mean pore diameter of the electrode. [85]

$$D_{\mathrm{Kn},i} = \frac{d_{\mathrm{p}}}{3} \sqrt{\frac{8RT}{\pi M_i}} \tag{4.12}$$

Using the parameters calculated above, the partial pressures of the species at the reaction sites are calculated by solving Fick's First Law of Diffusion in 1-D across the thickness of an electrode [13]. Equations (4.13a), (4.13b) and (4.13c) give the solution for hydrogen, water and oxygen respectively. For these three equations, the current density j [Am⁻²] is positive for FC mode and negative for EC mode. The bulk partial pressures were considered to be the average of the partial pressures at the inlet and outlet.

$$p_{\text{H}_2,\text{TPB}} = p_{\text{H}_2,\text{bulk}} - \frac{RT\delta_{\text{FE}}j}{2FD_{\text{eff},\text{H}_2}}$$

$$(4.13a)$$

$$p_{\text{H}_2\text{O,TPB}} = p_{\text{H}_2\text{O,bulk}} + \frac{RT\delta_{\text{FE}}j}{2FD_{\text{eff,H}_2\text{O}}}$$

$$p_{\text{O}_2,\text{TPB}} = p_{\text{O}_2,\text{bulk}} - \frac{RT\delta_{\text{AE}}j}{4FD_{\text{eff,O}_2}}$$
(4.13b)

$$p_{\text{O}_2,\text{TPB}} = p_{\text{O}_2,\text{bulk}} - \frac{RT\delta_{\text{AE}}j}{4FD_{\text{eff,O}_2}}$$
(4.13c)

Hauck et al. [2] introduced a new modification to the model, which was validated with experimental data. It was noticed that the concentration overpotentials predicted by the original model were higher than observed values. This was theorised to be caused by the porous support layer in the fuel electrode supported cell. The model considers the entire fuel electrode to be of the same porosity as the active layer. In practice, the support layer has significantly higher porosity than the active layer, and causes smaller diffusion losses. Thus, Hauck et al. modified the thickness of the fuel electrode in the model to fit the concentration overpotentials to the experimental data. This fitted value is used in this work as well.

4.3.5. Cell Voltage and Stack Power

Once the reversible voltage and all the overpotentials are calculated, the actual cell voltage is calculated. The expression for actual cell voltage is given in Equation (4.14a) for FC mode, and Equation (4.14b) for EC mode.

$$U_{\text{cell,FC}} = U_{\text{rev,FC}} - \eta_{\text{act,FE}} - \eta_{\text{act,AE}} - \eta_{\text{ohm}} - \eta_{\text{conc,FE,FC}} - \eta_{\text{conc,AE,FC}}$$
(4.14a)

$$U_{\text{cell,EC}} = U_{\text{rev,EC}} + \eta_{\text{act,FE}} + \eta_{\text{act,AE}} + \eta_{\text{ohm}} + \eta_{\text{conc,FE,EC}} + \eta_{\text{conc,AE,EC}}$$
(4.14b)

The stack power P_{stack} [W] is a product of the cell voltage U_{cell} [V], current density j [A m⁻²], cell area A_{cell} $[m^2]$ and number of cells N [-], as shown by Equation (4.15).

$$P_{\text{stack}} = U_{\text{stack}} \cdot I = U_{\text{cell}} \cdot j \cdot N \cdot A_{\text{cell}}$$

$$(4.15)$$

The total stack area (i.e. product of cell area and number of cells in the stack) determines the total current, and hence the scale of the entire system model. For simplicity, the performance of all the components in the system is modelled to be independent of the scale. Therefore, while the current density affects polarisation losses, the stack area does not affect the performance of the model. Thus, it can be changed without any sideeffects if the desired capacity of the system changes. For the purpose of this work, typical values are assumed, shown in Table 4.2.

4.4. Ammonia Synthesis Subsystem Model

Based on the literature study described in Section 3.3, the ammonia synthesis model was built on the Haber-Bosch process, since direct electrochemical synthesis is not currently feasible [74-77]. The following sections explain the various design choices made in the synthesis model.

4.4.1. Catalyst

Ammonia synthesis catalysts can be based on iron, ruthenium, osmium, cobalt, molybdenum, etc. [8]. While cobalt-molybdenum catalysts have shown high activity, catalysts based on iron and ruthenium based catalysts are the two main types currently in use in industry. Ruthenium catalysts are more active than iron at low temperatures, which can lower the synthesis pressure. However, iron is still the most dominant industrial catalyst due to its significantly lower cost [22]. Iron catalysts are also significantly more mature, having remained the mainstay of ammonia synthesis for over a century [86]. For the purpose of this work, higher temperature required for iron can also mean higher-exergy heat available for integration with the SOEC. Therefore, iron-based catalysts have been assumed in this model.

It is interesting to note that it has been shown in literature that enabling exothermic reactions within the SOEC can have significant thermodynamic benefits [6, 26] for stack and system performance. However, ammonia synthesis cannot be used as one of these internal exothermic reactions, since the nickel catalysts used in SOCs do not display any significant activity towards ammonia synthesis [87].

Both iron and ruthenium catalysts are significantly poisoned by oxygen containing compounds, including water. Therefore, the water content in the synthesis gas must be kept below 5 ppm which allows a lifetime of up to 14 years [8]. Therefore, a purification system has to be added to the fuel side outlets of the SOC.

4.4.2. Reactor

Ammonia synthesis reactors can either be tube-cooled single-stage reactors, or adiabatic multi-stage reactors with intercooling. Tube-cooled reactors can have complicated temperature profiles [8], which is difficult to capture in a 0-D model. Therefore, a three-stage adiabatic reactor with intercooling was implemented. Indirect external cooling was used, which has been found to be more efficient than quench cooling [7, 71].

Iron based catalysts have an operating temperature range of $380\text{-}500\,^{\circ}\text{C}$ [21, 73], limited by catalyst activity at the lower end, and catalyst poisoning and degradation at the higher end. For obtaining a high reaction rate with adequate safety margin, the temperature range used by Cheema and Krewer [73] is used. The inlet temperature of each bed is maintained at $400\,^{\circ}\text{C}$ while the maximum outlet temperature of each bed is capped at $500\,^{\circ}\text{C}$.

The reactors were modelled as equilibrium reactors (RGIBBS² block in Aspen Plus). The use of rigorous plug flow models (RPLUG³ block in Aspen Plus) was taken under consideration. Because this work is not concerned with techno-economics and equipment sizing, a rigorous model was set aside for future study, and a simple equilibrium reactor model was preferred instead. However, the reaction was not allowed to go to full equilibrium. Ammonia synthesis catalysts can typically approach at most 80 % of equilibrium [21]. "Approach to equilibrium" β [-] is defined as the ratio of the reaction quotient to the equilibrium constant, given by Equation (4.16). The RGIBBS model offers the option to limit the equilibrium using a temperature approach⁴. The value of temperature approach was chosen by testing an RGIBBS ammonia synthesis reactor at different pressures and inlet compositions. The temperature approach values at which the reaction approached 80 % of equilibrium was found to range from 22 °C to 35 °C. The median value of 30 °C was chosen for this model.

$$\beta = \frac{y_{\text{NH}_3}^2}{y_{\text{H}_2}^3 y_{\text{N}_2}} \cdot \left(\frac{y_{\text{eq,NH}_3}^2}{y_{\text{eq,H}_2}^3 y_{\text{eq,N}_2}}\right)^{-1} \tag{4.16}$$

Therefore the outlet of each reactor bed can either be at 30 °C approach to equilibrium, or at a temperature of 500 °C. Both these conditions are simulated for each successive reactor bed, and the condition with the lower yield (indicated by lower temperature) is chosen for input to the next bed. According to Appl [8], the pressure drop in the synthesis loop is between 5 bar and 20 bar. Thus, each of the three reactor beds has been assigned a pressure drop of 5 bar, giving the loop an overall pressure drop of \sim 15 bar.

4.4.3. Recycle Loop

There are many possible configurations of the recycling loop for ammonia synthesis. Examples of such designs from literature are shown in Appendix A. However, most complex configurations are relevant for impure feed gas from traditional fossil-fuel sources. For purified reactants produced from electrolysis, as is used in this design, a single-stage refrigerated condenser before mixing the fresh feed is sufficient and energetically favourable [8]. Therefore, a simple configuration has been used in this work. The flowsheet of the synthesis loop used in this model is shown in Figure 4.5.

The feed gas is provided in the stoichiometric $H_2:N_2$ ratio of 3:1, therefore there is no reactant accumulation. There are also no impurities implemented in the model. In any case, the only impurity possible in the

²RGIBBS is an inbuilt chemical reactor model in Aspen Plus. It is an equilibrium reactor which calculates equilibrium by minimising Gibbs energy of the mixture. It can carry out a reaction fully up to equilibrium, or up to a specified deviation from equilibrium.

³RPLUG is an inbuilt chemical reactor model in Aspen Plus. It carries out a rigorous simulation of a 1-D plug flow reactor using reaction kinetics and reactor geometry.

⁴In an equilibrium reactor model, temperature approach to equilibrium is the difference between the temperature at which equilibrium constant is calculated, and the actual reactor temperature.

system would be trace amounts of water, which will either attach to the catalyst, or react with the produced liquid ammonia. For all these reasons, no purge stream has been modelled in the system. The unreacted gas from the condenser is then recycled to be mixed with the fresh feed from the gas purification system, after being compressed to compensate for the pressure drops in the various components.

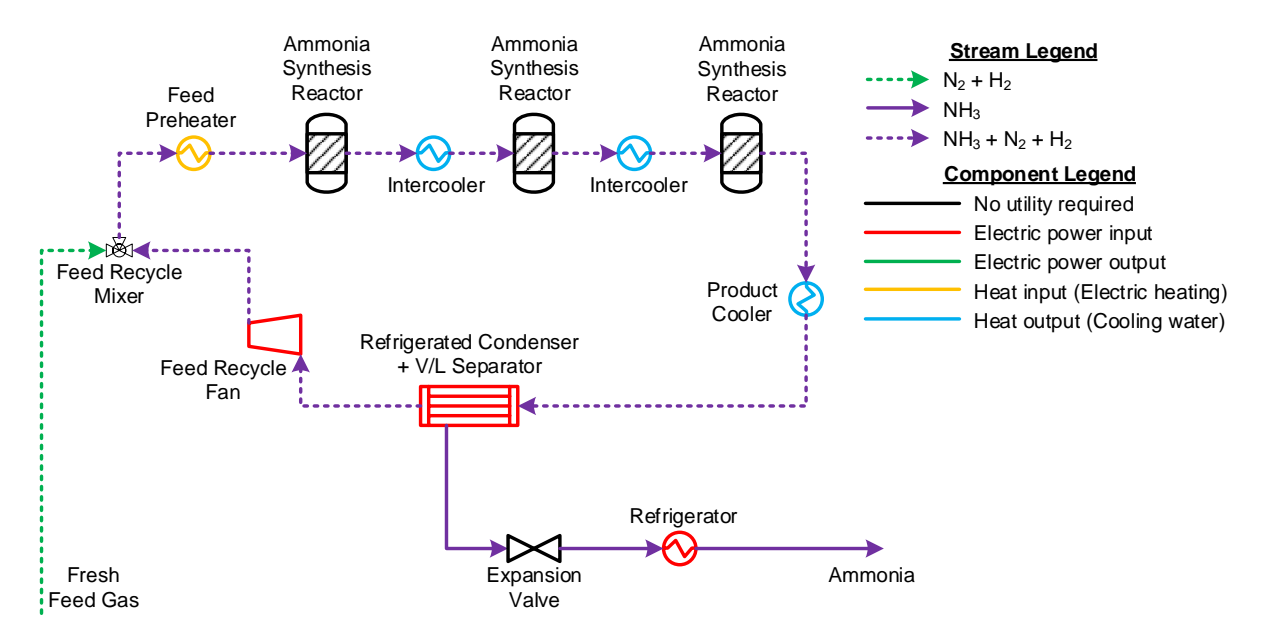


Figure 4.5: Process flowsheet for ammonia synthesis model.

4.4.4. Operating Parameters for Synthesis Subsystem Model

The reactor temperatures are fixed due to catalyst limitations as described in Section 4.4.2. This leaves two operating parameters to be chosen: the reaction pressure and the condensation temperature. Raising the reaction pressure and lowering the condensation temperature both cost additional work for feed gas compression and condenser refrigeration, but they increase conversion rates, reduce recycle flows and thus reduce the heating, cooling and re-compression costs that accompany large recycle flows. There is no easy way to choose these parameters from literature, since they are highly dependent on the particular system configuration under consideration [8]. Therefore, these parameters were chosen such that the exergy efficiency of the loop was maximised.

The reaction/loop pressure (measured at the outlet of the third reactor bed) was varied from 100 bar to 400 bar, while the condensation temperature was varied from $-33\,^{\circ}\text{C}$ (the boiling point of ammonia at atmospheric pressure) to $30\,^{\circ}\text{C}$ (the maximum cooling possible using ambient water at $30\,^{\circ}\text{C}$). Moreover, the compression of the feed gas from ReSOC stack pressure was also included in the optimisation, for a range of stack pressures from 1.5 bar to 10 bar.

For the purposes of the exergy analysis, there were two possible ways to deal with heating and cooling duty. One way was to assume that heating and cooling duties are provided by external utility (electricity and cooling water respectively), while another option was to assume that all the heating and cooling streams can be integrated somewhere in the overall ReSOC system. While the stack pressure had negligible effect on the optimisation, the assumption regarding heat integration was a vital variable for the optimisation. Without the assumption of heat integration, both the optimum reaction pressure and condenser temperature were the maximum possible values; (400 bar and 30 $^{\circ}$ C). This was because the exergy losses in the feed preheater and product cooler are extremely high without heat integration, and minimising recycle flow rates by raising the pressure reduces these losses. Meanwhile, the optimum temperature of 30 $^{\circ}$ C completely eliminated refrigeration work. But when these heat streams are assumed to be integrated, the heating/cooling losses are less significant, therefore slightly higher recycle flows can be tolerated, so the pressure can be reduced to reduce energy costs for compression. Therefore, in the scenario with integration, the exergy efficiency peaks at more moderate values: reactor outlet pressure of 170 bar and a condensation temperature of 25 $^{\circ}$ C (which implies further refrigeration of 5 $^{\circ}$ C after the use of cooling water down to 30 $^{\circ}$ C).

Finally, the values from the heat integration assumption were chosen (170 bar; 25 °C). The assumption was

considered to be justified, since the product cooler is easily able to provide more heat than is required by the feed preheater. The observations made in Section 6.4 were found to satisfy this assumption. As described in that section, the remaining heat from the product cooler and intercoolers would be eventually integrated into the feed water evaporation for the SOEC.

Table 4.4 summarises the optimised/prescribed parameters that were described in this section.

Parameter	Value	Unit
H ₂ :N ₂ ratio of fresh feed	stoichiometric, 3	-
Reactor inlet temperature	400	°C
Maximum allowed reactor outlet temperature	500	°C
Temperature approach to equilibrium	30	°C
Reactor inlet pressure	185.03	bar
Reactor outlet pressure	170	bar
Pressure drop per reactor bed	5	bar
Ammonia condensation temperature	25	°C

Table 4.4: Operating parameters for ammonia synthesis loop.

4.5. Water Separation / Gas Purification Subsystem

As mentioned in Section 4.4.1, iron catalysts used for ammonia synthesis are extremely sensitive to poisoning by oxygen containing compounds. Therefore these compounds must be restricted to under 20 ppm for feasible operation, or under 5 ppm for a long lifetime of 14 years [8]. In systems which use electrolysis as the hydrogen source, the only possible catalyst poison is water. The assumption is that the stack is structurally sound, and the pressure throughout the system can be kept slightly over atmospheric, so presence of oxygen from the atmosphere or the air side of the stack is neglected. Water content cannot be reduced to such low levels merely by condensation and vapour/liquid separation. Therefore, further purification is required. The flowsheets for the purification systems in each mode are shown in Figure 4.6, and the operating parameters for this subsystem are listed in Table 4.5.

Parameter		Unit
Water condensation temperature	30	°C
Pressure ratio across membrane (permeate)	10	-
Pressure drop along the membrane (retentate)	15	mbar
Pressure drop in adsorption bed	10	%

Table 4.5: Operating parameters for gas purification subsystem.

The first step in both modes is condensation and vapour/liquid separation, in order to remove the bulk of the water vapour from the gases. The remaining water vapour is then separated in a purification system.

In EC mode, the fuel side exhaust contains only hydrogen and water. Therefore, a simple membrane purification system is implemented after condensation and flashing. A compressor is used to pressurise the stream to create sufficient pressure difference across the membrane. The outlet pressure of the membrane module is chosen to be slightly above atmospheric pressure to avoid possible oxygen contamination, since this is the lowest pressure point in the entire system. A typical pressure ratio of 10 is maintained across the membranes [88], while the retentate is assumed to suffer a pressure drop of 15 mbar.

However, in FC mode, the fuel side exhaust contains nitrogen from the ammonia, apart from unused hydrogen and water. Since water molecules are between nitrogen and hydrogen in size, finding suitable membranes would be challenging due to hydrogen permeating. Therefore, a temperature swing adsorption system has been preferred, where the water vapour is selectively adsorbed and then desorbed with heat. In Aspen Plus, this has been modelled with a combination of an ideal separator block to simulate the adsorption, a heater block to simulate desorption, and a cooler block to condense the desorbed water vapour. The ideal

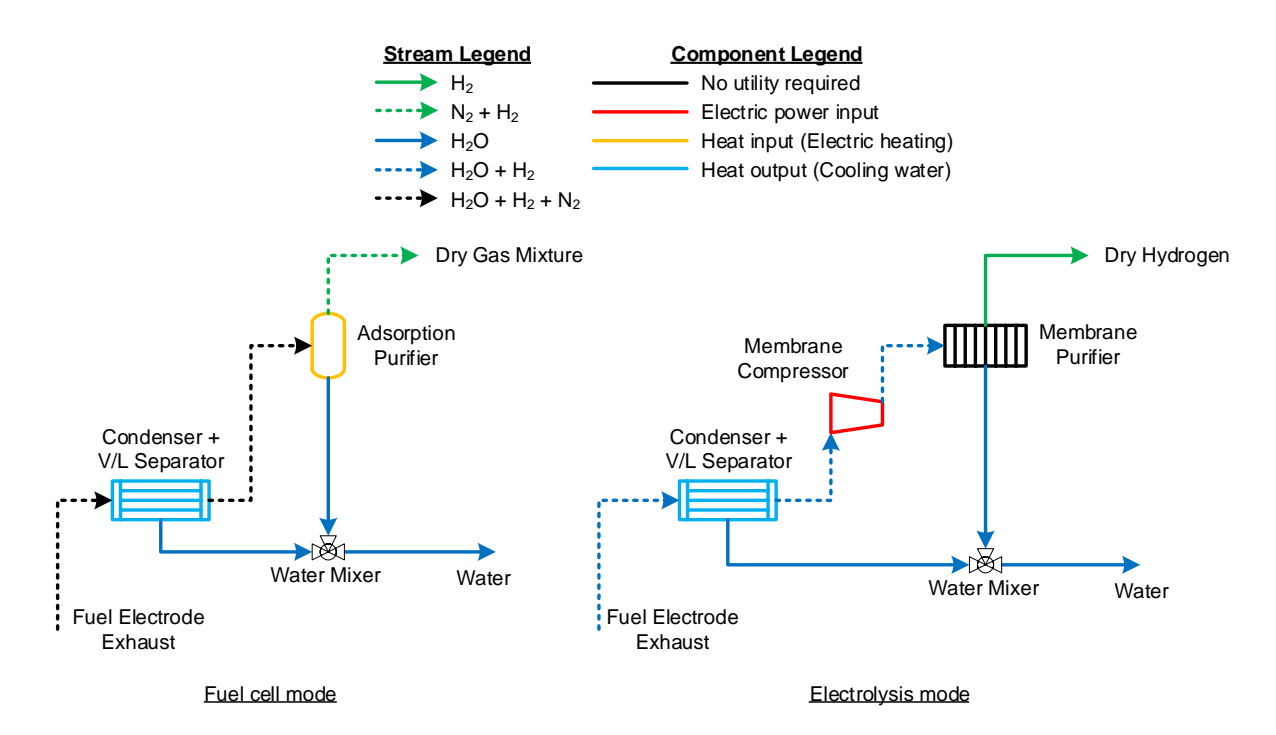


Figure 4.6: Process flowsheets for water separation / gas purification in each mode.

separator block splits the stream into pure gases and pure liquid water. The heater block evaporates this water, simulating desorption. The desorbed water vapour is then condensed before mixing with the bulk water stream. This is a highly simplified model, and might underestimate the desorption energy requirements. However, this underestimation is tolerable because the amount of water vapour remaining after the bulk condenser is very small, and thus the energy requirements are expected to be negligibly small compared to other components in the system. The pressure drop in an adsorbent bed was assumed to be 10 % [89].

4.6. Other Balance of Plant Components

The simple BoP components which are not part of a separate subsystem are described in this section. The operating parameters used for these BoP components are summarised in Table 4.6.

4.6.1. Storage Tanks

Ammonia is an easily liquefiable gas and hence, ammonia is stored as a liquid for higher energy density, and ease of further pressurisation (if required). The two most preferred liquefied storage conditions are either pressurised ambient temperature storage, or refrigerated ambient pressure storage [15]. In the basic configuration, the latter option is chosen and ammonia is stored at $-33\,^{\circ}$ C and 1 atm. The tank is assumed to be perfectly insulated. The purified nitrogen-hydrogen mixture produced from the fuel cell is stored at 190 bar. This is because this gas is reused in the ammonia synthesis loop, which has an inlet pressure of \sim 185 bar. Being a liquid, water is stored as at ambient conditions, and air is taken and exhausted from the atmosphere.

4.6.2. Turbomachinery

There are multiple locations in the system where turbomachinery⁵ is needed to make pressure changes, as seen from Figures 4.1 and 4.2. These are described in the following paragraphs, in descending order of pressure ratios. All the turbomachinery is assumed to be perfectly insulated from the environment.

Hydrogen has to be compressed from atmospheric pressure to ammonia synthesis pressure in EC mode, while nitrogen has to be compressed from ReSOC stack pressure to storage tank pressure. These constitute the sections with the highest pressure ratio (varying from 19 to 190, depending on stack pressure). However, these have relatively low flow rates compared to sweep air. Because of high pressure ratio and relatively low flow compression of hydrogen, these are modelled as multi-stage reciprocating compressors with intercooling [90].

⁵The term "turbomachinery" will be used in this report when referring to compressors and turbines simultaneously.

Parameter	Value	Unit
Ammonia storage temperature	-33	°C
Ammonia storage pressure	1	atm
Gas storage temperature	25	°C
Gas storage pressure	190	bar
Water storage temperature	25	°C
Water storage pressure	1	atm
Reciprocating hydrogen compressor efficiency	70	%
Axial turbomachinery efficiency	85	%
Pressure drop in heaters/coolers/heat exchangers	15	mbar
Minimum temperature difference in heat exchangers	5	°C

Table 4.6: Miscellaneous BoP operating parameters.

The number of stages was chosen through limits on output temperatures in hydrogen compressors, which is \sim 250 °C [91]. The efficiency of hydrogen compressors can vary from 50 % to 80 % based on suction pressure. A typical polytropic efficiency of 70 % was considered for this model. Before each compression stage, the stream was fully cooled down with cooling water to 30 °C to reduce the compression work.

Secondly, ammonia, water and air have to each be pressurised from atmospheric pressure up to stack pressure (1.5-10 bar). The compressor for the membrane purifier also has a similar range of pressure ratios. Water and ammonia, being stored as liquids, are pressurised using pumps. Meanwhile, sweep air is expected to have high flow rate because of its role in thermal management, but the pressure ratio is relatively low (1.5-10). Therefore, a single stage axial compressor was used. Similarly, a single stage axial turbine was used for expanding the exhaust air to atmospheric pressure. All these pieces of turbomachinery were assigned a nominal isentropic efficiency of 85 % [92 cited in 93].

Lastly, there are a few sections which require very slight compression or expansion. These include all recycle and recirculation loops viz. sweep air recirculation, hydrogen recirculation for the SOEC inlet and the reactant gas recycle for ammonia synthesis. The reactant gas also has to be expanded from the tank pressure to the synthesis loop pressure. All of these processes have a pressure ratio of very close to 1, with the highest being \sim 1.09 for the ammonia recycle compression. Such processes would typically be carried out with fans for compression and valves for expansion. But for simplicity, these have also been modelled as axial compressors/turbines with 85 % isentropic efficiency.

4.6.3. Heaters, Coolers and Refrigerators

Heaters, coolers and refrigerators make up a large part of the BoP. In the basic configuration of the Aspen model, they were modelled with simple heater blocks. In the improved configurations analysed later in this report, these heating and cooling processes (except refrigeration) have been integrated with each other using heat exchanger blocks where possible. Where heat integration is not sufficient, the remaining heat is assumed to be provided by electricity, and cooling is provided up to ambient temperatures by cooling water or air. One exception is the evaporation of ammonia, for which the heating function can also be fulfilled by ambient water/air. All heater blocks have been assumed to have a pressure drop of 15 mbar [81].

In case of refrigerators, the coefficient of performance (CoP) for the required temperature was estimated using an Aspen Plus model of a simple ideal vapour compression refrigeration cycle [94] with R717 (ammonia) refrigerant.

4.6.4. Heat Exchangers

In the basic configuration, no heat exchangers are used. However, in later improved configurations, heat integration is carried out. Some major heaters and coolers are integrated using heat exchangers. This heat integration has been carried out separately from the main process models. The following assumptions are used for heat exchangers:

• Minimum temperature difference between the two flows is 5 °C.

- Pressure drop that was assumed in the basic configuration is maintained. That means all the heat exchangers that replace a particular heater/cooler, are assigned a cumulative pressure drop of 15 mbar.
- All heat exchangers are in a simple counter-flow configuration.
- The equipment is perfectly insulated from the environment.

4.7. Performance Analysis

There is a wide variety of ways to analyse the performance of power systems. The choice of performance metric depends on the context and application of the system. This section will define the various metrics used in this thesis, and will explain the motivation for their choice. The calculation methods and reference data used will also be described.

Some fundamental assumptions have been made to simplify the analysis of the system. These assumptions are as follows:

- The ReSOC energy storage system as a whole is fully isolated. To elaborate, the only connection with the
 outside world is through electricity supply and demand (and air or cooling water when required). The
 fuel storage is completely isolated from the environment and the amount of fuels produced in EC mode
 are completely consumed in FC mode.
- The system operates in steady state. That is, the current density is constant throughout operation in any one mode, and no start-up or shut-down effects are considered.
- The system is assumed to be perfectly insulated, and no heat is exchanged with the environment, except when specifically intended through cooling water, or in ambient temperature storage tanks.
- The operating time for each mode is considered equal.
- Unless explicitly mentioned otherwise, the stack operating parameters are the identical for both modes.
- The system performance is independent of the scale of the system.

4.7.1. Definitions of Efficiency

The most fundamental metric for the thermodynamic analysis of any energy storage system is the round trip efficiency. It is a measure of how much of the energy stored in the system can be retrieved. Based on the assumptions stated earlier in this section, the round trip efficiency $\eta_{\rm RT}$ [%] can be defined as the ratio of net electric power production in FC mode $P_{\rm net,FC,out}$ [W] to the net electric power consumption in EC mode $P_{\rm net,EC,in}$ [W], shown in Equation (4.17).

$$\eta_{\rm RT} = \frac{P_{\rm net,FC,out}}{P_{\rm net,EC,in}} \tag{4.17}$$

It can also be beneficial to note the round trip efficiency of the stack itself, separate from the balance of plant. This enables us to see the points at which the stack itself is most efficient, and design the system to work around those conditions. In the electrolysis mode, the stack has to be provided not only with electricity, but also with heat in some cases. Therefore, the round trip efficiency of the stack is defined as the ratio of the electric output of the stack in fuel cell mode, and the total energy input to the stack in electrolysis mode. It must be noted that the heat input of electrolysis $\dot{Q}_{\text{stack,EC,in}}$ [W] should be considered as zero (not negative) in exothermic mode. This can also be written more simply in terms of cell voltage U_{cell} [V] and thermoneutral voltage U_{tn} [V], as shown by Equation (4.18).

$$\eta_{\text{RT,stack}} = \frac{P_{\text{stack,FC,out}}}{P_{\text{stack,EC,in}} + \dot{Q}_{\text{stack,EC,in}}} = \frac{U_{\text{cell,FC}}}{\max(U_{\text{cell,EC}}, U_{\text{tn,EC}})}$$
(4.18)

The system energy efficiency (or first law efficiency) of each mode is defined using the lower heating values of the fuel flows to/from storage \dot{H}_{LHV} [W]. As explained in Section 4.1, apart from ammonia, hydrogen is also stored in the system. Therefore, the expression for efficiency has to take both fuels into consideration. The two fuels are stored and consumed in different modes. Thus, the system LHV efficiency η_{LHV} [%] is defined as shown in Equations (4.19a) and (4.19b) for FC and EC mode respectively.

$$\eta_{\text{LHV,FC}} = \frac{P_{\text{net,FC,out}}}{\dot{H}_{\text{LHV,NH}_3} - \dot{H}_{\text{LHV,H}_2}} \tag{4.19a} \qquad \eta_{\text{LHV,EC}} = \frac{\dot{H}_{\text{LHV,NH}_3} - \dot{H}_{\text{LHV,H}_2}}{P_{\text{net,EC,in}}} \tag{4.19b}$$

The LHV of any stream is simply a product of the flow rate and the LHV value of the fuel. The LHV values of the fuels used are shown in Table 4.7.

Table 4.7: Lower heating val	ues of the fuels	relevant to this system.

Chemical S ₁	pecies	Molecular Mass	Lower Heating Value		
Ammonia	[15]	$17.031\mathrm{g}\mathrm{mol}^{-1}$	$18.577\mathrm{kJ}\mathrm{g}^{-1}$	316.389 kJ mol ⁻¹	
Hydrogen	[95]	$2.016\mathrm{gmol^{-1}}$	$119.930\mathrm{kJ}\mathrm{g}^{-1}$	$241.767 \text{kJ} \text{mol}^{-1}$	

The system exergy efficiency (or second law efficiency) is defined on similar terms as the LHV efficiency. This is shown in Equation (4.20a) and (4.20b) for FC and EC mode respectively, with Ex_i [W] denoting the total exergy flow in the stream i. This is a slightly modified version of functional exergy efficiency, where the exergy of air flows has been ignored. There are two reasons to choose this modified definition of functional exergy efficiency.

- In the basic configuration, the air is taken from and released into the atmosphere. Incoming air has nearly zero exergy. Air exhaust after expansion/cooling is not stored in any mode, and therefore can simply be considered as an exergy loss to the environment. Meanwhile, all the other chemicals are stored and reused, and therefore need to be included in the efficiency definition.
- More importantly, defining the exergy efficiency this way allows us to simply multiply the exergy efficiency of two modes to get the round trip efficiency of the energy storage system.

$$\eta_{\text{ex,FC}} = \frac{P_{\text{net,FC,out}}}{\dot{E}\dot{x}_{\text{NH}_3,\text{in}} - \dot{E}\dot{x}_{\text{N}_2/\text{H}_2,\text{out}} - \dot{E}\dot{x}_{\text{H}_2\text{O,out}}}$$
(4.20a)

$$\eta_{\text{ex,EC}} = \frac{\dot{E}x_{\text{NH}_3,\text{out}} - \dot{E}x_{\text{N}_2/\text{H}_2,\text{in}} - \dot{E}x_{\text{H}_2\text{O},\text{in}}}{P_{\text{net,EC},\text{in}}}$$
(4.20b)

Preliminary Analysis

This chapter begins with preliminary studies at the level of the ReSOC stack. The variation of stack voltage with operating parameters is briefly described. An exergy analysis is carried out at the stack level, and the effect of internal ammonia cracking is studied. Following that, the basic configuration of the ReSOC system described in Section 4.1 is analysed. The maximum possible efficiency that can be attained by a very simple system is explored, and the optimum operating region is established. Finally, through exergy analysis, the components needing improvement are identified.

5.1. Stack Performance Analysis

The thermodynamic performance of the stack is studied in this section. The purpose of this section is to study how the stack voltage and performance varies with the stack operating parameters. This will set a foundation for further analysis at the system level, since the stack the core component of the system. This study also analyses the effect of internal ammonia cracking on the cooling duty required for the stack. As noted in Section 4.1.3, the stack operating parameters were varied within the following range:

Stack Temperature 650 °C-800 °C

Stack Pressure 1.5 bar-10 bar

Current Density 2500 Am⁻²-10000 Am⁻²

Fuel/Steam Utilisation 80 % (constant)

The air flow entering the stack was dictated by heat production / consumption of the stack, since the temperature difference across the stack was held constant at $100\,^{\circ}$ C. The fuel/steam input flow rates were varied proportional to current density in order to maintain the fuel/steam utilisation at the desired level. However, note that the results in this report are normalised by the ammonia flow rate consumed or produced. Therefore, while the simulations were carried out with constant stack area, the normalised results give the same effect as if the stack area is varied with respect to the current density while holding fuel/steam flow constant. With these input parameters, the simulations were carried out to analyse the voltage and performance of the stack.

The base case operating point was 800 °C, 1.5 bar and 5000 Am⁻². The results of the base case operating point are summarised in Table 5.1. The average Nernst voltage in FC mode is higher than in EC mode. This is because the average concentration of hydrogen in the fuel cell mode is higher than the average concentration of steam, which increases the Nernst voltage. The reverse is true for the electrolysis mode. The Ohmic overpotential has the largest contribution to the losses, followed by the activation losses at the air electrode. The activation losses at the air electrode are higher, since the reaction with oxygen requires involves four electrons per molecule of oxygen, compared to two electrons for hydrogen/steam on the fuel side. The activation and ohmic overpotentials are the identical for both modes, since they depend only on temperature and current density. The small differences in concentration overpotentials arise from different fuel side compositions in each mode, as well as different fresh air flow rates in each mode (due to different stack heat duty).

A comparison of the stack heat duty leads to an important takeaway from the base case stack analysis. The benefit of internal cracking of ammonia is shown by the significantly lower heat duty of the stack in the FC mode. The FC mode heat duty is smaller than the EC mode heat duty by a factor of two, whereas comparing the cell voltages in each mode with the thermoneutral voltage, the heat duty of FC mode would be expected to be larger. This change is entirely the result of heat consumption by the internal ammonia cracking reaction. A lower heat duty means that the air flow required is also reduced, along with its associated compression and heating losses. However, it must be noted that these benefits are seen at the system level and not at stack level. The stack round trip efficiency as expressed by Equation (4.18) is unaffected by the net heat output of the stack in fuel cell mode.

Parameter	Unit	FC Mode	EC Mode
Nernst voltage	V	975.8	941.8
Thermoneutral voltage	V	N/A	1315.9
Cell voltage	mV	882.2	1035.4
Total overpotential	mV	93.6	93.6
Activation, fuel-side	mV	1.3	1.3
Activation, air-side	mV	35.5	35.5
Ohmic	mV	56.1	56.1
Concentration, fuel-side	mV	0.5	0.5
Concentration, air-side	mV	0.3	0.2
Stack power output	kJ/mol _{NH3}	204.29	-239.76
Stack heat output	kJ/mol _{NH3}	32.61	-64.94
Exergy destruction in stack	kJ/mol _{NH3}	27.15	8.32
Stack round trip efficiency	%	67.04	

Table 5.1: Stack performance results - Base case (T = 800 °C, p = 1.5 bar, j = 5000 Am⁻², $U_f = 0.8$).

5.1.1. Stack Level Parametric Analysis

The effects of operating parameters on the stack performance are analysed by the observed variation in cell voltage. Each parameter was individually varied within the range mentioned above, while keeping the other parameters constant. The results of this sensitivity analysis were very similar to the results with hydrogen.

The variations of stack performance using hydrogen/steam are well known, therefore they are not described in this section. These results are described in detail in Appendix B. To summarise them briefly, increasing the temperature increased the cell voltage in FC mode, and decreased it in EC mode. Increasing the pressure increased the cell voltage in both modes. Increasing the current density decreased the cell voltage in FC mode, and increased it in EC mode.

The presence of nitrogen from the cracked ammonia on the fuel side of the stack in fuel cell mode did not affect the voltages significantly. This can explained by looking at the form of the Nernst equation (Equation (2.8)). The Nernst voltage depends on the ratio of the concentrations of hydrogen and steam, and while each component is diluted by the presence of nitrogen, the ratio of their concentrations remains the same. This same thing also happens in the overpotentials. Therefore, the cell voltages are not affected by the use of ammonia instead of hydrogen.

5.1.2. Thermoneutral Electrolysis Regions

The loci of thermoneutral points for different current densities are shown in Figure 5.1. The regions above these curves are regions of endothermic operation, while the regions under these curves are regions of exothermic operation. The figure also confirms that the ReSOC system in electrolysis mode can operate endothermically throughout most of the considered range of operating parameters. The location of the thermoneutral point can be a very important consideration for choosing the operating point in electrolysis mode, as will be seen in Section 5.2.

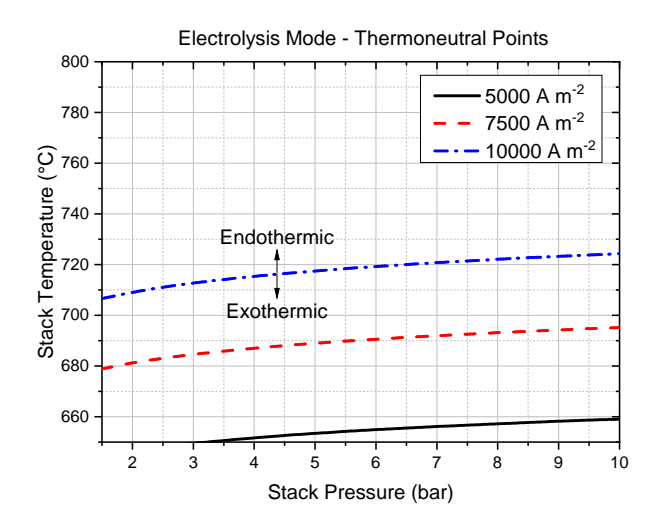


Figure 5.1: Locus of thermoneutral points in electrolysis mode.

5.1.3. Conclusion of Stack Performance Analysis

The key takeaways of the stack-level studies are summarised below:

- The voltage variation of the stack with ammonia is similar to the behaviour observed with hydrogen.
- Higher stack temperature is always beneficial for stack performance within our desired operating range, in both modes.
- Higher stack pressure is favourable for stack performance in fuel cell mode. However, within our desired operating range, lower stack pressure is favourable in electrolysis mode.
- Higher current density is always detrimental to stack performance, and the stack operates in the so-called "Ohmic" region throughout the chosen range of operating parameters.
- As expected, internal ammonia cracking reduces the heat duty of the stack by more than half.

5.2. System Analysis - Basic Configuration

The basic configurations for each mode have been described previously in Section 4. In this section, through simulations and thermodynamic analysis, the optimum operating point for this base case configuration is determined. This can help us to estimate whether it is feasible to operate the system in such a basic configuration, or whether improvements are needed. Exergy analysis is further used to point out the processes needing improvement.

Methodology

The basic configuration simulation was first run with the base case stack parameters ($800\,^{\circ}$ C, $1.5\,$ bar and $5000\,\text{Am}^{-2}$). These results allowed us to find out the components which have the largest effects on system performance. A sensitivity analysis was then carried out, using a discrete variation of stack operating parameters within the same range as mentioned in the previous section. This showed us whether it could be thermodynamically feasible to operate a simple, inexpensive system and to predict the most efficient operating points for such a system. The optimum operating point was chosen from the data of this sensitivity analysis, based on maximum round trip efficiency. It must be noted that the number of discrete points used for sensitivity analysis is limited by computation time. Therefore, the optimised operating parameters are only approximate. Additionally, the convergence of the simulation in Aspen Plus was given a (relatively) large tolerance. Therefore, the efficiency values could have an error of the order of 0.1 %-points. However, this was ignored since it could not affect any major trends of efficiency.

Result Summary

The following sections undertake a closer analysis of the effect of each of the three varied parameters on the system performance. But first, the results of the base case and optimised operating points are summarised.

From Table 5.2, it is immediately seen that operation with the base case parameters is not thermodynamically feasible in the basic configuration, because the system was not able to produce net power output in the fuel cell mode, which is represented as negative efficiency. The processes/components which cause the major share exergy losses in the system are shown in Figure 5.2. Because of the lack of heat integration, thermal loads contributed the majority of the exergy losses. Exergy destruction from heating, and exergy loss to the environment (from condenser cooling and from hot air exhaust) made up almost all the exergy losses. These losses are highly dependent on the level of excess airflow. Since the excess airflow is used only for thermal management, it was predicted that reducing the heat demand/production by the stack could reduce the airflow and improve the efficiency.

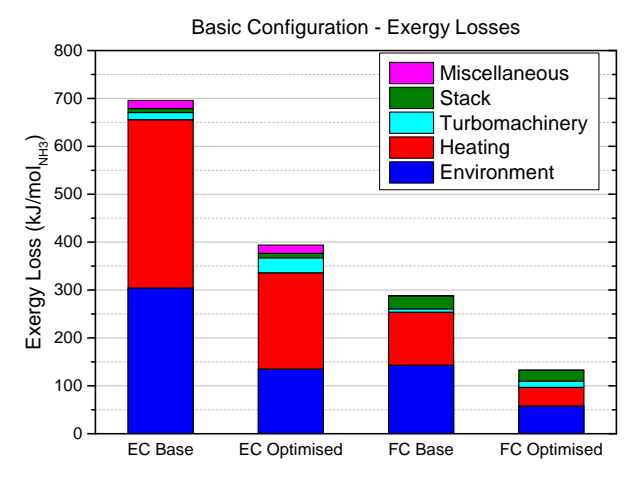


Figure 5.2: Distribution of system exergy losses with the basic configuration - Base case and optimised case.

The optimised case exergy losses are also shown in Table 5.2. These results supported this prediction in the previous paragraph. The fresh air flow in the optimised case was $\sim 30\%$ smaller than the base case, while the heating and environment losses decreased even faster (40-60%). These additional savings were found to come from pressurisation. The temperature rise caused by air compression reduced the additional heat demand, further reducing exergy losses in heating. The exergy extracted by the air turbine significantly reduced the exergy losses to the environment. Meanwhile, the exergy destruction in the turbomachinery increased by a much smaller amount, since turbomachinery is far more exergetically efficient than electric heating.

Base Case Optimised for RTE Parameter Unit FC Mode **EC Mode** FC Mode **EC Mode** °C 800 700 Stack temperature bar Stack pressure 1.5 8.5 $A\,m^{-2}$ 5000 2500 Current density -26.00 129.84 Net power output kJ/mol_{NH3} -958.31 -656.08 204.29 -239.77 215.76 -258.98 Stack power output kJ/mol_{NH3} -6.30 0.94 -10.00 Turbomachinery power input kJ/mol_{NH2} 11.75 kJ/mol_{NH3} Heating power input 224.00 704.53 84.98 404.85 Refrigeration power input kJ/mol_{NH}₂ 2.24 2.24 Fresh air flow mol/mol_{NH3} 9.80 19.22 6.47 13.52 393.70 Total exergy losses kJ/mol_{NH₂} 288.38 695.86 132.53 Destruction in stack kJ/mol_{NH3} 27.15 8.32 22.56 9.37 kJ/mol_{NH3} Destruction in synthesis reaction 4.64 4.66 kJ/mol_{NH3} Destruction in expansion 5.89 15.38 1.35 4.32 Destruction in compression kJ/mol_{NH2} 5.92 10.96 7.17 16.21 200.71 Destruction in heating kJ/mol_{NH3} 110.47 351.17 38.64 Destruction in refrigeration kJ/mol_{NH3} 1.08 1.08 4.42 Destruction in mixing kJ/mol_{NH3} 0.16 4.56 0.04 Destruction in separation kJ/mol_{NH3} 0.16 6.50 0.19 6.78 Loss to environment kJ/mol_{NH2} 143.17 304.33 58.04 135.08 System energy efficiency % -10.66 25.45 53.24 37.17 % System exergy efficiency -9.91 27.38 49.49 39.99 % -2.71System round trip efficiency 19.79

Table 5.2: System simulation results - Basic configuration.

Now, the effect of variation of each parameter is analysed in detail in the following sections.

5.2.1. Temperature Variation

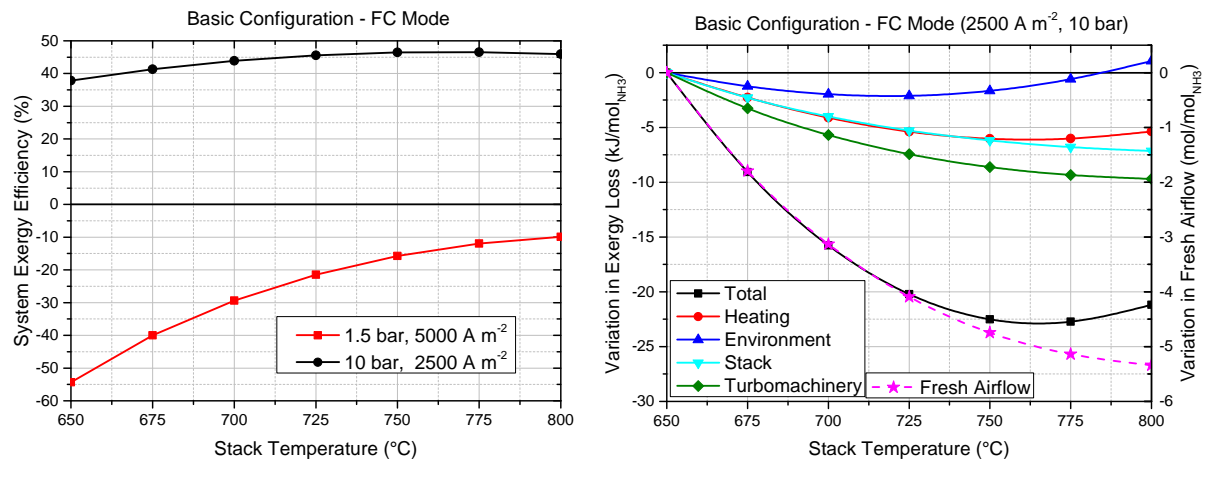
Fuel Cell Mode

The stack temperature affected the system performance in many ways. On the fuel side, as the temperature rises, more heat was needed to preheat the fuel, which raised the exergy destruction from electric heating. The produced steam was cooled and condensed from a higher temperature, leading to higher thermal exergy losses to the environment. Similarly, on the air side, the exergy losses for preheating and release of hot exhaust (per mole of air flow) were higher at higher temperatures.

However, there were also beneficial effects of higher temperature. As explained in Section 5.1.1, the stack power output increased with temperature, meaning lower heat generation and lower exergy destruction. The lower heat generation also led to a decrease in the flow rate of air required for cooling.

In the majority of situations, the decrease in airflow was so significant that the total losses from air preheating and exhaust decreased, despite the increase in these losses on a per mole basis. The losses in turbomachinery also went down with the air flow. All these improvements together were able to overcome the increase in losses on the fuel side, leading to a monotonic increase in the overall efficiency with temperature. In 5.3a, the graph for $5000\,\mathrm{A\,m^{-2}}$ is an example of these situations.

However, there was an exception to this monotonic trend at very low current densities. $2500 \,\mathrm{A\,m^{-2}}$ is used as an example in the figure. At these levels, the stack was already very efficient. The rate of decrease of airflow became smaller as the temperature rose. Eventually, it could not compensate for the increasing losses from the fuel side, and the increasing losses (per mole) on the air side. This led to a decrease in the system efficiency



- (a) Variation in system exergy efficiency.
- (b) Variation in exergy losses and fresh airflow. The plots are differential, with first point of each line as datum.

Figure 5.3: Variation of fuel cell system performance with stack temperature - Basic configuration.

in these particular cases. This trend is further elaborated in Figure 5.3b, which plots the changes in exergy destruction and airflow with temperature, with the first point of each line used as the datum. The reversal in the trends of heating and environment losses is clearly seen, with the exergy loss to the environment at $800\,^{\circ}$ C being even larger than at $650\,^{\circ}$ C, due to the increased losses from the steam condenser.

Electrolysis Mode

The effect of temperature in the electrolysis mode depended on the thermal region of operation. If the electrolysis stack was in the exothermic region, the system was affected by temperature in exactly the same way as in the fuel cell mode: higher temperature raised the system efficiency.

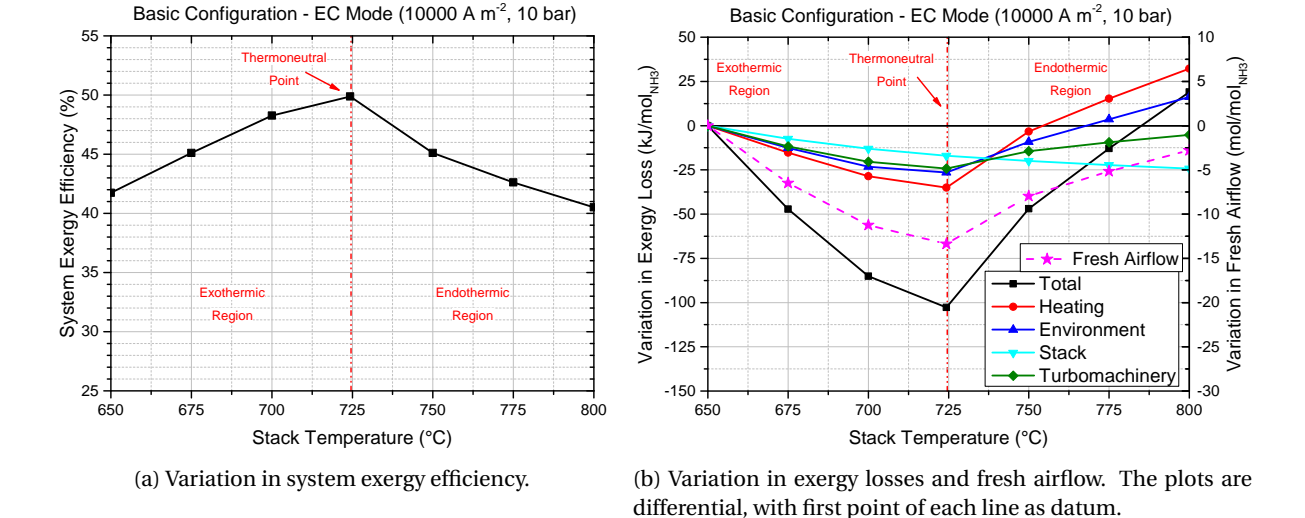


Figure 5.4: Variation of electrolysis system performance with stack temperature - Basic configuration.

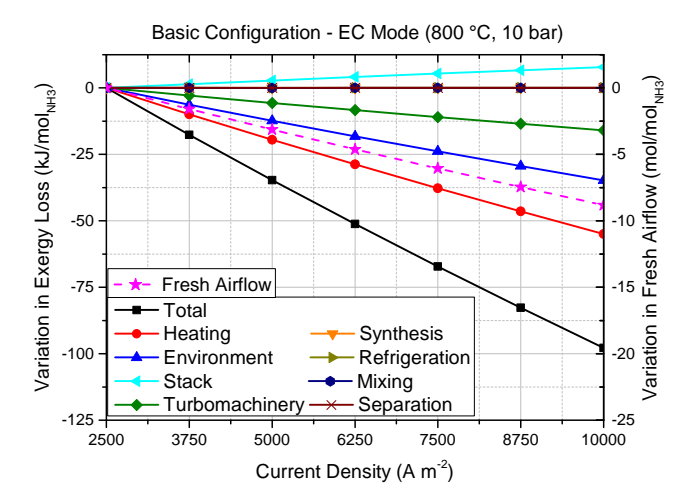
However, this trend changed in the endothermic mode. As the temperature rose further, the stack voltage went down and the stack went deeper into endothermic mode. Therefore the airflow required to heat the stack was increased. While the total energy provided to the reduction reaction through the stack and the air superheater was almost constant (equal to the enthalpy change of the reaction), more preheating was required for the higher air flow. This significantly raised the exergy destruction in heating. Meanwhile, the environment losses increased a little slower, because the air-side turbine was able to extract more exergy per mole of air in the form of electric power, due to higher turbine inlet temperature (TIT). However, the minor benefit of

higher TIT did not compensate for the large increase in preheating and environment losses. Therefore, in endothermic mode, higher temperature was detrimental to the electrolysis system.

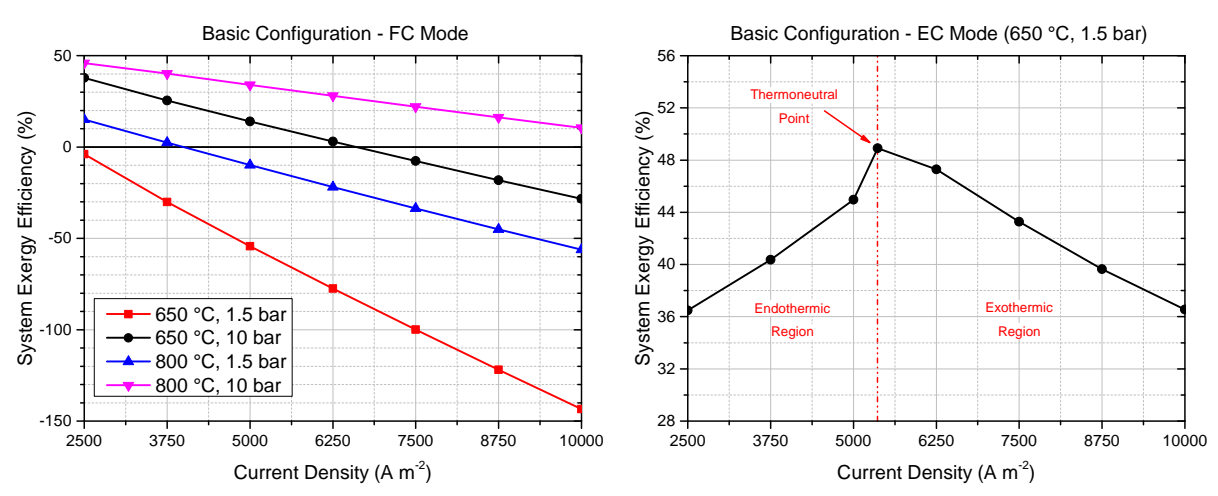
A natural consequence of these two trends in each region was that the electrolysis system efficiency was maximum at the thermoneutral point, as clearly visible in Figure 5.4a. These two trends are presented in detail in Figure 5.4b.

5.2.2. Current Density Variation

The effect of current density on the basic system is shown in Figure 5.5a. The figure is an example from electrolysis mode, but this is valid for either mode. As the current density increased, the overpotentials also rose linearly, and likewise, the exergy losses in the stack increased linearly as well. Since the operation point in the example was in the endothermic region, larger stack losses meant a lower heat demand for the stack. Therefore, the required airflow also reduced linearly.



(a) Dependence of exergy losses on current density and fresh airflow



 $\ \, \text{(b) Variation of system exergy efficiency in fuel cell mode}$

(c) Variation of system exergy efficiency in electrolysis mode

Figure 5.5: Variation of the system performance with current density - Basic configuration. The exergy losses and airflow values are differential, with the first point of each line as the datum.

From the figure, it can be seen that the (normalised) exergy losses in ammonia synthesis, refrigerators, mixers and separation processes were absolutely unaffected by current density. The only components that were affected apart from the stack itself, are heaters, turbomachinery and environment (i.e. coolers and air exhaust). Additionally, it is also notable that the change in losses on air-side components far outweighed the change in stack losses.

This tells us that the only way current density affected the system is through the stack, or the air-side BoP

components. This is because the component operating parameters on the fuel-side of the BoP were constant, while all the material flow rates (except air) were directly proportional to the current density. Therefore, when normalised by ammonia flow rates, the component mass, energy and exergy flow rates all become independent of current density. However, the airflow was not proportional to the current density, but rather proportional to the stack heat demand/generation. Since the overpotentials were linearly dependent on current density (in Ohmic region), the stack heat generation (or heat demand) actually had a quadratic dependence on current density. Therefore, when normalised by ammonia flow rate, the airflow and all the air-side BoP mass/energy/exergy flows became linearly dependent on current density, and not independent like the fuel-side mass/energy/exergy flows.

Once it is understood that only the stack and air-side BoP losses are affected by the current density, and that the BoP losses dominate the stack losses, it is straightforward to explain the variation of system exergy efficiency with current density. This variation shown in Figures 5.5b and 5.5c for each mode.

In the fuel cell mode, increased current density was detrimental to the performance, since the stack goes deeper into the exothermic mode, requiring more cooling, and hence more airflow. Whereas in electrolysis mode, it is seen that the system was most efficient at the thermoneutral point, where the required airflow was zero.

5.2.3. Pressure Variation

Fuel Cell Mode

Pressure had a highly beneficial effect on the basic system in fuel cell mode, as seen in Figure 5.6a. The most important driver of this improvement was the same as the one seen in the previous sections. Higher pressure increased the cell voltage, reducing heat generation and exergy losses, while increasing the stack power output. Lower heat generation reduced the required cooling airflow and the corresponding exergy losses from electric air preheating and release of hot exhaust were also reduced alongside. Additionally, the compressor outlet was hotter at higher pressures. This also contributed to reducing the exergy losses in air preheating.

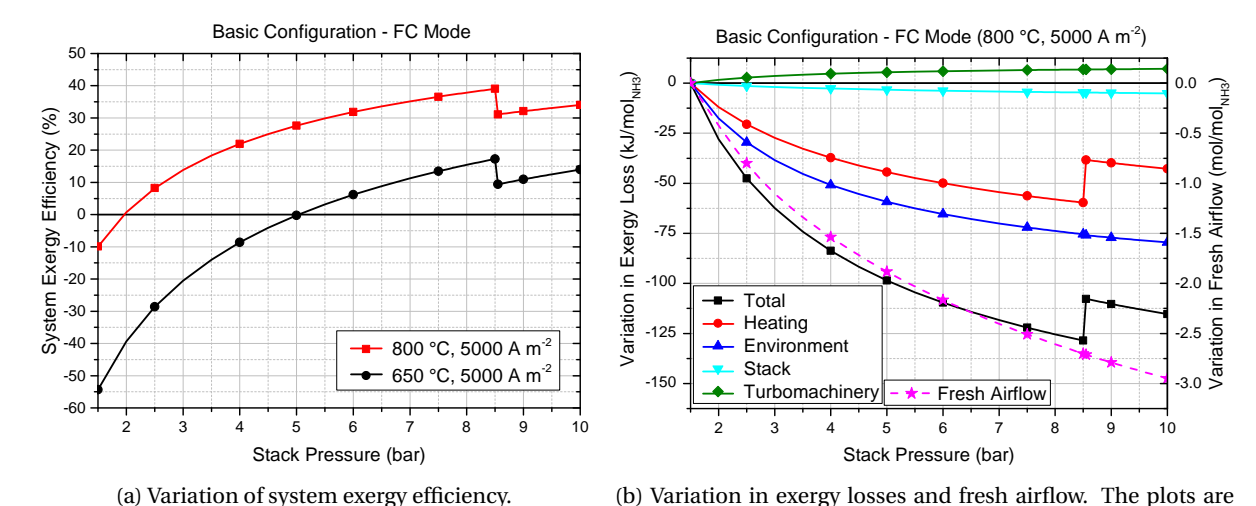


Figure 5.6: Variation of fuel cell system performance with stack pressure - Basic configuration.

differential, with first point of each line as datum.

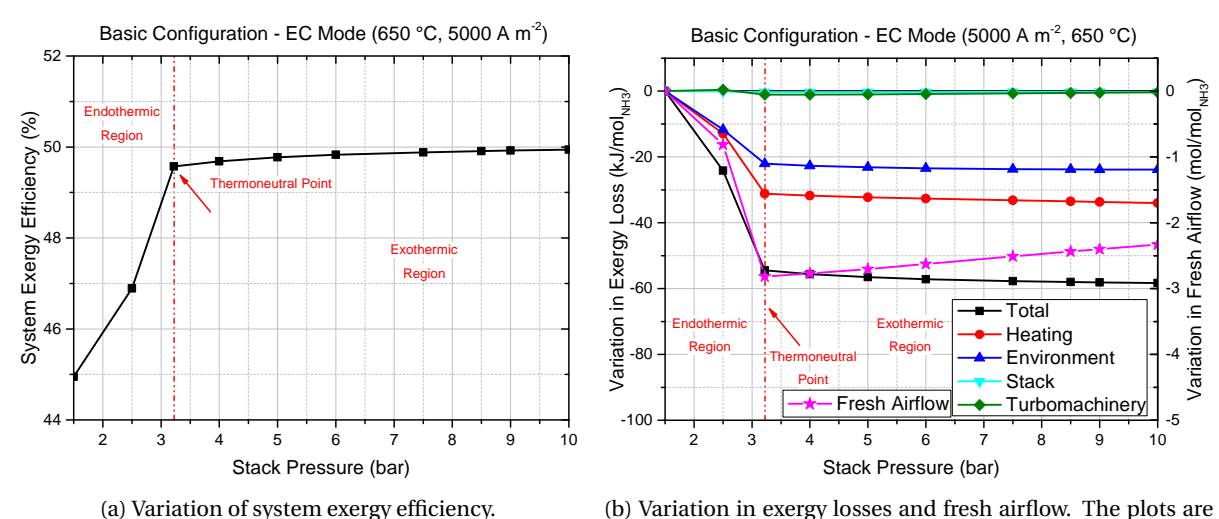
Unlike with temperature or current density, increasing pressure ratio had a very strong effect on the specific work output of the turbomachinery (which was in effect a Brayton cycle). An increase in stack pressure also implied a lower pressure ratio for compression of the nitrogen-hydrogen mixture up to 190 bar. All this led to an increase in the net increase in power output from turbomachinery. As the power throughput of the turbomachinery increased, the total exergy destruction in the turbomachinery also increased. However, as seen in the Figure 5.6b, this increase was much smaller than the reduction in heating and environment losses.

Because of the overwhelming effect of the airflow reduction, the system efficiency monotonically increased with pressure. However, there was one discontinuity in the monotonic trend at \sim 8.5 bar. This was the result of the method of evaporation of liquid ammonia. Under \sim 8.5 bar, ammonia has a low boiling point and it could be vaporised using heat from the atmosphere. However, above \sim 8.5 bar, the boiling point of ammonia exceeds 20 °C, and therefore external electric heating was required to vaporise the ammonia, leading to a drop

in the efficiency. After this one discontinuity, the rising trend of efficiency was maintained. This discontinuity is clearly seen in the graph of heating losses in Figure 5.6b.

Electrolysis Mode

At low pressures, the electrolysis stack was endothermic. As noted in Section 5.1.1, increasing the pressure increases the cell voltage. Therefore an increase in pressure took the stack closer to thermoneutral operation. This improved the system efficiency by reducing the required airflow, as has already been explained in the case of temperature and current density variations.



(b) Variation in exergy losses and fresh airflow. The plots are differential, with first point of each line as datum.

Figure 5.7: Variation of electrolysis system performance with stack pressure - Basic configuration

However, unlike the other parameters, raising the pressure further from the thermoneutral point was observed as not affecting the system performance significantly, as seen in Figure 5.7a.

At lower pressure, the air preheating was done with electric heating. This energy was lost to the environment in the absence of heat integration. At higher pressures, the preheating of the air was assisted by the temperature increase in the compressor. While the total power consumption for the compressor and electric heating remained similar, the energy added by the compressor could be partially recovered in the air turbine. Additionally, the expansion of oxygen generated by the electrolysis at high pressure further added to the turbine power. For these reasons, the power consumption of the BoP decreased at higher pressure. This more than compensated for the increase in stack power input, which occurred because Nernst voltage increases with rising stack pressure. Therefore, the overall power input (and hence efficiency) of the electrolysis system decreased slightly as the pressure was increased further into the exothermic region.

This effect is also analysed from an exergy perspective in Figure 5.7b. The figure shows that in the exothermic region, the exergy losses decreased slowly as the pressure was increased. This decrease was led by the decrease in exergy destruction in the electric heaters, as well as by decreased losses to the environment. At higher pressures, the air turbine was able to extract more exergy from the air exhaust in the form of electric exergy. Therefore, the losses to the environment decreased. Further, as the pressure increased, the compressor outlet temperature increased. Therefore the electric air heating after the compressor occurred at higher temperatures, thus reducing the exergy destruction slightly. Similarly, the boiling point of water was higher, meaning that most of the latent heat was also added at higher temperatures. For these reasons, the exergy destruction in electric heaters also decreased.

5.2.4. Conclusion of Basic Configuration Study

The key take-aways of the basic configuration study are summarised as follows:

• The basic configuration system was not thermodynamically feasible at the base case parameters, having a negative RTE. After parametric optimisation, the system attained a RTE of 19.79%. While the basic configuration is thermodynamically feasible after parametric optimisation, the RTE of 19.79% is too low for any energy storage system. Therefore, further improvements to the system have to be explored.

- Both before and after parametric optimisation, the largest sources of exergy destruction were heating and cooling of the streams. This confirmed the need for heat integration as the first and foremost improvement.
- In almost all cases, the highest efficiencies occurred when approaching thermoneutral points. The sole
 exception was that in electrolysis mode, pressure could be increased beyond the thermoneutral point if
 required without any significant efficiency penalty.
- The FC mode is always exothermic, and reducing the heat generation simply entailed operation at higher temperatures, higher pressures and lower current density. However, the boiling point of the ammonia fuel made operation under 8.5 bar more favourable than operation at 10 bar. In most cases, the maximum temperature was preferable, but at very low current density, the optimum fuel cell temperature shifted to a slightly lower value as the improvements in stack heat generation began to taper off.
- For electrolysis mode, the highest efficiency is typically found at a thermoneutral point, which depends on the combination of all the stack parameters.
- The optimal operating points for each mode, as well as for round trip efficiency, are shown in Table 5.3. These three optima occur at different points, due to the conflicting trends in the two modes. It must be noted that the fuel cell efficiency had a much larger range of variation than electrolysis efficiency. Therefore, the optimum RTE point is much closer to the optimum point for FC mode than to the optimum point for EC mode.

Table 5.3: Optimal operating points for basic configuration

Paramater	Unit	Optimum FC Mode	Optimum EC Mode	Optimum RTE
Stack temperature	°C	775	659	700
Stack pressure	bar	8.5	10	8.5
Current density	Am^{-2}	2500	5000	2500
FC mode exergy efficiency	%	52.47	16.45	49.49
EC mode exergy efficiency	%	35.55	50.26	40.00
Round trip efficiency	%	18.65	8.27	19.79



Improved Configurations and Analysis

Introduction

In this section, heat integration schemes are designed to eliminate the largest sources of exergy loss discovered in the previous chapter. The results of the previous chapter show that while energy storage with ReSOC using ammonia is feasible, the maximum round trip efficiency of a basic system is less than 20%, and hence not acceptable. Exergy analysis also showed that heating and cooling/exhaust losses were the biggest factors hampering the efficiency.

One of the research activities stated in Section 3.5 was testing the feasibility of operating a ReSOC system without an afterburner in an attempt to avoid the exergy losses in combustion. Accordingly, the heat integration in all the configurations in this chapter is done without introducing an afterburner.

Another one of the research activities stated in Section 3.5 included optimising the relative location of the air turbine and the air recuperative heat exchanger. The energy contained in the exhaust air from the stack can be used either for preheating the inlet flows or extracted in the form of work from a turbine. This trade-off is driven by the relative location of the turbine and the heat exchanger(s). The effect of this choice on the system performance deserves to be studied in order to optimise the system efficiency. Therefore, in this chapter, two different configurations are designed with different relative placement of the turbine. The heat integration schemes are also appropriately modified for each configuration.

6.1. Fuel Cell Mode - Hot Turbine Configuration

The basic configuration of the fuel cell mode was improved through the use of heat integration and recirculation of air electrode exhaust, which is analysed in this section. The first configuration designed was the "hot turbine" configuration. It is named so because the inlet temperature of the air turbine was high, since it was placed upstream from the recuperation heat exchanger(s), as shown in the process flowsheet in Figure 6.1. The system flowsheet also shows the recirculation of the air electrode exhaust back to the inlet. The heat integration is shown through the red dashed arrows. The heat integration scheme is shown in greater detail in Figure 6.2.

Design of Heat Integration Scheme

The heat integration scheme is shown in Figure 6.2. The heat exchangers were all placed in counter flow configuration to achieve the most heat transfer with the least temperature difference.

The fuel electrode exhaust from the stack was used to heat both the inlet streams to the required stack inlet temperature. The exhaust air coming from the turbine outlet was colder than the stack temperature (the temperature difference depending on pressure ratio of the turbine), and therefore could not be used to heat the fresh air stream to the required stack inlet temperature.

The fuel electrode exhaust was split into two heat exchangers HEX2 and HEX4. The fuel flow had a relatively low heat capacity and a more steady flow rate compared to the fresh air. Therefore, ratio of the stream split was chosen such that the fuel stream was heated exactly up to the required temperature in HEX2; the rest of the fuel electrode exhaust was sent to the HEX4 to heat the fresh air. The previously split flows were mixed together again, before being used to preheat the fuel in HEX1. This re-mixing was done to increase the heat

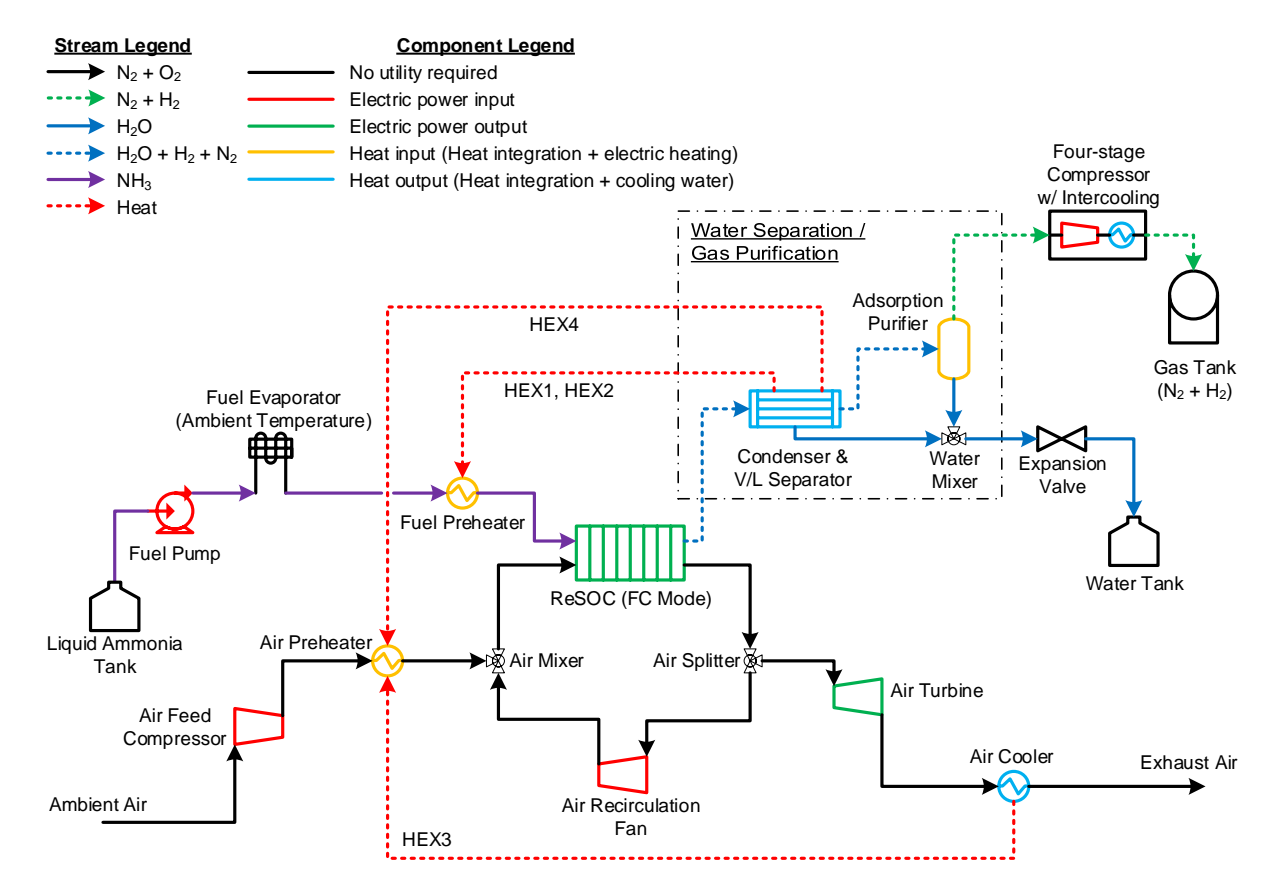


Figure 6.1: Process flowsheet for fuel cell mode - Improved hot turbine configuration.

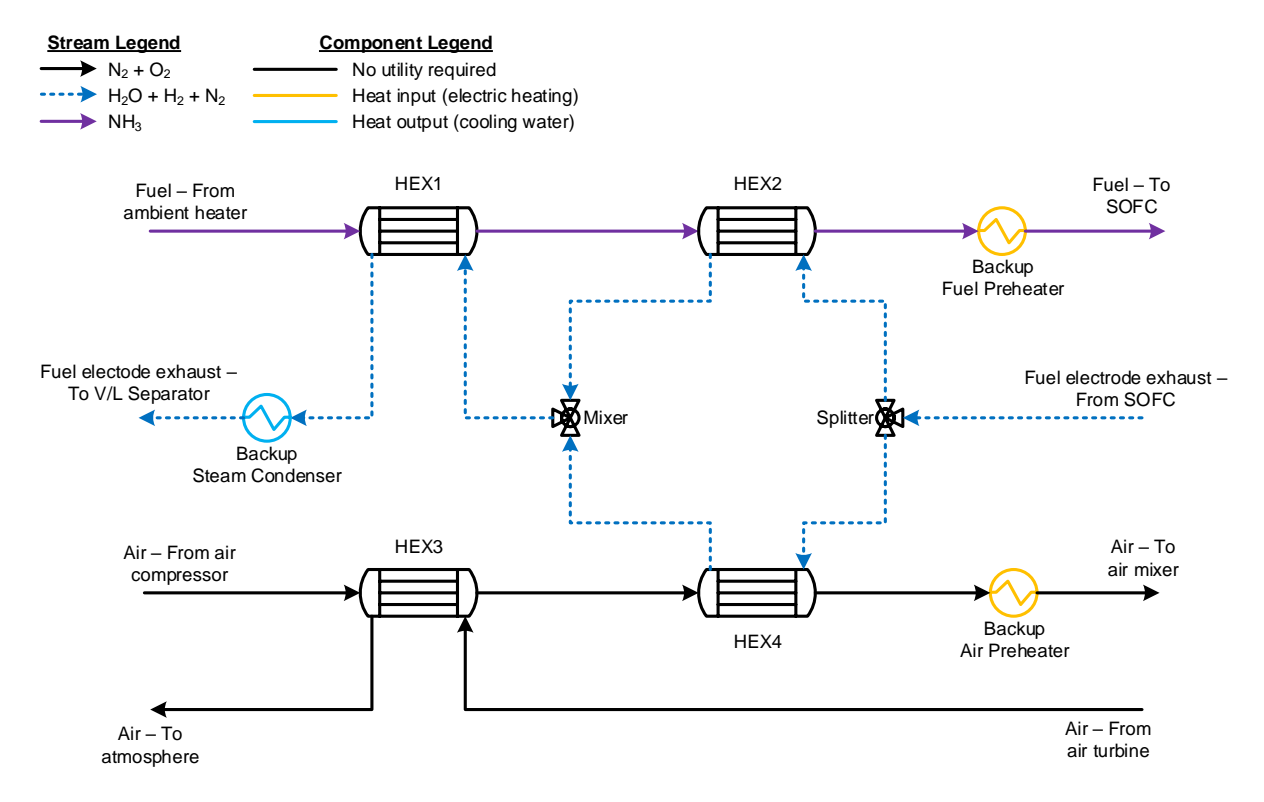


Figure 6.2: Heat integration scheme for fuel cell mode - Improved hot turbine configuration.

capacity of the hot stream, to reduce the chances of temperature reversal inside HEX1 in case steam started condensing in HEX1.

The fresh air was preheated using the exhaust air in HEX3. At high pressures, this was not possible at all, and this heat exchanger was bypassed. This is because at high pressures, the compressor heats up the inlet air too much, while the turbine cools the exhaust air too much, leading to an adverse temperature gradient for HEX3.

In the hot turbine configuration, there was a shortage of high-temperature ($400-800\,^{\circ}$ C) heat due to the placement of the exhaust air turbine, whereas low temperature ($<400\,^{\circ}$ C) heat was available in ample amount from the steam condenser and exhaust air. Therefore, the low temperature ($<250\,^{\circ}$ C) heat from compressor intercoolers, though significant in quantity, was found to not affect the system efficiency significantly. Therefore, these intercoolers were not included in the heat integration scheme.

Backup heaters and coolers were placed at the end of each stream (except air exhaust) in order to take the streams to the desired temperature if heat integration was insufficient.

The simulation methodology and the analysis of the results leading to these optimum values are discussed in detail in the following sections.

6.1.1. Methodology

The configuration described above was simulated for various operating points. As in the previous sections, the parameters varied included the stack temperature, stack pressure, and current density. The values tested for each parameter are as follows:

Stack Temperature 650 °C, 700 °C, 750 °C, 800 °C

Stack Pressure 1.5 bar, 2.5 bar, 5 bar, 7.5 bar, 10 bar

Current Density 2500 Am⁻², 5000 Am⁻², 7500 Am⁻², 10000 Am⁻²

The system was tested at different combinations of the values given above, leading to a total of 80 discrete operating points. Apart from these parameters, the air recirculation ratio was also varied. The air recirculation ratio is defined as the fraction (or percentage) of the stack air electrode outlet that is recirculated to the inlet. For every stack operating point (i.e. combination of temperature, pressure and current density), the air recirculation was varied until the maximum efficiency was achieved for that operating point.

Just like in the basic configuration studies, the fuel flow was varied according to the current density, in order to keep the fuel utilisation constant at 80 %. The fresh air flow rate from the atmosphere was controlled in order to provide the cooling needs of the stack, with the temperature difference across the stack maintained at $100\,^{\circ}\text{C}$.

The following sections analyse the results in terms of variation of each of the four parameters: air recirculation, stack temperature, stack pressure, and current density.

6.1.2. Effect of Air Recirculation Variation

These are: the reduction in fresh airflow, and the reduction in fresh air preheating temperature. These two primary effects led to other effects on the net power, exergy destruction and system efficiency, which are described below.

The primary effects of increasing air recirculation were a reduction in the required fresh airflow, and a reduction in the fresh air preheating temperature. Since the temperature difference across the stack was constant, the total airflow input to stack needed to be constant. Therefore, as the air recirculation was increased, the fresh airflow had to be reduced in order to maintain the total airflow input to the stack. Further, as the air recirculation was increased, due to the addition of a greater amount of hot air, the temperature of the fresh air had to be reduced, so that the mixed airflow to the inlet of the stack could be maintained at a constant temperature.

At zero recirculation, for most points, the heat integration could not meet the entire air preheating demand, since the heat capacity of the fuel electrode exhaust was less than the heat capacity of the fresh air. Therefore, electric heating still had to be used. But as recirculation was increased, because of the reduction in the fresh airflow and the reduction in preheating temperature, the electric power required for fresh air preheating reduced.

In the hot turbine configuration, the turbomachinery (referring to the combination of compressor and turbine) on the air side acted like an open Brayton cycle, converting the heat generation of the stack into

electric power. As the fresh and exhaust airflows reduced due to recirculation, the power output of this cycle also reduced.

Lastly, increasing recirculation of exhaust air, and decrease of fresh air flow led to a reduction in the oxygen content of the air provided to the stack. Because of this, especially at high recirculation ratios, the stack power output reduced, since the Nernst voltage reduced due to lower oxygen content.

Overall, the effect of reducing electric air preheating was very dominant, as seen in Figure 6.3a. Therefore the system efficiency increased with increasing recirculation. However, after the electric preheating requirement reached zero, increasing the recirculation further led to a decrease in efficiency since the reduction in turbine power and stack power dominated. Therefore, the optimum recirculation ratio was the point where electric preheating of the air was zero.

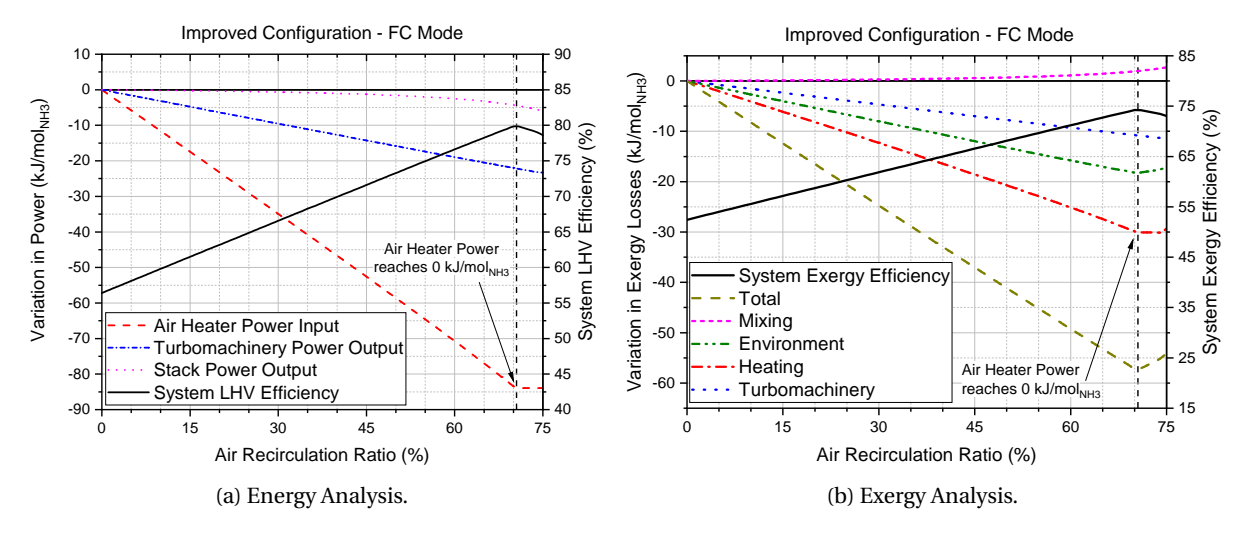


Figure 6.3: Effect of air recirculation on fuel cell system performance. Power / Exergy loss values show the variation compared with first point of each line as datum. The operating parameters used in this example: $800\,^{\circ}$ C, $10\,\text{bar}$ and $7500\,\text{A}\,\text{m}^{-2}$.

The variation of efficiency can also be analysed through a study of variations in exergy losses, as shown in Figure 6.3b. The exergy losses in the system were largely dictated by the fresh airflow. As the fresh airflow reduced due to increasing recirculation, the exergy destruction in electric heating, turbomachinery, and exergy losses to the environment through the air exhaust, all decreased. The only exception was the exergy destroyed in the air mixer, which increased slightly due to the increased mixing of hot recirculated air with the relatively colder fresh air. Overall, the total exergy losses reduced drastically with increasing air recirculation.

Beyond the point where electric air preheating could be eliminated, the exergy destruction in heating stopped decreasing. Additionally, the losses to the environment started increasing with further increase in air recirculation, since the heat from the fuel electrode exhaust, which was being used for fresh air preheating in HEX4, was now released to the environment in the condenser since the fresh air flow was now even lower than what the heat exchangers were capable of heating. Therefore, the efficiency started decreasing beyond the point where electric heating was eliminated.

There is also one interesting and notable effect regarding air recirculation in the hot turbine configuration. As mentioned previously, increasing the air recirculation reduced the oxygen content available to the stack. Since the fuel cell needs oxygen to consume, a minimum concentration of oxygen has to be maintained at the air electrode. According to literature [96], oxygen content below 4 % leads to irreversible damage to the cells. The fresh air molar flow $\dot{n}_{\text{fresh-air}}$ [mols⁻¹] for a given outlet oxygen mole fraction $y_{\text{O}_2,\text{out}}$ [-] can be calculated by Equation (6.1), based on the molar rate of oxygen consumption in the fuel cell $\dot{n}_{\text{O}_2,\text{consumed}}$ [mols⁻¹] and the mole fraction of oxygen in the fresh air $y_{\text{O}_2,\text{atm}}$ [-]. Accordingly, assuming 21 % oxygen content in the atmosphere, the minimum fresh airflow for this fuel cell model $\dot{n}_{\text{fresh-air,min}}$ can be given by Equation (6.2).

$$\dot{n}_{\text{fresh-air}} = \frac{\dot{n}_{\text{O}_2,\text{consumed}}}{y_{\text{O}_2,\text{atm}}} \times \left[1 - \left(\frac{1 - y_{\text{O}_2,\text{atm}}}{y_{\text{O}_2,\text{atm}}} \cdot \frac{y_{\text{O}_2,\text{out}}}{1 - y_{\text{O}_2,\text{out}}} \right) \right]^{-1}$$
(6.1)

$$\dot{n}_{\text{fresh-air,min}} = \frac{\dot{n}_{\text{O}_2,\text{consumed}}}{0.21} \times \left(1 - \frac{0.79}{0.21} \cdot \frac{0.04}{0.96}\right)^{-1} = 5.6471 \, \dot{n}_{\text{O}_2,\text{consumed}}$$
(6.2)

This constraint also constrained the maximum air recirculation ratio. At such operating points where the stack was at its most efficient (i.e. at low current density, high pressure, high temperature; recall from Section 5.1.1), the required stack inlet airflow was very low. At these points, when the air recirculation was increased, the minimum fresh airflow limit calculated by Equation (6.2) was quickly reached. This meant that the air recirculation could not be increased further, despite the electric air preheating having not been eliminated entirely. This occurred only at 10 out of the 80 operating points investigated (8 of these 10 points being at the lowest current density: $2500\,\mathrm{Am^{-2}}$). This effect is represented in Figure 6.4. Since this limitation occurred at the points of highest stack efficiency, this effect also limited the maximum possible system efficiency of the hot turbine configuration.

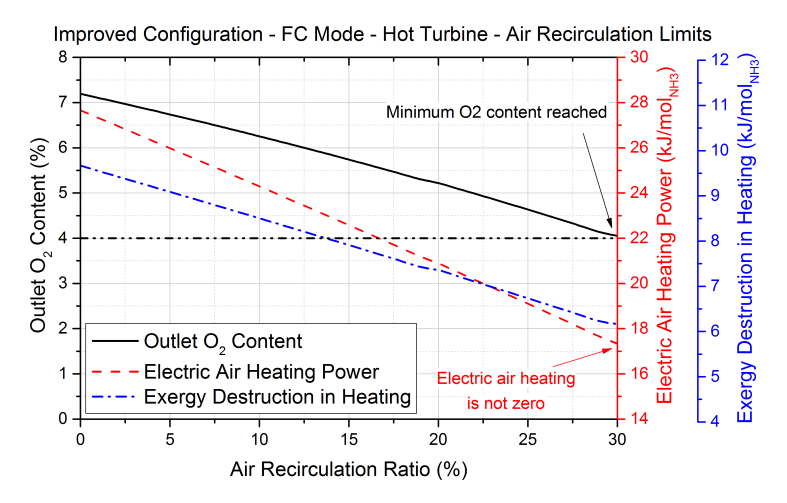


Figure 6.4: Exceptional cases - Air recirculation limit reached before elimination of electric heating. Stack parameters used in this example: $800\,^{\circ}$ C, $10\,\text{bar}$, $2500\,\text{A}\,\text{m}^{-2}$.

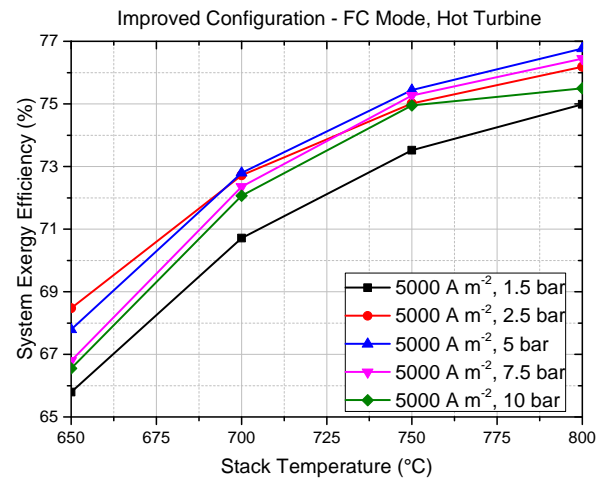
6.1.3. Effect of Stack Temperature Variation

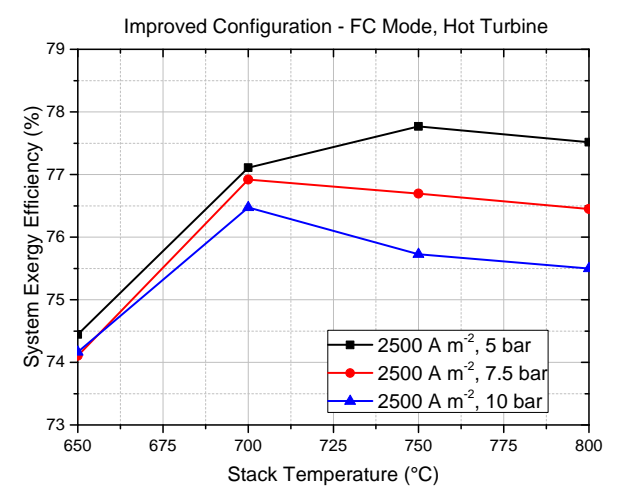
In the vast majority of cases tested, the system efficiency increased monotonically with temperature in the given range, as shown in Figure 6.5a. Figure 6.5c explains these results through exergy analysis.

Stack temperature has a very large beneficial effect on the overpotentials, as mentioned in Section 5.1.1. Therefore, the exergy destruction in the stack was seen to diminish rapidly with temperature. This also meant that the required inlet airflow to the stack was lower. Since the heat capacity of the hot fuel electrode exhaust flow was less than the fresh air, an increase in temperature of the hot stream could not provide the same increase of temperature in fresh air. The fresh airflow had to reduce. But the reduction of airflow due to better stack efficiency was not sufficient, leading to an increase in air recirculation ratio in order to eliminate the electric preheating.

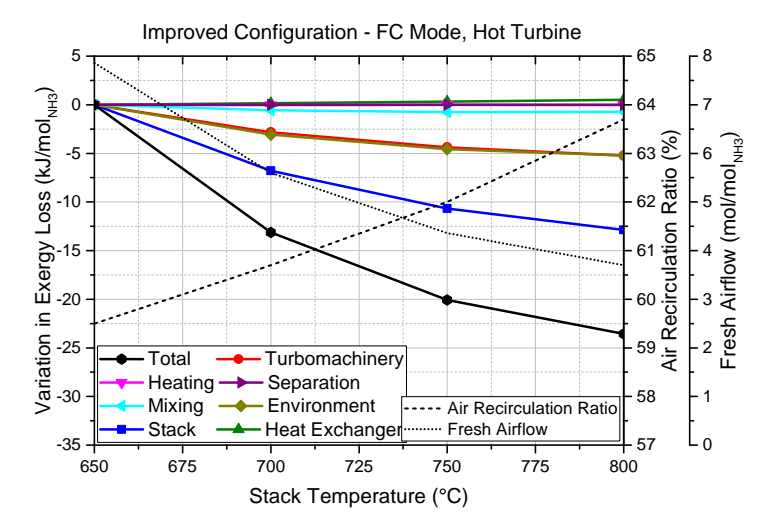
As was mentioned previously, this heat integration configuration was able to entirely eliminate the electric fuel preheating, while the electric preheating of fresh air was eliminated for most points. Because of this, the exergy destruction in heating remained very low, and nearly independent of stack temperature. The exergy destruction in heat exchangers increased due to the larger heat transfer up to higher temperatures, but this increase was minuscule compared to the other factors.

In HEX3 of Figure 6.2, the hot exhaust air always had lower heat capacity than the cold fresh air, since some oxygen was consumed in the fuel cell. This meant that the outlet temperature of exhaust air was dependent on the inlet temperature of the cold fresh air, which in turn depended on the compressor pressure ratio. Therefore, the temperature of the exhaust air outlet remained independent of stack temperature, and

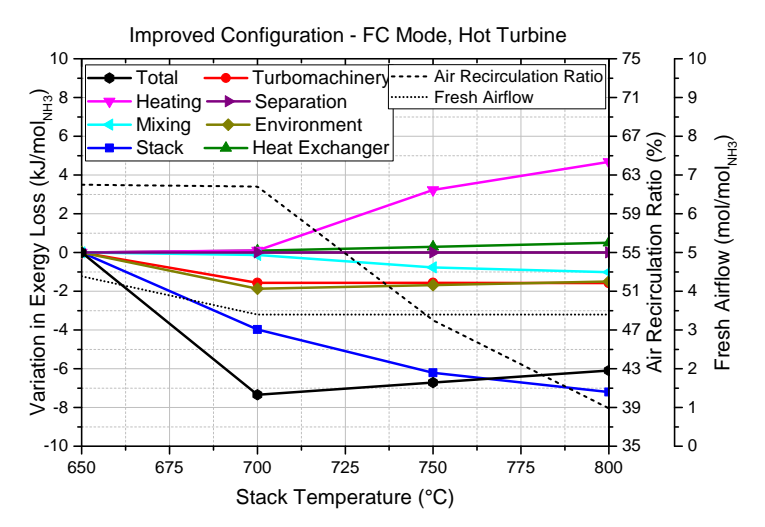




- (a) Variation of system exergy efficiency: examples of the most common results (i.e. with no oxygen starvation).
- (b) Variation of system exergy efficiency: the three exceptional results (i.e. at oxygen starvation limit).



(c) Variation of exergy losses: one of the common results. Stack parameters used in this example: $5000 \, \text{Am}^{-2}$, 5 bar.



(d) Variation of exergy losses: one of the exceptional results. Stack parameters used in this example: $2500\,\mathrm{A\,m^{-2}}$, $7.5\,\mathrm{bar}$. Minimum airflow limit had been reached at $700\,^\circ\mathrm{C}$.

Figure 6.5: Variation of fuel cell system performance with stack temperature, in hot turbine configuration. The exergy losses are differential, with the first point of each line as the datum.

the reducing airflow ensured that exergy losses to the environment due to air exhaust went down with stack temperature. Meanwhile, the exergy loss to the environment from the steam condenser was observed to increase, since the energy content of the steam generated in the stack increased with higher stack temperature, but only a portion of this increase was passed to the air in HEX4. However the reduction of air exhaust losses overshadowed the steam condensing losses, leading to a reduction in total exergy losses to the environment. The exergy destruction in turbomachinery was also seen to reduce, simply due to the lower airflow.

Due to all these factors, it can be seen from Figure 6.5c that the overall exergy destruction reduced with stack temperature, therefore increasing the system efficiency.

However, this monotonic trend was found to change in those cases where electric air preheating was not eliminated completely, due to reaching the minimum oxygen content limitation. In these cases, the system efficiency was actually found to decrease with temperature after the air recirculation was limited. This trend is depicted in Figure 6.5b, with an exergy analysis in Figure 6.5d.

The reduction in stack exergy destruction showed the same trend as the common cases. Since the fresh airflow was limited, while the total inlet airflow reduced due to better stack efficiency, the air recirculation that was required also reduced sharply with increasing temperature. The mixing losses were seen to reduce because of the sharp fall in air recirculation ratio. Because the fresh airflow was limited to the minimum value, the corresponding reduction in turbomachinery losses also stagnated. The reduction in environment losses due to air exhaust also stagnated. Meanwhile, the increase in losses due to water condensation continued, leading to an increase in total exergy losses to the environment after the airflow was limited. Most importantly, since the electric air preheating was no longer able to be eliminated through heat integration, the exergy losses in destruction increased along with the electric power for heating.

Despite the reduction in stack losses, the stagnation in turbomachinery losses, along with the increase in heating losses resulted in an increase in the total exergy loss, and a corresponding fall in the system efficiency.

6.1.4. Effect of Current Density Variation

The effect of current density on the improved system was found to match the effect of current density in the fuel cell system basic configuration. At all operating points, the system efficiency was found to decrease with increasing current density, as seen in Figure 6.6a.

Figure 6.6b shows the variation in exergy losses, classified by the components. The exergy destruction in the stack showed the largest increase, due to larger polarisation losses and heat generation in the stack. The resulting increase in airflow caused all the other losses to increase as well.

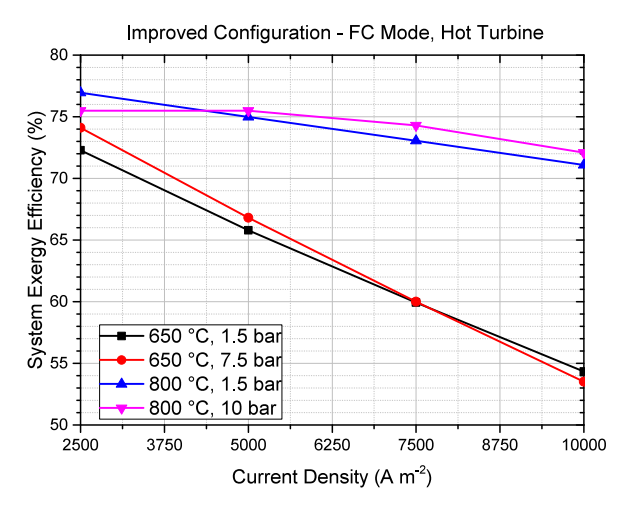
In HEX4, the (constant) fuel electrode exhaust flow could not fully preheat the rising fresh airflow demand. Therefore, the air recirculation had to be increased to moderate the rise in fresh airflow. The resulting drop in air preheating requirement allowed the fuel electrode exhaust to heat the fresh airflow. Note that the preheating requirement depends on the fresh airflow and the preheating temperature, and recirculation reduces both these factors together. This means that the preheating demand has a stronger dependence on recirculation than the airflow itself does. Therefore, at higher current densities, when the recirculation was increased by a certain value in order to eliminate the electric air preheating, the fresh airflow fell at a slower rate than the preheating demand did. Therefore, the fresh airflow actually increased with the current density, albeit slower than it would have increased without recirculation.

Since the rise in air recirculation allowed the fresh air preheating demand to be satisfied, the exergy destruction in electric heating remained negligible. Mixing losses increased due to greater air recirculation.

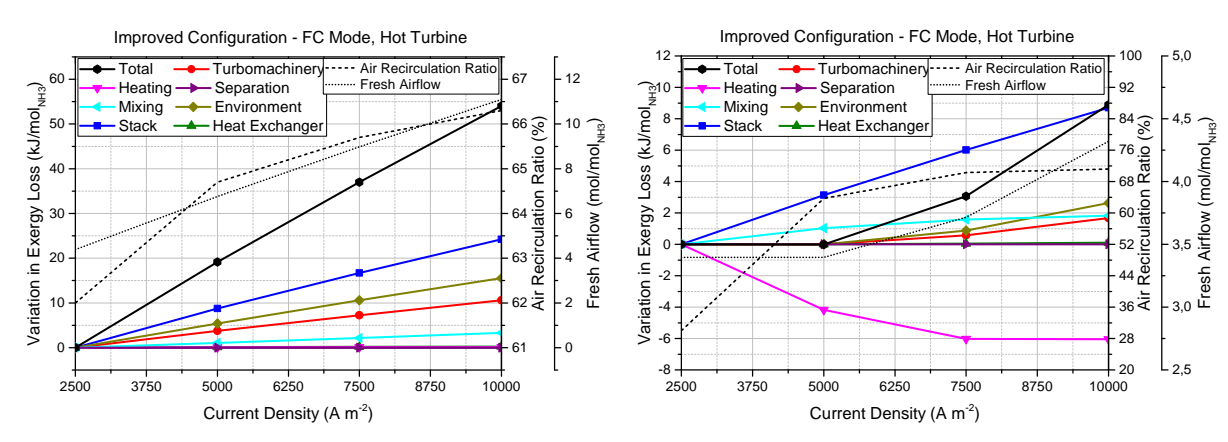
With inlet temperatures and pressure ratios being constant, the turbomachinery losses solely depended on the increasing airflow. Similarly, the increasing exergy losses to the environment were also dictated by the rising exhaust airflow.

This monotonic trend held true even in cases where the lowest current density point was limited by minimum fresh airflow. The most extreme example of the fresh airflow restriction ($2500\,\mathrm{Am^{-2}}$, $800\,^{\circ}$ C, $10\,\mathrm{bar}$) is included in Figure 6.6a, where the first two point still remains very slightly higher than the second point.

Figure 6.6c shows the reason for this. Note that the restriction on recirculation is active at the first two points, as indicated by the constant airflow. As the current density increased, the stack air demand increased as well, and the restriction on recirculation was slowly eased, allowing more recirculation. This meant that the heat integration was more effective at eliminating electric heating for air, and the exergy losses associated with electric heating decreased. However, this was strongly countered by the increase in losses in the stack and air mixer, leading to a small net increase in total exergy loss. Further, as the restriction on recirculation was removed completely, the fresh airflow rose and the turbomachinery and environment losses rose with it. The improvement in heating losses stagnated as the electric heating remains almost zero.



(a) Variation of system exergy efficiency for various operating points.



- (b) Variation of exergy losses: example of common cases. Stack parameters used in this example: 650 °C, 7.5 bar.
- (c) Variation of exergy losses: example of exceptional cases. Stack parameters used in this example: 800 °C, 10 bar.

Figure 6.6: Variation of fuel cell system performance with current density, in hot turbine configuration. The exergy loss values are differential, with the first point of each line as the datum.

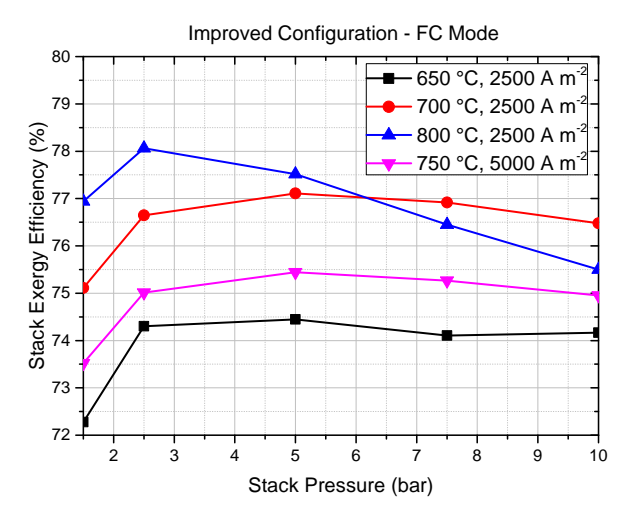
Thus, the system efficiency always reduced with an increase in current density, at all the tested operating points.

6.1.5. Effect of Stack Pressure Variation

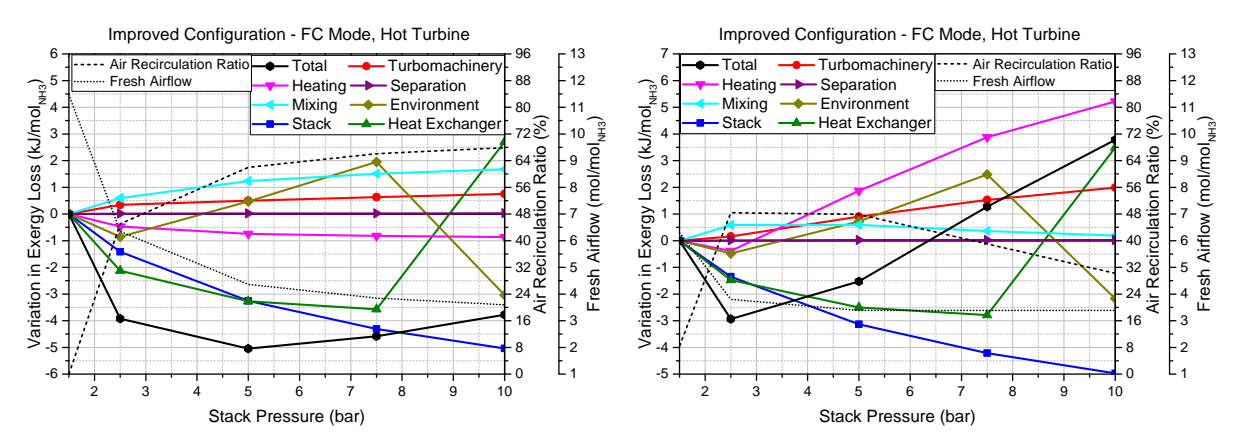
In all the tested cases, it was observed that pressure variation did not have a monotonic effect on the system exergy efficiency. At low pressures, increasing the pressure improved the efficiency. Eventually, a peak was reached and upon increasing the pressure further, the efficiency began to decline. This is shown in Figure 6.7a. The position of the peak varied according to the other parameters. In cases where the minimum fresh airflow limitation was hit as pressure was raised (as explained in 6.1.2), the efficiency was limited as well, and the peak shifted further towards lower pressure.

Figure 6.7b shows the variation of exergy losses and fresh airflow, for a points which don't reach the minimum fresh airflow limit. Since the Nernst voltage rises with pressure, while the overpotentials are approximately constant (see Section 5.1.1), the heat generation was expected to go down with pressure. This behaviour was indeed observed as the exergy destruction in the stack reduced significantly with pressure.

In the hot turbine configuration, the main effect of pressure on the system performance was through the air-air heat exchanger (HEX3 in Figure 6.2). At the low stack pressure of 1.5 bar, HEX3 was able to recover a large amount of heat, and there was no electric heating required, even with no air recirculation. As the pressure ratio rose, the fresh air compressor outlet temperature increased, and the exhaust air turbine outlet temperature decreased. Both these factors together had a significant negative impact on the heat transfer



(a) Variation of system exergy efficiency for various operating points.



- (b) Variation of exergy losses: example of common cases. Stack parameters used in this example: 750 °C, 5000 Am⁻².
- (c) Variation of exergy losses: example of exceptional cases. Stack parameters used in this example: 800 °C, 2500 Am⁻².

Figure 6.7: Variation of fuel cell system performance with stack pressure, in hot turbine configuration. The exergy loss values are differential, with the first point of each line as the datum.

potential in HEX3. At some operating points, (low stack temperature combined with high stack pressure) HEX3 even had an adverse temperature gradient, and had to be bypassed altogether.

Because of this diminished heat integration, when the pressure was increased, the fresh airflow had to be reduced in order to avoid electric preheating. While the reducing stack losses did reduce the total stack airflow, it was not sufficient and the air recirculation had to be increased significantly as well. This also entailed an increase in exergy losses from mixing. The electric preheating for both air and fuel sides was always zero, therefore, the heating losses remained very low, mainly from the water desorption heater.

As the pressure increases, the power through the air turbine and compressor increased, despite the reduction in airflow. This means that the exergy losses in each of these components also increased with pressure. The pressure ratio across the nitrogen-hydrogen compressors reduced, decreasing their power input and exergy destruction. However, the air-side turbomachinery had a larger effect. It must be noted that while the power of the compressor and turbine increased individually, the net power production decreased. This is because as the fresh airflow (through the compressor) decreased, the exhaust airflow in the turbine decreased proportionally much faster, since the fuel cell stack consumed a fixed amount of oxygen. Therefore, the compressor power increased faster than the turbine power.

Lastly, we consider losses to the environment and in the heat exchangers. The environment loss was made out of many components: the exhaust losses from the air, and the thermal exergy losses from the steam condenser, compressor intercoolers and the ammonia evaporator. As the heat extraction through HEX3 became

lower and lower, the exergy losses through the air exhaust increased sharply. Similarly, as air entering HEX4 was also hotter, the heat extraction from fuel electrode exhaust also reduced, increasing the steam condensation losses. As the heat transferred in HEX3 and HEX4 fell, the exergy destruction in the heat exchangers fell accordingly.

As the stack pressure rose, the pressure ratio in each compressor stage fell, reducing the stage outlet temperature, and hence the exergy lost through the intercoolers. Similarly, the latent heat of ammonia evaporation was released at higher temperature (i.e. closer to ambient), therefore the exergy lost in ammonia evaporation also reduced.

Notice the sharp shift in environment and heat exchanger losses between 7.5 bar and 10 bar. Recall from Section 5.2.3, that below 8.5 bar, the ammonia evaporation was done using the environment, while above this pressure, the evaporation had to be done with external heat supply. In this improved configuration, the evaporation above 8.5 bar was done using the fuel electrode exhaust in HEX1. Therefore, the exergy loss to the environment through the steam condenser reduced, while the exergy destruction in HEX1 increased by the same amount. Since there was no electric heating involved, there was no sudden increase in total exergy loss, and there is discontinuity expected in the trend of system efficiency, unlike the basic configuration.

Figure 6.7c shows the variation in exergy losses and airflow for points that do hit the minimum airflow limit. Everything except the heating and mixing losses was the same as above.

As the pressure rose, the reducing stack losses led to lower stack airflow. However, once the minimum fresh airflow limit was reached, in order to reach lower stack airflow, the air recirculation had to be reduced. This led to a reduction in mixing losses.

Meanwhile, since the electric air heating could no longer be fully eliminated, the heat requirement began to rise with pressure as HEX3 became less useful. This led to a large increase in heating exergy destruction, which dominated all the other losses, leading to an increase in the total exergy loss, and a faster reduction in system efficiency compared to the regular operating points.

6.1.6. Conclusion of Hot Turbine Configuration Analysis

- The peak system exergy efficiency attained with this improved hot turbine configuration was 78.06%, compared to 52.47% in the basic configuration. This occurred at the operating point of $800\,^{\circ}$ C, 2.5 bar and $2500\,\mathrm{Am}^{-2}$.
- Air recirculation was very beneficial to the system performance by reducing electric air preheating requirements. The optimum air recirculation was at the point when electric air preheating was zero.
- The electric preheating could be fully eliminated in 70 out of 80 tested points. In 10 points where stack efficiency was high, electric preheating could not be eliminated, because recirculation had to be limited to avoid oxygen starvation.
- High temperature is always beneficial for the fuel cell hot turbine configuration, except in regions of oxygen starvation.
- The optimum stack pressure for this configuration varies between 2.5 bar and 5 bar depending on other parameters.
- · Lower current density is always favourable for this configuration.

6.2. Fuel Cell Mode - Cold Turbine Configuration

The second configuration designed to improve the basic configuration in fuel cell mode was the "cold turbine" configuration. The name comes from the fact that the inlet temperature of the air turbine was relatively lower, since the turbine was placed downstream of the recuperation heat exchanger(s) in the air electrode exhaust stream, as shown in Figure 6.8. The red dashed lines show the heat flows in the heat exchangers. The detailed heat integration scheme is shown in Figure 6.9. Two schemes had to be designed for the CT fuel cell configuration: one for very low stack pressures (1.5 bar), and one for other pressures. The reason for these different schemes is outlined below.

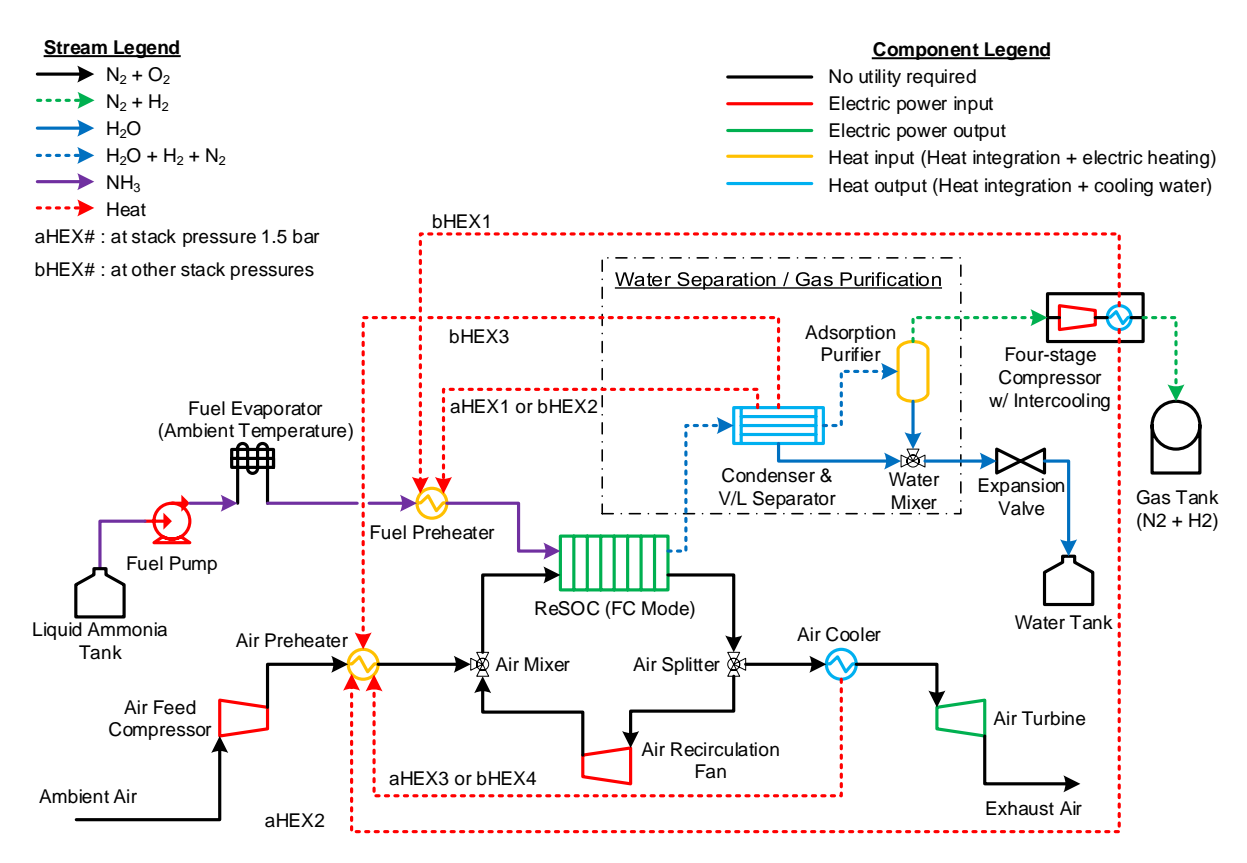
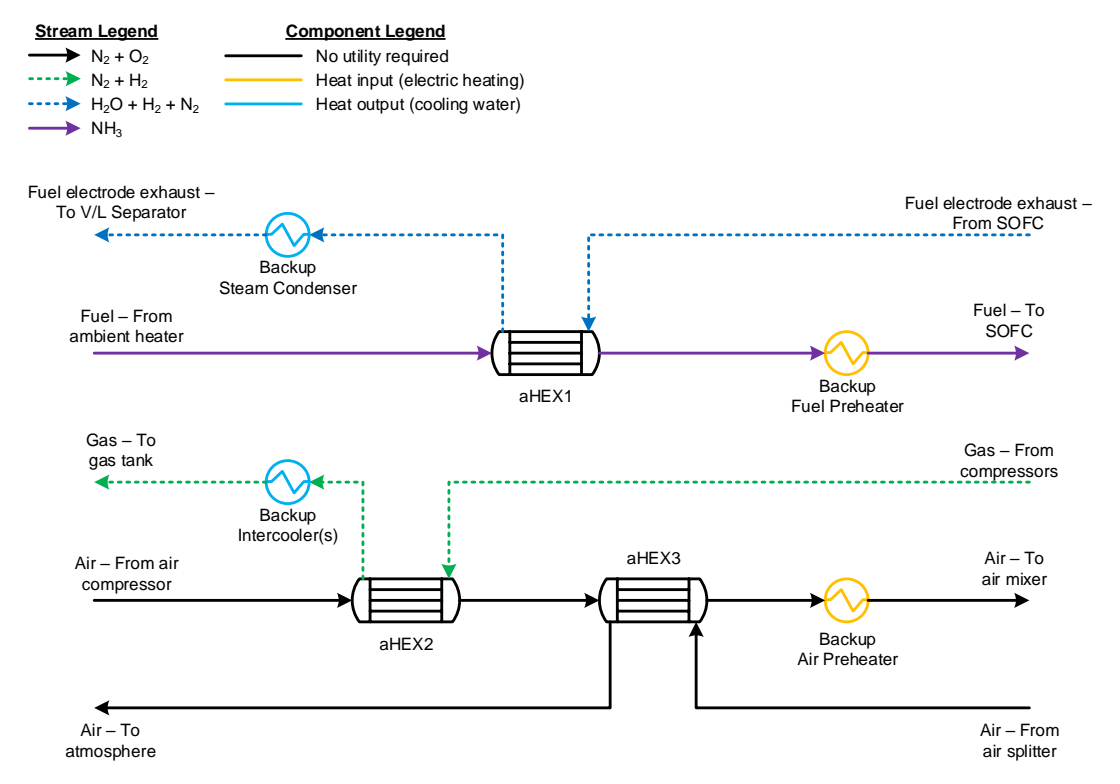


Figure 6.8: Process flowsheet for fuel cell mode - Improved cold turbine configuration.

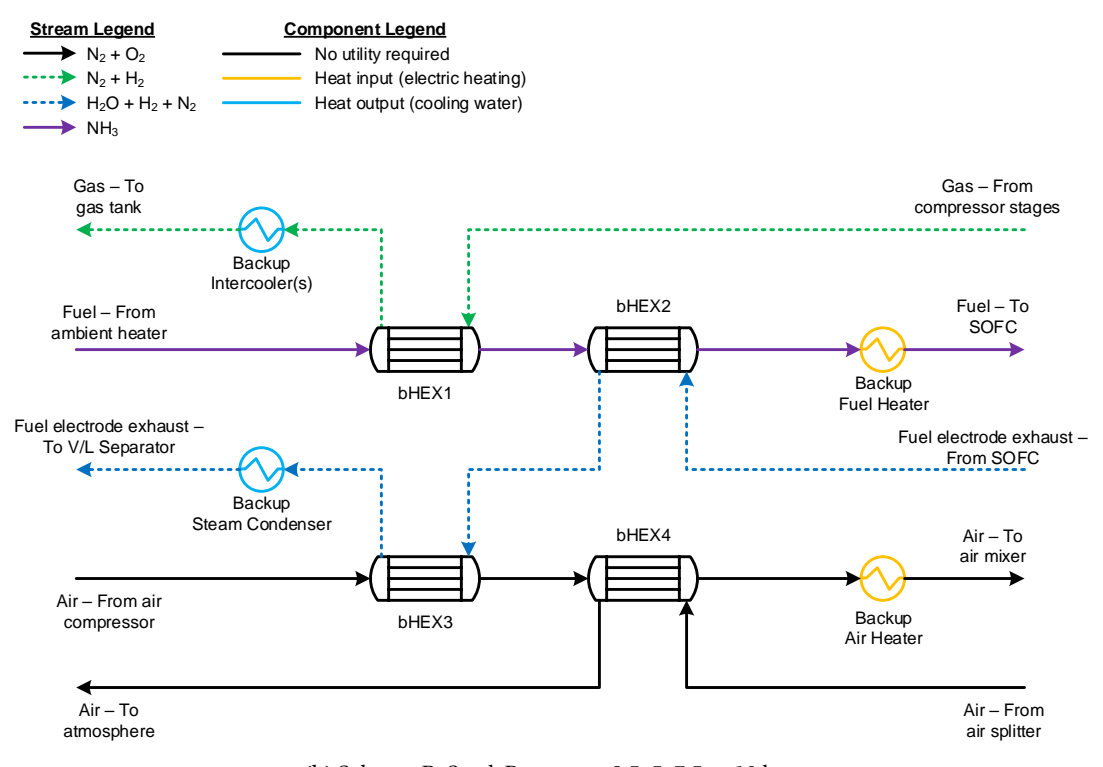
Design of Heat Integration Scheme

In the cold turbine configuration, the air heat exchanger was to be placed upstream from the turbine. Since the heat extracted from the air exhaust would reduce the turbine inlet temperature (TIT) of the air turbine in this configuration, it was desirable to use the minimum amount of heat possible from the air exhaust while also avoiding electric heating. Therefore, the air-to-air heat exchanger (aHEX3 in Fig. 6.9a or bHEX4 in Fig. 6.9a) was placed downstream of all other heat exchangers, to be used only if required, to take the fresh air to high temperatures. This meant that low temperature heat was now needed to heat the fresh air before the air-to-air heat exchanger, and therefore the heat from the multi-stage compressor intercoolers was also integrated. The location where the intercooler heat is used is the main difference between the two heat integration schemes A and B. The streams from all four intercoolers were combined into one stream for simplicity, but the combined stream properties were assigned as conservative approximations (i.e. the combined stream was assigned the lowest temperature from among the four intercooler streams, and the lowest heat capacity multiplied by four, was assigned as the heat capacity of the combined stream).

The first scheme considered (Scheme A) is shown in Figure 6.9a, where the intercooler heat was used to preheat the air in aHEX2. But the intercooler heat was limited to 250 °C as per the design of the multistage compressor. Therefore, aHEX2 could only heat the fresh air to such low temperatures. Additionally, the cold air temperature from the air compressor increased with stack pressure while the intercooler temperature from the nitrogen-hydrogen gas compression decreased with stack pressure, thus increasing the chance of



(a) Scheme A: Stack Pressure = 1.5 bar.



(b) Scheme B: Stack Pressure = 2.5, 5, 7.5 or 10 bar.

Figure 6.9: Heat integration schemes for fuel cell mode - Improved cold turbine configuration.

an adverse temperature gradient in aHEX2. Therefore, this scheme A was preferably not used, especially at higher pressures.

The alternate scheme (Scheme B) is shown in Figure 6.9b. Here, the intercooler heat was used to preheat the fuel in bHEX1. In this way, the heat extracted from the fuel electrode exhaust in bHEX2 could be reduced, and the fuel electrode exhaust coming from bHEX2 was found to be available at temperatures higher than 250 °C. This made it possible to preheat the air to higher temperatures in bHEX3 than would be possible in aHEX2. Therefore, Scheme B was more preferable.

However, at very low stack pressures (1.5 bar), it was found that steam in the exhaust would start to condense midway through bHEX3, thus creating adverse temperature gradients inside. Therefore, the use of scheme B was problematic for low stack pressure. Therefore, scheme A was used only for stack pressure of 1.5 bar, while scheme B was used for all other pressures.

In each scheme, backup heaters and coolers were placed at the end of each stream (except air exhaust) in order to take the streams to the desired temperature if heat integration was insufficient.

6.2.1. Methodology

The methodology used for studying this configuration was identical to the one used for hot turbine configuration. The parameters varied included the stack temperature, stack pressure, and current density. The values tested for each parameter are as follows:

Stack Temperature $650\,^{\circ}$ C, $700\,^{\circ}$ C, $750\,^{\circ}$ C, $800\,^{\circ}$ C

Stack Pressure 1.5 bar, 2.5 bar, 5 bar, 7.5 bar, 10 bar

Current Density 2500 Am⁻², 5000 Am⁻², 7500 Am⁻², 10000 Am⁻²

For each combination of the above parameters, air recirculation ratio was varied till the optimum efficiency was obtained for that operating point.

The effect of varying each of these parameters is studied in the following sections.

6.2.2. Effect of Air Recirculation Variation

The primary effects of air recirculation, as mentioned before, are a reduction in the fresh airflow and a reduction in the air preheating temperature.

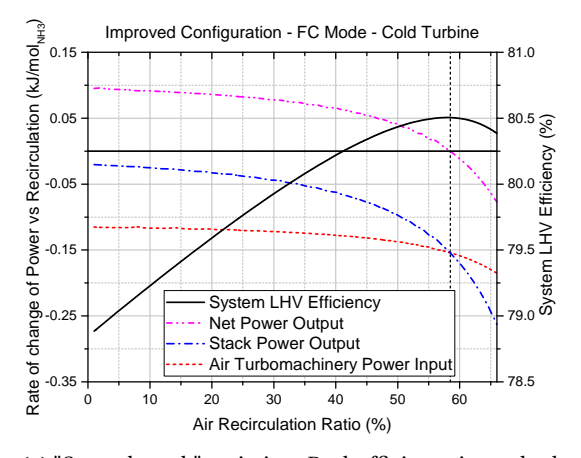
First, the system is analysed from an energy perspective. In the cold turbine configuration, there was always enough heat available from the stack air exhaust to preheat the fresh air stream. Similarly, the fuel electrode exhaust was also able to heat the fuel feed stream at all points. Therefore, the electric preheating for the feed streams was completely eliminated in this configuration, without requiring air recirculation.

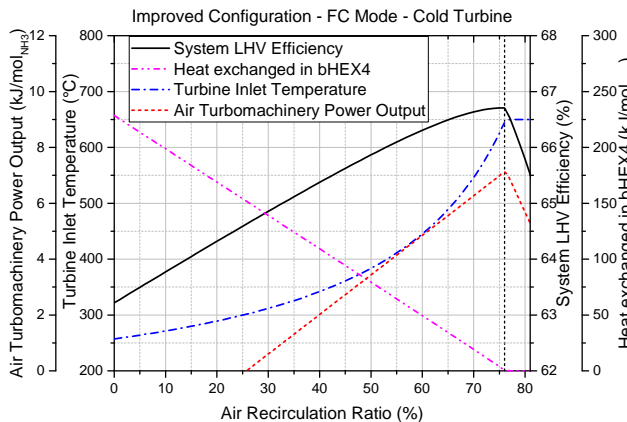
However, in the cold turbine configuration, due to the low TIT, the air turbine was able to extract less power than the air compressor needed, leading to a net power demand from the air turbomachinery. When the air recirculation was increased, the net power demand of the air turbomachinery reduced due to two complementary factors. Firstly, the airflow through the entire air turbomachinery reduced. Secondly, the required air preheating temperature went down, which also means less heat was extracted from the air exhaust. This increased the inlet temperature of the air turbine, increasing the turbine specific power output. The compression power for air recirculation was insignificant in comparison. In some cases, the TIT became high enough that the air-side turbomachinery started producing net power output.

On the other hand, as already discussed for the hot turbine configuration, the stack power output also went down with increasing air recirculation. The reduction in stack power was not linear, but accelerated as the recirculation increases.

The optimum air recirculation could be reached in two possible ways. In most cases, the rate of reduction in the stack power output tended to overtake the rate of reduction in turbomachinery power input at some recirculation value. This is shown in Figure 6.10a, which plots the rate of change of the power of various components for every %-point increase in recirculation. Since this phenomenon appears as a smooth peak on the efficiency curve, this will be referred to as "smooth peak" hereafter in this chapter.

In some other situations, the optimum air recirculation is reached differently. In these cases, usually the TIT was high enough that the turbomachinery produces net power. As the recirculation was increased, the fresh air preheating demand would become so low that no heat was required to be exchanged in bHEX4. This meant that the TIT of the air turbine reached its maximum value and stagnated, stopping the rise in the turbomachinery power output. If the recirculation was increased beyond this point of TIT stagnation,





(a) "Smooth peak" variation: Peak efficiency is reached when the rate of change of stack and turbomachinery power cancel each other, and rate of change of the net system power output is zero. Stack parameters used in this example: $800\,^{\circ}$ C, $7.5\,\text{bar}$, $5000\,\text{Am}^{-2}$.

(b) "Sharp peak" variation: Peak efficiency is reached when no heat is exchanged in bHEX4, and maximum turbine inlet temperature is reached. Stack parameters used in this example: 650 °C, $2.5\,\mathrm{bar}, 5000\,\mathrm{Am}^{-2}.$

Figure 6.10: Effect of air recirculation on system performance - Energy analysis.

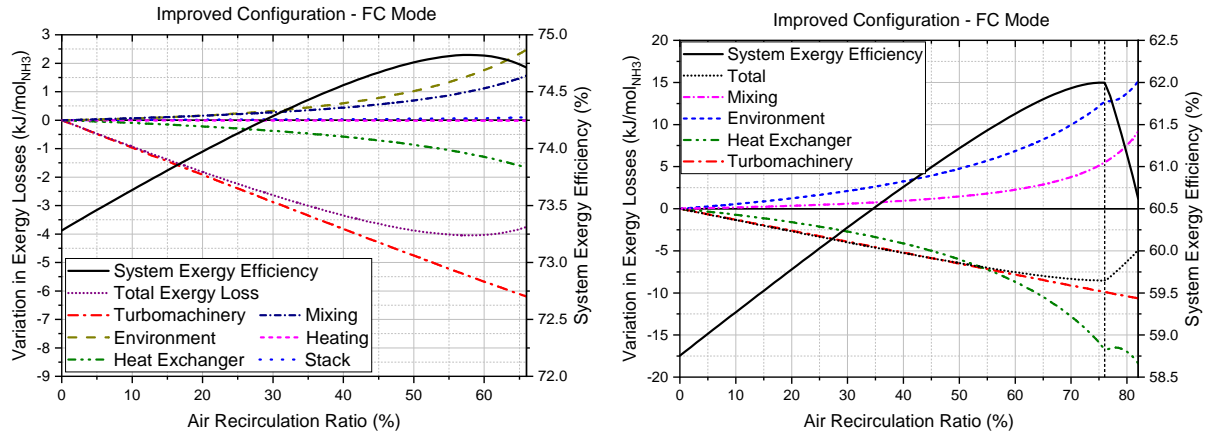
the reducing airflow lowered the turbomachinery output. Along with the reducing stack power output, this sharply dropped the efficiency after this point. This situation occurs at higher recirculation ratios than the former scenario, when the turbine power gains are large enough to overcome the losses in stack power. This is shown in Figure 6.10b. Since this phenomenon appears as a sharp peak on the efficiency curve, this will be referred to as "sharp peak" hereafter in this chapter.

The "smooth peak" variation usually occurred when the stack efficiency was high, i.e. high stack temperature and/or low current density. Accordingly, the "sharp peak" occurred when the stack efficiency was very low, i.e. low temperature and high current density. The reason for this can also be explained from the energy analysis. Firstly, it must be noted that the fresh and exhaust airflows reduce linearly with recirculation ratio, for a given airflow through the stack. The slope of this linear trend is higher if the stack inlet airflow is higher (see Appendix C for details). Accordingly, the rate of change of turbomachinery power is also approximately proportional to the total stack airflow. Lastly, the rate at which recirculation leads to reduction in the oxygen content of the air through the stack also depends on the total stack inlet airflow. Oxygen content reduces faster with recirculation if the total stack inlet airflow is low (see Appendix C for details). This would imply that the Nernst voltage (and hence, stack power output) also reduces faster if the total stack inlet airflow is low.

When the stack was more efficient, the total airflow through the stack was low. Therefore, the rate of reduction of turbomachinery power input was also low. Meanwhile, the rate of reduction of oxygen content in the air was high. Therefore, the stack power output would reduce at a faster rate, overtaking the turbomachinery benefits sooner, i.e. at a lower air recirculation ratio, before the air turbine inlet temperature reached its maximum. This would result in a "smooth peak". On the other hand, when the stack was less efficient, the airflow required through the stack was high. This meant that the rate of change of turbomachinery power input with respect to recirculation was high. But the higher airflow meant that the oxygen content would reduce at a lower rate, and thus the losses in stack power output would not catch up to the turbomachinery power gains fast enough. At a high enough recirculation ratio, the air turbine would reach its maximum inlet temperature before the stack losses could catch up, thus resulting in a "sharp peak".

From an exergy perspective, the driving forces behind the variation of performance are very different. While the stack power reduction was one of the major factors in energy analysis, the exergy destruction in the stack did not vary too much, since the recirculation does not affect overpotentials as much as it affects the Nernst voltage. The biggest exergy factor leading to the performance improvement was the reduction in exergy destruction in turbomachinery, caused by reducing airflow. Exergy destruction in heat exchangers also fell, as the heat duty of the air-side heat exchangers reduced. However, this was approximately compensated by additional exergy losses by mixing the hot recirculated air with the relatively colder fresh air. As the TIT increased while the pressure ratio remained constant, the temperature of the exhaust air also increased, leading to larger exergy losses to the environment, despite lower flow rate of air. The optimum air recirculation

occurred when the rate of increase of environment losses overtook the rate of decrease of turbomachinery losses.



- (a) Stack parameters used in this example: 800 $^{\circ}\text{C}, 7.5\,\text{bar}, 2500\,\text{A}\,\text{m}^{-2}.$
- (b) Stack parameters used in this example: $650\,^{\circ}$ C, $2.5\,\text{bar}$, $5000\,\text{A}\,\text{m}^{-2}$.

Figure 6.11: Effect of air recirculation on system performance - Exergy analysis.

Now we come to the other situation, where the turbine reached maximum TIT. Figure 6.11b shows the variation of exergy losses in this case. Before the maximum TIT was reached, the trends of losses were the same as the smooth peak case. This changed once the maximum TIT was reached as the heat transfer in bHEX4 reached zero.

Since this situation occurred at higher recirculation ratios, the mixing losses were found to be increasing very rapidly as the preheated air was being mixed at lower and lower temperatures. Like the efficiency plot, the exergy losses also show a sharp discontinuity where the maximum TIT was reached. As soon as the TIT was reached, bHEX4 became completely inactive, and the exit temperature of the fuel electrode exhaust coming from bHEX3 started rising, since the pinch point was no longer the limiting factor in the heat exchange. Initially, the average temperature difference in bHEX3 rose faster than the heat transfer decreased, hence the momentary rise in exergy destruction. Thereafter, the heat transfer in bHEX3 fell rapidly, reducing the exergy destruction once more. At the point the TIT reached the maximum, the rise of environment losses slowed down, since the exhaust temperature of air was no longer rising. Thereafter, the rising exit temperature of exhaust from bHEX3 dominated the rise in environment losses.

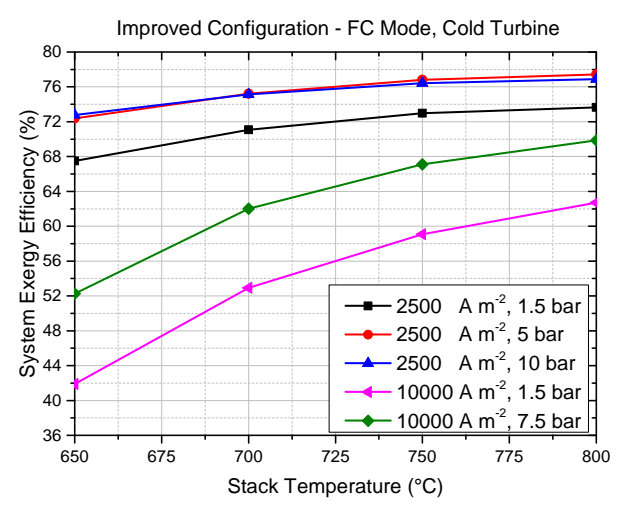
After this point, the environment losses rose faster than the fall in heat exchanger losses. Moreover, the rise in mixing losses was also far greater than the reduction in turbomachinery losses. All these factors together led to a sharp fall in efficiency after this point.

6.2.3. Effect of Stack Temperature Variation

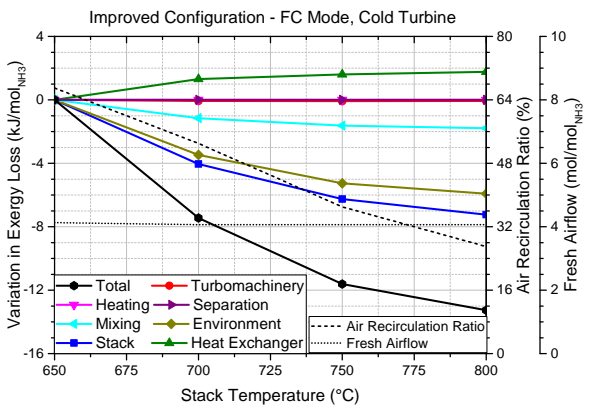
Figure 6.12 shows an example of the variation of system performance in fuel cell mode, in the cold turbine configuration. As shown by Figure 6.12a, the system exergy efficiency was found to monotonically increase with rising stack temperature. This was found to be the case for all 20 combinations of current density and stack pressure, some of which are shown in the figure.

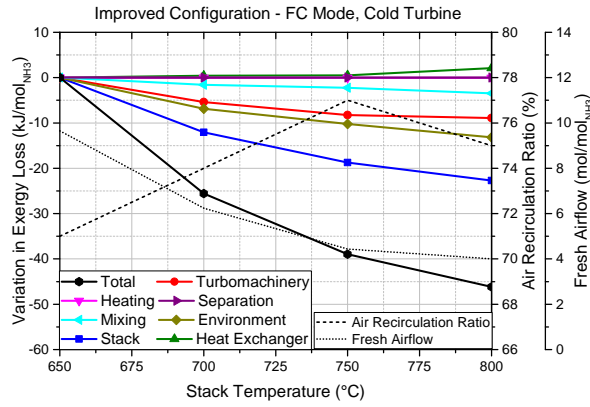
Figure 6.12b shows the trends of airflow and exergy losses as a function of stack temperature, in those cases where the efficiency has a smooth peak. As mentioned in Section 6.2.2, when the stack was more efficient, the reduction in stack power increased quickly, leading to the smooth peak phenomenon at lower optimum recirculation ratios. Similarly, when the stack temperature was increased, there was a decrease in stack inlet airflow, as well as the optimum air recirculation ratio. The fresh airflow depends on both the stack inlet airflow as well as on the recirculation. An interesting observation is that in the smooth peak case, the optimum fresh airflow remained almost independent of temperature. The precise reason for this could not be found at the time of writing, but it can be taken up as future work.

Now coming to the exergy losses, as discussed, the losses in the stack reduced as temperature increases. Since the recirculation decreased while having the same fresh airflow, it implies that the heat transfer relied more on heat exchangers and less on mixing. The exergy destruction in those two components varied accordingly, increasing for heat exchange, and decreasing for mixing. On a related note, since the heat transfer relied



(a) Variation of exergy efficiency for various operating points.





- (b) Variation of exergy losses: smooth peak operating points. Stack operating parameters used in this example: $2500\,\mathrm{Am}^{-2}$, $5\,\mathrm{bar}$
- (c) Variation of exergy losses: sharp peak operating points. Stack operating parameters used in this example: $10\,000\,\mathrm{A\,m^{-2}}$, 7.5 bar

Figure 6.12: Variation of fuel cell system performance with stack temperature, in cold turbine configuration. Exergy loss values in the plots are differential, with first point of each graph as datum.

more on heat exchange with the exhaust air, the turbine inlet (and outlet) temperature for the air turbine declined, leading to lower losses to the environment. Since the fresh airflow was constant, the exergy losses in turbomachinery were constant too. The electric heating of air was eliminated in all cases, therefore exergy losses in heating were also negligible and constant.

Overall, the large decline in stack losses and environment losses led to an overall increase in efficiency with temperature for the smooth peak cases.

On the other hand, Figure 6.12c compares the same values, for cases with sharp efficiency peaks. The trends of fresh airflow and recirculation in this case was similar to the hot turbine configuration, i.e. falling airflow and rising recirculation. This was because, in the HT configuration, the maximum efficiency had been obtained when the electric heater reached zero duty, whereas in this case (CT configuration), maximum efficiency was obtained when the amount of heat transferred in bHEX4 reached zero. These are analogous conditions.

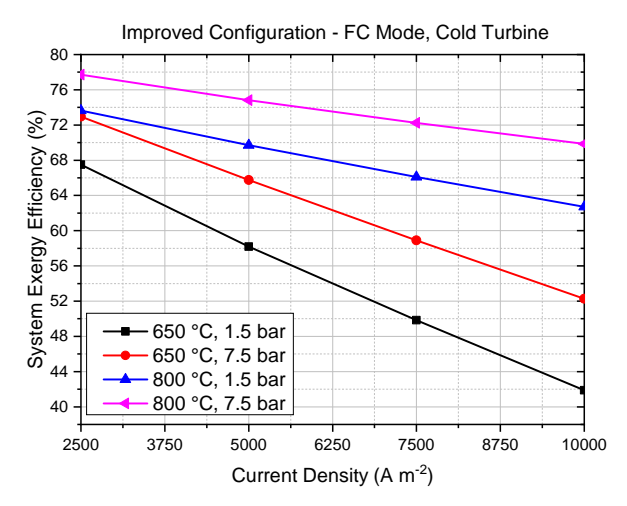
The stack losses decreased with rising stack temperature, as expected. As the fresh airflow decreased, so did the exergy losses in turbomachinery. The turbine inlet temperatures were, of course, equal to the stack temperature in the sharp peak cases. Therefore, the turbine exhaust temperatures were almost the same too, and the falling airflow ensured that the exergy losses to the environment from exhaust declined as well. While higher stack temperature implies more heat transfer requirement, the heat exchanger losses did not increase much, since the fresh airflow was reducing. Similarly, mixing losses also decreased despite increasing recircu-

lation, since the total airflow was reducing as well.

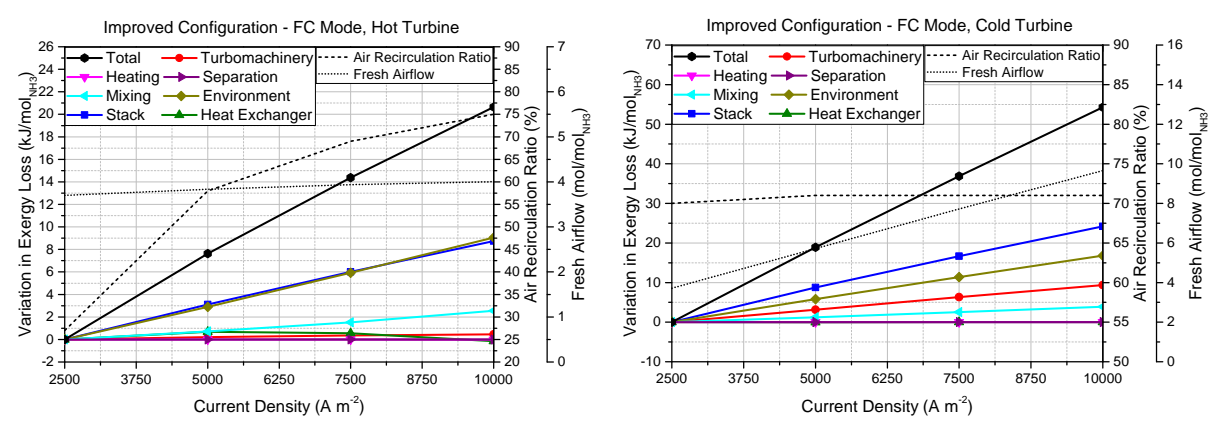
Overall, for operating points with sharp peaks, all exergy losses declined, or stayed constant, leading to better efficiency at higher temperatures.

6.2.4. Effect of Current Density Variation

Figure 6.13a shows the variation of system efficiency with current density. This configuration followed the familiar pattern seen in the basic and hot turbine configurations; the efficiency linearly declines with current density. This was the case for all points (i.e. both smooth peak and sharp peak).



(a) Variation of system exergy efficiency for various operating points.



- (b) Variation of exergy losses: smooth peak operating points. Stack operating parameters used in this example: $800\,^{\circ}\text{C}$, $7.5\,\text{bar}$
- (c) Variation of exergy losses: sharp peak operating points. Stack operating parameters used in this example: $650\,^{\circ}\text{C}$, $7.5\,\text{bar}$

Figure 6.13: Variation of fuel cell system performance with current density, in cold turbine configuration. Exergy loss values in the plots are differential, with first point of each graph as datum.

Figure 6.13b shows the exergy loss and airflow variation with current density, for the smooth peak points. The variation of fresh airflow in this case was similar to that found for the temperature variation case in the previous section. As the stack became less efficient at higher current densities, the optimum air recirculation ratio increased, alongside the increase in the total stack inlet airflow. The fresh airflow in this case also remained independent of current density, just like the case for temperature variation, and the explanation for this can also be taken up in the future.

Coming to the exergy losses, as mentioned in Section 6.2.2, when the recirculation increased, the air exhaust temperature also increased, causing the losses to the environment to increase. Similarly, the increase in recirculation caused more exergy destruction in mixing. The turbomachinery losses did not increase since the airflow and the was constant. Overall, since all the losses either increased or remained constant, the system

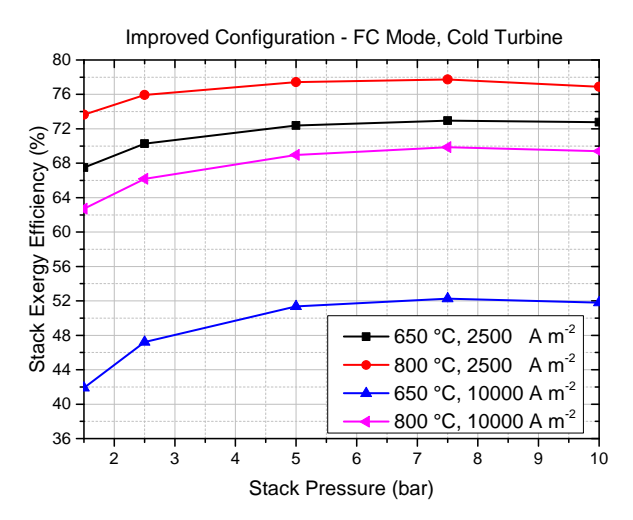
efficiency decreased with current density.

Figure 6.13c shows the exergy loss and airflow variation with current density, for the sharp peak points. In this case, the optimum fresh airflow increased at higher current density. This was similar to the case with the hot turbine configuration.

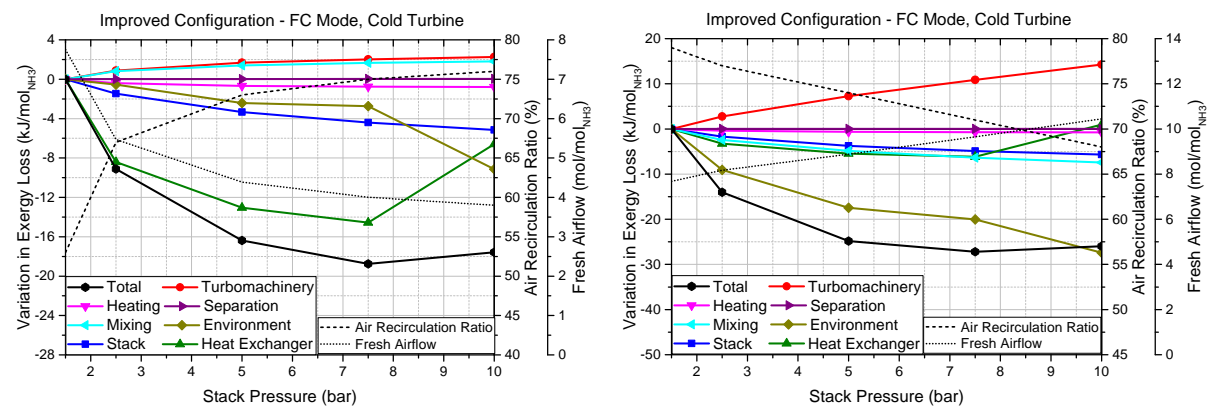
The stack losses losses increased linearly, as expected. The increase in fresh airflow caused a linear increase of all the associated losses: turbomachinery, mixing and losses to the environment through air exhaust. These losses remained relatively constant on a per mole basis, except for minor variations from the composition of the air. The heating losses remained constant, since electric heat was used only for the water desorption. The change in exergy destruction in heat exchangers was also negligible, since the losses were already small to begin with. Overall, since all the losses either increased or remained constant, the system efficiency decreased with current density.

6.2.5. Effect of Stack Pressure Variation

The effect of pressure variation in cold turbine configuration was the same as that in hot turbine configuration: an initial increase in system efficiency followed by a gradual decrease at higher pressures, as shown in Figure 6.14a.



(a) Variation of system exergy efficiency for various operating points.



(b) Variation of exergy losses: smooth peak operating points. Stack operating parameters used in this example: $800\,^{\circ}\text{C}, 10\,000\,\text{Am}^{-2}$

(c) Variation of exergy losses: sharp peak operating points. Stack operating parameters used in this example: $650\,^{\circ}$ C, $10\,000\,\mathrm{A\,m^{-2}}$

Figure 6.14: Variation of fuel cell system performance with pressure, in cold turbine configuration. Exergy loss values in the plots are differential, with first point of each graph as datum.

Figure 6.14b shows the effect of pressure on exergy losses, for the points with a smooth peak. The trends of most of the losses were same as the hot turbine configuration (See Section 6.1.5), with a few differences. The

major difference in the two was the loss to environment, which increased with pressure in the hot turbine configuration, but decreased with pressure in the cold turbine configuration. In the cold turbine configuration, since most of the heat integration is carried out from the fuel electrode exhaust, and not from air electrode exhaust, the air exhaust temperature was relatively high. As the pressure rose, the airflow reduced, reducing the heat extraction from the exhaust further. However, this was compensated by the increasing temperature drop caused by the turbine placed after bHEX4. Ultimately, the air exhaust temperature remained approximately constant, and the reduced airflow led to reduced losses to the environment. Apart from this, lower heat extraction from the fuel electrode exhaust in bHEX3 also increased the environment losses, but to a lesser extent. Therefore, the overall environment losses reduced with pressure, but slowly. The discontinuities in heat exchanger and environment losses between 7.5 bar and 10 bar have already been explained before in Section 6.1.5.

Figure 6.14c shows the trend of exergy losses in the case of sharp peak points. Note that while the stack became more efficient and the total stack inlet airflow decreased, the fresh airflow actually increased with rising pressure for these points. The optimum fresh airflow and recirculation corresponds to zero heat transfer in bHEX4. At higher pressure, the compressor outlet temperature increased. Since the limiting stream in bHEX3 was the hot one, a higher inlet temperature for the cold stream meant that the larger cold stream flow rate could be tolerated in bHEX3. Therefore, the optimum fresh airflow at higher pressures was higher, and the corresponding air recirculating was lower.

Most of the major loss trends (environment, heat exchange) remained the same as the smooth peak points, but with different relative magnitudes. Since both the specific work of the turbomachinery and the fresh airflow increased with pressure, the turbomachinery exergy destruction increased quite quickly with pressure. As the recirculation ratio decreased, the mixing losses decreased too.

6.2.6. Conclusions of the Cold Turbine Configuration Analysis

- The peak system exergy efficiency attained with this improved cold turbine configuration was 77.73 %, compared to 52.47 % in the basic configuration. This occurred at the operating point of 800 °C, 7.5 bar and $2500\,\mathrm{A\,m^{-2}}$.
- Air recirculation played an important role in maximising the system efficiency. In this configuration, air recirculation reduces the air compressor power, and increases the TIT of the air turbine, thus reducing the net turbomachinery power input.
- Higher temperature is always beneficial for the performance of this configuration.
- The optimum stack pressure for this configuration was approximately 7.5 bar.
- Lower current density is always favourable in this configuration.

6.3. Fuel Cell Mode - Comparison of Hot and Cold Turbine Configurations

In this section, the two configurations designed for the fuel cell mode are compared, to see whether it is more beneficial to devote the stack exhaust for fresh air preheating, or to produce power more from the air turbine.

In Figure 6.15, the performance of the two improved fuel cell configurations are compared, for all the 80 stack operating points tested. The figures clearly show that the cold turbine configuration performed poorly in comparison with the hot turbine configuration, with an average efficiency difference of 3.7 %-points, and a maximum difference as high as 12.4 %-points. The only exceptions were 4 operating points in the very high efficiency region (highlighted in the graph for $2500\,\mathrm{A\,m^{-2}}$). The only reason cold turbine configuration performed slightly better at these points is because the hot turbine configuration was heavily handicapped in that region, because it reached the maximum allowed air recirculation defined by the oxygen starvation limit. Additionally, in general, the efficiency difference between the two configurations was smaller when the stack was operating at higher pressure.

Upon carrying out an exergy analysis of the differences in the two configurations, it was seen that the exergy losses in the cold turbine configuration were on average $9.59\,\mathrm{kJ/mol_{NH_3}}$ larger. The exergy losses in the two configurations are compared at different pressures in Table 6.1. It can be seen that the exergy losses to the environment contribute significantly to the difference of total exergy losses between the configurations. Exergy destruction in heat exchangers, mixers and turbomachinery also play a smaller role.

However, the detailed trends of exergy loss each component do not present a very clear picture at this stage. Therefore, more analysis is needed, which can be taken up as future work. Nevertheless, this study of hot and cold turbine fuel cell configurations results in a clear observation that the hot turbine configuration is preferable for the vast majority of operating points, except a few points at the lowest current densities.

Parameter	Unit	Point 1 (lov	w pressure)	Point 2 (high pressure)		
Parameter	Onit	HT Config.	CT Config.	HT Config.	CT Config.	
Stack temperature	°C	700		700		
Stack pressure	bar	2.5		7.	.5	
Current density	$\mathrm{Am^{-2}}$	75	00	7500		
Fresh air flow	mol/mol _{NH3}	11.22	5.50	6.30	5.10	
Air Recirculation	%	41	74	66	74	
Net power output	kJ/mol _{NH3}	181.65	163.31	178.32	174.09	
Stack output	kJ/mol _{NH3}	175.31	173.61	179.53	178.69	
Turbomachinery input	kJ/mol _{NH3}	-6.89	4.41	0.85	9.77	
Heating input	kJ/mol _{NH3}	0.54	0.19	0.35	0.53	
Total exergy losses	kJ/mol _{NH3}	80.72	99.07	84.05	88.29	
ReSOC stack	kJ/mol _{NH3}	37.19	37.24	34.19	34.21	
Expansion & Compression	kJ/mol _{NH3}	11.61	7.56	12.29	10.40	
Heat exchange	kJ/mol _{NH3}	4.17	7.43	2.69	3.10	
Electric heating	kJ/mol _{NH3}	0.59	0.50	0.24	0.16	
Mixing	kJ/mol _{NH3}	1.02	4.32	2.53	3.86	
Separation	kJ/mol _{NH3}	0.18	0.18	0.19	0.19	
Environment	kJ/mol _{NH3}	25.97	41.83	31.92	36.37	
System energy efficiency	%	74.49	66.97	73.13	71.39	
System exergy efficiency	%	69.23	62.24	67.96	66.35	

Table 6.1: Comparison of HT and CT configurations through energy and exergy analysis.

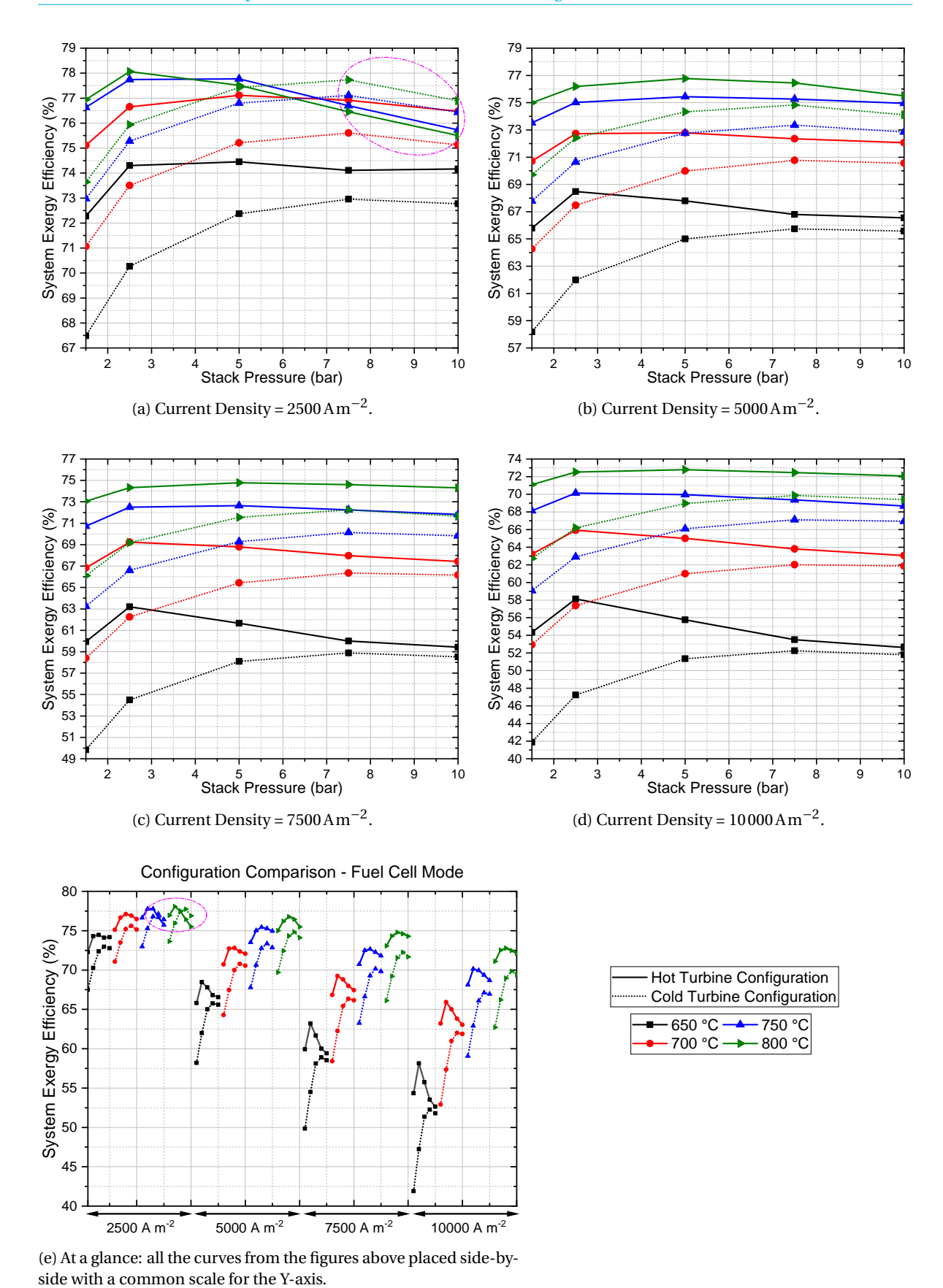


Figure 6.15: Efficiency comparison of hot and cold turbine configurations in fuel cell mode.

6.4. Electrolysis Mode - Hot Turbine Configuration

In this section, the improvement of the basic configuration in electrolysis mode is undertaken. Once again, the hot turbine configuration is undertaken first, where the air turbine is placed upstream of the recuperation heat exchanger. Figure 6.16 shows the system flowsheet for this configuration in electrolysis mode. The red dashed arrows show the heat flow for each heat exchanger in the integrated system. The heat integration scheme is shown in greater detail in Figure 6.17. Note that a high temperature electric heater was added just before the stack air inlet, which could not be integrated with any other stream. This was because its purpose was to heat the air above stack temperature in the endothermic operating region, and no other hot stream would be available for integration at that temperature.

6.4.1. Design of Heat Integration Scheme

Figure 6.17 shows the detailed configuration of the heat integration scheme. Most of the heat exchangers (HEX1 to HEX8) are required for preheating, evaporating, and superheating the feed water for the electrolysis. The large number of heat exchangers is because most of the hot streams available for integration have little heat available compared to the significant latent heat of the water. Therefore, many small hot streams together are required to generate the superheated steam required for electrolysis.

Additionally, the final stage product stream of the ammonia synthesis reactor is used to preheat the synthesis feed stream in HEX9, after providing some heat for water evaporation in HEX4. The heat extracted in HEX4 was limited so that the synthesis feed could be fully heated to the required temperature in HEX9. A significant part of the heat of the ammonia synthesis reactor is used to evaporate the water, via the two reactor intercoolers, represented by HEX5 and HEX6. These two observations about the heat integration from ammonia synthesis justify the assumption about heat integration that was made while choosing the synthesis loop parameters in Section 4.4.4.

The preheating of the air was considered to be of secondary importance in electrolysis mode compared to heating of the water/steam, and therefore, only one heat exchanger (HEX10) was provided for this purpose. Backup heaters and coolers were placed at the end of each stream (except air exhaust) in order to take the streams to the desired temperature if heat integration was insufficient.

6.4.2. Methodology

The methodology used for studying this configuration was identical to the one used for the fuel cell mode configurations. The parameters varied included the stack temperature, stack pressure, and current density. The values tested for each parameter are as follows:

Stack Temperature 650 °C, 700 °C, 750 °C, 800 °C

Stack Pressure 1.5 bar, 2.5 bar, 5 bar, 7.5 bar, 10 bar

Current Density 2500 Am⁻², 5000 Am⁻², 7500 Am⁻², 10000 Am⁻²

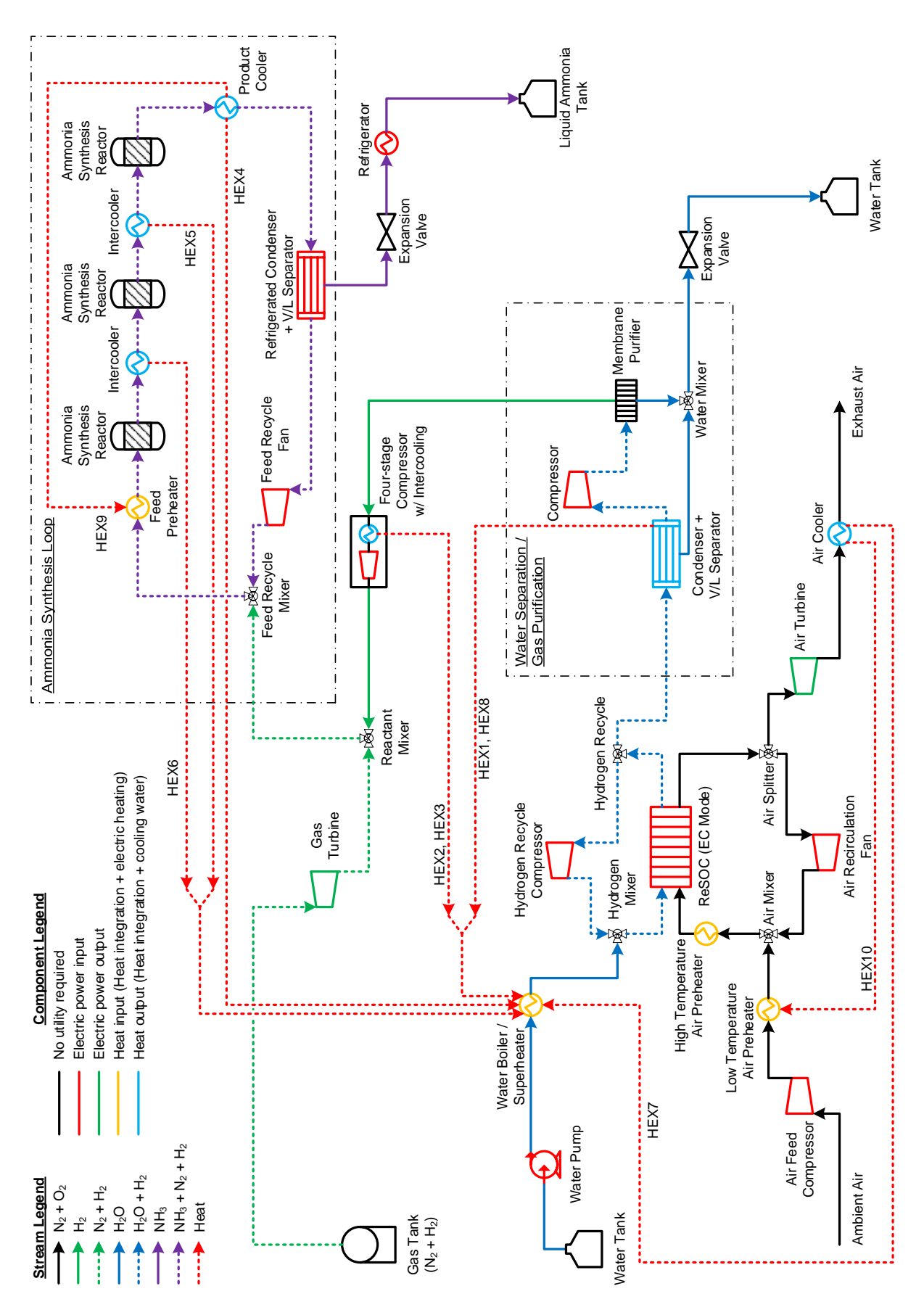
For each combination of the above parameters, air recirculation ratio was varied till the optimum efficiency was obtained for that operating point.

The effect of varying each of these parameters is studied in the following sections.

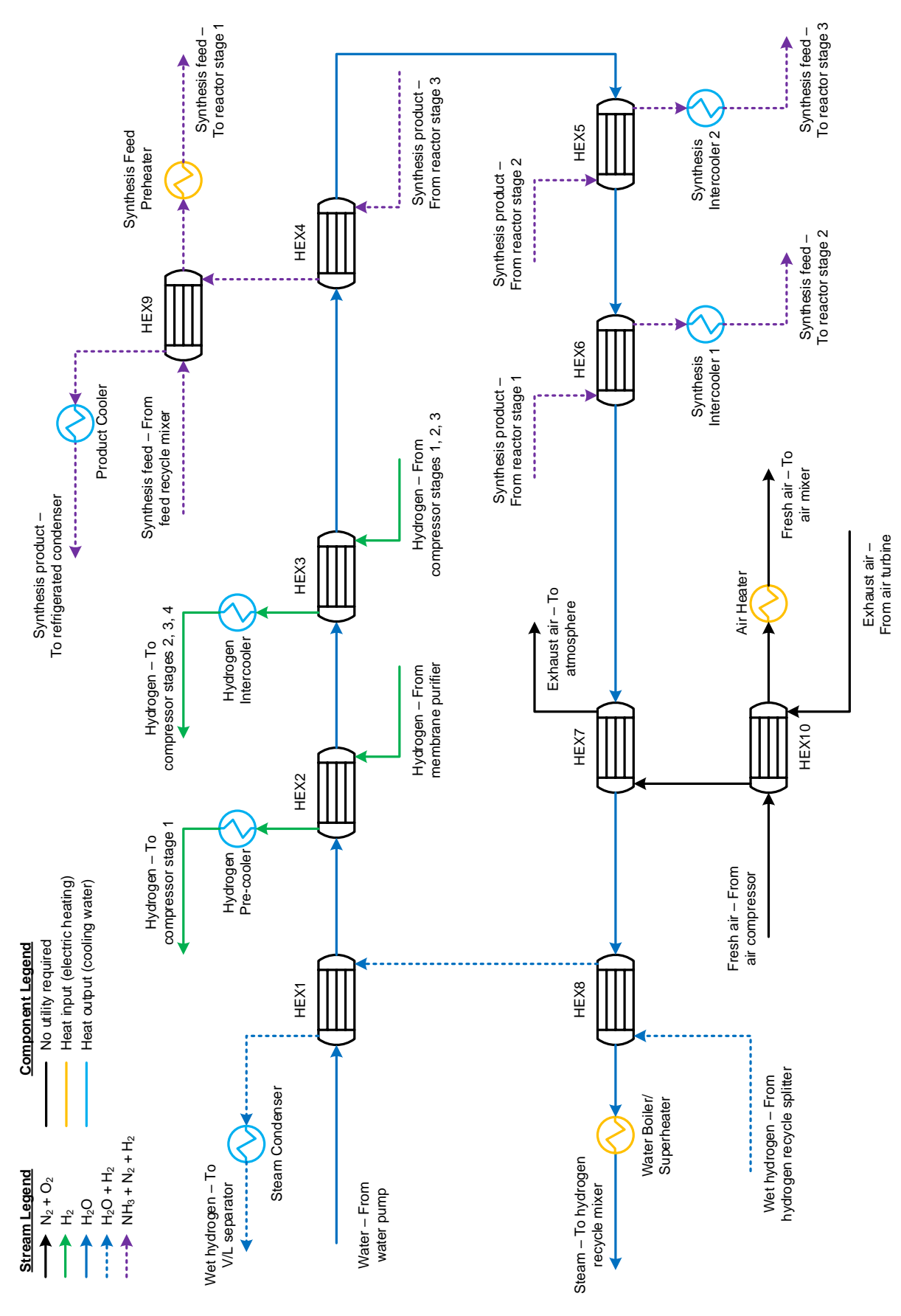
6.4.3. Effect of Air Recirculation Variation

When the electrolysis stack was operated in exothermic region, the air recirculation variation had exactly the same effects as observed in the fuel cell hot turbine system (except the rare effects relating to oxygen starvation, which does not exist in electrolysis). Therefore this section will not discuss the effect of recirculation on an exothermic electrolysis system.

The effect of air recirculation on an endothermic electrolysis system is shown in Figure 6.18a from an energy perspective. The most prominent result is that the maximum efficiency occurred at a very high recirculation, when the fresh airflow was eliminated entirely. The explanation for this is based on the power required for the air heater. Since all the heat integration had to be focused on water evaporation, and since this was the hot turbine configuration, there was only a little heat available from the hot air in HEX10 for preheating fresh air. Therefore, most of the fresh air preheating had to be done electrically. This heating power demand reduced as the fresh airflow decreased due to increasing recirculation. In the exothermic electrolysis and fuel cell modes, the optimum air recirculation was reached when the electric air preheating reached zero. This could never happen in the endothermic region, since the air had to be heated above the stack temperature.



 $Figure\ 6.16:\ Process\ flowsheet\ for\ electrolysis\ mode\ -\ Improved\ hot\ turbine\ configuration.$



 $Figure\ 6.17:\ Heat\ integration\ scheme\ for\ electrolysis\ mode\ -\ Improved\ hot\ turbine\ configuration.$

Therefore, the minimum electric heating occurs when the fresh airflow is exactly zero, which was found to correspond to the optimum air recirculation value.

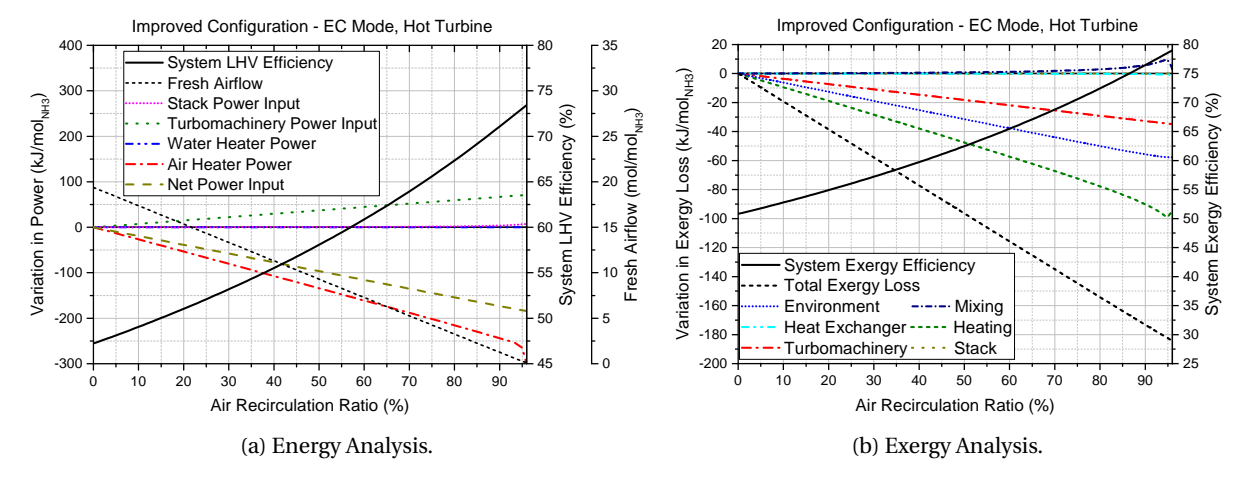


Figure 6.18: Effect of air recirculation on electrolysis system performance in endothermic region. Power / Exergy loss values are differential, with first point of each line as datum.

As mentioned before, the heating requirement of the water was entirely met by HEX1-HEX8. Despite the reducing airflow in HEX7, there was no electric power required for water heating. Just like fuel cell mode, the air-side turbomachinery acts like a Brayton cycle in hot turbine configuration, producing net power. This power reduced due to the falling airflow. However, this reduction in turbomachinery power output (alternatively shown as an increase of power input in Figure 6.18a) was much smaller than the power savings from decreasing electric air heating, resulting in a reduction in the net system power input. It must be noted that the increase in stack power input due to increasing oxygen content in the air-side channels is negligible.

The analysis from an exergy perspective is even more straightforward. As the electric heating demand fell, the exergy destruction in heating also fell proportionally. The exergy losses in the turbomachinery also reduced as the flow through the air-side turbomachinery went down while the pressure ratio and TIT were constant. The smaller airflow also reduced the losses to the environment through the air exhaust. The only loss that increase slightly was the exergy destruction in mixing of hot air with the cold fresh air. This was also be observed to fall sharply once the fresh air was eliminated, which also eliminated the mixing. This can be seen in Figure 6.18b.

Therefore, to summarise, the optimum air recirculation ratio corresponds to zero fresh airflow for an endothermic electrolysis system. This was observed to be true at all the endothermic operating points.

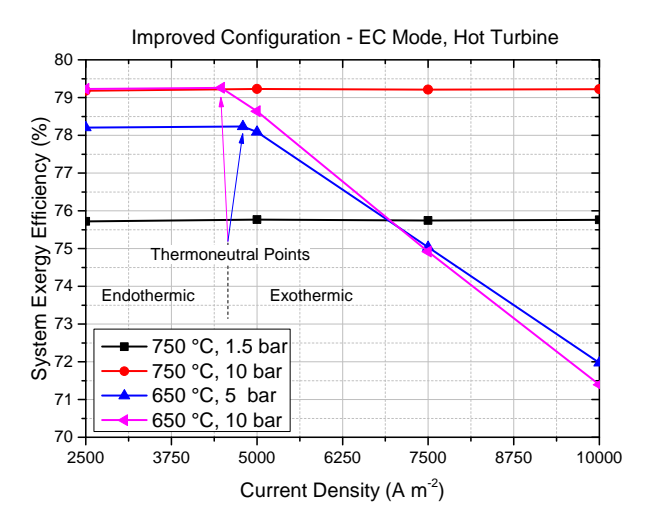
6.4.4. Effect of Current Density Variation

The effect of current density variation on electrolysis system efficiency is shown in Figure 6.19a. Two distinct trends are visible in the figure. In the exothermic region, the system efficiency decreased with rising current density. This behaviour was similar to the behaviour observed in the (always exothermic) fuel cell mode hot turbine configuration. Therefore, the explanation will not be repeated in this section; see Section 6.1.4.

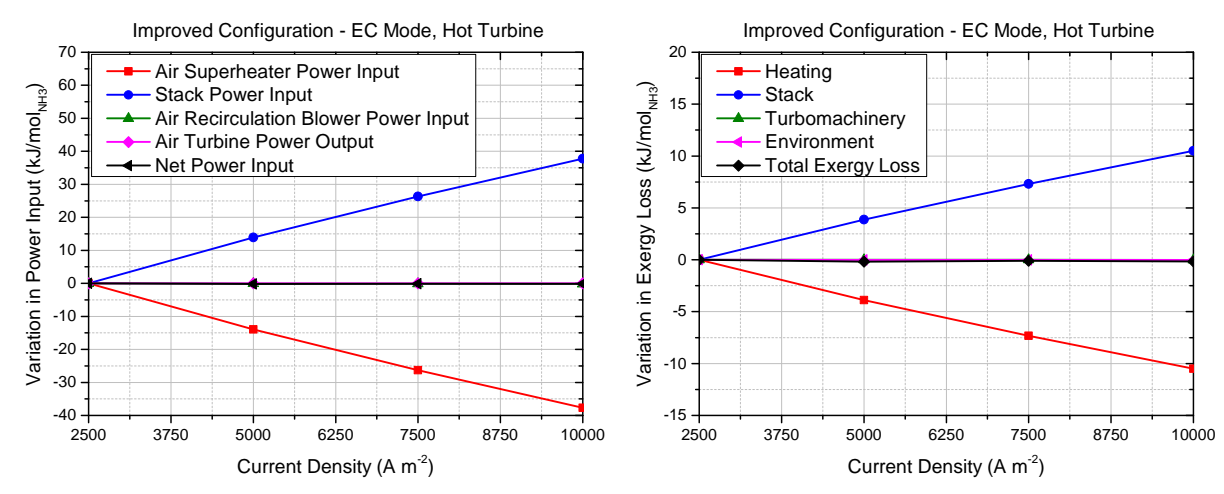
However, the most notable observation from this configuration is that the electrolysis system efficiency in endothermic region was found to be completely independent of current density. This is contradictory to the observations in the base case, where the efficiency increased with current density in endothermic region.

However, recall from Section 5.2.2 that the only way current density affected the entire system was through air-side BoP and the stack itself, with other BoP components being independent of current density. However, in the improved configuration, the fresh airflow was entirely eliminated during endothermic operation, for maximum efficiency. This meant that the only relevant components for the current density variation in endothermic region were the stack itself, the air recirculation blower, and the air superheater which provides heat for the endothermic stack. Out of the total energy required by the electrolysis reaction, a portion of this energy was provided by the electric power of the stack. Another portion was provided by the air superheater via electric heating, and a minuscule portion was provided by the friction in the stack generating heat and causing pressure drop in the stack (represented by the blower power).

Figure 6.19b compares the variation in the power input of these three components (with first point of



(a) Variation of system exergy efficiency for various operating points.



- (b) Variation of component power in endothermic region. Stack parameters used in this example: 750 °C, 10 bar.
- (c) Variation of exergy losses in endothermic region. Stack parameters used in this example: 750 °C, 10 bar.

Figure 6.19: Variation of electrolysis system performance with current density, in hot turbine configuration. The power and exergy loss values are differential, with the first point of each line as the datum.

each line as the datum). As the current density increased, the rising overpotentials caused the stack power to increase. The figure shows that the change in stack power was completely compensated by the change in superheater power (and the negligible blower power), while the net power input remained constant. This means that only the proportion of energy provided by these three components varied with the stack current density, while the total energy (normalised by amount of ammonia produced) remained the same, equal to the enthalpy change of the electrolysis reaction. The figure also shows the power output of the air turbine. Since the temperature and the (normalised) amount of oxygen generated was independent of current density, the power produced by the air turbine was also constant.

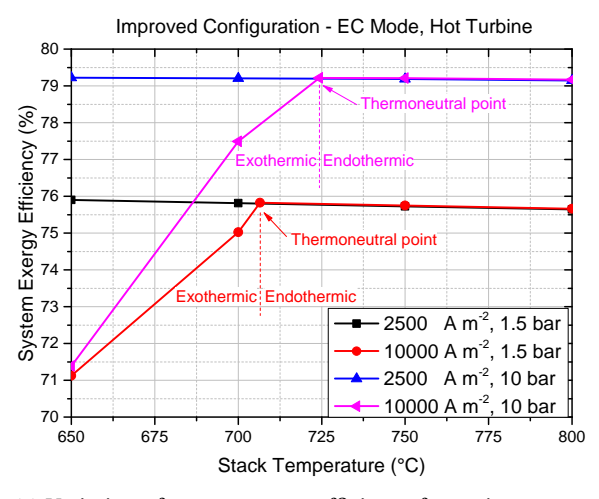
Therefore, keeping in mind that the rest of the BoP performance is not affected by the current density, and the stack and the air-side BoP were seen to compensate for changes in each other's power input, it can be understood why the system efficiency turned out to be independent of current density in the endothermic region.

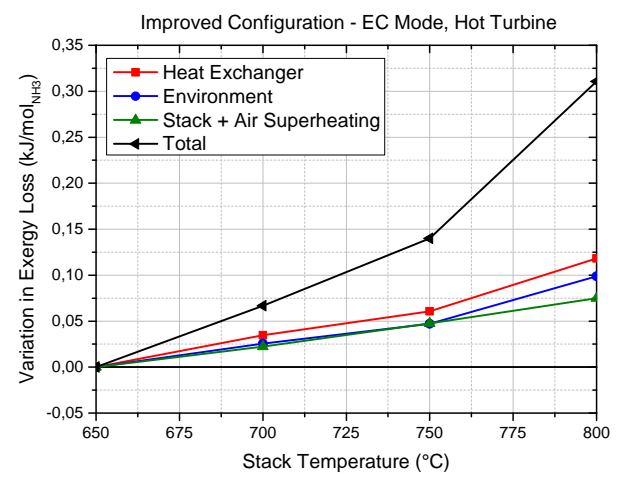
The argument from exergy analysis also runs along similar lines, shown in Figure 6.19c. As the rising current density increased the overpotentials (and therefore the exergy destruction) in the stack, the exergy destruction in the air superheater reduced by the same amount (neglecting the blower), since the inlet and outlet (normalised) flow exergy values were independent of current density. The exergy destruction in the air turbine was also independent of current density. Since the flow and temperature of the oxygen exhausted was

constant, the environment losses were also independent of current density.

6.4.5. Effect of Stack Temperature Variation

The effect of temperature variation on electrolysis system efficiency is shown in Figure 6.20a. Similar to current density variation, two distinct trends are visible in the figure. In the exothermic region, the exergy efficiency rose sharply with temperature. This behaviour is analogous to the hot turbine fuel cell mode (which is always exothermic). Therefore, the explanation will not be repeated in this section; see Section 6.1.4.





- (a) Variation of system exergy efficiency for various operating points.
- (b) Variation of exergy losses in endothermic region. Stack parameters used in this example: $2500\,\mathrm{A\,m^{-2}}$, $10\,\mathrm{bar}$. Note the small scale of the Y-axis.

Figure 6.20: Variation of electrolysis system performance with temperature, in hot turbine configuration. The exergy loss values are differential, with the first point of each line as the datum.

On the other hand, in the endothermic region, the system exergy efficiency was observed to decline slightly with rising stack temperature. The decline was consistent, but small enough (<0.5 %-points) to be considered negligible. The slight decline of efficiency in endothermic mode is explained through exergy analysis in Figure 6.20b. Note the scale of the graphs, as the values are quite small.

As explained in Section 6.4.4, the exergy destruction caused by overpotentials and the exergy destruction in the air superheater should add up to a constant value. However, in the case of temperature variation, the sum of these losses increased slightly with temperature. This was because the enthalpy change of the reaction increases very slightly with temperature. Therefore the overpotentials/heating required was slightly larger at higher temperatures, leading to a slightly higher exergy destruction.

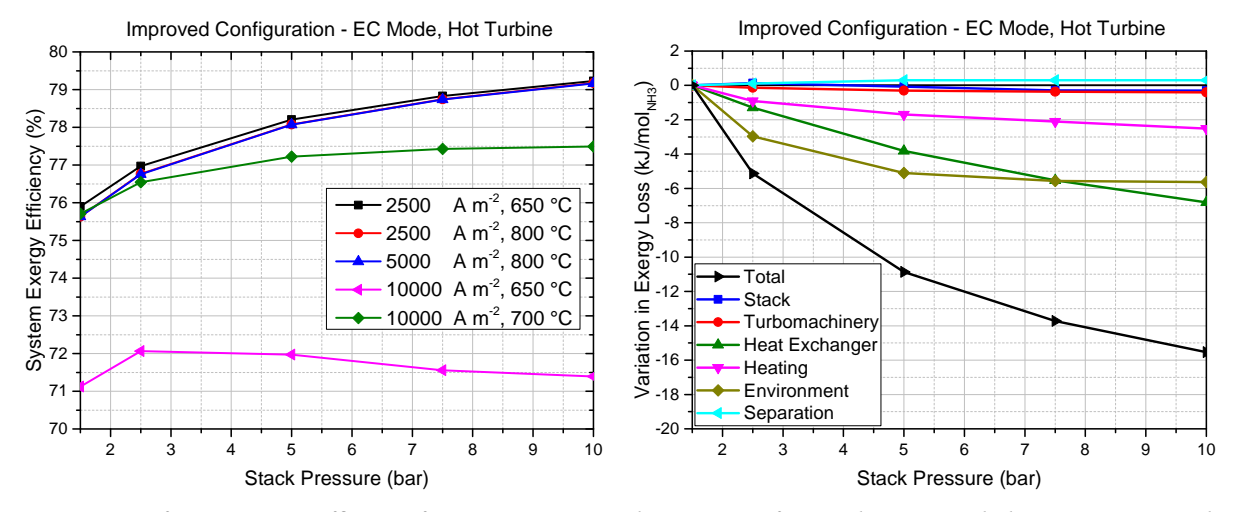
The exergy loss in heat exchangers also rose with temperature, simply because more heat needed to be transferred to take the steam to higher stack temperature. Lastly, the losses to the environment also increased. Upon analysis of the sub-components of environment loss, it is discovered that this increase in loss came mainly from the hydrogen compressor pre-cooler. Since the temperature of the hydrogen-steam mixture exhausted from the stack was higher, more heat was exchanged in both HEX8 and HEX1. This meant the temperature of water entering HEX2 was higher, and hence less heat could be extracted from the hydrogen in HEX2. The additional heat exergy was then wasted through the backup pre-cooler.

6.4.6. Effect of Stack Pressure Variation

The variation of the improved electrolysis system efficiency with stack pressure is shown in Figure 6.21a. The figure shows three lines clustered together at the top, which represent the points in the endothermic region. As explained in the previous section, in the endothermic region, current density had no effect on the system efficiency, while stack temperature had a very small negative effect. This is why in the chart, the two lines for $800\,^{\circ}\text{C}$ overlap perfectly, while the two lines for $2500\,^{\circ}\text{Am}^{-2}$ have a small offset between them.

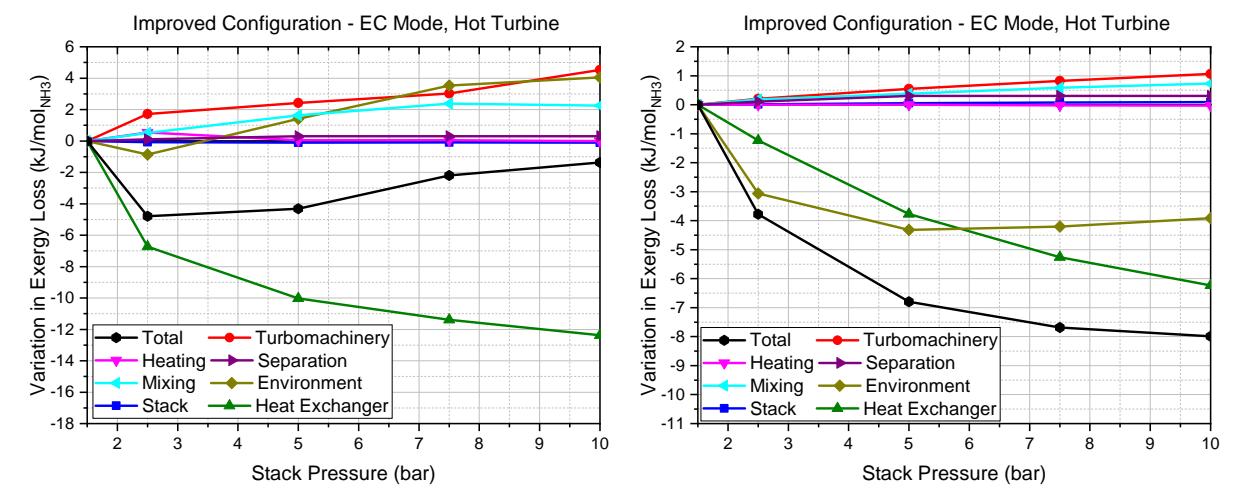
There are 4 combinations of temperature and current density which lead to exothermic operations across a range of pressures. In the exothermic region, the behaviour was quite different from endothermic, as seen from the two lines lower down in the chart. The effect of pressure here was similar to the fuel cell mode,

with the efficiency peaking in the middle of the range. But when the exothermic points were very close to thermoneutral (example of $10\,000\,\mathrm{A\,m^{-2}}$, SI700°C used here) the efficiency had a monotonic rise with pressure, following the trend which was seen in the endothermic region.



(a) Variation of system exergy efficiency for various operating points.

(b) Variation of exergy losses in endothermic region. Stack parameters used in this example: $800\,^{\circ}\text{C}$, $2500\,\text{Am}^{-2}$.



(c) Variation of exergy losses deep in the exothermic region. Stack parameters used in this example: $650\,^{\circ}\text{C}$, $10\,000\,\text{Am}^{-2}$.

(d) Variation of exergy losses slightly in the exothermic region. Stack parameters used in this example: $700\,^{\circ}$ C, $10\,000\,\mathrm{A\,m^{-2}}$.

Figure 6.21: Variation of electrolysis system performance with stack pressure, in hot turbine configuration. The exergy loss values are differential, with the first point of each line as the datum.

Figure 6.21b shows the variation of exergy losses in the endothermic region. The stack pressure affects the system differently, as compared to current density and temperature. Recall that the stack power and air superheater power added up to a value independent of current density and stack temperature, and the exergy losses in both those components also added up to another independent value. The sum of stack and superheater power was also independent of stack pressure. However, the sum of exergy losses was not independent of pressure. As the pressure increased, the stack power increased, thus reducing air superheating power and the corresponding exergy destruction. However, the increase in stack power was a result of Nernst voltage, and not overpotentials. Therefore, the stack losses did not increase. In fact, the overpotentials decreased slightly at higher pressure, leading to a small reduction in exergy destruction in the stack.

Further, the exergy destruction in heat exchangers also declined. This was mainly driven by an increase in the boiling point of water. The biggest improvement occurred in HEX1. At 1.5 bar, most of the heat from fuel electrode exhaust mixture was extracted in HEX1. Because of the low boiling point, this included sensible

preheating of water as well as evaporation. Integration of the sensible heat of the fuel electrode outlet flow with the latent heat of evaporation led to large losses. At higher pressures, say 10 bar, due to the high boiling point, HEX1 could only be used as an economiser, i.e. to preheat the water below its boiling point. Most of the heat from the fuel-side exhaust was extracted in HEX8, which involved superheating of the steam across smaller temperature differences. The latent heat addition was done in HEX3-HEX7, which necessary involved smaller temperature differences given the rather low temperature of the hot streams. Therefore, the overall exergy destruction at higher pressure was lower.

The exergy losses to the environment were also found to decrease overall. The losses through the hydrogen intercoolers increased, since less heat could be extracted for water evaporation. However, this was overshadowed by the savings in air exhaust losses. As the heat transfer in HEX3-HEX6 decreased due to rising boiling point, it was compensated by HEX7 (and to a smaller extent, HEX1/HEX8). Therefore, the air exhaust occurred at lower temperatures, reducing the environment losses.

Since all the major losses declined with rising pressure, the system efficiency always increased with pressure in endothermic region.

Figure 6.21c shows the behaviour by points deep in the exothermic region, through exergy losses. The exergy destruction in heat exchangers had the same trend as the endothermic region, reducing with pressure due to increasing boiling point. This was further exacerbated by HEX10, which was active in exothermic mode. The possibility of recuperation in HEX10 shrank as pressure increased due to rising compressor outlet temperature combined with failing turbine outlet temperature; an effect which was also seen in fuel cell mode. This further reduced the exergy destruction in heat exchangers. However, it was compensated by a rise in air exhaust temperature, which manifested as exergy loss to the environment.

The other losses followed the pattern of hot turbine fuel cell configuration. Air recirculation had to increase with pressure in order to eliminate the electric air preheating. This increased mixing losses. The increase in the power of air-side turbomachinery increased the exergy destruction there, despite lower airflow.

Initially, the reduction in heat exchanger losses was dominant, leading the system efficiency to increase. As pressure increased, these savings tapered off, and the increase in environment, turbomachinery and mixing losses turned the trend of system efficiency.

Lastly, Figure 6.21d shows the exergy losses for exothermic points which are close to the thermoneutral point. For these points, the fresh airflow was already low enough that these points followed the trend of the endothermic mode (where fresh airflow was zero). The effect of reduced heat transfer in HEX10 was muted due to the already starting value. The environment losses from air exhaust instead decreased due to the higher boiling point of water. Additionally, the low airflow also meant that the losses in mixing and turbomachinery were heavily diminished (though still increasing with pressure). This is why the slightly exothermic points mimic the endothermic points in system efficiency trends.

6.4.7. Conclusions of Hot Turbine Electrolysis Configuration Analysis

- The peak system exergy efficiency attained with this improved cold turbine configuration was 79.22 %, compared to 50.26 % in the basic configuration. There were multiple points where this efficiency could be obtained; all of them were at the maximum tested stack pressure of 10 bar.
- In the endothermic region, the variation of system performance is as follows:
 - Efficiency does not depend on current density at all.
 - Efficiency decreases at a very slow rate with increasing stack temperature.
 - High stack pressure leads to significantly higher efficiency.
- The above points highlight the fact that with the help of air recirculation, endothermic operation matches the performance of thermoneutral operation.
- Exothermic operation is much less efficient than thermoneutral or endothermic operation. Performance variation in exothermic electrolysis region is similar to the fuel cell hot turbine configuration.
- This configuration is able to eliminate the electric heat requirement for both steam and air heating. However, this is only possible at the chosen typical fuel/steam utilisation values. If the fuel utilisation (in FC mode) was higher, or if the steam utilisation was lower (in EC mode), then the flow rate of water/steam would be even larger, compared to the flow rates in the ammonia synthesis subsystem. This would lead to shortage of heat from the ammonia synthesis, resulting in the need for electric heating.

6.5. Electrolysis Mode - Cold Turbine Configuration

In this section, the cold turbine configuration for electrolysis is tested. This configuration was very similar in design to the hot turbine electrolysis configuration, with only two main differences. Firstly, since this is a cold turbine configuration, with reference to Figure 6.16, the air cooler was placed before the air turbine. Secondly, referring to Figure 6.17, HEX7 and HEX8 were interchanged, so that the air heat exchanger was last in line for evaporation of water, and thus only used if necessary.

6.5.1. Methodology

The simulation methodology was identical to all the previous cases in this chapter. Stack parameters were varied within the assigned ranges. At each stack operating point, the air recirculation ratio was varied to reach the optimum system efficiency for that operating point.

6.5.2. Effect of Air Recirculation Variation

Variation of air recirculation in the endothermic region yielded the following results, which are shown in Figure 6.22a from an energy perspective. In the endothermic region, the inlet air to the stack has to be heated above stack temperature. Despite the cold turbine configuration, due to minimum temperature difference limits in heat exchangers the air exhaust was unable to heat the fresh air even up to stack temperature. Therefore, electric air preheating as well as superheating was required. As the recirculation was increased and the fresh airflow decreased, the power required for air preheating decreased. Additionally, because of the increase in Nernst potential and stack power due to oxygen recirculation, the air superheating power also decreased accordingly, leading to a faster than linear decrease in overall air heating demand. Lastly, in cold turbine configuration, the air turbine typically produces less power than the air compressor requires. Therefore, as the airflow reduced, this net turbomachinery power input also reduced. Overall, the reduction in electric heating and the turbomachinery power input was able to overcome the increase in stack power input. This continued till the fresh airflow was eliminated entirely.

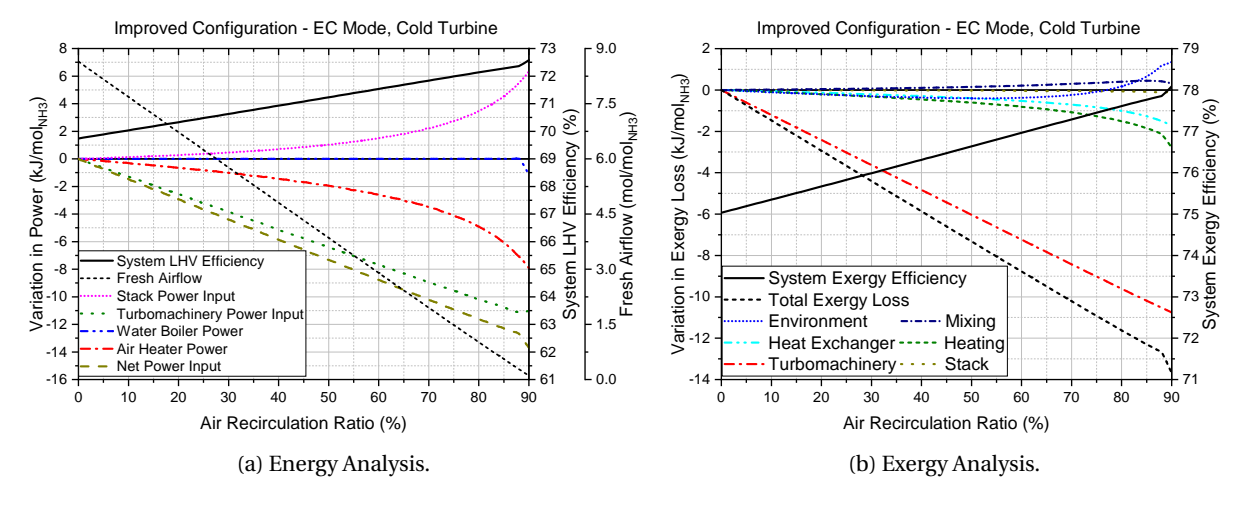


Figure 6.22: Effect of air recirculation on system performance of cold turbine electrolysis configuration. Stack parameters used in this example: $650\,^{\circ}$ C, $2.5\,$ bar, $5000\,$ Am $^{-2}$. The power/exergy loss values are differential, with the first point of each line as the datum.

The exergy losses shown in Figure 6.22b follow the same trends. As the fresh airflow decreased, the power throughput the air compressor, turbine and the air heaters decreased, leading to a fall in the exergy destruction in each of those components. Similarly, the exergy destruction in the air-to-air heat exchanger reduced due to the same reason. The exergy losses to the environment initially decreased on account of the smaller exhaust airflow. However, lower heat transfer in the air-to-air heat exchanger simultaneously increased the air exhaust temperature. At high recirculation ratios and low airflow, the effect of exhaust temperature became higher than the effect of reducing airflow, leading to an increase in the environment losses.

6.5.3. Discussion

Once it was confirmed that the optimum fresh airflow for the cold turbine electrolysis configuration was always zero in endothermic region, it was possible to predict that the cold turbine configuration would be less efficient than the hot turbine configuration. This section will discuss the analysis leading to this prediction. This was confirmed through simulations, but the results will not be discussed in detail.

Recall that the primary benefit of a cold turbine configuration is the possibility of better heat integration using hotter air, which comes at the cost of lower air turbine power output. However, it was shown in the previous sections that the hot turbine electrolysis configuration (at least for the fuel/steam utilisation values adopted in this thesis) was able to eliminate both electric air and steam preheating, which occurred when fresh airflow was reduced to zero using recirculation. Due to this result, the primary advantage of the cold turbine configuration over the hot turbine configuration was lost.

As a secondary consideration, even if both configurations were able to eliminate electric feed preheating, the configuration which could eliminate electric preheating while having lower oxygen content at the air electrode would have the benefit of lower stack power input (due to oxygen concentration effects on Nernst voltage). However, both HT and CT configurations found the peak in their efficiency when the fresh airflow was zero, which means oxygen content at the air electrode was 100 %. Therefore the CT configuration had no advantage from this perspective either.

Ultimately, the CT configuration was left with a lower air turbine power output, but identical stack and heating power inputs, which means it had a lower efficiency than the HT configuration. This analysis was indeed confirmed through simulation results. When the stack pressure was low, the two configurations produced almost identical results. This was because at low pressures, no heat was required to be transferred from the air exhaust to the steam. The steam was able to effectively extract sufficient heat from the other upstream heat exchangers because of its low boiling point. When the stack pressure (and thus, boiling point of water) was higher, the steam was able to extract less heat from other heat exchangers, and therefore more heat had to be extracted from the exhaust air. In these conditions, the CT configuration showed markedly lower efficiencies due to the lower turbine power output.

For the reasons mentioned above, the CT electrolysis configuration was not able to compete at the high efficiency points of interest (unlike the CT fuel cell configuration, which could compete with the HT configuration at least at the highest efficiencies). Therefore, there is no detailed analysis presented here. The CT electrolysis configuration will also not be used in the reversible system analysis for the same reason.

It is important to remember, however, that the CT configuration could become useful if the fuel or steam utilisation values are different, and the HT configuration can no longer eliminate electric feed preheating, as mentioned in Section 6.4.7.

6.6. Round Trip System Analysis

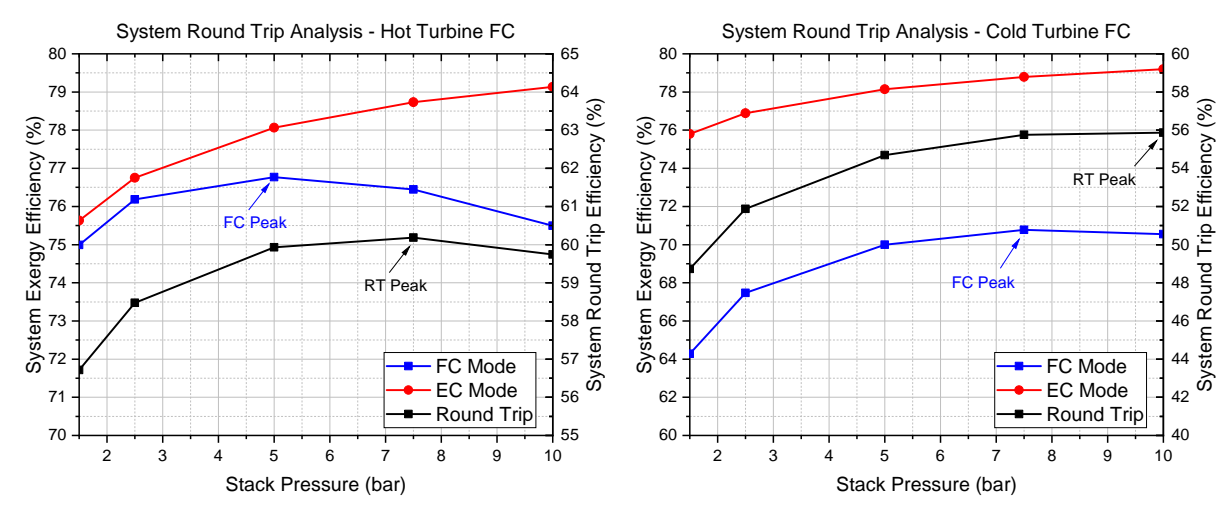
In this section, the optimum operating points for round trip efficiency are identified for all the relevant configurations studied in the previous sections. It was apparent from the previous sections that the fuel cell mode and electrolysis mode have very different trends with each of the three operating parameters, leading to very different optimum operation points for each mode. Therefore, it is useful to study how the optimum operating points for the round trip system are different compared to the individual modes of operation.

Additionally, although the hot turbine fuel cell configuration showed generally better performance, the hot and cold turbine fuel cell configurations remained in close competition at the points of greatest interest, i.e. high efficiency operating points. Therefore, it is also important to see which configuration achieves the highest round trip efficiency.

In Section 6.5 it has been made clear that the cold turbine electrolysis configuration was not competitive at any point of interest, therefore it is not considered here. Additionally, exothermic electrolysis is also not considered in this section for the same reasons. The operating points in the exothermic region for electrolysis mode also correspond to low efficiency points in the fuel cell mode as well, since they are typically operating points which cause very high overpotentials.

6.6.1. Variation in Optimum Stack Pressure

Recall that the system in fuel cell modes had a sweet spot of stack pressure for operation, which was around 7.5 bar in the cold turbine configuration, and varied between 2.5 bar and 5 bar, depending on other parameters, in hot turbine configuration. On the other hand, the endothermic electrolysis system displayed a monotonic improvement in efficiency with rising pressure. The combination of these two trends, as expected, retained the shape of the fuel cell mode trend, with the peak shifted to higher pressures, as seen in the two graphs in Figure 6.23. Note that this shift of peak is expected to take place in all cases though it may not necessarily be apparent from the data, since only 5 discrete pressures values were used in the simulations. For some cases in both configurations, the electrolysis efficiency rose fast enough with pressure to completely overcome the decline in fuel cell efficiency such that the maximum round trip efficiency would occur at the highest pressure, i.e. 10 bar.



- (a) Hot Turbine FC Configuration. Stack parameters used for this example: $800\,^{\circ}\text{C}$, $5000\,\text{Am}^{-2}$.
- (b) Cold Turbine FC Configuration. Stack parameters used for this example: 700 $^{\circ}\text{C}$, 5000 $\text{A}\,\text{m}^{-2}$.

Figure 6.23: Effect of reversible operation on optimum stack pressure.

6.6.2. Variation of Optimum Current Density and Stack Temperature

Unlike the stack pressure, the optimum values of current density were not significantly affected by round trip operation. This can be easily justified, if one recalls that the current density had no effect on the endothermic electrolysis system efficiency at all. Therefore, the optimum current density value remained the same as in the fuel cell mode.

On the other hand, increasing stack temperature was found to be very slightly detrimental to endothermic electrolysis efficiency. Therefore, it may be possible that the optimum temperature of the reversible system

could be at a lower value compared to the fuel cell mode, but it would strongly depend on the effect of other parameters too.

6.6.3. Optimised Parameters for the Reversible System

Based on all the analyses described in the previous two sections, the optimum operating point for a reversible system using the hot turbine fuel cell configuration is shown in Table 6.2. As discussed in the previous section, it is seen that the optimum pressure value increased from 2.5 bar for FC efficiency to an optimum of 5 bar for round trip efficiency. The optimum value of current density remained $2500 \,\mathrm{Am}^{-2}$.

However, the optimum temperature actually reduced from $800\,^{\circ}\text{C}$ to $750\,^{\circ}\text{C}$. This result can be explained as follows. For the optimum current density of $2500\,\text{A}\,\text{m}^{-2}$, if the system was operated at the optimum pressure of 5 bar, then the hot turbine FC system would be in the zone where its efficiency was determined by the oxygen starvation limit. In this zone, reducing the stack temperature increased the FC system efficiency. Additionally, the endothermic EC system preferred a lower stack temperature as well. Thus, there was an advantage for lower temperature in both modes, and therefore the optimum stack temperature was found to be at a slightly lower temperature in round trip operation, compared to the fuel cell mode.

Parameter	Unit	FC Mode	EC Mode	Reversible Mode
Stack Temperature	°C	800	650	750
Stack Pressure	bar	2.5	10	5
Current Density	Δ m ⁻²	2500	2500	2500

Table 6.2: Optimum operating points for each mode - Hot turbine FC configuration.

Note: Since the optimum EC mode efficiency is not affected by current density, the chosen optimum point is the one at the same current density as the FC mode.

The situation was different for the cold turbine FC configuration, shown in Table 6.3. Since the cold turbine FC system did not approach oxygen starvation at any point, any reduction in stack temperature was strongly unfavourable to FC mode, while it was only mildly beneficial to the EC mode. Therefore, the optimum temperature remained high, at $800\,^{\circ}$ C. The optimum pressure also appeared to remain the same as in FC mode (i.e. 7.5 bar). However, it may be the case that the actual optimum pressure was slightly higher, but the effect is not visible due to the small number of stack pressures sampled.

Parameter	Unit	FC Mode	EC Mode	Reversible Mode
Stack Temperature	°C	800	650	800
Stack Pressure	bar	7.5	10	7.5
Current Density	Am ⁻²	2500	2500	2500

Table 6.3: Optimum operating points in each mode - Cold turbine FC configuration.

Note: Since the optimum EC mode efficiency is not affected by current density, the chosen optimum point is the one at the same current density as the FC mode.

6.6.4. Final Round Trip Results

The optimum round trip efficiencies attained at the optimised points were 60.75 % for the hot turbine configuration, and 61.20 % for the cold turbine configuration. The energy and exergy values of the system at the two optimum operating points are shown in Table 6.4. The round trip efficiency values of the improved configurations at their optimised points showed a significant improvement over the basic configuration, which had attained an round trip efficiency of 19.79 %. Looking back to the results of the optimised basic configuration in Table 5.3, it can be seen that the total exergy losses the optimised basic system added up to 526.23 kJ/mol $_{\rm NH_3}$. In comparison, these losses were reduced to 129.28 kJ/mol $_{\rm NH_3}$ in the best case, which amounts to approximately 75 % reduction in exergy losses. The reduction in exergy losses achieved per process is noted in Table 6.5.

It is notable that the round-trip efficiency of the optimised cold turbine configuration is higher than the hot turbine configuration. This has to do with the fact that the hot turbine configuration operates at the

oxygen starvation limit with non-zero electric air preheating. As a result of this, the optimum operating points of the cold turbine fuel cell configuration match closely with the optimum points in the electrolysis mode, whereas the efficiency of the hot turbine fuel cell configuration is lower at these points.

These optimum points involve a value of current density that is at the lowest limit of the tested range. It may also be interesting to know the maximum possible operating efficiencies if the capital cost is a concern, and therefore higher current densities are desired. For a current density of $5000\,\mathrm{A\,m^{-2}}$, the maximum round trip efficiency achieved remains very high, at $60.19\,\%$. Naturally, this corresponds to the hot turbine fuel cell configuration, since there were no points of current density $5000\,\mathrm{A\,m^{-2}}$ or higher, where the cold turbine configuration could compete. Similarly, at a current density of $10\,000\,\mathrm{A\,m^{-2}}$, a maximum round trip efficiency of $57.08\,\%$ could be achieved, again using the hot turbine configuration in both modes.

Table 6.4: Energy and exergy analysis results of the improved configurations at the optimised operating points.

Downwater	II!t	Hot Turbine Config.		Cold Turbine Config.	
Parameter	Unit	FC Mode	EC Mode	FC Mode	EC Mode
Stack temperature	°C	750		800	
Stack pressure	bar	į	5	7.5	
Current density	$\mathrm{Am^{-2}}$	25	00	2500	
Fresh air flow	mol/mol _{NH3}	3.40	0.00	3.70	0.00
Air Recirculation	%	54.20	96.13	27.00	96.52
Net power output	kJ/mol _{NH3}	204.01	-335.88	203.95	-333.20
Stack output	kJ/mol _{NH3}	214.91	-252.02	220.85	-245.95
Turbomachinery input	kJ/mol _{NH3}	7.43	29.64	16.71	26.36
Heating input	kJ/mol _{NH3}	3.47	51.95	0.20	58.62
Refrigeration input	kJ/mol _{NH3}	-	2.26	-	2.26
Total exergy losses	kJ/mol _{NH3}	58.37	73.52	58.44	70.84
ReSOC stack	kJ/mol _{NH3}	21.82	6.59	19.75	4.91
Synthesis reaction	kJ/mol _{NH3}	-	4.73	-	4.73
Expansion & Compression	kJ/mol _{NH3}	7.08	9.01	8.22	8.96
Heat exchange	kJ/mol _{NH3}	2.91	18.54	5.03	16.87
Electric heating	kJ/mol _{NH3}	1.42	14.44	0.17	15.55
Refrigeration	kJ/mol _{NH3}	-	1.08	-	1.08
Mixing	kJ/mol _{NH3}	1.04	4.42	0.34	4.41
Separation	kJ/mol _{NH3}	0.18	6.82	0.19	6.82
Environment	kJ/mol _{NH3}	23.91	7.90	24.75	7.52
System energy efficiency	%	83.66	72.60	83.63	73.18
System exergy efficiency	%	77.76	78.11	77.73	78.74
System round trip efficiency	%	60.75		61.20	

Note: All the values correspond to operating parameters selected for maximum round trip efficiency. Hot/cold turbine configuration refers only to FC mode; EC mode is only used in hot turbine configuration.

6.7. Key Take-aways

Table 6.5: Comparison of exergy losses and round trip efficiency in the optimised basic and improved configurations.

Process	Exergy Losses (kJ/mol _{NH3})					
1100055	Basic	Improved	Improvemen	t		
ReSOC stack	31.93	24.66	7.27 (22	77 %)		
Synthesis reaction	4.66	4.73	-0.07 (-1	.50 %)		
Expansion & Compression	44.65	17.18	27.47 (61	.52 %)		
Heat exchange	N/A	21.90	-21.90	N/A		
Electric heating	239.35	15.72	223.63 (93	.43 %)		
Refrigeration	1.08	1.08	0	(0 %)		
Mixing	4.46	4.75	-0.29 (-	6.5 %)		
Separation	6.97	7.01	-0.04 (-0	.57 %)		
Environment	193.12	32.27	160.85 (83	.29 %)		
Total	526.23	129.28	396.95 (75	.43 %)		
System round trip efficiency	19.79	61.20	41.41 %-points			

6.7. Key Take-aways

In this chapter, the basic design of the ReSOC system was improved using heat integration to eliminate the largest exergy losses viz. heating and cooling. The heat integration schemes did not make use of an afterburner for additional heat. Air recirculation was used effectively for optimising the system in both modes. Variation of the placement of the air turbine relative to the recuperating heat exchanger was considered as a path to improve the efficiency. The key results from this chapter are listed below.

- Peak round trip efficiency of over 61% can be achieved. Such a system is able to operate effectively across the entire range of stack operating conditions. Even the worst-case round trip efficiency remain above 37%. Round trip efficiency over 57% can be achieved even at practical current densities like $10000\,\mathrm{Am^{-2}}$.
- It was found to be thermodynamically feasible to operate a ReSOC system without using an afterburner.
- Air recirculation is vital in achieving high efficiencies for heat integration schemes that lack the additional heat from an afterburner. The optimum values of air recirculation ranged from 0 % to as high as 79 %, depending on the exact operating points and system configurations.
- In the fuel cell mode, for most practical operating points, it is highly preferable to place the air turbine upstream from the heat recuperator (i.e. hot turbine). This was found to improve the round-trip efficiency by an average 2.8 %-points, or a maximum of 8.8 %-points, compared to a configuration with the turbine placed downstream (i.e. cold turbine). However, the hot turbine configuration faces restrictions from oxygen starvation at very high efficiency operating points. In a few such cases, the cold turbine configuration can be more efficient, although only by ~1 %-points.
- In the electrolysis mode, it is feasible to effectively utilise heat from ammonia synthesis and hydrogen compression to evaporate the feed water. For typical values of fuel/steam utilisation (=0.8), it is possible to eliminate electric air and steam preheating, though electric heat is still required to heat the stack in the endothermic region.
- For typical fuel/steam utilisation values, it is always preferable to use the hot turbine configuration even in electrolysis mode.
- For endothermic electrolysis, it is beneficial to not use any fresh sweep air from the environment, instead using only recirculated oxygen from the stack outlet for thermal management of the stack.
- The main reason for the upstream "hot" turbine configuration being preferable is that it allows for heat integration schemes that better utilise the heat from the stack, and features lower exergy destruction

in heat exchangers, and lower exergy loss to the environment through the steam condenser and air exhaust.

- In general, the optimum operating points for the system (purely from an efficiency perspective) are: high temperature, low current density, and intermediate pressure (5 7.5 bar).
- The largest exergy losses in the improved systems continue to come from exergy released to the environment. Nearly half of this comes from steam condensation in the fuel cell mode.
- The second largest portion of exergy destruction comes from the stack, particularly ammonia cracking in fuel cell mode. This is a largely unavoidable loss, since the cracking model is already very idealised.
- Evaporation of water in heat exchangers in the electrolysis mode causes another large portion of the exergy destruction.
- Lastly, electric air superheating to heat the endothermic electrolysis cell also destroys a significant amount of exergy.
- Three of these losses may be reduced further with inter-modal heat integration. High-temperature thermal energy storage could satisfy the thermal demand of electrolysis. Low-temperature energy storage could couple the condensation in FC mode with evaporation in EC mode. However, this may not improve efficiency unless the high temperature waste heat currently being used to evaporate water is put to better use.

Evaluation of the Use of Afterburner and Thermal Energy Storage

After having improved the round trip efficiency of the ReSOC system from $\sim\!20\,\%$ to $\sim\!61\,\%$ in the previous chapter, a few more modifications are tested in this chapter. The first part of this chapter involves the design of system with an afterburner in the fuel cell mode. The second part of this chapter evaluates the possibility of further improvements to the system using thermal energy storage for heat integration across the two operating modes

7.1. Comparison with Afterburner systems

The work in the previous chapter demonstrated the feasibility of a ReSOC system without an afterburner, and a high round trip efficiency was achieved even under pressurised operation where air-to-air recuperation is limited. However, in order to make a design recommendation regarding the afterburner, the efficiency must be compared to an analogous system with an afterburner. Further, it is desirable to understand the thermodynamic differences between the two process decisions. To that end, in this section, the system designed in the previous chapter is modified with an afterburner in the fuel cell mode, and its performance is studied through exergy analysis.

7.1.1. Fuel Cell System with Afterburner

The model of the fuel cell system with afterburner was based on the hot turbine configuration. This is due to the observations in Section 6.3 that the HT configuration provided better performance. Additionally, since the afterburner provides a significant amount of heat, the required recirculation was expected to be lower, and therefore the problems with oxygen starvation faced by the HT configuration were also not expected to occur.

Process Design

The process flowsheet of the fuel system with the afterburner is shown in Figure 7.1. The air for the afterburner was drawn from the stack air electrode exhaust (after the recirculation splitter). The amount of air drawn was such that it contained exactly the amount of oxygen needed for complete combustion. An assumption was made that the afterburner could completely utilise all the oxygen in the air. The remaining air was passed separately through an in-built heat exchanger in the afterburner to raise the TIT of the air turbine. The flue gas and the air outlets of the internal afterburner heat exchanger were assumed to be at the same temperature. The remaining system was identical to the system without the afterburner. The excess nitrogen that was sent to the afterburner along with the oxygen was purged before the compression stages. A heat exchanger and small turbine were placed in this purge stream to recover any compression energy. The air recirculation ratio was zero by default, but if required, was adjusted until the electric air preheating was eliminated. The thermal management of the stack was also unchanged, being controlled by varying the amount of fresh airflow.

The heat integration scheme for this system is shown in Figure 7.2. The scheme was very similar to the HT configuration without afterburner (see Figure 6.2), with some modifications. The fuel electrode exhaust was also used to preheat the excess nitrogen purge in HEX4 before expanding in the turbine. An extra heat

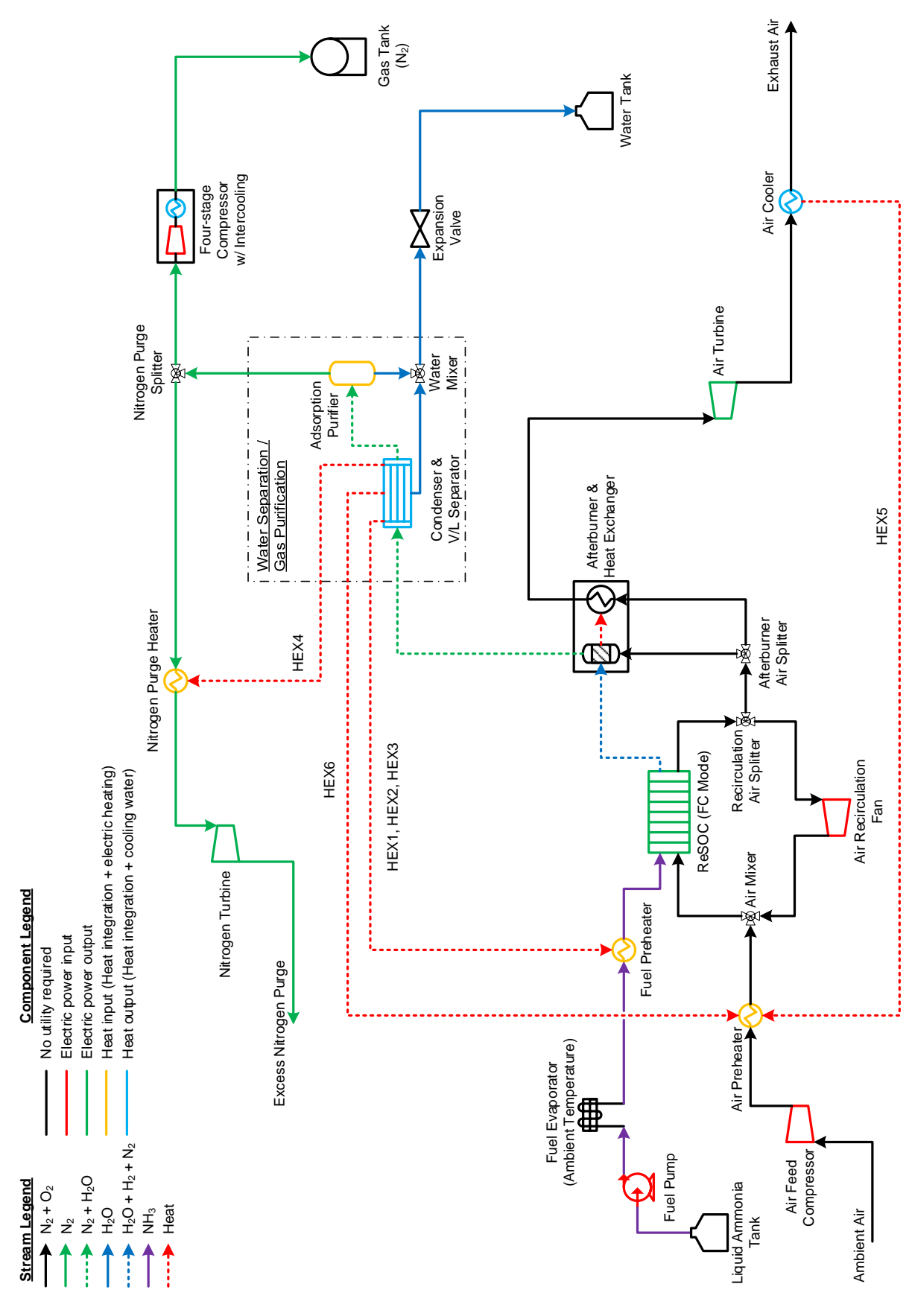


Figure 7.1: Process flowsheet for fuel mode - Afterburner configuration.

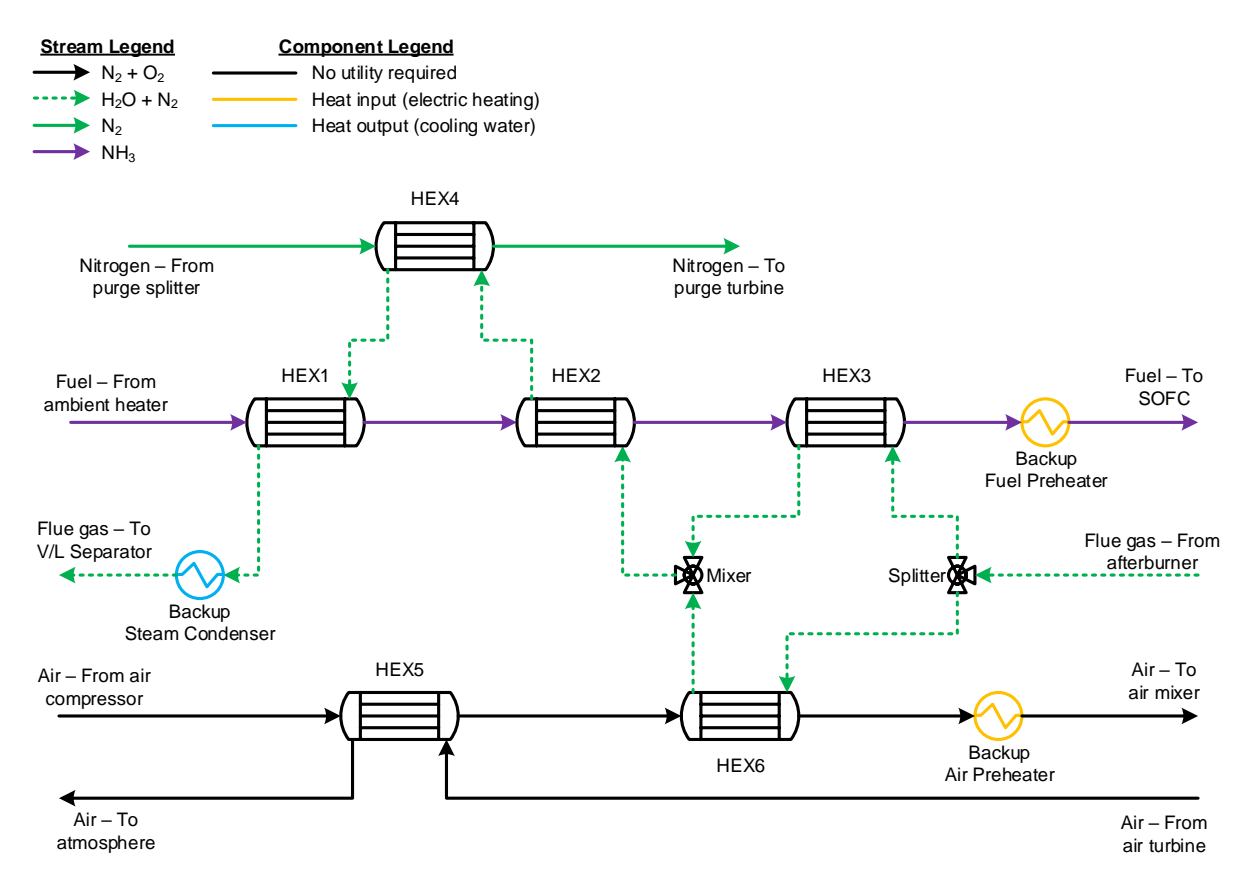


Figure 7.2: Heat integration scheme for fuel mode - Afterburner configuration.

exchanger HEX1 was also added to preheat the ammonia (especially at higher pressures), so that less heat transfer would be required in HEX2 and HEX3, and the TIT of the nitrogen turbine can be higher due.

Methodology

The methodology for simulations of this system is identical to all the previous simulations from Chapter 6.

Results for Fuel Cell Mode with Afterburner

A comparison between the results of the configurations with and without an afterburner is made with Table 7.1. The comparison is made at two operating points, one ordinary point $(700 \,^{\circ}\text{C}, 2.5 \,\text{bar}, 5000 \,\text{Am}^{-2})$, and one point where the system without afterburner is at the oxygen starvation limit $(800 \,^{\circ}\text{C}, 7.5 \,\text{bar}, 2500 \,\text{Am}^{-2})$.

It is notable that at both points, the system with afterburner provides greater power output than the original system. The heat generated by the afterburner is sufficient for preheating the fresh air, reducing the need for any air recirculation. Lower recirculation implies a higher fresh airflow for stack cooling. This larger airflow generates greater power output when passing through the air-side turbomachinery. Additionally, the afterburner increases the TIT of the air turbine, further boosting the power output. The lower recirculation also ensures higher oxygen content in the stack, raising the stack power output.

However, despite the larger net power output, the system efficiency was drastically lower. This is because the exergy stored in the nitrogen/hydrogen tank was significantly reduced due to the afterburner. A glance at the exergy loss values reveals significantly larger exergy destruction in the afterburner, the heat exchangers, and exergy losses to the environment. Combustion in the afterburner is already known to cause large exergy destruction. The exergy destruction in the heat exchangers was caused due to rather large temperature differences caused by the high afterburner temperature. Additionally, the preheating of the larger fresh airflow also caused greater exergy destruction in heat exchangers. The most significant increase in exergy losses was the loss to the environment, caused by the steam condenser cooling and air/nitrogen exhaust streams. These losses in heat exchangers and to environment indicated that the system could not effectively recover all the thermal exergy released from the afterburner. Even at Point 2 (at the oxygen starvation limit for the system

Table 7.1: Energy and exergy analysis comparison of systems in fuel cell mode: system with no afterburner (AB) vs. system with afterburner. Operating Point 1 is an example of an ordinary operating point. Operating Point 2 is an example of a point where the system without afterburner is at the oxygen starvation limit.

Demonstra	Unit	Operating Point 1		Operating Point 2	
Parameter		Without AB	With AB	Without AB	With AB
Stack temperature	°C	700		800	
Stack pressure	bar	2.5		7.5	
Current density	$\mathrm{Am^{-2}}$	5000	0	2500	
Fresh air flow	mol/mol _{NH3}	8.41	13.77	3.40	4.41
Air Recirculation	%	42	0	39	0
Net power output	kJ/mol _{NH3}	190.80	219.80	200.54	231.14
Stack output	kJ/mol _{NH3}	191.19	191.86	219.78	222.25
Net turbomachinery input	kJ/mol _{NH3}	-0.20	-28.78	5.62	-9.40
Heating input	kJ/mol _{NH3}	0.59	0.84	13.62	0.51
Total exergy losses	kJ/mol _{NH3}	71.58	115.83	61.84	104.49
ReSOC stack	kJ/mol _{NH3}	31.89	31.88	19.74	19.73
Afterburner	kJ/mol _{NH3}	-	9.28	-	9.24
Expansion & Compression	kJ/mol _{NH3}	9.61	11.89	7.71	7.95
Heat exchange	kJ/mol _{NH3}	3.98	15.77	2.88	17.35
Electric heating	kJ/mol _{NH3}	0.57	0.86	4.85	0.39
Mixing	kJ/mol _{NH3}	0.82	2.50	0.58	3.73
Separation	kJ/mol _{NH3}	0.18	0.26	0.19	0.49
Environment	kJ/mol _{NH3}	24.54	43.39	25.89	45.61
System exergy efficiency	%	72.72	65.49	76.43	68.87

without afterburner), the difference in heat exchanger and environment losses in the afterburner system was so large that it overshadowed even the electric heating losses.

When considering variations of stack operating parameters, the results of the system with the afterburner showed the same trends as the hot turbine configuration without the afterburner. The system exergy efficiency monotonically increased with rising stack temperature. Meanwhile, the efficiency decreased with an increasing current density, due to increased stack losses, and losses in the air-side BoP. There existed an optimum stack pressure, until which the efficiency initially increased with rising pressure, and then dropped as the pressure was increased further.

As mentioned above, the air recirculation required was zero in most cases. Only in cases of low stack temperature and high pressure, where the air-to-air recuperation was bad and the afterburner inlet and outlet temperatures were relatively low, some recirculation was required to eliminate the electric air preheating. However, these recirculation ratios were still significantly lower than they would be without an afterburner.

However, there were a few peculiarities, which once again, occurred at points where the stack was very efficient. Unlike the HT configuration without afterburner, there were no problems with oxygen starvation, since the recirculation ratios were lower. However, at these points, the airflow was too low to effectively recover the thermal exergy released by the afterburner. This would lead to increased losses to the environment, mainly through the steam condenser. For this reason, at the points with highest stack efficiency (low current density, high temperature), making the stack more efficient would actually reduce the system efficiency.

The consistently large environment losses suggested that there was an opportunity for using an auxiliary power cycle to utilise additional exergy from the afterburner. Using an auxiliary cycle would be preferable to making the stack operate at less efficient points, since it would mitigate exergy losses to the environment without introducing additional exergy destruction in the stack.

7.1.2. Fuel Cell System with Auxiliary Power Cycle

Since the motive of evaluating a ReSOC system with an afterburner is to provide a point of reference and comparison for the system configuration designed in the previous chapter, it is desirable to choose an optimistic scenario for the reference design, to enable a strong comparison. Therefore, according to the learning from the previous section, the afterburner system was modified by introducing an auxiliary power cycle. The process flowsheet of the system is shown in Figure 7.3.

An open Brayton cycle based on air was used for its simplicity, easy access to the working fluid and lack of a condenser. To get the highest efficiency for the sake of comparison, a cycle with recuperation/regeneration was used with a very low pressure ratio (~2.5), which corresponds to very high efficiency for a Brayton cycle at a given temperature ratio. The temperature ratio depended on the peak temperature that the afterburner could provide. The heat integration scheme was unaffected by the auxiliary cycle, and remained the same as Figure 7.2.

Methodology

Apart from the 4 variables already optimised in all the previous sections (temperature, pressure, current density and air recirculation), the auxiliary Brayton cycle also introduced another variable, viz. the airflow through the cycle. Due to the limited time frame of this thesis, it was only possible to optimise this system for a few operating points.

The operating points chosen for comparison were 5 values of stack pressure (1.5-10 bar) for a current density of $2500\,\mathrm{Am^{-2}}$ and a stack temperature of $800\,^\circ\mathrm{C}$. There are two significant considerations that make these five points the most relevant for comparison. These points include the maximum efficiency points for both the HT and CT fuel cell configurations. They also include three points of the HT configuration that are most affected by the oxygen starvation limit.

For each of these five points, the fresh airflow, air recirculation and auxiliary airflow were each optimised for maximum system efficiency.

Results for a System with an Auxiliary Power Cycle

The results for these five relevant points are compared between three configurations in Table 7.2. The table shows a consistent order of efficiencies. The auxiliary cycle greatly improved the efficiency of the afterburner system, by up to 8 %-points This benefit reduced at higher stack pressure, since at higher stack pressures, the air turbine associated with the stack itself could extract significant exergy from the afterburner exhaust. However, even with the auxiliary cycle, the afterburner system could not compete with the original system without an afterburner. The efficiency of the original system remained 2-6 %-points higher than the afterburner system, even after reaching the oxygen starvation limit. The reason for this is explained through Table 7.3, by comparing the exergy losses in the three configurations at one sample operating point.

Table 7.2: Efficiency comparison of systems in fuel cell mode: system with no afterburner (AB) vs. system with afterburner vs. system with afterburner and auxiliary cycle. Stack operating parameters: $800\,^{\circ}$ C, $2500\,\mathrm{Am}^{-2}$

Stack	System Exergy Efficiency	System Exergy Efficiency	System Exergy Efficiency
Pressure	without AB	with AB	with AB & aux. cycle
bar	%	%	%
1.5	76.94	62.93	70.63
2.5	78.06	67.20	72.71
5	77.52	69.17	73.67
7.5	76.45	68.87	73.52
10	75.50	68.13	72.95

With the auxiliary cycle, it was possible to bring down the exergy loss to the environment to the same level as the system without an afterburner. Additionally, the introduction of the auxiliary airflow reduced the outlet temperature of the afterburner. This reduced the exergy destruction in heat exchange, both within the internal heat exchanger of the afterburner, as well as in the other heat exchangers using the produced flue gas. However, the heat exchanger losses could not be reduced to the level of the system without the afterburner, since the air preheating still occurred through heat exchange rather than recirculation and mixing.

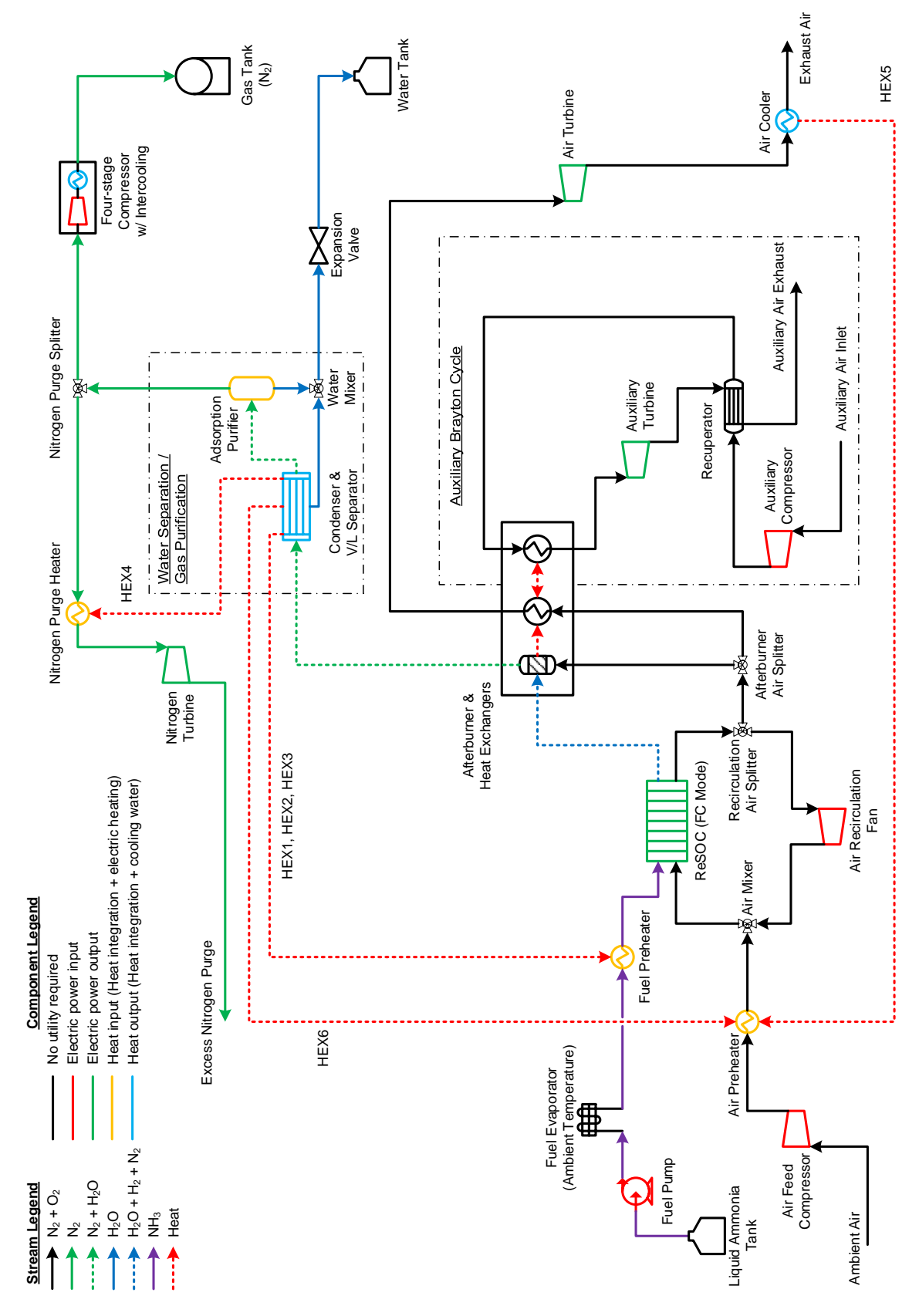


Figure 7.3: Process flowsheet for fuel cell mode - Auxiliary power cycle configuration.

Table 7.3: Energy and exergy analysis comparison of systems in fuel cell mode: system with no afterburner (AB) vs. system with afterburner vs. system with afterburner and auxiliary cycle.

Parameter	Unit	Without AB	With AB	With AB & aux. cycle
Stack temperature	°C	800		
Stack pressure	bar		5	
Current density	Am^{-2}		2500	
Air recirculation	%	48	0	0
Fresh airflow to stack	mol/mol _{NH3}	3.40	4.98	4.98
Airflow to auxiliary cycle	mol/mol _{NH3}	-	-	8.25
Net power output	kJ/mol _{NH3}	203.36	232.17	247.25
Stack output	kJ/mol _{NH3}	217.19	220.38	220.38
Auxiliary cycle output	kJ/mol _{NH3}	-	-	26.78
System turbomachinery input	kJ/mol _{NH3}	6.08	-12.46	-0.76
Heating input	kJ/mol _{NH3}	7.75	0.67	0.67
Total exergy losses	kJ/mol _{NH3}	59.02	103.47	87.34
ReSOC stack	kJ/mol _{NH3}	20.81	20.77	20.77
Afterburner	kJ/mol _{NH3}	-	8.87	8.87
Auxiliary cycle	kJ/mol _{NH3}	-	-	8.82
Expansion & Compression	kJ/mol _{NH3}	7.08	7.65	7.67
Heat exchange	kJ/mol _{NH3}	3.18	17.09	10.95
Electric heating	kJ/mol _{NH3}	2.84	0.54	0.54
Mixing	kJ/mol _{NH3}	0.80	3.40	3.40
Separation	kJ/mol _{NH3}	0.18	0.42	0.42
Environment	kJ/mol _{NH3}	24.13	44.74	25.90
System exergy efficiency	%	77.51	69.17	73.67

Despite these improvements, the significant exergy destruction caused by the combustion in the afterburner remained. The auxiliary cycle itself destroyed some exergy through its turbomachinery, recuperator and exhaust. Therefore, the overall exergy destruction remained high, and the overall exergy efficiency was lower than the system without the afterburner.

7.1.3. Electrolysis Mode for System with Afterburner

The effect of the presence or absence of an afterburner on the fuel cell mode was seen in the previous section. However, to complete the analysis for a reversible system, it is necessary to look at the effect of an afterburner on the electrolysis mode as well, which is taken up in this section.

The afterburner is not active in the electrolysis mode, since the objective in this mode is to produce fuel. However, the presence of the afterburner in the fuel cell mode has certain implications for the electrolysis mode as well. Firstly, because the energy storage system has to be balanced, all the fuel that was consumed in the fuel cell mode needs to be produced again in the electrolysis mode. Secondly, because the system is based on a ReSOC rather than separate fuel cell and electrolysis cell stacks, the area of the cells in the stack is same in both the operating modes.

The afterburner consumed any remaining hydrogen in the fuel cell mode. Therefore, there was no hydrogen stored in the nitrogen-hydrogen gas tank. Therefore, to maintain the production of ammonia at the same level, the electrolysis stack has to produce the hydrogen burnt in the afterburner as well as the hydrogen oxidised in the fuel cell. Since the stack size is constant, the effective current density utilised in the electrolysis mode has to be proportionally higher than the current density in the fuel cell mode. In this case, since the

fuel utilisation in the fuel cell mode was 80 %, the afterburner consumed 25 % of the fuel that was consumed electrochemically. Therefore, the electrolysis mode has to operate at a current density 25 % higher, producing 25 % more hydrogen than would be needed in a system without an afterburner.

Electrolysis System Model

The electrolysis model itself required no particular changes, since the afterburner itself was in the fuel cell mode. However, the heat integration scheme had to be changed. In Section 6.4.7, it was pointed out that it was possible that the hot turbine configuration would not be able to eliminate electric steam heating if the fuel utilisation in fuel cell mode was higher. Preliminary analysis showed that in this case, the hot turbine electrolysis configuration was unable to eliminate the electric steam preheating (except at 1.5 bar). Because of the afterburner, the flow rates in the electrolysis section of the system were 25 % higher than the system without an afterburner, but the flow rates in the ammonia synthesis section of the system were unchanged. The evaporation of water relied on heat from the ammonia synthesis. Because of the increase in water flow rate without an increase in ammonia production, not enough heat was available for water evaporation. The exhaust from the air turbine in HT configuration was found to be unable to compensate for this shortfall. Therefore, in this case, the cold turbine configuration had to be adopted for the electrolysis mode.

The process flowsheet for the cold turbine configuration is shown in Figure 7.4, while the heat exchanger scheme designed for this configuration is showed in Figure 7.5. Note that unlike other cold turbine configurations where the exhaust air heat exchanger was placed last to minimise the heat extraction when possible, that was not an option here due to the large heat demand from the additional steam. The main exhaust air heat exchanger was placed second-last, and required another low temperature heat exchanger to maximise the heat extraction.

Methodology

The electrolysis system was tested for the same 5 operating points that were used to test the fuel cell system with an auxiliary cycle in the previous section. The other constraints for the simulation were the same as those used throughout Chapter 6. However, as mentioned above, the current density for the electrolysis mode was taken to be 25 % higher than the corresponding operating point in fuel cell mode, in order to compensate for the hydrogen burnt in the afterburner.

Electrolysis system results

As expected, the general trends of electrolysis system efficiency were not changed by the introduction of the afterburner in fuel cell mode. The endothermic electrolysis system became more efficient at high stack pressures, while stack temperature and current density had negligible effects. Since this behaviour remains the same, the focus in this section will remain on only the same five operating points that were considered in the previous section with the auxiliary power cycle.

The system exergy efficiency for these five points in electrolysis mode are compared in Table 7.4. The most remarkable observation in these results is that the efficiency of the system with an afterburner is higher than the system without an afterburner. This is counter-intuitive, since production of 25 % more hydrogen for the same amount of ammonia should be expected to lead to greater exergy losses through all the electrolysis section components. This is verified in Table 7.5, which compares the exergy losses for both system designs at one operating point. It was indeed found to be the case that the introduction of an afterburner in FC mode also increased the exergy losses in the EC mode. A glance at the comparison of exergy losses shows that the losses associated with ammonia synthesis and refrigeration remained unchanged, while the other losses associated with the electrolysis process increased due to the larger production of hydrogen.

The increase in efficiency despite the increase in exergy losses can be explained by recalling the definition of the electrolysis system exergy efficiency from Equation (4.20b). The efficiency was defined as the proportion of the electrical exergy provided to the system that is able to be stored in the chemical storage tanks in the form of chemical or physical exergy. With the introduction of the afterburner, the exergy that was stored in the hydrogen/nitrogen tank was drastically lower due to the absence of unutilised hydrogen, while the exergy finally stored in the ammonia tank remained constant. This means a significantly larger amount of exergy was added to the chemical tanks in the electrolysis mode. Therefore, while the electric power input was increased, a greater proportion of this electrical exergy was converted into the exergy in the chemical tanks. This difference in tank storage is shown in Table 7.6.

Another way to explain this is to evaluate the ratio of exergy loss to the power input. As seen in Table 7.6, while more power is consumed and more exergy is lost, the increase in exergy losses is proportionally less

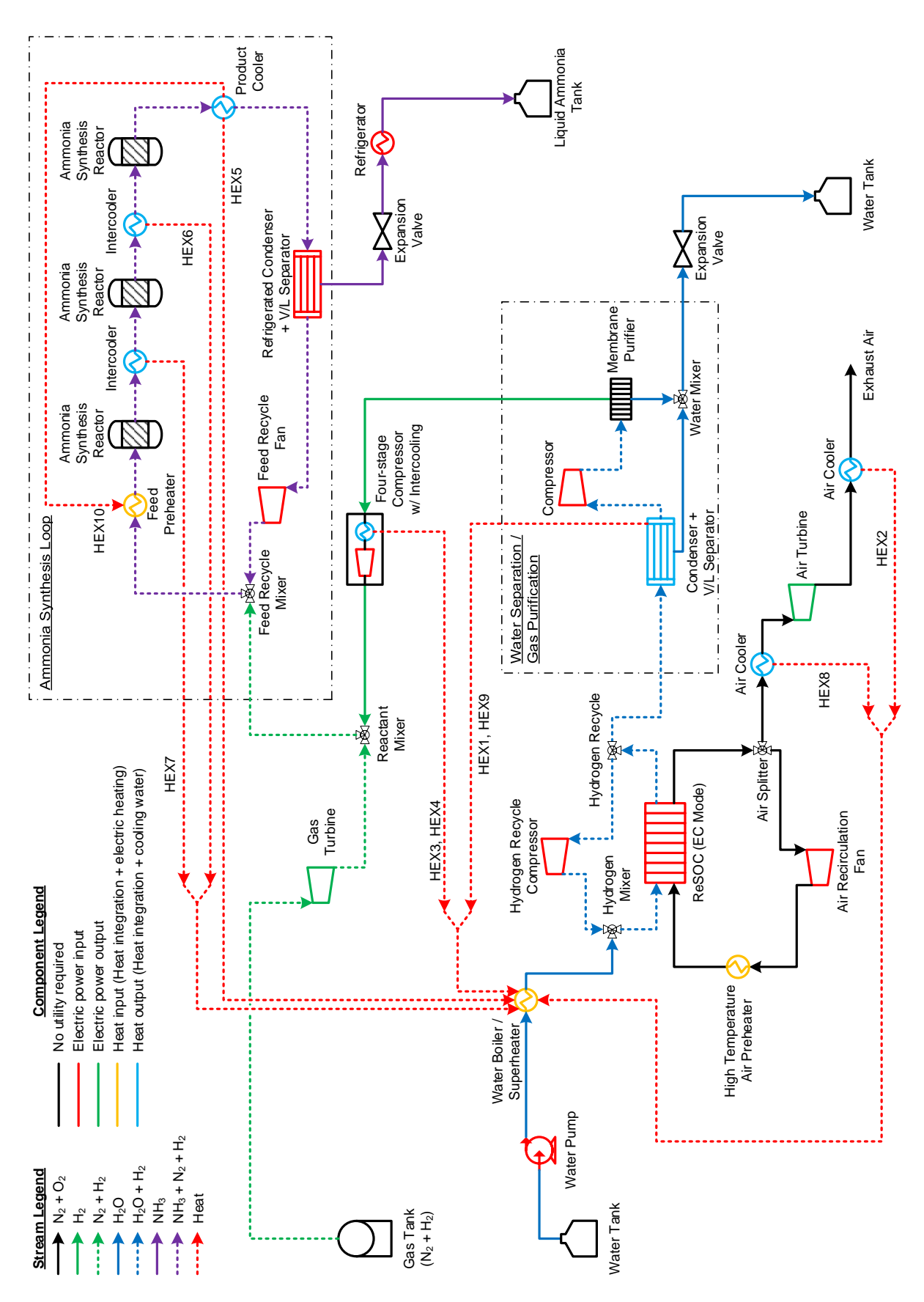


Figure 7.4: Process flowsheet for electrolysis mode - Afterburner configuration.

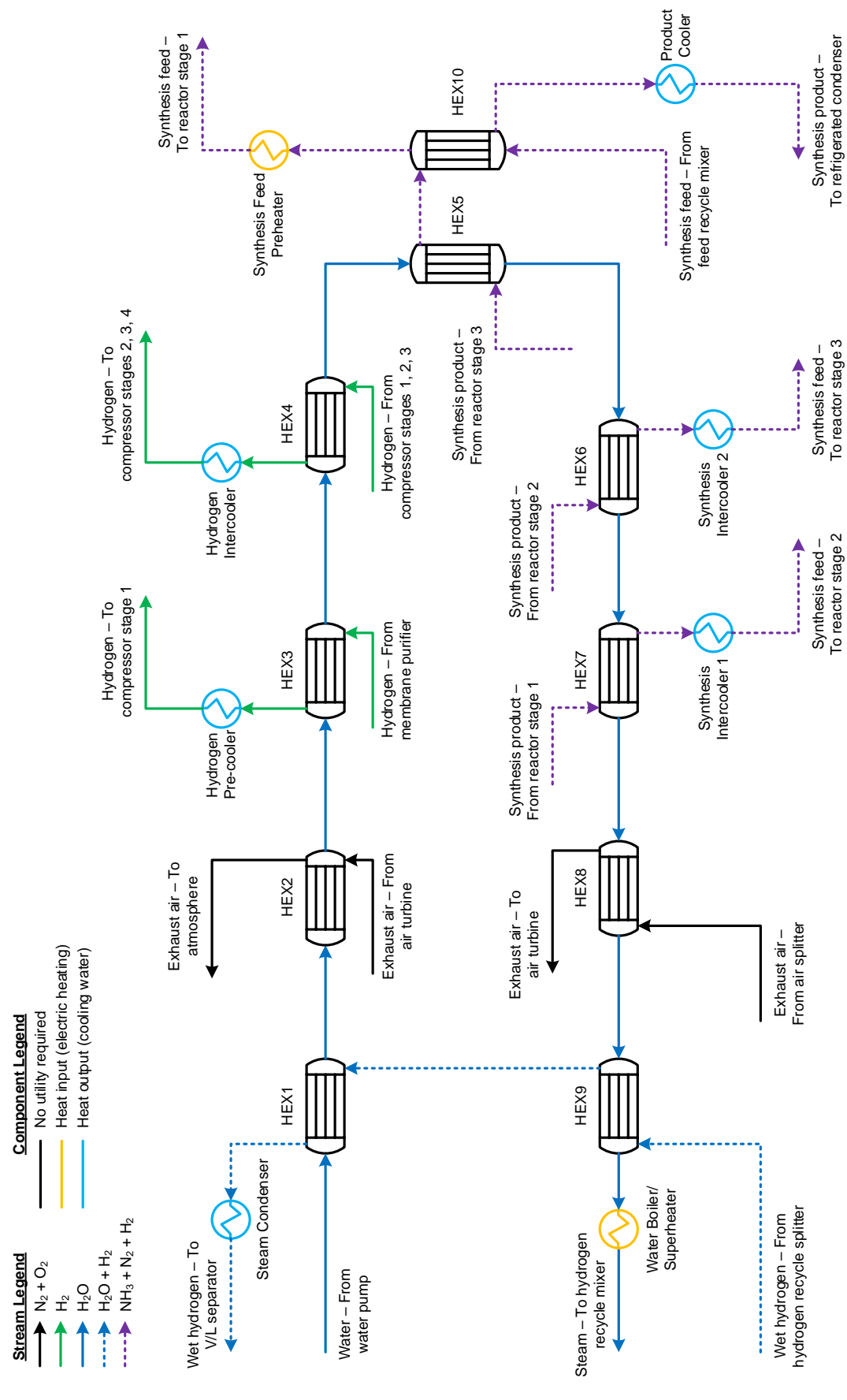


Figure 7.5: Heat integration scheme for electrolysis mode - Afterburner configuration.

Table 7.4: Efficiency comparison of systems in electrolysis mode: system without afterburner vs. system with afterburner (in FC mode). Stack operating parameters that are held constant: $800\,^{\circ}$ C, $2500\,\mathrm{Am}^{-2}$.

Stack	System Exergy Efficiency	System Exergy Efficiency
Pressure	without AB	with AB
bar	%	%
1.5	75.64	77.59
2.5	76.76	78.32
5	78.07	79.18
7.5	78.74	79.67
10	79.14	79.97

than the increase in power input, resulting in a larger portion of the electrical exergy being stored as useful exergy in the chemical tanks, i.e. higher system exergy efficiency.

7.1.4. Round Trip Operation for System with Afterburner

In the previous sections, the effect of introducing an afterburner was analysed in each mode. The efficiency of the fuel cell mode decreased, while the efficiency of the electrolysis mode increased. In this section, the combined effect of the afterburner on the reversible system is examined. The comparison of round trip efficiency for at all the five examined points is shown in Table 7.7.

Use of the afterburner was observed to consistently reduce the round trip efficiency of the ReSOC system. This observation is on expected lines, considering that the exergy destruction was seen to increase in both the FC and EC modes. In order to further understand the reason for this difference, the breakdown of exergy losses for the entire reversible system are presented in Table 7.8. The introduction of the afterburner led to an increase in nearly all categories of exergy loss, apart from the components of ammonia synthesis loop (mainly reaction and refrigeration). Out of the additional exergy loss, a significant chunk (20% each) was contributed by the afterburner and the auxiliary cycle, as expected from a wasteful process like combustion. The largest portion (27%) of the additional exergy destruction, however, comes from the heat exchangers. This is a combined effect of heat transfer losses caused in the process of evaporating additional water in the EC mode, as well as the losses caused by increased temperature difference in the FC mode heat exchangers due to the afterburner.

7.1.5. Conclusion of Afterburner Study

- The original system designed in Chapter 6 without an afterburner is more efficient than a system with an afterburner.
- Even after the addition of an auxiliary power cycle, the system with afterburner still achieves lower efficiencies.
- Therefore, in a reversible system, it is thermodynamically preferable to store and reuse the unutilised fuel from the fuel cell, rather than using an afterburner.

Table 7.5: Energy and exergy analysis comparison of systems in electrolysis mode: system with no afterburner (AB) vs. system with afterburner.

Parameter	Unit	Without AB	With AB
Stack temperature	°C	800	
Stack pressure	bar	5	
Current density	Am^{-2}	2500	3125
Fresh airflow	mol/mol_{NH_3}	0	0
Air recirculation	%	96.64	96.49
Net power input	kJ/mol _{NH3}	336.04	423.89
Stack input	kJ/mol _{NH3}	243.77	308.08
System turbomachinery input	kJ/mol _{NH3}	29.45	40.91
Heating input	kJ/mol _{NH3}	60.56	72.64
Refrigeration input	kJ/mol _{NH3}	2.26	2.26
Total exergy losses	kJ/mol _{NH3}	73.68	88.25
ReSOC stack	kJ/mol _{NH3}	4.95	7.09
Synthesis reaction	kJ/mol _{NH3}	4.73	4.73
Expansion & Compression	kJ/mol _{NH3}	9.01	10.89
Heat exchange	$kJ/mol_{ m NH_3}$	18.62	22.36
Electric heating	kJ/mol _{NH3}	16.09	19.31
Refrigeration	kJ/mol _{NH3}	1.08	1.08
Mixing	kJ/mol _{NH3}	4.42	6.26
Separation	kJ/mol _{NH3}	6.82	8.53
Environment	kJ/mol _{NH3}	7.96	8.01
System exergy efficiency	%	78.07	79.18

Table 7.6: Comparison of exergy stored in chemical tanks: system without afterburner (AB) vs. system with afterburner. Stack operating parameters: $800\,^{\circ}\text{C}$, $2500\,\text{Am}^{-2}$, $5\,\text{bar}$.

Parameter	Unit	Without AB	With AB
System power input in EC mode	kJ/mol _{NH3}	336.04	423.89
Net exergy added to chemical tanks in EC mode	kJ/mol _{NH3}	262.36	335.64
Exergy stored in ammonia tank	kJ/mol _{NH3}	343.91	343.91
Exergy drawn from gas (N ₂ /H ₂) tank	kJ/mol _{NH3}	80.47	6.92
Exergy drawn from water tank	kJ/mol _{NH3}	1.08	1.35
Exergy Lost	kJ/mol _{NH3}	73.68	88.25
Percentage of electrical exergy lost	%	21.93	20.82
System exergy efficiency	%	78.07	79.18

Table 7.7: Round trip efficiency comparison of systems: system without afterburner vs. system with afterburner and auxiliary cycle (in FC mode). Stack operating parameters that are held constant: $800\,^{\circ}$ C, $2500\,\mathrm{Am}^{-2}$.

Stack Pressure	Round trip efficiency without AB	Round trip efficiency with AB and aux. cycle
bar	%	%
1.5	58.20	54.80
2.5	59.92	56.95
5	60.52	58.33
7.5	60.20	58.57
10	59.75	58.34

Note: The RTE values for the system without afterburner correspond to the combination of HT fuel cell and HT electrolysis configurations, even for points were the CT fuel cell configuration would achieve higher RTE.

Table 7.8: Overall exergy analysis of reversible systems: system with no afterburner (AB) vs. system with afterburner and auxiliary power cycle.

Parameter	Unit	Without AB	With AB & aux. cycle
Stack temperature	°C	8	00
Stack pressure	bar		5
Current density	Am^{-2}	2500	FC: 2500, EC: 3125
Power input	kJ/mol _{NH3}	336.04	423.89
Power output	kJ/mol _{NH3}	203.36	247.25
Total exergy losses	kJ/mol _{NH3}	132.70	175.60
ReSOC stack	kJ/mol _{NH3}	25.76	27.86
Synthesis reaction	kJ/mol _{NH3}	4.73	4.73
Afterburner	kJ/mol _{NH3}	-	8.87
Auxiliary power cycle	kJ/mol _{NH3}	-	8.82
Expansion & compression	kJ/mol _{NH3}	16.09	18.56
Heat exchange	kJ/mol _{NH3}	21.80	33.31
Electric heating	kJ/mol _{NH3}	18.93	19.85
Refrigeration	kJ/mol _{NH3}	1.08	1.08
Mixing	kJ/mol _{NH3}	5.22	9.66
Separation	kJ/mol _{NH3}	7.00	8.95
Environment	kJ/mol _{NH3}	32.09	33.91
Round trip efficiency	%	60.52	58.33

7.2. Thermal Energy Storage

In Chapter 6, an improved ReSOC system was designed with heat integration and air recirculation. The operating parameters were optimised for both FC and EC modes individually, and then for reversible operation. However, the FC and EC modes were not coupled in any way apart from operating at the same stack parameters. One of the major advantages of a reversible SOC system is the possibility of using the excess heat generated in the fuel cell mode to offset the electric power consumption in electrolysis mode by operating in the endothermic electrolysis region. Utilising this feature requires thermal coupling of both modes. Since these modes are temporally separated, it implies the need for thermal energy storage (TES). There are studies in literature, as listed in Section 3.1, which state that integration of TES in a ReSOC system is beneficial. In this section, the ReSOC system is equipped with a hypothetical thermal energy storage system based on hypothetical phase change materials (PCMs), and the possible thermodynamic benefits of inter-modal heat integration are explored in the context of the designed ReSOC system using ammonia.

7.2.1. Modelling

The TES system was designed in a highly idealised manner, in order to gain an estimate of the maximum benefit that could be accrued from its use. As mentioned above, the TES system was designed as latent heat storage using a hypothetical PCM. This material could vary, based on the stack temperature being utilised. Kenisarin [97] lists several possible materials at different temperatures. The melting point of this material was assumed to be constant, and 10 °C below the stack temperature in the fuel cell mode. In electrolysis mode, the stack was assumed to operate a further 10 °C below the TES temperature, i.e. 20 °C below the stack in fuel cell mode. At such small temperature differences, the heat transfer between the stack and the TES was assumed to occur through hypothetical heat pipes integrated into the interconnects of the stack, as introduced through literature in Section 3.4. Liquid alkali metals like sodium or potassium could be potential materials for these heat pipes [78, 79]. The schematic stack models including the TES are shown in Figure 7.6. The heat flowing to/from the TES only affected the energy balance of the stack, which affected the amount of airflow. Apart from this calculation, the Aspen Plus model itself did not need to be changed.

The formula for calculation of exergy efficiency was modified to reflect the exergy transferred from to/from the TES. Just like the previous expressions for exergy efficiency (Equation (4.20)), these modified expressions were also formulated such that the round trip efficiency could be obtained simply as a product of the efficiency of the two modes. These modified expressions are shown in Equations (7.1). $Ex_{\rm TES}$ [kJ/mol_{NH3}] is the thermal exergy stored in the TES, which can be calculated by Equation (7.2), since the TES is assumed to operate at a constant temperature. The exergy destruction in the heat transfer across the 10 °C temperature difference was classified as part of the exergy destruction in the stack.

$$\eta_{\text{ex,FC}} = \frac{P_{\text{net,FC,out}}}{\vec{E} \dot{x}_{\text{NH_3,in}} - \vec{E} \dot{x}_{\text{N_2/H_2,out}} - \vec{E} \dot{x}_{\text{H_2O,out}} - \vec{E} \dot{x}_{\text{TES}}}$$
(7.1a)

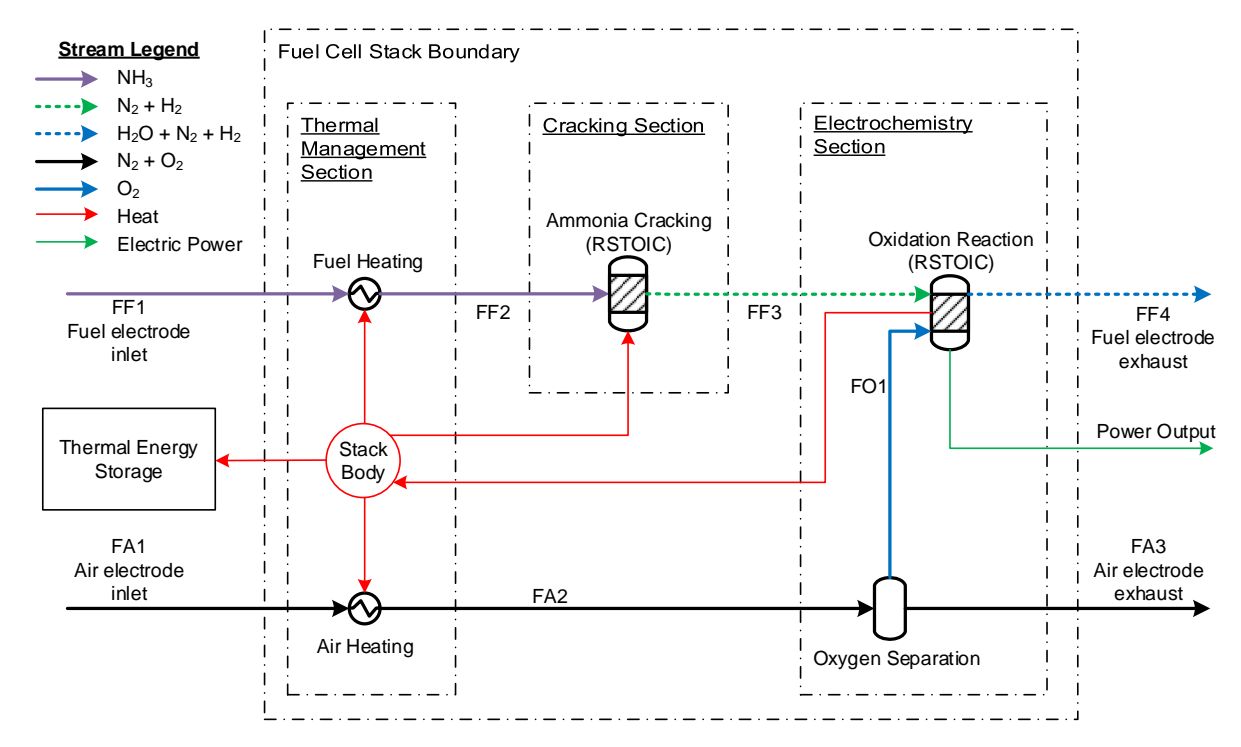
$$\eta_{\text{ex,EC}} = \frac{\vec{E}x_{\text{NH}_3,\text{out}} - \vec{E}x_{\text{N}_2/\text{H}_2,\text{in}} - \vec{E}x_{\text{H}_2\text{O},\text{in}} - \vec{E}x_{\text{TES}}}{P_{\text{net,EC,in}}}$$
(7.1b)

$$\dot{Ex}_{\rm TES} = \dot{Q}_{\rm TES} \left(1 - \frac{T_0}{T_{\rm TES}} \right) \tag{7.2}$$

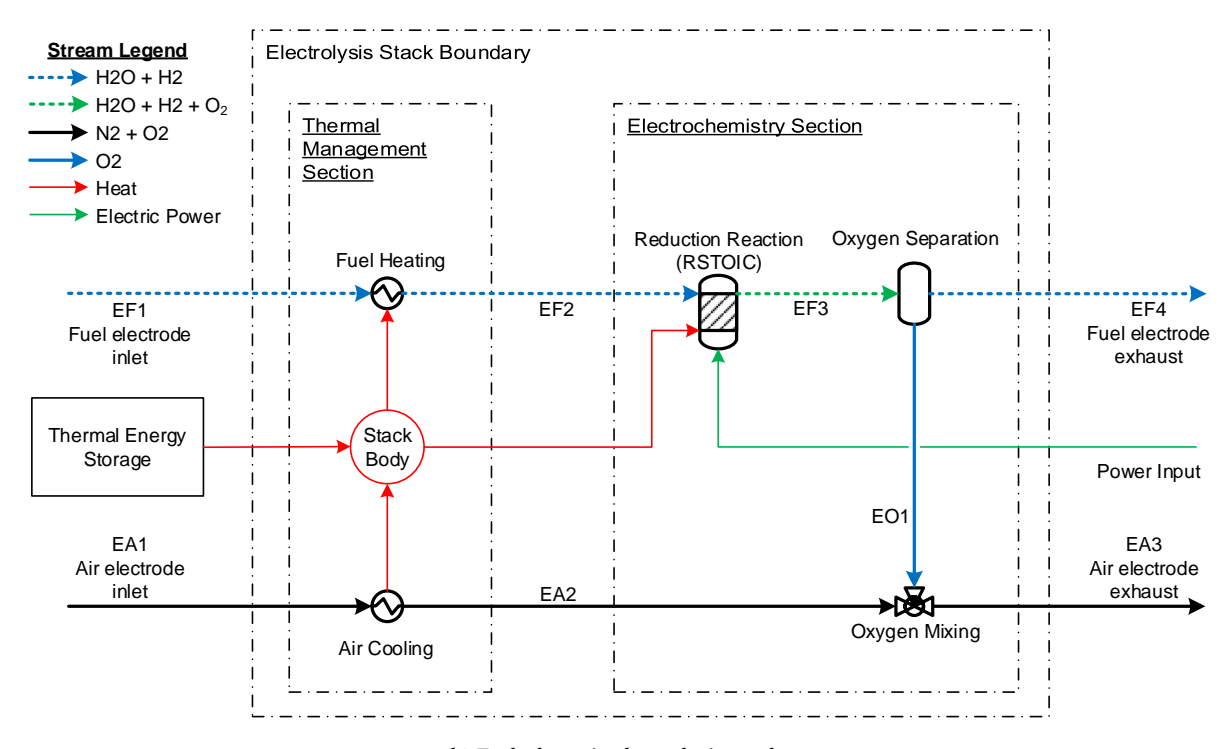
7.2.2. Simulation Methodology

According to the initial assumptions of the energy storage system in this work, all the fuel generated in the EC mode was used in the FC mode. The same principle also applied to thermal energy in the TES. The heat that was extracted in the EC mode was perfectly matched by the heat stored in the FC mode. Ensuring a proper heat balance required multiple rounds of simulations. It is also important to note that because endothermic electrolysis operation is a fundamental pre-requisite for a TES system to be useful, the system was not operated in conditions where the electrolysis is known to be exothermic.

Firstly, the amount of thermal power required by the electrolysis stack was calculated at each endothermic operating point. It has been shown in Section 6.4 that the electrolysis system is most efficient when there is no fresh airflow. Accordingly, the simulations were carried out just like Section 6.4, with zero fresh airflow. Since



(a) Fuel cell mode.



(b) Endothermic electrolysis mode.

Figure 7.6: Schematic of ReSOC stack models including thermal energy storage.

only recirculated air was used for thermal management, the thermal power required by the electrolysis stack was equal to the sum of the power inputs of the air superheater and the air recirculation compressor.

Secondly, at each corresponding operating point, the maximum heat that can be extracted from the fuel cell mode was calculated. This was done by fixing the amount of fresh airflow to be minimum, i.e. just on the boundary of oxygen starvation. This would ensure that the minimum amount of the heat generated by the stack would be lost in exhaust (since the air exhaust flow rate is positively correlated to the fresh airflow), leaving more heat to be stored. The air recirculation ratio was adjusted till exactly the point where the electric preheating was eliminated. Increasing the recirculation further would mean a larger cooling airflow through the stack, which would reduce the heat available for storage, without any efficiency benefits to the fuel cell mode. Using a lower recirculation value would incite the need for electric air preheating, and the large exergy losses associated with that, which were deemed undesirable. While the HT configuration saw non-zero recirculation ratios, most CT configuration points required zero recirculation. There were rare exceptions at high stack temperature and low pressure. This was due to the different heat integration scheme used as in Figure 6.9a at low pressure. At low fresh airflow rates, the exhaust air has proportionally much smaller flow (due to oxygen consumption) leading to insufficient preheating.

Thirdly, if the maximum amount of heat generated in the fuel cell was less than the heat required for electrolysis, no further simulations in the fuel cell mode were required. If the maximum amount of heat generated in the fuel cell mode was more than required for electrolysis, the fresh airflow was increased (with an appropriate recirculation ratio to ensure zero electric preheating) until the heat generation matched the heat demand from electrolysis. In CT configuration where the recirculation is not necessarily coupled to the airflow by electric heating elimination, a suitable combination of fresh airflow and recirculation was optimised for maximum efficiency / least exergy loss.

Lastly, the electrolysis model was simulated again, this time with consideration for the amount of heat stored in FC mode. If the heat stored in FC mode was less than the requirement in EC mode, the shortfall would be met through sweep air superheating, just like in the models without TES.

7.2.3. Variation in Heat Demand and Generation

The results of the first two rounds of simulations are described, where the heat demand of the electrolysis and the maximum heat available from the fuel cell are investigated.

Electrolysis Mode

In electrolysis mode, the fresh airflow was kept constant at zero. Therefore, the airflow through the stack and recirculation depend only on the heat demand, and not the other way around (unlike fuel cell mode). The net heat demand of the electrolysis stack depends only on how deep the operating point is into the endothermic region, i.e. how far the cell voltage is from the thermoneutral voltage. The variation of cell voltage for electrolysis was described in Section 5.1.1. In accordance with those trends, the heat demand in this case was observed to increase with a rise in stack temperature, decrease with a rise in stack pressure or current density.

Fuel Cell Mode

In the fuel cell mode, the amount of recirculation would be expected to affect the excess heat available for storage, since the recirculation affects the amount of cooling airflow through the stack. The recirculation, in turn, depends on factors external to the stack (namely the elimination of electric preheating). Therefore, the variation of air recirculation would be the first thing to study.

In the HT configuration, the fresh airflow is kept constant at the oxygen starvation limit. Even at this low level, the fresh airflow still has the highest heat capacity in all the heat exchangers it flows through. If the stack temperature is increased, the fresh air has to be provided with proportionally more energy before entering the stack. The internal energy of the steam or exhaust air flowing out of the stack also increases. However, due to their lower heat capacities, all that additional energy cannot be transferred to the fresh air. This results in the need for higher air recirculation to meet the additional air preheating needs caused by higher stack temperature. On the other hand, when stack pressure is increased, heat integration between the hot turbine exhaust air and the cold fresh air becomes difficult due to temperature changes in the turbomachinery. Because of less effective heat integration, higher recirculation is required at higher stack pressures. Lastly, the air recirculation is unaffected by current density, since the fresh airflow is no longer coupled to the stack losses, and therefore the normalised properties of all the material streams throughout the system stay constant. On the other hand, as mentioned previously, in the CT configuration, the recirculation was mostly zero, except in the combination of high temperatures and low pressures.

Now that the trends of air recirculation are known, it is possible to move on to investigating the net heat availability in FC mode. The heat generated in FC mode can be estimated through the study on stack voltage in Section 5.1.1. Accordingly, the heat generation decreases with a rise in temperature or pressure, and increases with a rise in current density. In the CT configuration, since there is no recirculation required, these general trends remain unchanged. In the HT configuration, recirculation increases with rising temperature or pressure. Therefore, the airflow through the stack increases with rising temperature or pressure, carrying away more heat. However, the heat generation itself is also lower at higher temperature or pressure. Therefore, the recirculation trend in the HT configuration actually supports the trend of heat generation, making it even stronger.

To summarise, in fuel cell mode, the excess heat available to the TES decreases with a rise in stack temperature or pressure, and increases with a rise in temperature. These downward trends are even stronger in HT configuration due to increasing air recirculation. Therefore, the CT configuration is able to provide more heat (and thermal exergy) to the TES. The thermal exergy available from the HT configuration ranges from $0\,kJ/mol_{NH_3}$ to $36.9\,kJ/mol_{NH_3}$, based on operating parameters. In the CT configuration, the thermal exergy availability ranges from $2.1\,kJ/mol_{NH_3}$ to $37.3\,kJ/mol_{NH_3}$.

Balancing of the TES

As seen in the above paragraphs, the heat demands of the EC mode and the excess heat availability from FC mode have exactly the opposite trends, since both depend on the stack efficiency. On one hand, at high temperature / low current density points, the EC mode is deeply endothermic and requires a lot of heat. But the stack being efficient, the heat generation in FC mode is low, and there is very little heat to spare. On the other hand, at low temperature / high current density points, the FC stack produces a lot of excess heat. However, so does the EC stack, and therefore the electrolysis requires very little additional heat. Because of this mismatch, it is likely that there is a very narrow range of mid-level stack efficiency where inter-modal integration through thermal energy storage can provide the most benefit. Indeed, while the maximum thermal exergy availability from the FC mode was $\sim 37\,\mathrm{kJ/mol_{NH_3}}$ in either configuration, due to the operating point mismatch with the electrolysis demand, the maximum heat actually stored was only $\sim 14\,\mathrm{kJ/mol_{NH_3}}$ in HT configuration and $\sim 24\,\mathrm{kJ/mol_{NH_3}}$ in CT configuration, which represented points of intermediate stack efficiency (e.g. low current density, but also low temperature and pressure).

7.2.4. System Performance with TES

After having studied the heat requirement and availability, the performance of the ReSOC system after incorporation of a balanced TES system is analysed. But before moving to analysing the balanced system, the effect of the amount of heat storage on the each mode has to be analysed. Especially in the fuel cell mode, however, the performance effect of extracting heat for storage directly from the stack requires further elaboration.

FC Mode Performance Variation

In both configurations of the fuel cell mode, increasing the amount of heat stored in the TES reduces the exergy destruction in the system. This can be explained by first starting from the condition where the maximum possible heat is being stored and slowly reducing the storage. Reducing the heat storage implies cooling the stack using more air. This cooling airflow can be increased either by increasing the air recirculation or increasing the fresh airflow. If the recirculation is increased, then part of the exergy extracted by the air is destroyed in mixing. Further, this reduces the required fresh air preheating temperature, meaning that the exergy that was being utilised in the air preheating heat exchangers is now lost to the environment through the air exhaust or the steam condenser. Increasing the recirculation also reduces the oxygen concentration available to the stack, reducing the Nernst voltage and increasing stack losses. On the other hand, consider increasing the fresh airflow. If this is done, the exhaust airflow increases as well, directly increasing the exergy losses through the air exhaust. The stack exergy destruction may decrease due to higher oxygen concentration, but may increase due to cooling done by air across a temperature difference of 100 °C rather than across 10 °C to the TES. But this has a smaller effect than exhaust losses. Additionally in the HT configuration, as the fresh airflow rises, the recirculation ratio has to rise (along with all its losses), because the constant steam flow cannot heat the rising airflow enough to avoid electric heating. Therefore, in FC mode, the more heat storage leads to the less exergy destruction, and therefore the maximum possible heat should be stored, taking care that no electric heating is needed.

However, the trend of fuel cell system exergy efficiency with heat storage is peculiar. Since the exergy losses monotonically decrease with increasing heat storage, the efficiency would be expected to increase alongside.

But this does not always happen. Since the fresh airflow is reduced to enable heat storage, the oxygen content in the stack reduces, leading to a drop in stack power. Additionally, the lower airflow reduces the net power output of the air-side turbomachinery. Therefore the system power output also reduces. Recall the definition of exergy efficiency from Equation (7.1a). This equation can be rewritten in terms of exergy loss/destruction $\dot{E}x_{\rm D,FC}$ [kJ/mol_{NH3}] and system power output $P_{\rm net,FC,out}$ [kJ/mol_{NH3}] as shown in Equation (7.3).

$$\eta_{\text{ex,FC}} = \frac{P_{\text{net,FC,out}}}{\dot{E}\dot{x}_{\text{NH}_3,\text{in}} - \dot{E}\dot{x}_{\text{N}_2/\text{H}_2,\text{out}} - \dot{E}\dot{x}_{\text{H}_2\text{O,out}} - \dot{E}\dot{x}_{\text{TES}}} = \frac{P_{\text{net,FC,out}}}{P_{\text{net,FC,out}} + \dot{E}\dot{x}_{\text{D,FC}}} = \frac{1}{1 + \frac{\dot{E}\dot{x}_{\text{D,FC}}}{P_{\text{net,FC,out}}}}$$
(7.3)

Therefore, the efficiency does not correlate directly to exergy loss, but rather to the ratio of the exergy loss and the power output. At different stack operating points, this ratio changes at different rates with respect to heat storage. Therefore, the efficiency does not show a clear trend. At most operating points, the exergy loss tends to fall faster than the power output falls when more heat is stored. Therefore, the efficiency behaves intuitively and increases with a fall in exergy destruction. However, at some points (relating to very high stack efficiency, i.e. 800 °C and 2500 Am⁻²), the oxygen content is already low due to low fresh airflow and high recirculation. If fresh airflow is reduced further for the purpose of heat storage, the stack power falls proportionally faster than the exergy losses from exhaust, because the exhaust losses are already very low. Therefore, at these few points, the efficiency counter-intuitively decreases, even though the exergy loss also decreases. Figure 7.7 shows two examples in the HT configuration: one where efficiency increases with heat storage, and one where efficiency decreases with heat storage. The changes in the power output and exergy loss are represented as a percentage of their original value, to illustrate the effect of the relative changes in the two values. Note that the decrease in efficiency in the second case is very small.

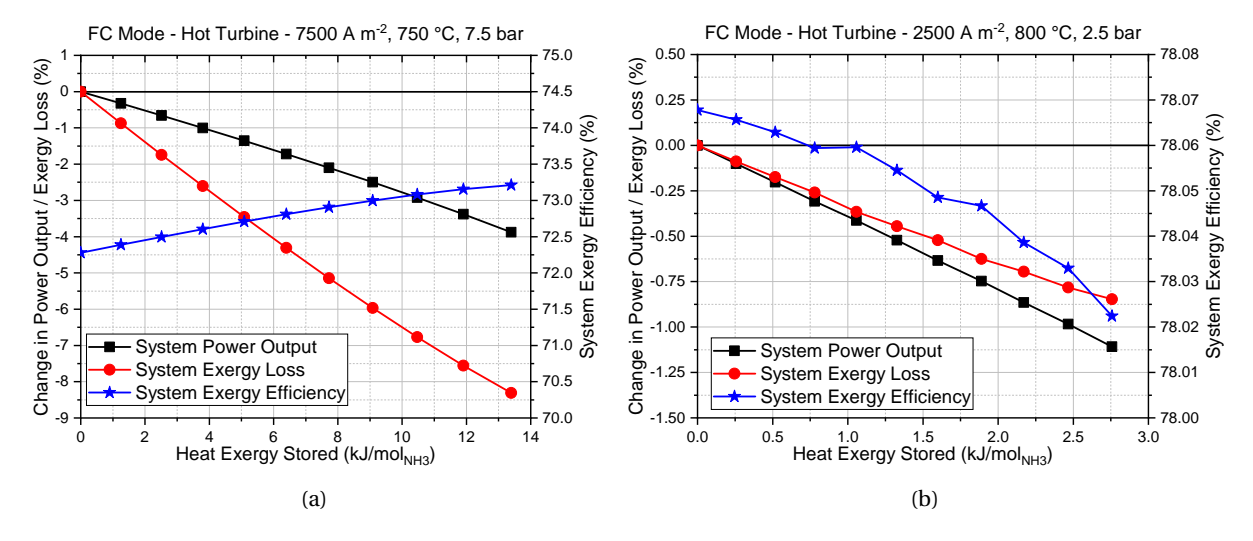


Figure 7.7: Variation of system exergy efficiency, exergy loss, and system power output with respect to amount of heat exergy stored in the TES.

Even in the cases where the efficiency improves with heat storage, the rate of efficiency improvement with respect to heat storage is very inconsistent across operating points. This most often seen in the HT configuration, because the its high recirculation ratios affect the stack power strongly, thus changing the ratio of exergy loss and power. Therefore, the maximum efficiency improvement from heat storage in HT configuration is found to be only 0.98 %-points, which does not occur at the operating point with maximum heat storage. In comparison, the CT configuration sees a more steady correlation between heat storage and efficiency across operating points, probably due to the lower recirculation ratios used on average. Therefore, it achieves a maximum improvement of 5.55 %-points, exactly at the operating point with maximum heat storage.

Despite the counter-intuitive trends of efficiency improvement, the efficiency has been defined in this way primarily because the system is an electricity storage system. This definition of exergy efficiency keeps all electric exergy on one side, and all other exergy storage (chemical or thermal) on the other. Therefore, despite this occasionally peculiar behaviour, this definition of exergy efficiency is still considered acceptable. It must be noted that even at those few points where efficiency decreases with heat storage, it is still desirable to store the maximum heat possible. This is because in a reversible energy storage system, it is desirable to reduce the

combined exergy losses in both modes. Increasing heat storage reduces the losses in each mode, irrespective of the behaviour of the FC mode efficiency value.

As mentioned above, the maximum efficiency improvement in the HT configuration is only 0.98 %-points, at $7500\,\mathrm{Am^{-2}}$, $750\,^\circ\mathrm{C}$ and $10\,\mathrm{bar}$. Therefore, it does not significantly change the trends of system efficiency with respect to the operating parameters, compared to the regular HT configuration without the TES as discussed in Section 6.1. The efficiency continues to monotonically increase with rising stack temperature, and monotonically decrease with rising current density. As before, in the high-efficiency region where electric heating is not eliminated, the efficiency decreases with an increase in stack temperature. The optimum operating pressure continues to be between $2.5\,\mathrm{bar}$ and $5\,\mathrm{bar}$.

In the CT configuration, the maximum efficiency improvement is found to be $5.55\,\%$ -points, at $7500\,\mathrm{A\,m^{-2}}$, $800\,^\circ\mathrm{C}$ and $1.5\,\mathrm{bar}$, due to the much higher heat storage of $\sim\!24\,\mathrm{kJ/mol_{NH_3}}$. This still does not significantly change the trend of efficiency compared to the regular CT configuration as discussed in Section 6.2. The efficiency continued to monotonically increase with rising temperature, and decrease with rising current density. However, in case of pressure variations in the CT configuration, the improvement in efficiency from the use of TES was markedly higher at low pressures. This is simply a result of higher heat storage possibility at lower pressure as explained in Section 7.2.3. Because of this, the optimum pressure in most cases moved downwards to 5 bar, compared to 7.5 bar in the regular system.

EC Mode Performance Variation

The effect of heat storage being made available to the endothermic electrolysis system is rather straightforward. As per the learning from Section 6.4, there is no fresh airflow used for thermal management, which is handled purely through recirculation of the produced oxygen. Therefore, most of the system remains unaffected by the TES system. The heat extracted from the TES is used directly to meet the heat requirements of the endothermic steam reduction reaction. This reduces the electric heat that needs to be provided to the recirculated oxygen stream. Thus, the system power input and the system exergy loss both reduce as more heat is extracted from storage.

The system exergy efficiency defined in Equation (7.1b) can be rewritten in terms of system power input $P_{\text{net,EC,in}}$ [kJ/mol_{NH₃}] and system exergy loss $\vec{E}x_{\text{D,EC}}$ [kJ/mol_{NH₃}], in Equation (7.4). The efficiency therefore depends on the ratio of exergy loss and power input.

$$\eta_{\text{ex,EC}} = \frac{\vec{E}x_{\text{NH}_3,\text{out}} - \vec{E}x_{\text{N}_2/\text{H}_2,\text{in}} - \vec{E}x_{\text{H}_2\text{O},\text{in}} - \vec{E}x_{\text{TES}}}{P_{\text{net,EC},\text{in}}} = \frac{P_{\text{net,EC},\text{in}} - \vec{E}x_{\text{D,EC}}}{P_{\text{net,EC},\text{in}}} = 1 - \frac{\vec{E}x_{\text{D,EC}}}{P_{\text{net,EC},\text{in}}}$$
(7.4)

From simulations, it is observed that the exergy efficiency of the electrolysis system tends to be 2-8 % higher than the exergy efficiency of the electric air superheating process required to support the endothermic reaction. Therefore, reducing the amount of electric heating by using stored heat increases the overall efficiency of the endothermic electrolysis system at any given temperature. It must be noted that in order to use stored heat, the temperature of the electrolysis is reduced by 20 °C. In Section 6.4, it had been shown that in endothermic region, reducing the temperature slightly improves system efficiency. Therefore the stack temperature reduction combined with the heat extraction from storage improves the efficiency of the system. However, since the electrolysis system has a much larger power requirement to begin with, the improvement in efficiency is relatively small. The maximum improvement in electrolysis system efficiency was 0.50 %-points at $5000\,\mathrm{Am^{-2}}$, $750\,^{\circ}\mathrm{C}$ and $1.5\,\mathrm{bar}$, if coupled with the fuel cell mode in HT configuration, and $0.58\,$ %-points at $7500\,\mathrm{Am^{-2}}$, $800\,^{\circ}\mathrm{C}$ and $1.5\,\mathrm{bar}$, if coupled with the CT fuel cell configuration (due to the higher heat stored by the CT configuration).

The trends of electrolysis system efficiency with changing stack operating parameters remains very similar to the regular system without TES. Recall that the system efficiency increased with pressure in endothermic region. This trend is too strong to be affected by the less than 0.58 %-points increase offered by the TES. Therefore, the system efficiency continues to increase with rising pressures. On the other hand, in the regular system, recall that the efficiency remains almost independent of stack temperature or current density. Therefore, the efficiency improvements from the TES change the trend of efficiency.

For low current density points, the quantity of heat stored is dictated by the availability in FC mode. This is larger at lower temperatures, and accordingly the efficiency decreases with temperature. For points with high current density, the quantity of heat stored is dictated by the absorption capacity of the EC mode. This increases with temperature due to lower overpotentials. Therefore, for these points, the efficiency rises with temperature.

There is a similar trend for current density. At low temperatures and high current densities, the heat storage quantity is dictated by the EC mode, and this decreases with increasing current density, resulting in a lower efficiency. At high temperatures and low current densities, the heat storage is dictated by FC mode, and the heat transferred increases with current density. Therefore, the efficiency also increases with current density.

Therefore, 10 bar remains the optimum pressure for the EC mode with TES. However, due the very small changes, the optimum temperature and current density are not straightforward to predict. The optimum current density is an intermediate value like $7500\,\mathrm{A\,m^{-2}}$, and the optimum temperature is $750\,^{\circ}\mathrm{C}$ for coupling with HT configuration, and $800\,^{\circ}\mathrm{C}$ for coupling with CT configuration. However, the variations with current density and stack temperature are less than $0.5\,\%$ -points, therefore are not of great concern.

Reversible System Performance Variation

In this section, the performance improvement offered by TES to the round trip system performance is analysed, in order to draw final conclusions about the viability of introducing TES to the ammonia ReSOC system.

It has been mentioned multiple times in the previous sections, that the change in efficiency caused by the use of TES is not large enough to significantly alter the trends of efficiency with respect to the stack operating parameters. Naturally, this remains true when both the modes are combined as well. The trends of round-trip efficiency with all three stack parameters remain very close to the corresponding trends in the regular system without TES. Only the optimum pressure value for various combinations of temperature and current density can sometimes shift upwards or downwards. Overall, the maximum efficiency points for both the HT and CT configurations are exactly the same points as for the regular system.

Conclusions for Investigation of TES

The maximum RTE improvement in the reversible system with an HT configuration in mode is only ~ 1 %-points. Correspondingly, due to the higher heat storage possibility, the maximum RTE improvement achieved using the CT configuration is 4.5 %-points. However, as mentioned previously, the maximum heat storage, and hence RTE improvement, occurs at points of intermediate stack efficiency. However, these are not typically the points of greatest interest. At the points of maximum efficiency, the TES system did not bring about any significant benefit. For the HT configuration, in fact, the improvement to the region of high efficiencies is so little that the optimum RTE remains at a point where no heat storage is possible (due to oxygen starvation limit)! Moreover, for the CT configuration, an improvement of only 0.59 %-points is achieved for the peak efficiency. Therefore, thermal energy storage, though beneficial in theory, does not improve the peak efficiency of the designed system.

7.3. Key Take-aways

7.3. Key Take-aways

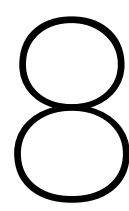
In the first part of this chapter, the system from Chapter 6 was modified with an afterburner in the fuel cell mode. This served as a point of comparison, to better understand the benefits of operating a system without an afterburner.

- The results of this section confirm that it is thermodynamically preferable to store unutilised fuel and reuse it in the EC mode, than to burn it in an afterburner.
- The expected saving from removing an afterburner from the system is the elimination of exergy losses caused by combustion.
- The use of an afterburner also requires higher exergy losses in electrolysis, caused by the generation of additional hydrogen to recover the fuel burnt in the afterburner.
- An afterburner in the FC mode generates significant heat at high temperatures. The temperature difference causes large exergy losses when this heat is utilised through heat exchangers. This remains the largest source of exergy destruction, causing larger losses than the combustion itself.
- The use of an afterburner is particularly wasteful at low pressures, when a lot of thermal exergy is unutilised by the air turbines and is lost to the environment.
- A system with an afterburner needs to be supported by the incorporation of an auxiliary cycle, which greatly reduces the losses to the environment. However, even a highly efficient power cycle includes significant exergy losses of its own.
- At the high efficiency operating points which are of interest, elimination of the afterburner increases the efficiency of the system by 1.4-3.4 percentage points. If an auxiliary cycle is not used with the afterburner, the difference is even higher: between 4-6 percentage points.

The second part of this chapters attempts to improve the efficiency of the system from Chapter 6 by utilising the heat produced in the fuel cell mode to drive part of the endothermic reaction in electrolysis mode. A hypothetical PCM-based thermal energy storage system was modelled for this purpose.

- Implementation of TES reduces exergy losses in both modes. In FC mode, the savings come from reduced exergy losses to the environment. In EC mode, the savings come from reduced exergy destruction in electric heating.
- Results from literature credit TES with increasing the peak round trip efficiency by values from 10 percentage points [42] up to 29 %-points [27].
- However, for the system designed in this work, the introduction of TES improved the peak round trip efficiency by a mere 0.59 %-points. The maximum improvement was 4.5 %-points, which occurred at much lower base RTE, and a current density of $7500\,\mathrm{Am}^{-2}$.
- The primary reason for the lacklustre effect of TES is the low availability of high-temperature heat at the points of highest RTE. For example, at the point of peak RTE in the cold turbine fuel cell configuration, the heat available for storage from the fuel cell is a mere 8 % of the heat required by the electrolysis.
- This low heat availability is a result of three design choices: internal endothermic ammonia cracking, reliance on air recirculation for fresh air preheating, and the lack of an afterburner. The first two choices make productive use of the heat generated by the fuel cell, whereas the last choice prevents the generation or more heat from combustion.
- A point to be noted is that the unavailability of excess heat for TES is not a disadvantage, and rather is a testament to the high efficiency of the designed system.
- On the other hand, if high power density is a priority, then the introduction of the TES at 7500 Am⁻² can be a viable alternative. The 4.5 %-point improvement at this operating point, though small, is not insignificant.

The results of this chapter show that neither an afterburner nor a thermal energy storage system are able to significantly increase the round trip efficiency of an energy storage system based on ammonia and ReSOCs. Though the results are negative in terms of further improvement, they serve to highlight the benefits of the system designed in Chapter 6. Systems like a high-temperature TES are difficult to implement due to insulation, and material stability challenges. Additionally, afterburners and their associated auxiliary power cycles also increase the number of components and complexity of the system, in addition to their exergy destruction. Therefore, while there is no techno-economic evaluation carried out in this thesis, it is safe to say that the recommendation not to use afterburners or thermal energy storage is likely to have positive implications on the capital cost of such a system.



Conclusions and Future Work

8.1. Conclusions and Discussion

- A high efficiency energy storage system using ammonia in ReSOCs is developed. The developed system design is able to attain a peak round trip efficiency as high as 61.20 %. While this peak is achieved at a low current density of $2500\,\mathrm{Am^{-2}}$, the model can maintain round trip efficiencies over 57 % even at current densities as high as $10000\,\mathrm{Am^{-2}}$.
- The efficiency is comparable to that reported by thermodynamically well-studied models in literature. For example, the methanol-based ReSOC model of Giannoulidis [42], reported an efficiency of 56.72 %, which was attained after using thermal energy storage between the two modes.
- The current model is able to achieve efficiency in the same range as similar models despite having no thermal energy storage or afterburner to assist with the heat demands of the feed streams.
- The utility of air recirculation in optimising the system performance has been demonstrated.
- Therefore it has been demonstrated that ammonia is definitely a suitable candidate for use in ReSOC based energy storage system.
- The various design decisions taken have been studied and explained using exergy analysis.

The purpose of this thesis was to develop a high efficiency process design for an energy storage system based on ReSOCs using ammonia. Such a design was successfully developed with a round trip efficiency higher than 60 %. The development was accompanied by detailed thermodynamic analyses.

The developed system is most efficient at the highest possible stack temperature (with some exceptions at very low current density), due to reduced exergy destruction in the fuel cell stack, as well as lower exergy destruction in the BoP components due to lower airflow. The choice of optimum pressure is more complicated, and depends on the other parameters. High pressures are preferred in electrolysis mode, whereas intermediate pressures (2.5-5 bar) are preferred in fuel cell mode. Ultimately, the optimum pressure varies between 5 and 7.5 bar.

After optimisation, electric heating of the input streams is completely eliminated. This effectively eliminates one of the major sources of exergy losses in the basic system. However, even after optimisation, the largest source of exergy losses continues to be external cooling, mainly for the steam condenser. Even after elimination of electric heating, evaporation of water in the electrolysis mode remains a process with high exergy destruction, since it uses sensible waste heat to provide latent heat, meaning that temperature differences are invariably large. Integrating these two processes using low temperature thermal energy storage (TES) can help eliminate both these major losses, and is a good point for future work. However, the heat from the ammonia synthesis shall have to be redirected to purposeful use.

Electric heating is still used in heating the stack for endothermic electrolysis. The use of high temperature TES using heat from the fuel cell mode was attempted to reduce the losses associated with this. TES was found to improve round trip efficiency in general. However there was negligible improvement in the peak round trip efficiency, because very little excess heat was available in the fuel cell mode at the most efficient operating

Table 8.1: Comparison of all the major configurations analysed in this thesis. All the configurations are compared at their own optimum operating points for round trip efficiency.

Configuration No.	1	2	3	4	5	
Process	Exergy Losses (kJ/mol _{NH3})					
ReSOC stack	31.93	28.41	24.66	26.73	25.04	
Synthesis reaction	4.66	4.73	4.73	4.73	4.73	
Expansion & Compression	44.65	16.09	17.18	18.82	16.69	
Heat exchange	-	21.45	21.90	30.66	21.26	
Afterburner	-	-	-	9.24	-	
Auxiliary Power Cycle	-	-	-	11.21	-	
Electric heating	239.35	15.86	15.72	19.09	14.00	
Refrigeration	1.08	1.08	1.08	1.08	1.08	
Mixing	4.46	5.46	4.75	9.98	4.46	
Separation	6.97	7.00	7.01	9.02	7.01	
Environment	193.12	31.81	32.27	32.78	31.34	
Total	526.23	131.89	129.28	173.33	125.59	
System round trip efficiency	19.79 %	60.75 %	61.20 %	58.57 %	61.79 %	

Configuration Legend:

- 1. Basic FC, Basic EC (see Chapter 5)
- 2. Hot Turbine FC, Hot Turbine EC (see Chapter 6)
- 3. Cold Turbine FC, Hot Turbine EC (see Chapter 6)
- 4. Hot Turbine FC + Afterburner + Aux. Power Cycle, Cold Turbine EC (see Chapter 7)
- 5. Cold Turbine FC, Hot Turbine EC, Thermal Energy Storage (see Chapter 7)

points. This is because very little heat is produced by the stack at those points, most of which gets consumed by ammonia cracking and inlet stream preheating.

The presence of ammonia as a fuel has both drawbacks and benefits. The primary drawback is the exergy destruction in the additional processing that goes into synthesis and consumption of ammonia. However, these are compensated by the exergy savings from elimination of electric heating in the feed water evaporator, that is enabled only because of heat integration from ammonia synthesis reactors (and hydrogen compressor intercoolers). In the fuel cell mode, the significant cooling effect of internal ammonia cracking reduces the airflow required for stack cooling, and the associated exergy losses in the BoP.

The heat integration in this work is accomplished without the use of an afterburner in either mode. Operation without an afterburner in fuel cell mode increases the round trip efficiency by 1.4 - 3.4 %-points. This is made possible only through extensive air recirculation, which plays a vital role in making the system function without electric air heating or an afterburner in fuel cell mode. While air recirculation itself is not a new concept, it has been heavily relied upon in this work for the specific purpose of enabling the elimination of the afterburner. Even in the cold turbine configuration where air preheating is not an issue, air recirculation is desirable for reducing the air compression work which the air turbine cannot supply due to low turbine inlet temperature.

It is known from literature that the electrolysis mode performs the best when the airflow is minimal, which typically occurs in the thermoneutral zone. In the system designed in this work, the fresh airflow from the environment is maintained to be zero even in endothermic mode by using only recirculated oxygen for the stack thermal management, thus gaining the benefits of thermoneutral operation even in the endothermic mode. Because of zero fresh airflow, the electrolysis system efficiency remains almost independent of current density and temperature throughout endothermic mode.

Finally, the location of the air turbine in the exhaust stream plays an important role in the heat integration scheme for preheating the inlet streams. For simple systems, placing the turbine upstream, before any recuperation ("hot turbine") can boost the round-trip efficiency of the system across most operating points, by 3-8 %-points, which is a significant amount. In general, the higher efficiency comes from lower exergy losses

8.2. Future Work 109

to the environment, and lower exergy destruction in heat exchangers and mixers. Finding the precise reasons behind these trends will require further study in the future.

Table 8.1 compares all the major configurations of the energy storage system studied in this work, in terms of exergy losses and round trip efficiency. The table shows that the two improved configurations (#2 and #3) and the thermal energy storage system (#5) achieve approximately the same peak efficiency of \sim 61 %. Therefore, any of these three configurations can be recommended. However, configuration #2 is the recommended design, since it does not require a thermal energy storage. Additionally, as discussed in Section 6.3, the hot turbine configuration (#2) consistently gets better results than the cold turbine configuration (#3), except for 4 out of 80 points.

To summarise, a high efficiency ReSOC system for energy storage was successfully developed using ammonia. Exergy analysis was carried out for all the designed configurations. High round trip efficiency was achieved without the use of afterburners, or thermal energy storage, making the system simple and possibly reducing the capital cost.

8.2. Future Work

- The work in this thesis focused purely on thermodynamic optimisation. Techno-economic analysis of such a system can lead to further insights about the benefits of air recirculation and designs without an afterburner.
- 2. High temperature heat storage was found to be not useful to boost the peak efficiency. However, integration of steam condensation in FC mode with water evaporation in EC mode using low temperature TES can be investigated further.
- 3. The hot turbine configuration was found to be generally much more efficient than the cold turbine configuration. However, obtaining clear reasons for this observation will require further analysis in detail
- 4. More complex combinations of turbine and heat exchanger placement in the air stream can be investigated, along with auxiliary power cycles, to reduce the losses to the environment even further.
- 5. Wang et al. [43] used pure oxygen stored from the EC mode in the FC mode. The effects of such an arrangement for stacks with internal cracking and no afterburner can be investigated through detailed exergy analysis.



Ammonia Synthesis Loop

Recycle Loop Configurations

Examples of possible recycle loop configurations are shown in Figure A.1. The figure and the comparative analysis is taken from Appl [8].

In the simple configuration (Config. A), the ammonia condensation is carried out immediately after the reactor, before mixing with the fresh (makeup) feed gas. This is most suitable if the makeup gas is very pure. This configuration achieves the highest ammonia concentration at the condenser inlet (enabling better separation) and the lowest ammonia content at the reactor inlet (enabling higher conversion).

If the makeup gas has impurities like water or carbon dioxide, ammonia can also be condensed after mixing with the makeup gas (Config. B). This can help remove some impurities from the feed, since water and carbon dioxide dissolve in liquid ammonia, and are removed from the loop along with the ammonia. However, mixing the feed gas reduces the ammonia concentration at the condenser, therefore achieving lower separation at the same temperature, and leading to higher ammonia concentration at the reactor inlet. Additionally, all the ammonia has to be compressed in the recycle gas compressor.

The compression of ammonia can be avoided by mixing the gases at a lower pressure, and compressing the recycle gases after the ammonia separation. This is shown in Config. C.

Lastly, the condensation can also be split up into two pressures, as in Config. D. Before compression and mixing, the lower pressure ammonia can be condensed with refrigeration. After mixing and compression, the some more ammonia can be condensed at the higher pressure with cooling water.

In this work, the simple Configuration A was chosen, since the feed gas was already purified.

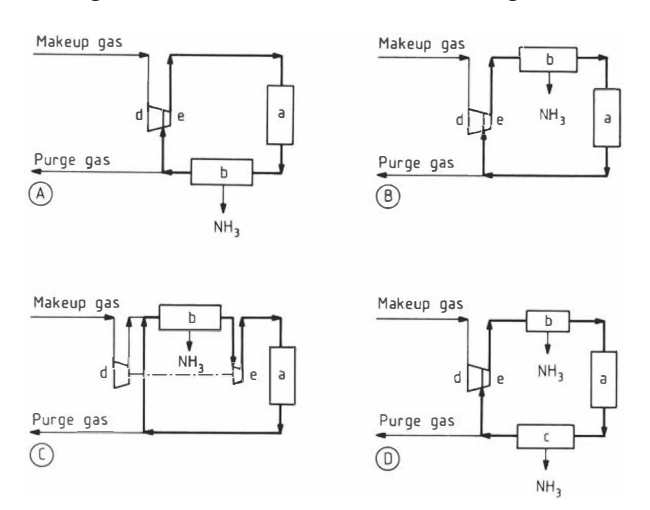


Figure A.1: Various recycling configurations for ammonia synthesis. The components are labelled as follows: a = Synthesis Reactor, b = Refrigerated Condensation, c = Ambient Condensation, d = Feed/Make-up gas compressor, e = Recycle gas compressor. Figure taken from the work of Appl [8].



Stack Performance Tests

The results of stack study from Section 5.1 are described in detail in this appendix. Figure B.1 shows the effect of stack temperature, pressure and current density on the Nernst voltage, overpotential, and cell voltage for each mode.

Temperature Variation

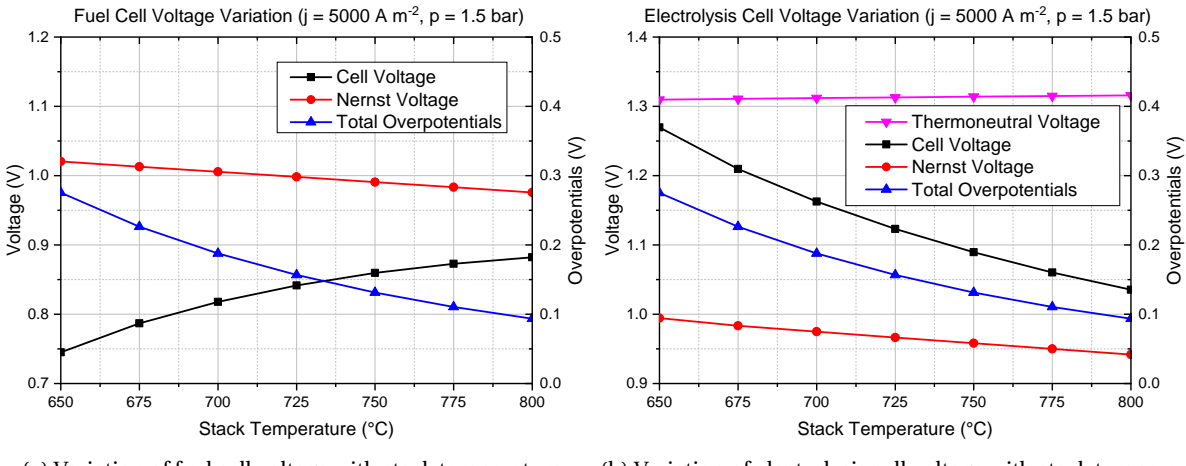
Temperature change has a large effect on stack performance. The Nernst voltage always decreases with an increase in temperature. Moreover, the activation and Ohmic overpotentials also become smaller at higher temperatures (the concentration overpotential is negligible in this range). In electrolysis mode, both these effects combine to create a large decrease in cell voltage at higher temperatures. In fuel cell mode, the reductions in Nernst voltage and the overpotential oppose each other. But it can be observed from Figure B.1a, that the change in overpotential is larger than the change in Nernst voltage. Therefore, in fuel cell mode, the cell voltage decreases with rising temperature, following the trend of the overpotential. Looking at the changing slope of the total overpotential, it can be predicted that at some higher temperature, the Nernst voltage reduction will start to dominate, reversing the improving trend of the fuel cell voltage. But this does not occur within the temperature range considered in this thesis.

Pressure Variation

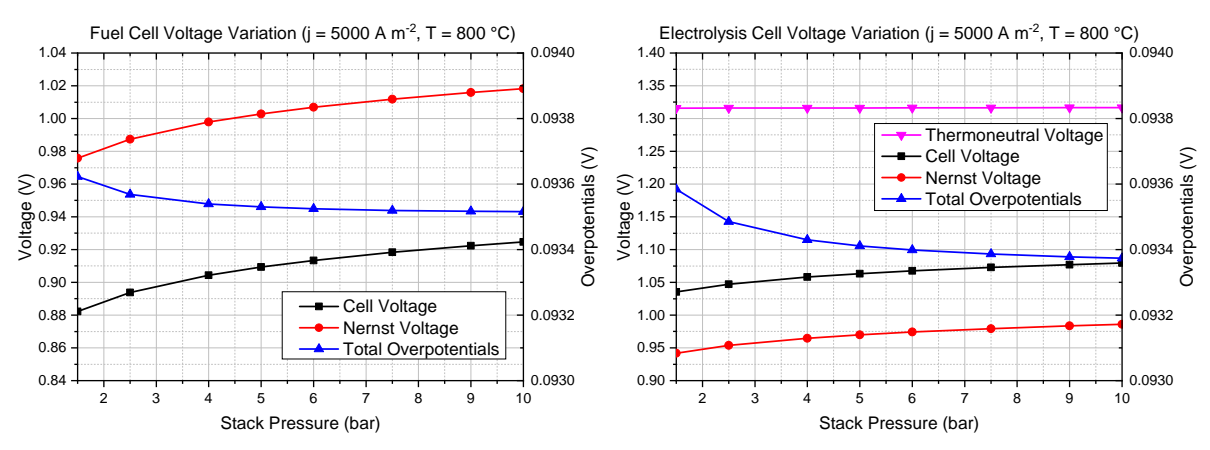
Increasing pressure also increases the Nernst potential in both modes. But, as can be seen from the scale of the right-side Y-axis in Figures B.1c and B.1d, the stack pressure has a very minuscule effect on the total overpotential. The small improvement arises from better diffusion which reduces concentration overpotentials. At much higher current density and/or much higher fuel/steam utilisation, the concentration overpotentials would be more significant, and pressure-driven reductions in the overpotentials might be more visible on the overall cell performance. However, it has been observed that even at the upper limits of current density and fuel utilisation considered in this thesis, the concentration overpotential still does not dominate. Therefore, the cell voltage entirely follows the trend of Nernst potentials, increasing with pressure.

Current Density Variation

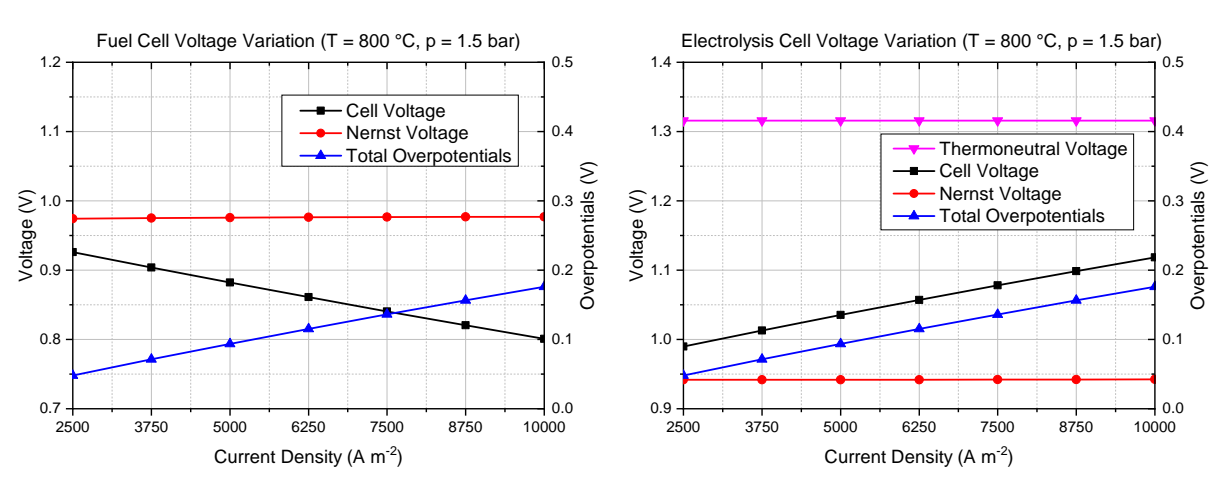
As expected, current density does not affect the Nernst voltage (except negligible variations caused by oxygen concentration due to changing excess air ratio). All the overpotentials increase with current density. The overall change in overpotentials is linear within our operating range. This is expected, because at this range of current density, the activation overpotentials are high but change slowly, and the concentration overpotentials are negligibly small. Therefore, the linear Ohmic overpotential dominates the overall trend. In effect, the cell voltage is also linearly dependent on the current density.



- (a) Variation of fuel cell voltage with stack temperature.
- (b) Variation of electrolysis cell voltage with stack temperature.



- (c) Variation of fuel cell voltage with stack pressure.
- $\label{thm:continuous} \mbox{(d) Variation of electrolysis cell voltage with stack pressure.}$



- (e) Variation of fuel cell voltage with current density.
- (f) Variation of electrolysis cell voltage with current density.

Figure B.1: Variation of cell voltage with stack operating parameters.



Fuel Cell Air Flow Variations

Methodology

The purpose of this section is to find the qualitative relationship between air recirculation, the various flow rates and the oxygen concentrations of the fresh airflow, the recirculated airflow, the stack inlet airflow, the stack outlet airflow and the exhaust airflow. These are shown in Figure C.1.

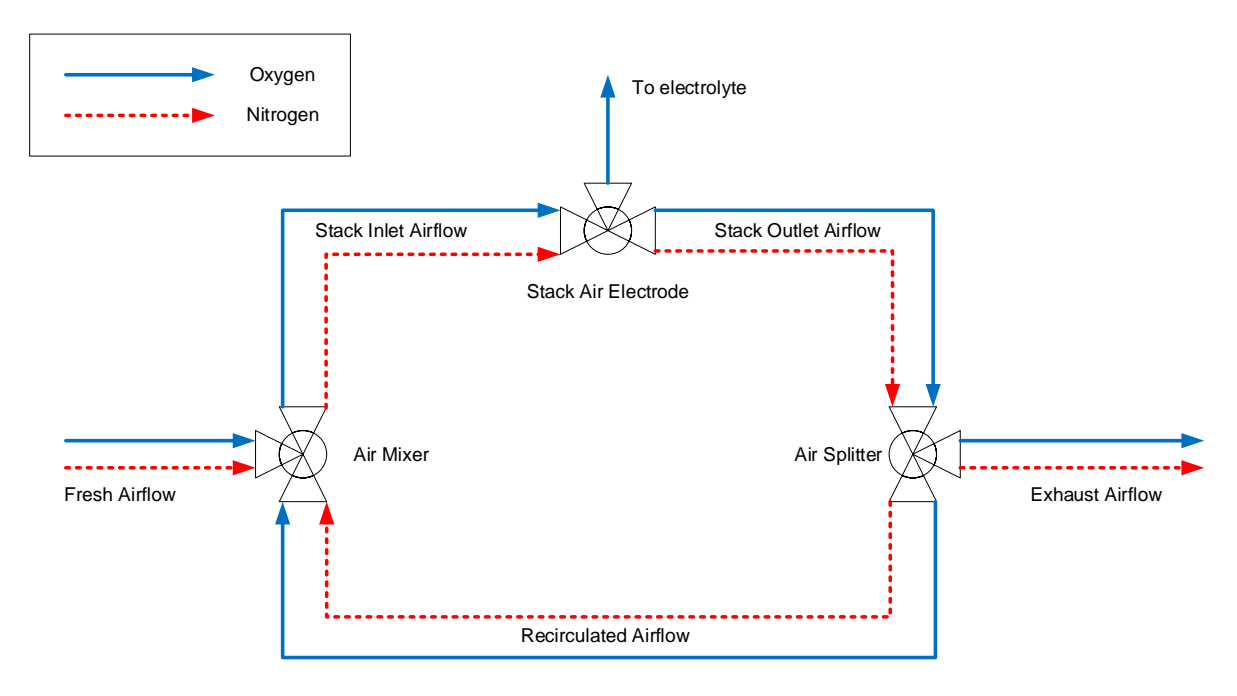


Figure C.1: Simple schematic for air flows in a fuel cell stack with recirculation

From the figure, there are 11 flow rate variables. To solve for these 11 variables, 11 constraints are required. 6 constraints are obtained from species balance equations:

- 2 constraints for species balance of oxygen and nitrogen at air mixer
- 2 constraints for species balance of oxygen and nitrogen at air splitter
- 2 constraints for species balance of oxygen and nitrogen at stack air electrode

2 constraints come from known quantities:

• 1 constraint from known composition of the fresh airflow (21 % oxygen from atmosphere).

• 1 constraint from known oxygen consumption in the stack (assumed constant at 1 mols⁻¹ for this calculation).

3 constraints come from variables which are varied as independent variables during this calculation:

- 1 constraint from the fixed total flow rate of the stack inlet airflow. (two arbitrary values are tested; $32 \, \text{mol} \, \text{s}^{-1}$ and $64 \, \text{mol} \, \text{s}^{-1}$).
- 2 constraints from the air recirculation ratio, one each for oxygen and nitrogen (values are varied from 1 % to 85 %).

Therefore, we have 11 variables and 11 constraints, and this system can be solved accordingly. The solution was carried out by iterative numerical calculations in MS Excel. The relevant results are plotted in the following graphs.

Fresh and Exhaust Airflows

The variation of fresh and exhaust airflows with varying air recirculation are seen in Figure C.2. Naturally, the two figures are similar, since the fresh and exhaust flows maintain a constant difference of 1 mols⁻¹ (i.e. the oxygen consumption in the stack).

The important point to note is that both the airflows vary linearly with air recirculation, and that the slope of their variation is almost proportional to the total stack inlet airflow.

Oxygen Content at the Stack Inlet and Outlet

The variation of oxygen content with air recirculation is shown in Figure C.3, whereas their variations with fresh airflow is shown in Figure C.4.

From Figure C.3, it is seen that both the inlet and outlet oxygen content dropped faster with recirculation when the stack inlet airflow was lower. Therefore the Nernst voltage would also be expected to reduce faster with increasing recirculation if the stack inlet airflow would be lower.

It is interesting to note from Figure C.3b that the outlet oxygen content depends solely on the fresh airflow, and not on the total stack inlet airflow or on air recirculation. This was also solved analytically to arrive at the expression for minimum allowed airflow shown in Equations (6.1) and 6.2.

Ratio of Recirculated Airflow to Fresh Airflow

The air recirculation ratio is defined as the fraction of the stack outlet airflow that is recirculated. The ratio of this recirculated airflow to the fresh airflow (at constant stack inlet airflow) also varied accordingly. This variation is shown in Figure C.5.

An interesting observation is that as the total stack inlet airflow increases, the ratio of recirculated air to the fresh air increases, at constant air recirculation ratio. This means that at the same air recirculation ratio, the fresh air preheating temperature required to attain the stack inlet temperature is lower.

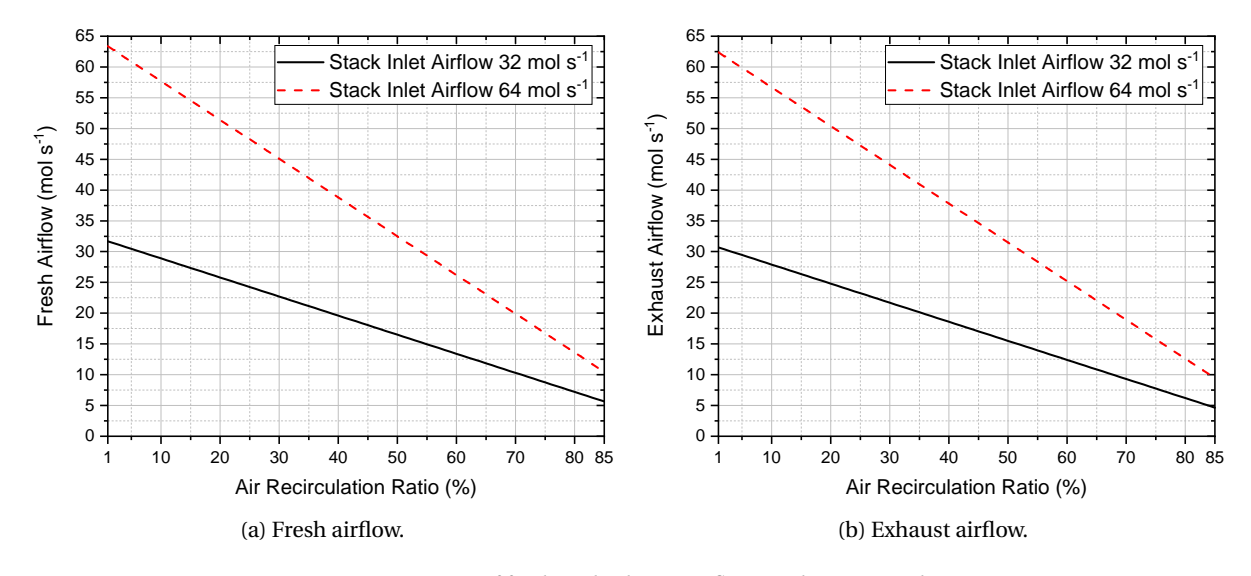


Figure C.2: Variation of fresh and exhaust airflows with air recirculation.

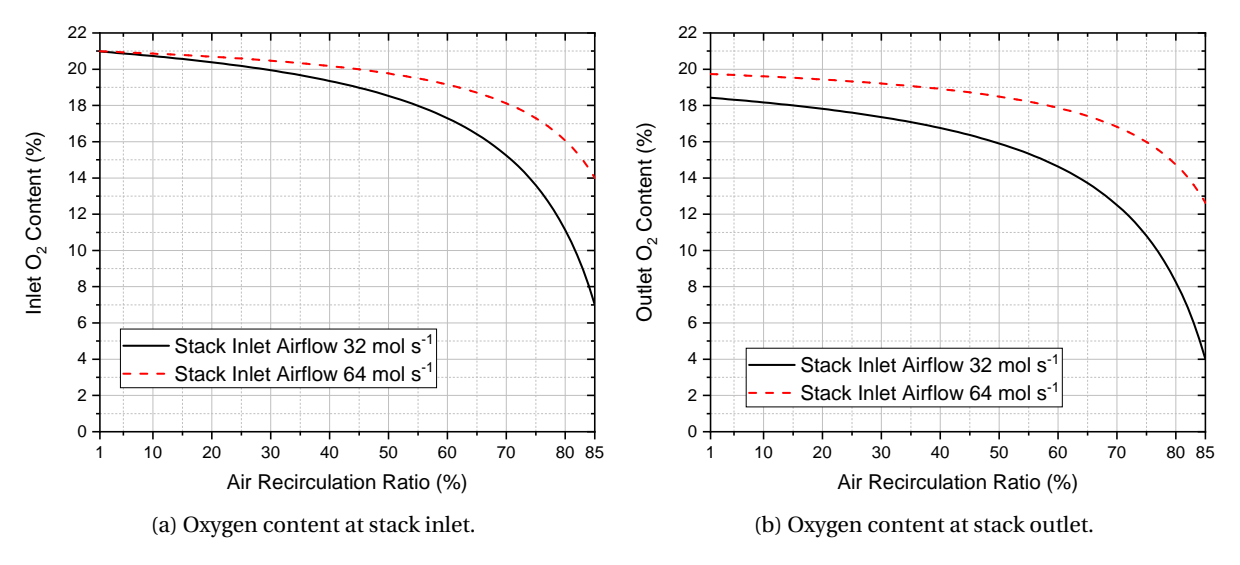


Figure C.3: Variation of oxygen content with air recirculation.

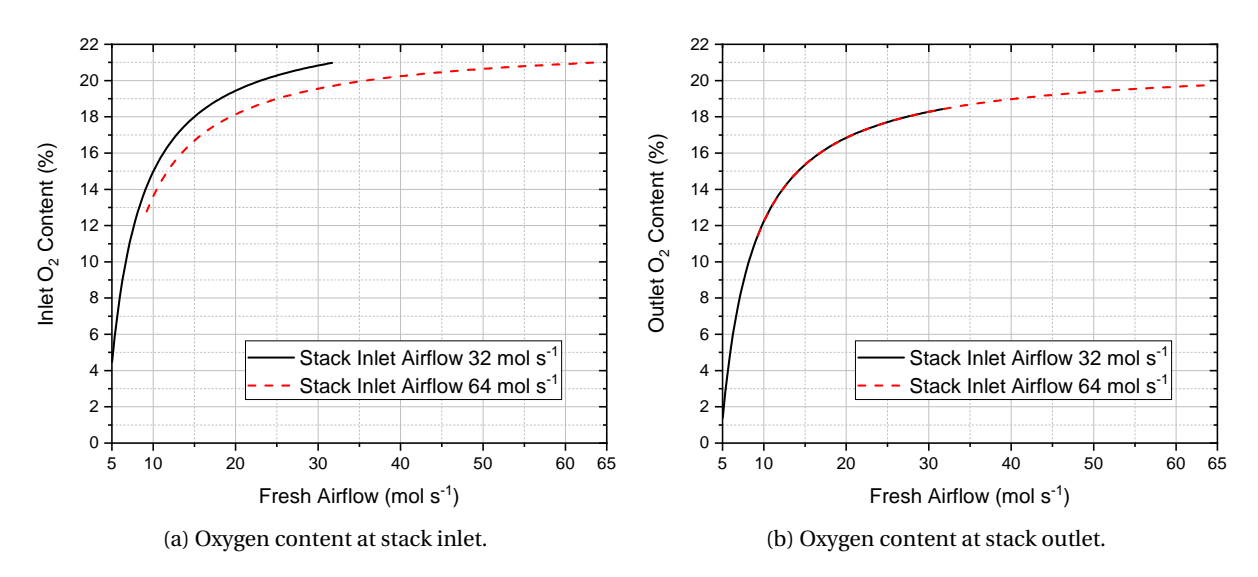


Figure C.4: Variation of oxygen content with fresh airflow.

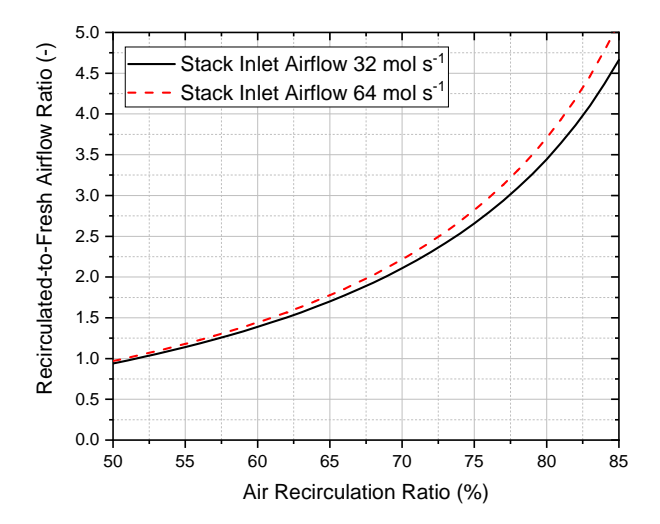


Figure C.5: Variation of the ratio of recirculated airflow to fresh airflow, based on variation in air recirculation ratio.



Exergy Flow Diagrams

The comparison between the basic configuration and the improved configuration (both at their optimum operating points) is represented through exergy flow diagrams in Figures D.1, D.2, D.3 and D.4. These diagrams constitute a detailed graphical representation of the results from Tables 5.3, 6.4, and 6.5.

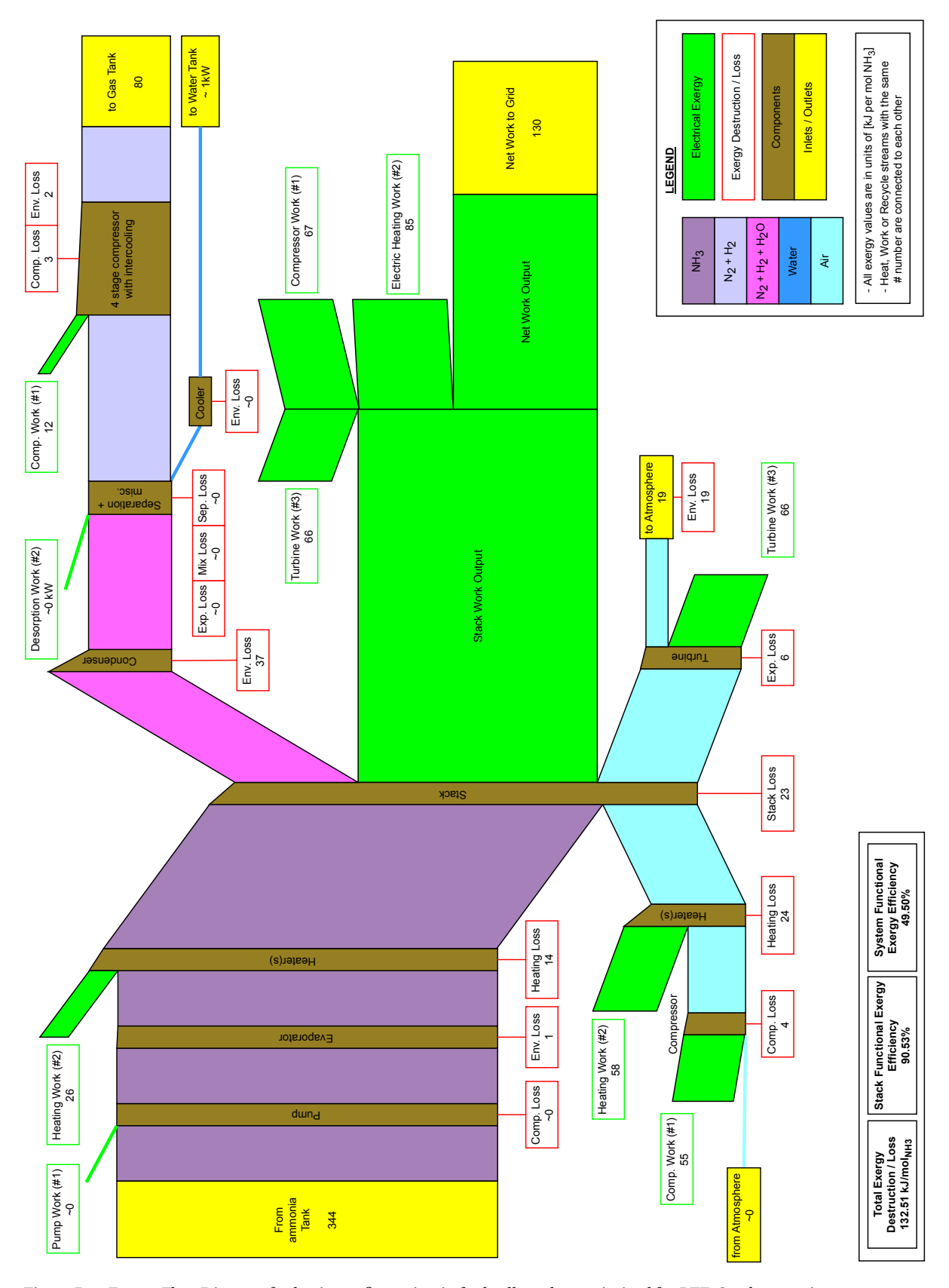


Figure D.1: Exergy Flow Diagram for basic configuration in fuel cell mode - optimised for RTE. Stack operating parameters: $700\,^{\circ}$ C, 8.5 bar, $2500\,\text{Am}^{-2}$.

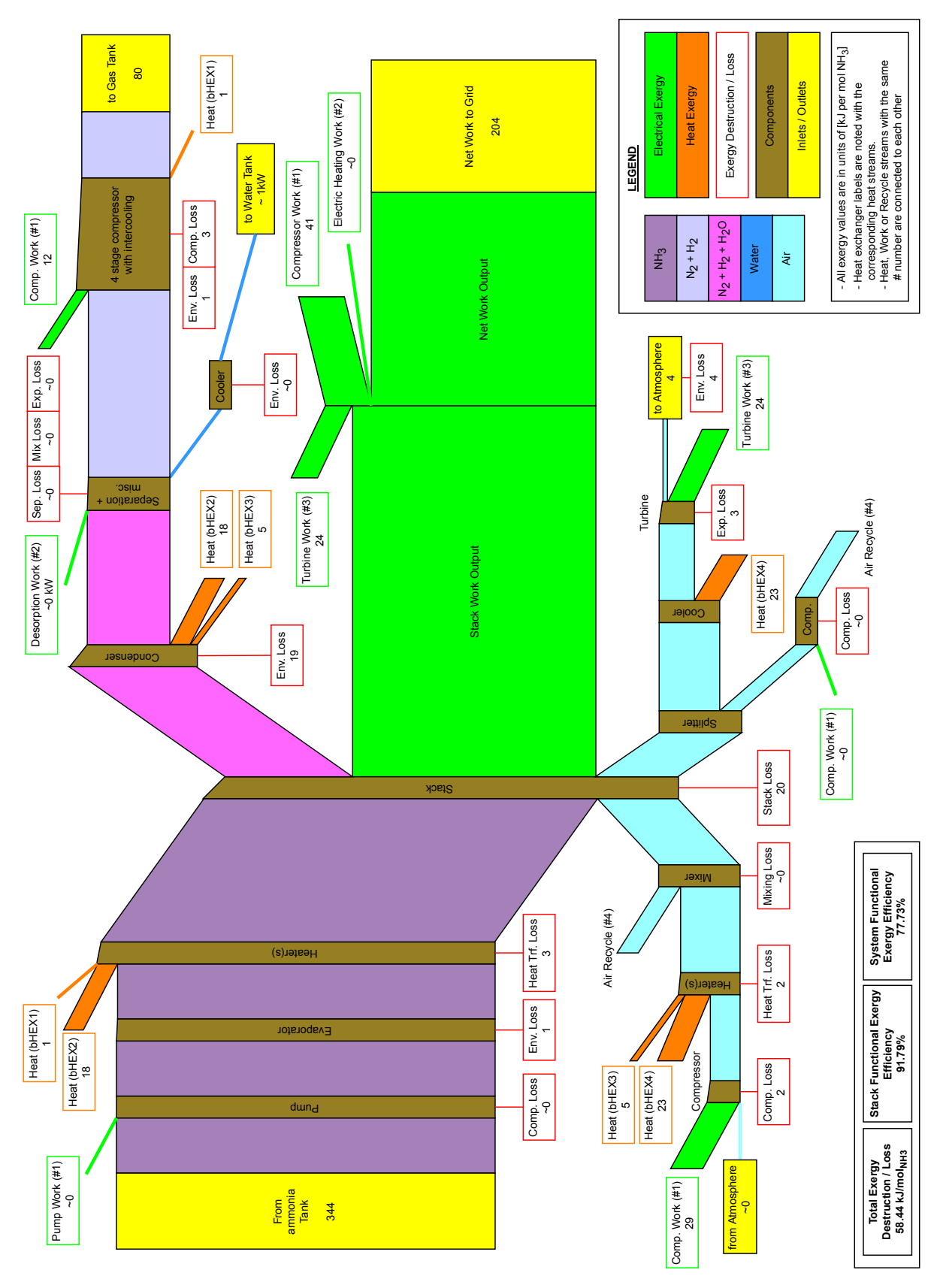


Figure D.2: Exergy Flow Diagram for improved configuration in fuel cell mode - optimised for RTE. Stack operating parameters: $800\,^{\circ}$ C, $7.5\,\text{bar}$, $2500\,\text{A}\,\text{m}^{-2}$.

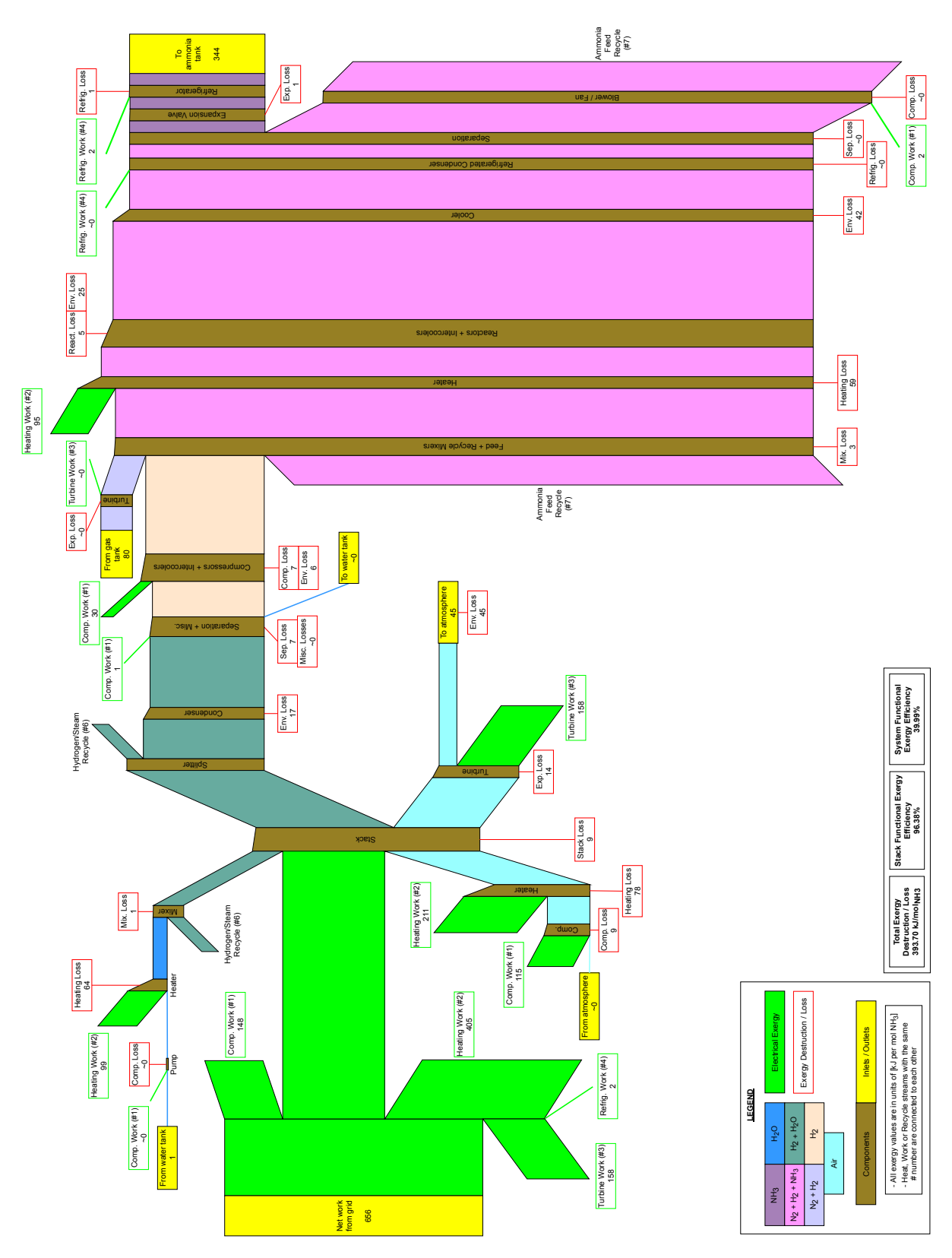


Figure D.3: Exergy Flow Diagram for basic configuration in electrolysis mode - optimised for RTE. Stack operating parameters: $700\,^{\circ}$ C, $8.5\,\text{bar}$, $2500\,\text{Am}^{-2}$.

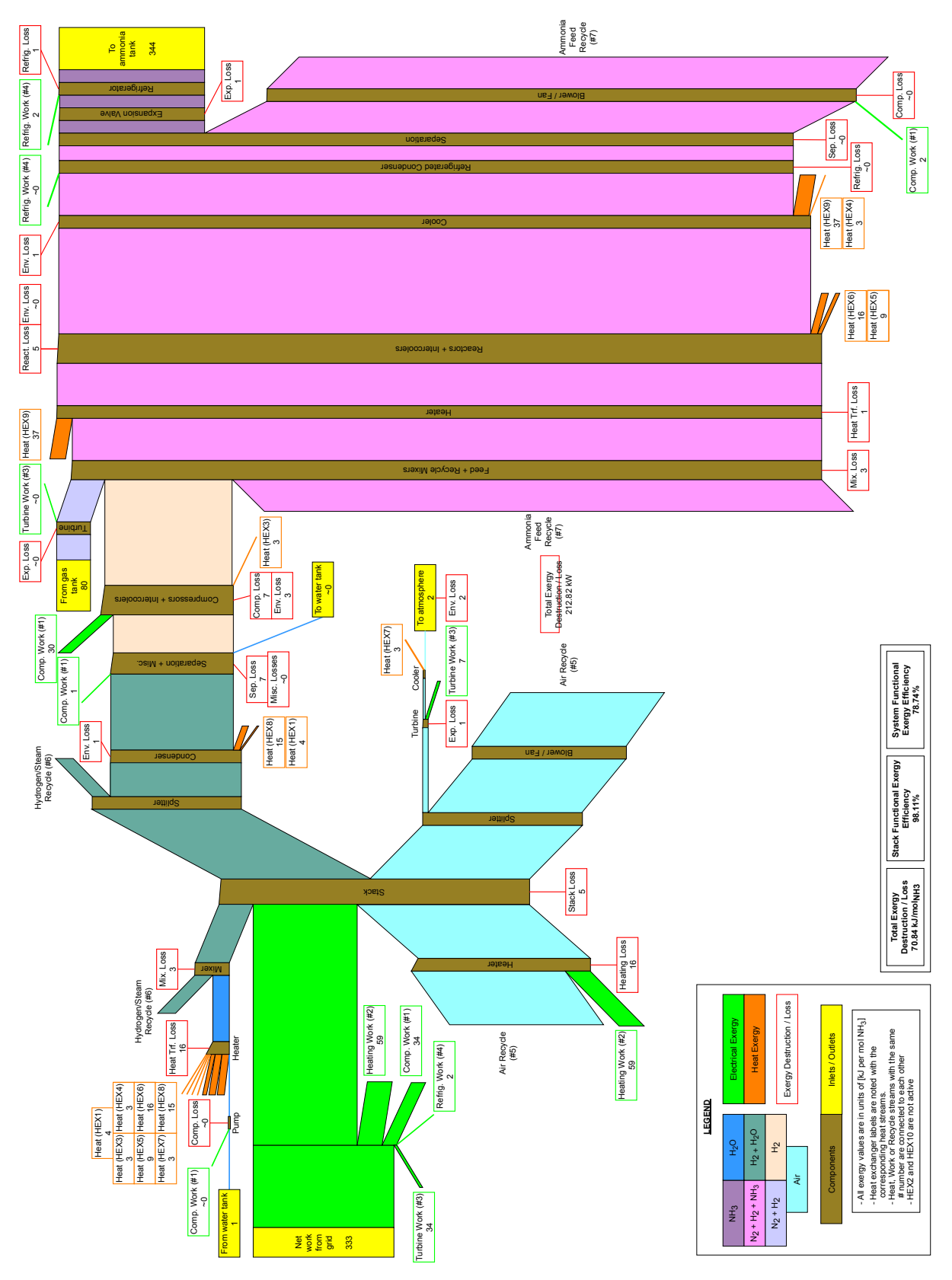


Figure D.4: Exergy Flow Diagram for improved configuration in electrolysis mode - optimised for RTE. Stack operating parameters: $800\,^{\circ}$ C, $7.5\,$ bar, $2500\,$ Am $^{-2}$.

- [1] D. R. Morris and J. Szargut, "Standard chemical exergy of some elements and compounds on the planet earth", *Energy*, 11(8):733–755, 1986. ISSN 0360-5442. doi:10.1016/0360-5442(86)90013-7.
- [2] M. Hauck, S. Herrmann, and H. Spliethoff, "Simulation of a reversible SOFC with Aspen Plus", *International Journal of Hydrogen Energy*, 42(15):10329–10340, 2017. ISSN 0360-3199. doi:10.1016/j.ijhydene.2017.01.189.
- [3] A. Buttler, R. Koltun, R. Wolf, and H. Spliethoff, "A detailed techno-economic analysis of heat integration in high temperature electrolysis for efficient hydrogen production", *International Journal of Hydrogen Energy*, 40(1):38–50, 2015. ISSN 0360-3199. doi:10.1016/j.ijhydene.2014.10.048.
- [4] S. Diaz Rodriguez, "Design and Modeling of an Energy Storage System based on Solid Oxide Reversible Cells with Syngas as Fuel and Co-Electrolysis of CO₂ and H₂O", Master's thesis, Delft University of Technology, 2018. URL http://resolver.tudelft.nl/uuid:4689ac2b-d4eb-4ace-a112-d63259c6f2ad.
- [5] M. Magno, L. Benini, R. Giuffrida, S. Leonardi, and D. Brunelli, "A portable hybrid hydrogen fuel cell-battery power unit for wireless sensor network", 2014 International Symposium on Power Electronics, Electrical Drives, Automation and Motion, SPEEDAM 2014, pages 173–178, 2014. doi:10.1109/SPEEDAM.2014.6872099.
- [6] C. H. Wendel, "Design and Analysis of Reversible Solid Oxide Cell Systems for Electrical Energy Storage", Doctoral thesis, Colorado School of Mines, 2015. URL http://hdl.handle.net/11124/17130.
- [7] M. H. Khademi and R. S. Sabbaghi, "Comparison between three types of ammonia synthesis reactor configurations in terms of cooling methods", *Chemical Engineering Research and Design*, 128:306–317, 2017. ISSN 0263-8762. doi:10.1016/j.cherd.2017.10.021.
- [8] M. Appl, "Ammonia, 2. Production Processes", in *Ullmann's Encyclopedia of Industrial Chemistry*. Wiley-VCH, 2011. ISBN 9783527306732. doi:10.1002/14356007.002_011.
- [9] IEA. "Renewables 2019". Technical report, IEA, Paris, 2019. URL https://www.iea.org/reports/renewables-2019.
- [10] NREL. "Utility-scale energy technology capacity factors". (Accessed February 9, 2020). URL https://www.nrel.gov/analysis/tech-cap-factor.html.
- [11] P. Breeze. *Power System Energy Storage Technologies*. Academic Press, 2018. ISBN 9780128129029. doi:10.1016/C2016-0-03680-X.
- [12] X. Luo, J. Wang, M. Dooner, and J. Clarke, "Overview of current development in electrical energy storage technologies and the application potential in power system operation", *Applied Energy*, 137:511–536, 2015. ISSN 0306-2619. doi:10.1016/j.apenergy.2014.09.081.
- [13] F. Yang and R. Pitchumani, "Transport and Electrochemical Phenomena", in *Fuel Cell Technology: Reaching Towards Commercialization*, N. Sammes, Ed., pages 69–163. Springer, London, 2006. ISBN 9781846282072. doi:10.1007/1-84628-207-1_4.
- [14] M. Ni, M. K. Leung, K. Sumathy, and D. Y. Leung, "Potential of renewable hydrogen production for energy supply in Hong Kong", *International Journal of Hydrogen Energy*, 31(10):1401–1412, 2006. ISSN 0360-3199. doi:10.1016/j.ijhydene.2005.11.005.
- [15] M. Appl, "Ammonia, 1. Introduction", in *Ullmann's Encyclopedia of Industrial Chemistry*. Wiley-VCH, 2011. ISBN 9783527306732. doi:10.1002/14356007.a02_143.pub3.

[16] R. O'Hayre, S.-W. Cha, W. G. Colella, and F. B. Prinz. *Fuel Cell Fundamentals*, 3rd Edition. John Wiley & Sons, 2016. ISBN 99781523110247. URL https://app.knovel.com/hotlink/toc/id:kpFCFE0004/fuel-cell-fundamentals/fuel-cell-fundamentals.

- [17] S. Dharmalingam, V. Kugarajah, and M. Sugumar, "Chapter 1.7 membranes for microbial fuel cells", in *Microbial Electrochemical Technology*, S. V. Mohan, S. Varjani, and A. Pandey, Eds., Biomass, Biofuels and Biochemicals, pages 143–194. Elsevier, 2019. ISBN 9780444640529. doi:10.1016/B978-0-444-64052-9.00007-8.
- [18] University of Cambridge, DoITPoMS. "Solid oxide fuel cells (sofcs)". (Retrieved January 7, 2020). URL https://www.doitpoms.ac.uk/tlplib/fuel-cells/high_temp_sofc.php.
- [19] D. R. Burgess, Jr., "Thermochemical data", in *NIST Chemistry WebBook, NIST Standard Reference Database Number* 69, L. P. J. and W. G. Mallard, Eds. National Institute of Standards and Technology, Gaithersburg MD, 20899. doi:10.18434/T4D303. (Retrieved January 7, 2020).
- [20] A. L. Dicks and D. A. J. Rand. *Fuel Cell Systems Explained*, 3rd Edition. John Wiley & Sons, 2018. ISBN 9781118613528. URL https://app.knovel.com/hotlink/toc/id:kpFCSEE01P/fuel-cell-systems-explained/fuel-cell-systems-explained.
- [21] Z. Kirova-Yordanova, "Exergy analysis of industrial ammonia synthesis", *Energy*, 29(12-15 SPEC. ISS.): 2373–2384, 2004. ISSN 0360-5442. doi:10.1016/j.energy.2004.03.036.
- [22] A. Vojvodic, A. J. Medford, F. Studt, F. Abild-Pedersen, T. S. Khan, T. Bligaard, and J. Nørskov, "Exploring the limits: A low-pressure, low-temperature Haber–Bosch process", *Chemical Physics Letters*, 598:108–112, 4 2014. ISSN 0009-2614. doi:10.1016/j.cplett.2014.03.003.
- [23] J. Szargut. Exergy Method: Technical and Ecological Applications. WIT Press, Southampton, U.K., 2005. ISBN 1853127531.
- [24] L. Riekert, "The efficiency of energy-utilization in chemical processes", *Chemical Engineering Science*, 29 (7):1613–1620, 1974. ISSN 0009-2509. doi:10.1016/0009-2509(74)87012-0.
- [25] J. Xiang, M. Calì, and M. Santarelli, "Calculation for physical and chemical exergy of flows in systems elaborating mixed-phase flows and a case study in an IRSOFC plant", *International Journal of Energy Research*, 28(2):101–115, 2 2004. ISSN 0363-907X. doi:10.1002/er.953.
- [26] D. M. Bierschenk, J. R. Wilson, and S. A. Barnett, "High efficiency electrical energy storage using a methane–oxygen solid oxide cell", *Energy & Environmental Science*, 4:944–951, 2011. doi:10.1039/C0EE00457J.
- [27] R. Cuellar, "Analysis of 5 MW hydrogen power system with thermal energy storage", Master's thesis, University of Jyväskylä, 2013. URL http://urn.fi/URN:NBN:fi:jyu-201406041915.
- [28] E. I. Al-musleh, D. S. Mallapragada, and R. Agrawal, "Continuous power supply from a baseload renewable power plant", *Applied Energy*, 122:83–93, 2014. ISSN 0306-2619. doi:10.1016/j.apenergy.2014.02.015.
- [29] F. Sebastiani, "Thermodynamic and Exergy Analysis of Reversible Solid Oxide Cell Systems", Master's thesis, Delft University of Technology, 2014.
- [30] M. Sensoli, "Power to Gas to Power Conversion Systems with Thermal Energy Storage", Master's thesis, Politecnico di Milano, 2015. URL http://hdl.handle.net/10589/116966.
- [31] R. Mor, "Energy, Exergy and Cumulative Exergy Losses Analysis of Bidirectional Solid Oxide Cell System", Master's thesis, Delft University of Technology, 2015.
- [32] S. Jensen, C. Graves, M. Mogensen, C. Wendel, R. Braun, G. Hughes, Z. Gao, and S. Barnett, "Large-scale electricity storage utilizing reversible solid oxide cells combined with underground storage of CO₂ and CH₄", *Energy & Environmental Science*, 8(8):2471–2479, 2015. ISSN 1754-5692. doi:10.1039/C5EE01485A.
- [33] C. H. Wendel, P. Kazempoor, and R. J. Braun, "A thermodynamic approach for selecting operating conditions in the design of reversible solid oxide cell energy systems", *Journal of Power Sources*, 301:93–104, 2016. ISSN 0378-7753. doi:10.1016/j.jpowsour.2015.09.093.

[34] C. H. Wendel, Z. Gao, S. A. Barnett, and R. J. Braun, "Modeling and experimental performance of an intermediate temperature reversible solid oxide cell for high-efficiency, distributed-scale electrical energy storage", *Journal of Power Sources*, 283:329–342, 2015. ISSN 0378-7753. doi:10.1016/j.jpowsour.2015.02.113.

- [35] C. H. Wendel, P. Kazempoor, and R. J. Braun, "Novel electrical energy storage system based on reversible solid oxide cells: System design and operating conditions", *Journal of Power Sources*, 276:133–144, 2015. ISSN 0378-7753. doi:10.1016/j.jpowsour.2014.10.205.
- [36] C. H. Wendel and R. J. Braun, "Design and techno-economic analysis of high efficiency reversible solid oxide cell systems for distributed energy storage", *Applied Energy*, 172:118–131, 2016. ISSN 0306-2619. doi:10.1016/j.apenergy.2016.03.054.
- [37] E. Reznicek, "Design and Simulation of Reversible Solid Oxide Cell Systems for Distributed Scale Energy Storage", Master's thesis, Colorado School of Mines, 2016. URL http://hdl.handle.net/11124/170645.
- [38] E. Reznicek and R. J. Braun, "Renewable Energy-Driven Reversible Solid Oxide Cell Systems for Grid-Energy Storage and Power-to-Gas Applications", *ECS Transactions*, 78(1):2913–2923, 2017. doi:10.1149/07801.2913ecst.
- [39] P. Di Giorgio and U. Desideri, "Potential of Reversible Solid Oxide Cells as Electricity Storage System", *Energies*, 9(8), 2016. ISSN 1996-1073. doi:10.3390/en9080662.
- [40] P. Mottaghizadeh, S. Santhanam, M. P. Heddrich, K. A. Friedrich, and F. Rinaldi, "Process modeling of a reversible solid oxide cell (r-SOC) energy storage system utilizing commercially available SOC reactor", *Energy Conversion and Management*, 142:477–493, 2017. ISSN 0196-8904. doi:10.1016/j.enconman.2017.03.010.
- [41] S. Santhanam, "Process Systems Analysis of Reversible Solid Oxide Cell (rSOC) Reactors for Electricity Storage and Sector Coupling", Doctoral thesis, University of Stuttgart, 2018. doi:10.18419/opus-10210.
- [42] S. Giannoulidis, "A Thermodynamic Investigation of an Electricity Storage System based on Reversible Solid Oxide Cells with Methanol as Fuel and Steam Electrolysis", Master's thesis, Delft University of Technology, 2018. URL http://resolver.tudelft.nl/uuid:9dce340b-e735-4307-9f96-49c093d96548.
- [43] G. Wang, A. Mitsos, and W. Marquardt, "Conceptual design of ammonia-based energy storage system: System design and time-invariant performance", *AIChE Journal*, 63(5):1620–1637, 5 2017. ISSN 0001-1541. doi:10.1002/aic.15660.
- [44] O. Siddiqui and I. Dincer, "Design and analysis of a novel solar-wind based integrated energy system utilizing ammonia for energy storage", *Energy Conversion and Management*, 195(April):866–884, 2019. ISSN 0196-8904. doi:10.1016/j.enconman.2019.05.001.
- [45] K. H. Rouwenhorst, A. G. van der Ham, G. Mul, and S. R. Kersten, "Islanded ammonia power systems: Technology review & conceptual process design", *Renewable and Sustainable Energy Reviews*, 114(April): 109339, 10 2019. ISSN 1364-0321. doi:10.1016/j.rser.2019.109339.
- [46] R. D. Farr and C. G. Vayenas, "Ammonia High Temperature Solid Electrolyte Fuel Cell", *Journal of The Electrochemical Society*, 127(7):1478–1483, 1980. doi:10.1149/1.2129934.
- [47] R. Metkemeijer and P. Achard, "Ammonia as a feedstock for a hydrogen fuel cell; reformer and fuel cell behaviour", *Journal of Power Sources*, 49(1):271–282, 1994. ISSN 0378-7753. doi:10.1016/0378-7753(93)01822-Y. Proceedings of the Third Grove Fuel Cell Symposium The Science, Engineering and Practice of Fuel Cells.
- [48] N. Gamanovich and G. Novikov, "Electrochemical Oxidation of Ammonia in High-Temperature Fuel Cells", *Russian Journal of Applied Chemistry*, 70(7):1136–1137, 1997. ISSN 1070-4272.
- [49] N. Gamanovich, V. Gorbunova, and G. Novikov, "Oxidation of alcohol-ammonia mixtures in high-temperature fuel cell with various electrodes", *Russian Journal of Applied Chemistry*, 74(5):746–749, May 2001. ISSN 1608-3296. doi:10.1023/A:1012780614904.

[50] A. Wojcik, H. Middleton, I. Damopoulos, and J. Van Herle, "Ammonia as a fuel in solid oxide fuel cells", *Journal of Power Sources*, 118(1-2):342–348, 2003. ISSN 0378-7753. doi:10.1016/S0378-7753(03)00083-1.

- [51] J. Staniforth and R. M. Ormerod, "Clean destruction of waste ammonia with consummate production of electrical power within a solid oxide fuel cell system", *Green Chem.*, 5:606–609, 2003. doi:10.1039/B307396N.
- [52] N. Dekker and G. Rietveld, "Highly Efficient Conversion of Ammonia in Electricity by Solid Oxide Fuel Cells", *Journal of Fuel Cell Science and Technology*, 3(4):499–502, 2006. ISSN 1550-624X. doi:10.1115/1.2349536.
- [53] G. Fournier, I. Cumming, and K. Hellgardt, "High performance direct ammonia solid oxide fuel cell", *Journal of Power Sources*, 162(1):198–206, 2006. ISSN 0378-7753. doi:10.1016/j.jpowsour.2006.06.047.
- [54] Q. Ma, R. Peng, Y. Lin, J. Gao, and G. Meng, "A high-performance ammonia-fueled solid oxide fuel cell", *Journal of Power Sources*, 161(1):95–98, 2006. ISSN 0378-7753. doi:10.1016/j.jpowsour.2006.04.099.
- [55] Q. Ma, R. R. Peng, L. Tian, and G. Meng, "Direct utilization of ammonia in intermediate-temperature solid oxide fuel cells", *Electrochemistry Communications*, 8(11):1791–1795, 2006. ISSN 1388-2481. doi:10.1016/j.elecom.2006.08.012.
- [56] Q. Ma, J. Ma, S. Zhou, R. Yan, J. Gao, and G. Meng, "A high-performance ammonia-fueled SOFC based on a YSZ thin-film electrolyte", *Journal of Power Sources*, 164(1):86–89, 2007. ISSN 0378-7753. doi:10.1016/j.jpowsour.2006.09.093.
- [57] G. Meng, C. Jiang, J. Ma, Q. Ma, and X. Liu, "Comparative study on the performance of a SDC-based SOFC fueled by ammonia and hydrogen", *Journal of Power Sources*, 173(1):189–193, 2007. ISSN 0378-7753. doi:10.1016/j.jpowsour.2007.05.002.
- [58] L. Zhang, Y. Cong, W. Yang, and L. Lin, "A Direct Ammonia Tubular Solid Oxide Fuel Cell", *Chinese Journal Of Catalysis*, 28(9):749–751, 2007. ISSN 1872-2067. doi:10.1016/S1872-2067(07)60062-X.
- [59] M. Ni, D. Y. Leung, and M. K. Leung, "Electrochemical modeling of ammonia-fed solid oxide fuel cells based on proton conducting electrolyte", *Journal of Power Sources*, 183(2):687–692, 2008. ISSN 0378-7753. doi:10.1016/j.jpowsour.2008.05.018.
- [60] M. Ni, D. Y. Leung, and M. K. Leung, "An improved electrochemical model for the NH₃ fed proton conducting solid oxide fuel cells at intermediate temperatures", *Journal of Power Sources*, 185(1):233–240, 2008. ISSN 0378-7753. doi:10.1016/j.jpowsour.2008.07.023.
- [61] M. Ni, D. Y. Leung, and M. K. Leung, "Mathematical modeling of ammonia-fed solid oxide fuel cells with different electrolytes", *International Journal of Hydrogen Energy*, 33(20):5765–5772, 2008. ISSN 0360-3199. doi:10.1016/j.ijhydene.2008.07.021.
- [62] A. Fuerte, R. Valenzuela, M. Escudero, and L. Daza, "Ammonia as efficient fuel for SOFC", *Journal of Power Sources*, 192(1):170–174, 2009. ISSN 0378-7753. doi:10.1016/j.jpowsour.2008.11.037.
- [63] M. Ni, "Thermo-electrochemical modeling of ammonia-fueled solid oxide fuel cells considering ammonia thermal decomposition in the anode", *International Journal of Hydrogen Energy*, 36(4):3153–3166, 2011. ISSN 0360-3199. doi:10.1016/j.ijhydene.2010.11.100.
- [64] J. Yang, A. F. S. Molouk, T. Okanishi, H. Muroyama, T. Matsui, and K. Eguchi, "A Stability Study of Ni/Yttria-Stabilized Zirconia Anode for Direct Ammonia Solid Oxide Fuel Cells", *ACS Applied Materials & Interfaces*, 7(51):28701–28707, 12 2015. ISSN 1944-8244. doi:10.1021/acsami.5b11122.
- [65] A. F. S. Molouk, T. Okanishi, H. Muroyama, T. Matsui, and K. Eguchi, "Electrochemical and catalytic behaviors of Ni-YSZ anode for the direct utilization of ammonia fuel in solid oxide fuel cells", *Journal of the Electrochemical Society*, 162(10):F1268–F1274, 2015. ISSN 1945-7111. doi:10.1149/2.1011510jes.
- [66] G. Cinti, G. Discepoli, E. Sisani, and U. Desideri, "SOFC operating with ammonia: Stack test and system analysis", *International Journal of Hydrogen Energy*, 41(31):13583–13590, 2016. ISSN 0360-3199. doi:10.1016/j.ijhydene.2016.06.070.

[67] A. Afif, N. Radenahmad, Q. Cheok, S. Shams, J. H. Kim, and A. K. Azad, "Ammonia-fed fuel cells: A comprehensive review", *Renewable and Sustainable Energy Reviews*, 60:822–835, 2016. ISSN 1879-0690. doi:10.1016/j.rser.2016.01.120.

- [68] B. Stoeckl, V. Subotić, M. Preininger, M. Schwaiger, N. Evic, H. Schroettner, and C. Hochenauer, "Characterization and performance evaluation of ammonia as fuel for solid oxide fuel cells with Ni/YSZ anodes", *Electrochimica Acta*, 298(2019):874–883, 2019. ISSN 0013-4686. doi:10.1016/j.electacta.2018.12.065.
- [69] D. Frattini, G. Cinti, G. Bidini, U. Desideri, R. Cioffi, and E. Jannelli, "A system approach in energy evaluation of different renewable energies sources integration in ammonia production plants", *Renewable Energy*, 99:472–482, 2016. ISSN 0960-1481. doi:10.1016/j.renene.2016.07.040.
- [70] G. Cinti, D. Frattini, E. Jannelli, U. Desideri, and G. Bidini, "Coupling Solid Oxide Electrolyser (SOE) and ammonia production plant", *Applied Energy*, 192:466–476, 4 2017. ISSN 0306-2619. doi:10.1016/j.apenergy.2016.09.026.
- [71] M. Penkuhn and G. Tsatsaronis, "Comparison of different ammonia synthesis loop configurations with the aid of advanced exergy analysis", *Energy*, 137:854–864, 2017. ISSN 0360-5442. doi:10.1016/j.energy.2017.02.175.
- [72] A. Sánchez and M. Martín, "Optimal renewable production of ammonia from water and air", *Journal of Cleaner Production*, 178:325–342, 3 2018. ISSN 0959-6526. doi:10.1016/j.jclepro.2017.12.279.
- [73] I. I. Cheema and U. Krewer, "Operating envelope of Haber–Bosch process design for power-to-ammonia", *RSC Advances*, 8(61):34926–34936, 2018. ISSN 2046-2069. doi:10.1039/C8RA06821F.
- [74] S. Giddey, S. Badwal, and A. Kulkarni, "Review of electrochemical ammonia production technologies and materials", *International Journal of Hydrogen Energy*, 38(34):14576–14594, 11 2013. ISSN 0360-3199. doi:10.1016/j.ijhydene.2013.09.054.
- [75] X. Guo, Y. Zhu, and T. Ma, "Lowering reaction temperature: Electrochemical ammonia synthesis by coupling various electrolytes and catalysts", *Journal of Energy Chemistry*, 26(6):1107–1116, 11 2017. ISSN 2095-4956. doi:10.1016/j.jechem.2017.09.012.
- [76] F. Jiao and B. Xu, "Electrochemical Ammonia Synthesis and Ammonia Fuel Cells", *Advanced Materials*, 1805173:1805173, 12 2018. ISSN 0935-9648. doi:10.1002/adma.201805173.
- [77] S. Chen, S. Perathoner, C. Ampelli, and G. Centi, "Chapter 2 Electrochemical Dinitrogen Activation: To Find a Sustainable Way to Produce Ammonia", in *Horizons in Sustainable Industrial Chemistry and Catalysis*, S. Albonetti, S. Perathoner, and E. A. Quadrelli, Eds., Volume 178 of *Studies in Surface Science and Catalysis*, pages 31–46. Elsevier, 2019. doi:10.1016/B978-0-444-64127-4.00002-1.
- [78] M. Dillig, J. Leimert, and J. Karl, "Planar High Temperature Heat Pipes for SOFC/SOEC Stack Applications", *Fuel Cells*, 14(3):479–488, 2014. doi:10.1002/fuce.201300224.
- [79] M. Dillig, T. Meyer, and J. Karl, "Integration of Planar Heat Pipes to Solid Oxide Cell Short Stacks", *Fuel Cells*, 15(5):742–748, 2015. doi:10.1002/fuce.201400198.
- [80] B. Yu, W. Q. Zhang, J. Chen, J. M. Xu, and S. R. Wang, "Advance in highly efficient hydrogen production by high temperature steam electrolysis", *Science in China, Series B: Chemistry*, 51(4):289–304, 2008. ISSN 1006-9291. doi:10.1007/s11426-008-0054-z.
- [81] B. Tjaden, M. Gandiglio, A. Lanzini, M. Santarelli, and M. Järvinen, "Small-scale biogas-SOFC plant: Technical analysis and assessment of different fuel reforming options", *Energy and Fuels*, 28(6):4216–4232, 2014. ISSN 1520-5029. doi:10.1021/ef500212j.
- [82] D. Noren and M. Hoffman, "Clarifying the Butler–Volmer equation and related approximations for calculating activation losses in solid oxide fuel cell models", *Journal of Power Sources*, 152:175–181, 2005. ISSN 0378-7753. doi:10.1016/j.jpowsour.2005.03.174.
- [83] E. Hernández-Pacheco, D. Singh, P. N. Hutton, N. Patel, and M. D. Mann, "A macro-level model for determining the performance characteristics of solid oxide fuel cells", *Journal of Power Sources*, 138(1):174–186, 2004. ISSN 0378-7753. doi:10.1016/j.jpowsour.2004.06.051.

[84] V. Gnielinski, S. Kabelac, M. Kind, H. Martin, D. Mewes, K. Schaber, and P. Stephan. *VDI-Wärmeatlas*, 10th Edition. Springer, Berlin, 2002.

- [85] I. K. Kookos, "On the diffusion in porous electrodes of SOFCs", *Chemical Engineering Science*, 69(1):571–577, 2012. ISSN 0009-2509. doi:10.1016/j.ces.2011.11.013.
- [86] H. Liu, "Ammonia synthesis catalyst 100 years: Practice, enlightenment and challenge", *Chinese Journal of Catalysis*, 35(10):1619–1640, 10 2014. ISSN 1872-2067. doi:10.1016/S1872-2067(14)60118-2.
- [87] A. T. Larson and A. P. Brooks, "Ammonia catalysts", *Industrial and Engineering Chemistry*, 18(12):1305–1307, 1926. doi:10.1021/ie50204a035.
- [88] Y. Huang, T. C. Merkel, and R. W. Baker, "Pressure ratio and its impact on membrane gas separation processes", *Journal of Membrane Science*, 463:33–40, 2014. ISSN 1873-3123. doi:10.1016/j.memsci.2014.03.016.
- [89] A. A. Moran, "Limits of Small Scale Pressure Swing Adsorption", Doctoral thesis, Cleveland State University, 2018. URL https://engagedscholarship.csuohio.edu/etdarchive/1050.
- [90] A. Witkowski, A. Rusin, M. Majkut, and K. Stolecka, "Comprehensive analysis of hydrogen compression and pipeline transportation from thermodynamics and safety aspects", *Energy*, 141:2508–2518, 2017. ISSN 0360-5442. doi:10.1016/j.energy.2017.05.141.
- [91] E. Tzimas, C. Filiou, S. D. Peteves, and J.-B. Veyret. "Hydrogen Storage: State-of-the-Art and Future Perspective". Technical report, European Commission Joint Research Centre, Petten, The Netherlands, 2003. URL http://publications.jrc.ec.europa.eu/repository/handle/JRC26493.
- [92] H. D. Baehr. *Thermodynamik: Grundlagen und technische Anwendungen*. Springer, Berlin, 2006. ISBN 9783540325130.
- [93] N. Hartmann, O. Vöhringer, C. Kruck, and L. Eltrop, "Simulation and analysis of different adiabatic Compressed Air Energy Storage plant configurations", *Applied Energy*, 93:541–548, 2012. ISSN 0306-2619. doi:10.1016/j.apenergy.2011.12.007. (1) Green Energy; (2) Special Section from papers presented at the 2nd International Energy 2030 Conference.
- [94] G. F. Hundy, A. R. Trott, and T. C. Welch. *Refrigeration and Air Conditioning*, 4th Edition. Butterworth-Heinemann/Elsevier, Oxford, U.K., 2008. ISBN 9780750685191.
- [95] G. Lauermann, P. Häussinger, R. Lohmüller, and A. M. Watson, "Hydrogen, 1. properties and occurrence", in *Ullmann's Encyclopedia of Industrial Chemistry*, pages 1–15. Wiley-VCH, 2013. ISBN 9783527306732. doi:10.1002/14356007.a13_297.pub3.
- [96] N. Thambiraj, C. Suciu, I. Waernhus, A. Vik, and A. C. Hoffmann, "Effect of oxygen depletion to the cathode on the working of solid oxide fuel cells", *ECS Transactions*, 78(1):875–887, 2017. ISSN 1938-6737. doi:10.1149/07801.0875ecst.
- [97] M. M. Kenisarin, "High-temperature phase change materials for thermal energy storage", *Renewable and Sustainable Energy Reviews*, 14(3):955–970, 2010. ISSN 1364-0321. doi:10.1016/j.rser.2009.11.011.